Experimental and Numerical Nonlinear Dynamics and Stress Field Analysis of Post-Buckled Composite Plates

Han-Gyu Kim

A dissertation
submitted in partial fulfillment of the
requirements for the degree of

Doctor of Philosophy

University of Washington

2019

Reading Committee:

Richard Wiebe, Chair

Gregory R. Miller

S. Michael Spottswood

Program Authorized to Offer Degree:
Civil Engineering

University of Washington

Abstract

Experimental and Numerical Nonlinear Dynamics and Stress Field Analysis of Post-Buckled Composite Plates

Han-Gyu Kim

Chair of the Supervisory Committee:
Richard Wiebe
Civil and Environmental Engineering

Thermally-buckled composite panels in aircraft may experience dynamic snap-through due to aerodynamic loading, which can accelerate damage growth (or delamination) in these structures. Therefore, characterizing post-buckled dynamic response and corresponding stress fields can be an important step to help assure the structural integrity of composite structures. To address this issue, this work experimentally and numerically investigates nonlinear dynamics and snap-through of post-buckled laminated composite plates under harmonic loading. In addition, stress fields induced by these phenomena are simulated to explore their potential impact on the fatigue failure of composite structures.

The experimental investigation made in this work is intended to lead to a better fundamental understanding of the aforementioned phenomena and to provide benchmark data for robust model validation in the nonlinear regime. The dynamic response of a post-buckled composite specimen under various harmonic scenarios is captured using a full-field digital image correlation system. The spatio-temporal complexity and parameter sensitivity of the dynamic response are explored and the snap-through boundaries of the specimen are characterized.

Several numerical models are built using in-house finite element codes written in MATLAB and are calibrated using the static full-field measurement of the buckled shape of the

specimen. The primary objectives of the modeling done in this work are to develop reliable simulation tools for numerical analysis of nonlinear dynamics, and to investigate the impact of nonlinear dynamics and snap-through on stress fields. A model based on the classical laminated plate theory and nonconforming (semi-C^1 continuity) cubic Hermite elements (free of shear locking) is shown to achieve excellent agreement with the experimental observations including the snap-through boundaries. As a 'truth' model in the thin plate limit, this model provides a new tool for developing benchmark data (displacement fields) for validation of computationally-demanding models which involve high computational costs or potential locking issues.

For accurate and direct computation of stress fields, another model is generated based on the first-order shear deformation theory and bi-linear elements (C^0 continuity). The shear and membrane locking issues of this model are exposed through linear and nonlinear analyses of its displacement and stress fields. To address these locking issues, two types of assumed strain methods are employed: the mixed interpolation of tensorial components (MITC4) and the enhanced assumed strain (EAS) method. The geometrically-nonlinear analysis presented herein shows that the EAS method effectively controls both shear and membrane locking, whereas the MITC4 method alleviates only shear locking with strong oscillations of membrane stresses which imply the occurrence of membrane locking.

The simulation results obtained using the EAS model reveal that post-buckled response generates larger-amplitude stresses than the pre-buckled cases and that snap-through can induce a significant increase in stress amplitudes, thereby potentially affecting fatigue life. By developing reliable simulation tools for analysis of nonlinear dynamics and consequent stress fields, this work makes an important step forward in investigating the impact of these phenomena on the structural integrity of composite structures for supersonic- or hypersonic-speed flight.

TABLE OF CONTENTS

ACKNOWLEDGMENTS

I would first like to thank my adviser, Professor Richard Wiebe. Since I first met him, he has always been an experienced adviser, a thoughtful mentor, and a good friend to me for the past five years. Without his vision, inspiration, trust, and patience, I could not have achieved any of the work presented herein. He showed me a perfect example of a scholar and of a mentor which I wish to pursue in my postdoctoral career. Whenever I reflect on my time at the graduate school, I realize how fortunate I am to have a chance to work with him.

I would like to sincerely thank my committee members, Professors Gregory R. Miller, Marco Salviato, I. Y. (Steve) Shen, Mark E. Tuttle, and Jinkyu Yang, and Dr. S. Michael Spottswood. It was a true honor for me to have these members in my committee. All of them are respected experts in my research field and gave me valuable advice and insights for my research along with strong support for my postdoctoral career. I would like to thank Professor Miller and Dr. Spottswood once again for serving as my reading committee. They went the extra mile to make thorough review of my dissertation. Their suggestions and inputs helped this dissertation become more complete.

Many people supported the experimental work presented herein. I would like to express my gratitude to Dr. Spottswood for granting access to the Air Force Research Laboratory (AFRL) equipment, and to Dr. David A. Ehrhardt and Dr. Ricardo A. Perez for their support at AFRL. I would also like to thank Bill Kuykendall for his support at the Mechanical Test Lab, Michelle Hickner for her support at the Composites Lab, and J. Sean Yeung for his help at the Computed Tomography Facility.

Without my mentors, colleagues, and family, I could not have completed my degree suc-

cessfully. I would like to extend my thanks to Professors Sung-Uk Choi, Jun Hwan Lee, Sang-Ho Lee, Yun Mook Lim, and Hong Gyoo Sohn at Yonsei University, and Professor Chungwook Sim at the University of Nebraska for their support for and advice on my academic career decision. I would like to thank Professors Jun Hwan Lee and Chungwook Sim once again for all their support and encouragement given to me for the past five years. I would also like to thank my friends and colleagues at the University of Washington, Kamal A. Ahmed, Solomon A. Haile, Seunghyun Ko, Minyong Lee, Chi-Pu (Tom) Lin, Huy Si Nguyen, Xinsheng (Shawn) Qin, Andrew O. Winter, and Tianye (Andrew) Yang for their great help throughout my graduate program. Finally, I would like to thank my lovely family and my wonderful wife, Ji Eun for giving me their support and love.

DEDICATION

to my parents, Heesung, Kwisook, Yeomin, and Bokju, and to my lovely wife, Ji Eun

Chapter 1
INTRODUCTION

1.1 Motivation

Constrained panels of airplanes and space shuttles can buckle due to thermally-induced axial loading such as aerodynamic heating during high-speed flight [83]. Such post-buckled structures may also experience conventional fatigue in linear regimes. However, in extreme cases represented by dynamic snap-through, the structures are subjected to large-amplitude deformations, which could potentially lead to low-cycle fatigue failure of the structures.

While this phenomenon is important in both metallic and composite structures, this work focuses on laminated composites. The applications of composite materials have significantly grown over the last two decades in diverse industrial fields such as aerospace, automotive, and civil engineering [25, 26, 54, 104]. For example, 50 % of the airframe and primary structure (including the fuselage and wings) of the Boeing 787 (see Fig 1.1) is made up of composite materials [29]. For military aircraft, the Lockheed Martin F-35 has a composite fuselage and wing structure, and composites comprise 35 % of its airframe weight [26, 61].

The aforementioned aerodynamic phenomenon poses a potential threat to structural integrity of these composite structures. For example, potentially high strains (and consequent high stresses) that post-buckled composite structures experience under dynamic loading may accelerate initiation and propagation of delamination in these structures, which can lead to loss of the global stability [1]. Delamination appears as debonding of adjacent layers and is one of the most dominant failure-modes of laminated composite structures [105]. Therefore, characterizing post-buckled dynamic response and corresponding stress fields can be a pivotal step in developing reliable simulation tools to predict consequent damage growth, thereby improving the safety of composite structures.

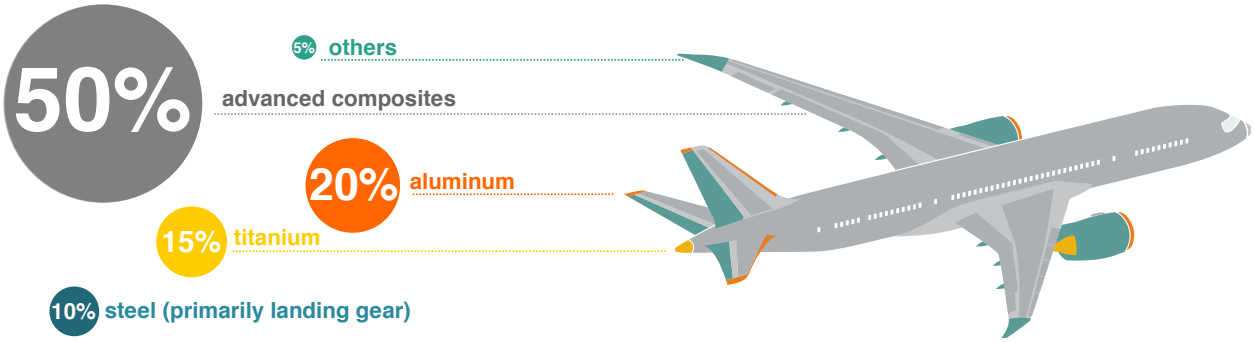

Figure 1.1: Materials in the airframe and primary structure of the Boeing 787. This figure was reproduced based on Ref [29].

Despite such importance, simulation of dynamic snap-through of post-buckled plates remains challenging and in the case of composite laminates, to the best of the author's knowledge, very little research has been done. Furthermore, most of the studies on nonlinear dynamics focus on characterizing the dynamic response of structures in terms of displacement fields but do not cover its impact on stress fields and fatigue. To address this issue, this work experimentally and numerically investigated nonlinear dynamics and snap-through of post-buckled composite plates under harmonic loading conditions. In addition, stress fields induced by these phenomena were analyzed through dynamic simulation using reliable numerical models, which were developed in-house for this work.

The primary focus of this work is on investigation of nonlinear dynamics and corresponding stress fields which post-buckled composite structures can experience. The potential impact of these phenomena on the structural integrity of composite structures is of particular interest with respect to fatigue. Some of the fundamental concepts relevant to these topics are introduced in the following sections.

1.2 Nonlinear dynamics of post-buckled systems

Post-buckled structures can demonstrate nonlinear and potentially chaotic behavior, including snap-through between their stable equilibria as illustrated in Fig 1.2. These phenomena

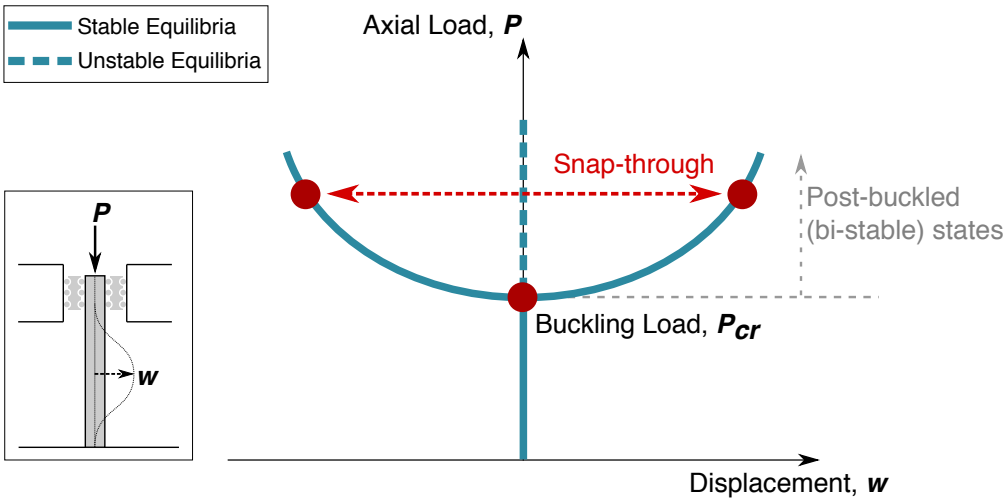

Figure 1.2: Schematic drawings of a structure under axial loading and its equilibrium path.

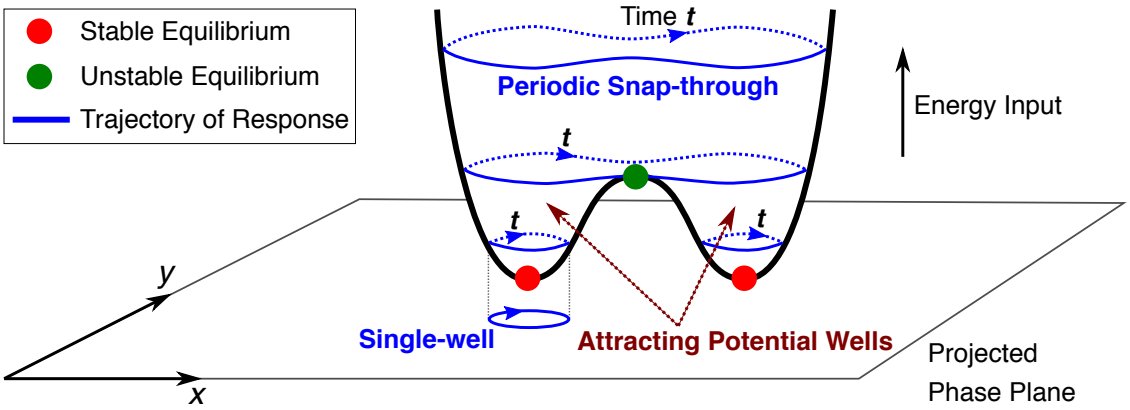

Figure 1.3: Schematic drawings of the energy contour and projected phase portrait of the post-buckled (bi-stable) structure shown in Fig 1.2. The contour and portrait were drawn based on the work of Strogatz [85].

are not observed in familiar linear systems. Previous works have investigated the nonlinear dynamics of bi-stable metallic systems such as single degree-of-freedom (DOF[1]) linkage systems [97] and post-buckled beams (or shallow arches) [18, 96, 98]. Some results relevant to the work herein are summarized in this section.

[1]Its plural 'degrees of freedom' is denoted by DOFs in this work.

The characteristic behaviors of post-buckled structures under harmonic loading are illustrated in Fig 1.3. The energy contour forms two attracting potential wells around two stable equilibria (static) due to the bi-stability of the structures. With small energy input (i.e., small-amplitude loading), such structures oscillate around one of their stable equilibria inside one of the two wells. These oscillations are projected onto the phase plane as elliptical trajectories and are called the single-well response of the structures. As forcing amplitudes increase at the same forcing frequency (i.e., larger energy input), the response trajectories may jump into the other well (i.e, snap-through) and the structures oscillate around the stable equilibrium within this well. This transition can intermittently occur in a chaotic manner and thus is called chaotic snap-through (c-snap). With further increase in the forcing amplitude, the structures can demonstrate persistent snap-through in a (nearly) periodic manner, which is named periodic snap-through (p-snap). In this case, the response trajectories travel 'above' the two wells encompassing both of the stable equilibria. The forcing parameters which cause transitions between the single-well and snap-through response types form boundaries between the response regions in the harmonic forcing parameter (HFP) space. These thresholds are named snap-through boundaries. These nonlinear systems are extremely sensitive to initial conditions and thus co-existing responses are usually present in the HFP space [95]. The work herein explored these phenomena for bi-stable composite plates.

Crucially, these complex nonlinear responses possible in post-buckled systems make model validation using only a small set of experimental data insufficient. For a more robust validation, this work characterized and compared experimental and numerical snap-through boundaries in the HFP space. This ensures that the model is capable of accurately capturing the rich and complex behaviors observed in bi-stable systems.

1.3 Fatigue of composite structures

Fracture and fatigue induced by mode-I delamination (see Fig 1.4 for fracture modes) have been extensively covered in the literature. However, mode-II delamination still remains

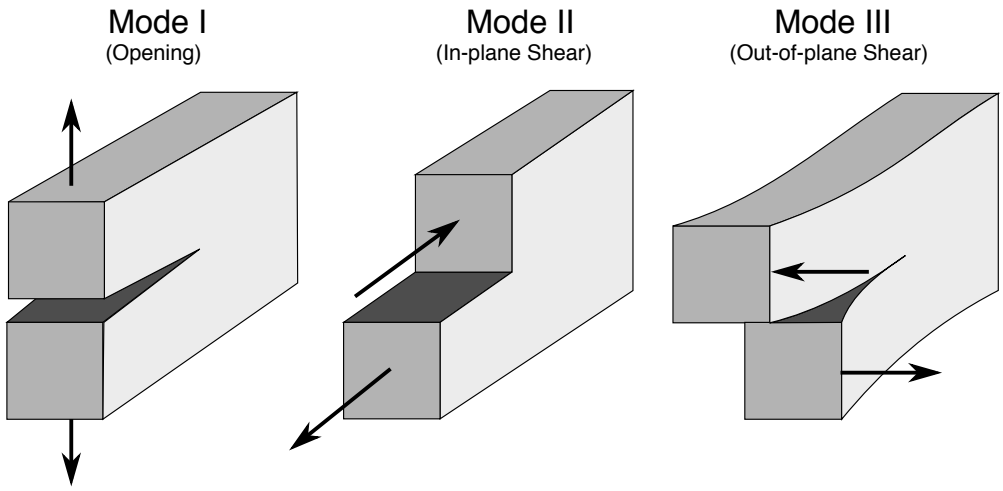

Figure 1.4: Fracture modes. This figure was drawn based on the work of Anderson [4].

obscure due to its unstable crack propagation and difficulties in measuring mode-II delamination growth [82]. Nonetheless, delamination propagates predominantly in mode II in many practical circumstances as shown in the case of composite plates under low velocity impact [19]. For example, the first editions of the ASTM standard test methods for mode-I fracture and fatigue were published in 1994 [5] and 1997 [6], respectively. On the other hand, the first ASTM manual for mode-II fracture testing [7] was released in 2014, and there still is no standard test manual for mode-II fatigue.

One of the primary focuses of this work is on investigating the impact of stress fields induced by nonlinear dynamics on delamination growth in fatigue of composite structures. For constrained composite panels under transverse loading, delamination is expected to propagate primarily in mode II. This work made a preliminary investigation of mode-II fatigue through lab testing. Some results are discussed here; however, they are a part of a larger project that will be completed in the future. The tests were conducted using an end-notched flexure (ENF) test setup (see Fig 1.5), which was based on ASTM D7905/D7905M-14 [7]. The loading condition for the test and delamination growth with loading cycles are illustrated in Fig 1.6. The digital image correlation (DIC) analysis of transverse shear strains

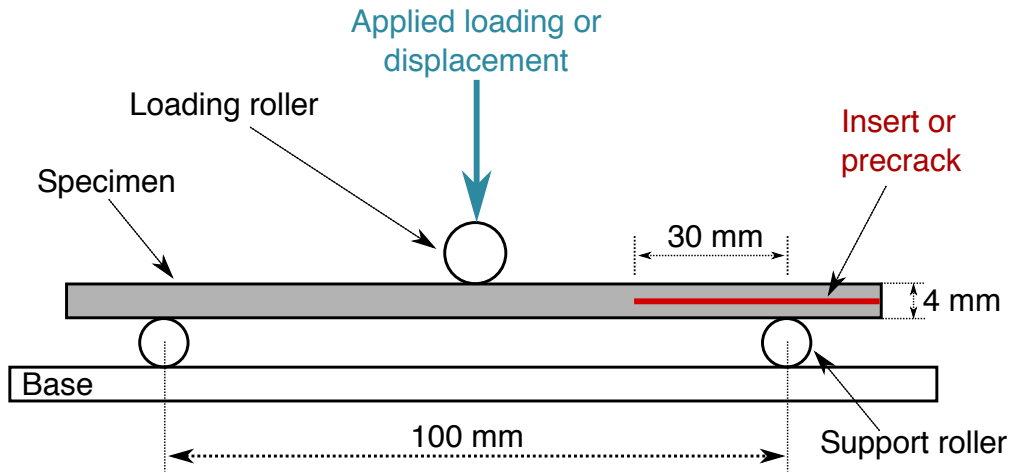

Figure 1.5: Schematic drawings of an ENF test setup. The figure was drawn based on Ref [7].

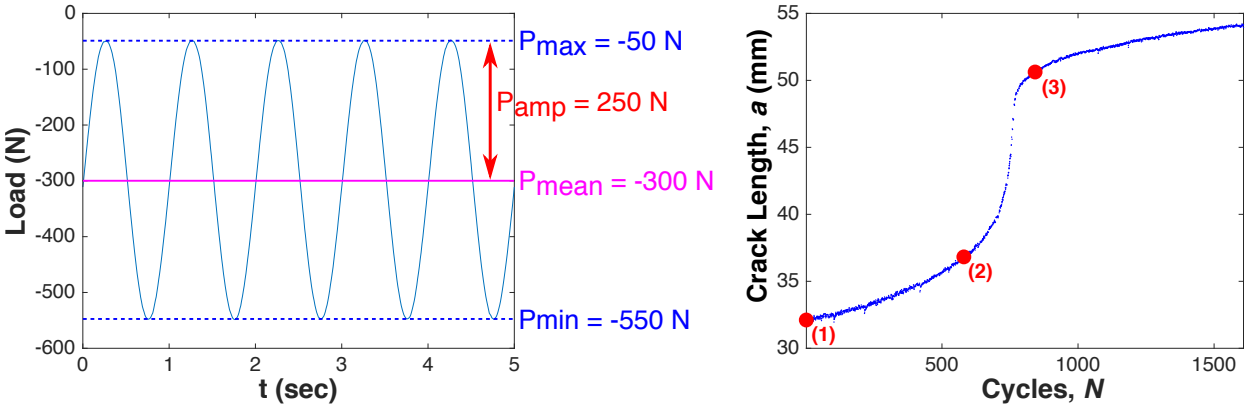

(a) (b)

Figure 1.6: Loading condition for a fatigue test using the experimental setup shown in Fig 1.5 and resulting crack growth. (a) Quasi-static cyclic loading in a wave form applied to the midspan of the specimen. The forcing frequency was 2 Hz. (b) Crack growth with loading cycles. The crack length was estimated by a compliance method proposed in the ASTM manual [7] and well matched the DIC measurement shown in Fig 1.7.

in the crack growth stages is shown in Fig 1.7. These test results indicate that composite structures under inertially-applied transverse dynamic loading can also experience fatigue predominantly in mode II depending on loading amplitudes. Using the data collected in

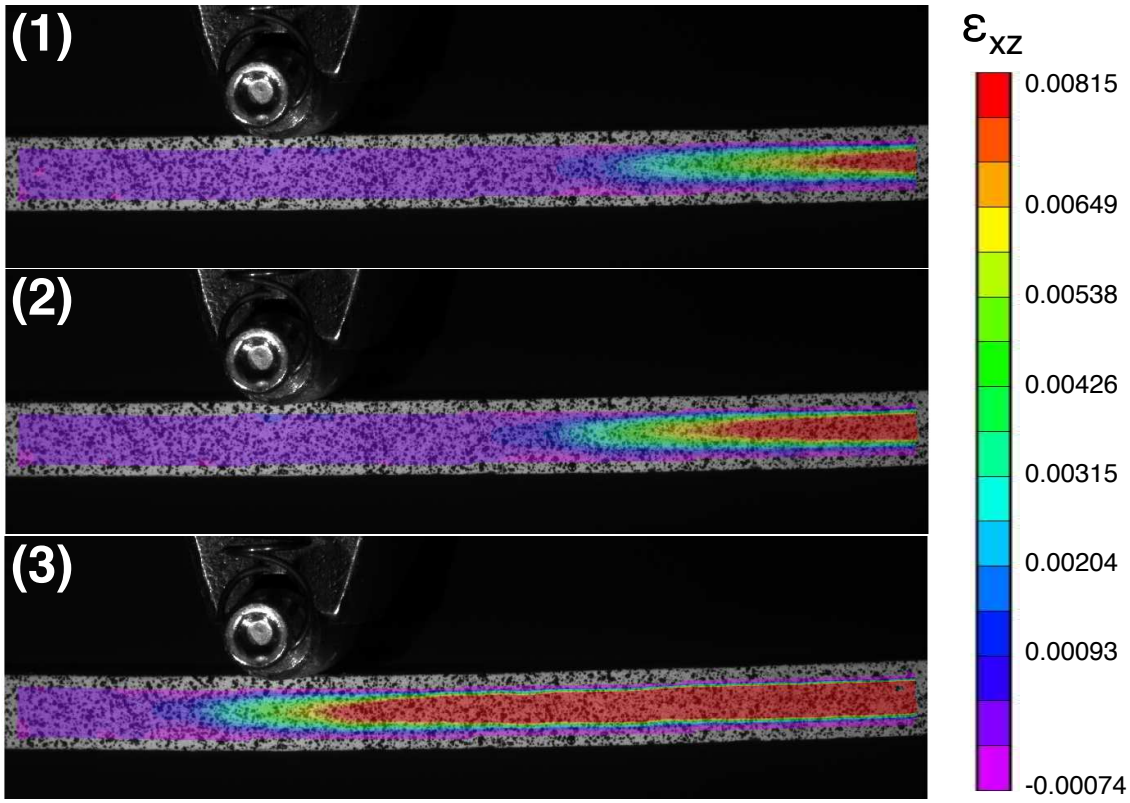

Figure 1.7: DIC analysis of transverse shear strains ε_{xz} at the crack growth levels shown in Fig 1.6b: (1) the initial state, (2) 620 cycles, and (3) 850 cycles. The numbers in the parentheses correspond to the numbers indicated in Fig 1.6b. The crack tip is expected to be located in the cyan regions.

these tests, delamination in mode-II fracture and fatigue will be further investigated in future work to characterize fracture process zones using cohesive crack models [12]. In addition, based on stress analysis using numerical models developed in this work, fatigue tests with inertially-applied loading will be designed and be conducted in future work.

1.4 Overview

In Chapter 2, experimental results are presented and relevant physics are discussed. The experimental investigation made in this work was intended to acquire a better fundamental understanding of nonlinear dynamics and snap-through, and to create benchmark data for

model validation. For experimental characterization of nonlinear dynamics and snap-through boundaries, a post-buckled composite plate specimen was tested under various harmonic loading scenarios. The static full-field[2] measurement of the buckled shape of the specimen was made using a DIC system. Using the system, the three-dimensional (3-D) snapshots of the specimen's characteristic behaviors under harmonic loading were taken and the spatio-temporal complexity of the behaviors was analyzed. In addition, to explore the parameter sensitivity of the specimen, frequency-sweep tests were performed using a double-point laser vibrometer. Finally, damping of the specimen was investigated through free-decay tests.

In Chapter 3, a numerical model of the post-buckled specimen is introduced, and its simulation results are presented. Based on the static full-field measurement of the buckled shape of the specimen, the model was generated by adopting the classical laminated plate theory along with nonconforming (semi-C^1 continuity) cubic Hermite elements and Rayleigh damping. The theory is comparable to Euler–Bernoulli beam theory and thus disregards deformations induced by transverse shear strains. Therefore, the model cannot directly predict transverse shear strains using strain-displacement relations. The damping was calibrated based on the experimental data of the free-decay tests. The nonlinear dynamic behaviors of the model were simulated under various harmonic loading scenarios and were compared with the experimental observations in displacement fields.

In Chapter 4, the model is extended to a shear-deformable model based on the first-order shear deformation theory, which is comparable to Timoshenko beam theory and assumes constant transverse strain fields through the plate thickness. This extension was done to achieve direct and accurate computation of transverse shear strain and stress fields. The model was built using four-node elements and bi-linear interpolations (C^0 continuity). The performance of the model was assessed by comparing it with closed-form solutions to cylindrical bending problems. The comparison results and relevant issues, in particular shear locking, are

[2]The term 'full-field' here denotes a full displacement field (i.e., displacements in all of x-, y-, and z-axes in Cartesian coordinates) and full coverage of the surface of specimens in contrast to single-/multiple-point measurement.

discussed. The models presented in Chapters 3 and 4 are based on the displacement-based variational principle and thus these two chapters are combined in 'Part I. Modeling and simulation: displacement-based approach'.

In Chapter 5, remedies for locking issues and their implementation are introduced. To address locking, this work adopted assumed strain methods. Numerical implementation of these methods and their effectiveness in alleviating shear locking are discussed.

In Chapter 6, geometrically-nonlinear models of the post-buckled specimen are generated based on the assumed strain methods. The modeling results are compared with the full-field DIC measurement for validation. The initial static stress fields of the post-buckled specimen (i.e., at time $t = 0$) are predicted using the models. The stress analysis shows another locking issue called membrane locking and its remedy is discussed.

In Chapter 7, dynamic simulation and stress analysis results are presented. Using the model introduced in Chapter 6, the nonlinear dynamic behaviors of the specimen under harmonic loading were simulated and the corresponding stress fields were analyzed. Based on the stress analysis, the impact of nonlinear dynamics and snap-through on fatigue of composite structures is discussed. The models introduced in Chapters 5 to 7 are based on assumed strain methods and thus these chapters are included in 'Part II. Modeling and simulation: assumed strain-based approach'.

Finally, in Chapter 8, a summary of the findings and contributions is made with a brief description of future work.

Chapter 2

EXPERIMENTAL NONLINEAR DYNAMICS OF POST-BUCKLED PLATES

2.1 Introduction

The nonlinear dynamics and characteristic response types of bi-stable metallic systems such as single DOF linkage systems and post-buckled beams were introduced in the previous chapter. In this chapter, these phenomena are experimentally investigated for post-buckled composite plates in order to discuss relevant physics and obtain benchmark data for modeling.

For the experimental investigation, a laminated plate specimen in the post-buckled state was tested under high-frequency harmonic loading, which was inertially applied by an electrodynamic shaker. The initially-buckled shape of the specimen was measured in 3-D full field prior to the dynamic tests. This measurement was intended to provide data required for calibration of the initial static equilibrium of numerical models. For full-field measurement, this work employed the DIC technique, particularly the binocular stereovision technique [28]. Using a DIC system, the dynamic response of the post-buckled specimen under harmonic loading scenarios was captured in full field. The spatio-temporal complexity of the dynamic response of the specimen is discussed based on the DIC data.

In addition, the sensitivity of the dynamic response of the specimen to forcing parameters was explored through frequency-sweep tests. A laser vibrometer (velocity-sensing) was used for these tests instead of the DIC system because the DIC technique inherently generates large data sets and thus was not suitable for this type of prolonged test. Based on the test results, the snap-through boundaries of the specimen are characterized in the HFP space. The snap-through boundaries provide a robust tool for model validation, especially given the complex response possible in post-buckled systems.

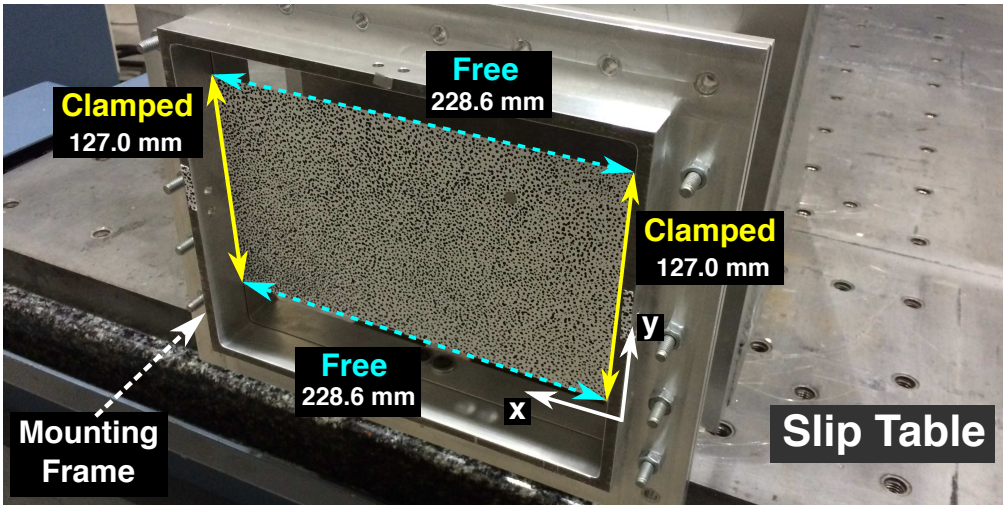

Figure 2.1: The test article with clamped-clamped-free-free boundary conditions. The specimen was post-buckled (not visible at photograph scale).

Finally, damping of the specimen was investigated through free-decay tests using a displacement-sensing laser sensor. These tests were intended to obtain parameters required for damping calibration of numerical models.

2.2 Experimental setup for forced dynamic tests

2.2.1 Fabrication and mounting of the specimen

A laminated composite plate specimen was fabricated using a plain-weave prepreg[1], T800H-6K/3900-2. The weave prepreg has orthotropic material properties:

$$E_{11} = E_{22} = 75.9 \text{ GPa}, \; G_{12} = 3.96 \text{ GPa}, \text{ and } \nu_{12} = \nu_{21} = 0.037. \tag{2.1}$$

These in-plane properties were obtained from previous work [37], in which out-of-plane plane properties were not covered. Shear-deformable plate models generated in this work, however, require transverse shear moduli (G_{13} and G_{23}). Therefore, these properties of the prepreg

[1]A prepreg is an abbreviation of pre-impregnated fibers. Prepregs are manufactured in a form of sheets which contain fibers in designed orientations and are impregnated with resin [86].

were estimated in this work following the method used for the in-plane properties in the previous work. This estimation process is described in Appendix A, in which the properties are shown to be

$$G_{13} = G_{23} = 3.32 \text{ GPa}. \tag{2.2}$$

The specimen was laid up as $[45]_4$ (i.e., four prepreg layers with 45 degree fiber angle[2]). The dimensions were $228.6 \times 127.0 \times 0.72$ mm for length, width, and thickness, respectively. The lamina and laminate constitutive relations are presented in detail in Appendix B. Using the relations, the nonzero laminate stiffness components of the specimen required for modeling are given by

$$\begin{aligned} &A_{11} = A_{22} = 31.2 \text{ MPa-m}, \ A_{12} = 25.5 \text{ MPa-m}, \\ &A_{44} = A_{55} = 2.39 \text{ MPa-m}, \ A_{66} = 26.3 \text{ MPa-m}, \\ &D_{11} = D_{22} = 1.35 \text{ Pa-m}^3, \ D_{12} = 1.10 \text{ Pa-m}^3, \ D_{66} = 1.14 \text{ Pa-m}^3, \end{aligned} \tag{2.3}$$

where $\mathbf{A}$ and $\mathbf{D}$ are extensional and bending stiffness, respectively, and the bending-extensional coupling stiffness $\mathbf{B} = \mathbf{0}$.

As shown in Fig 2.1, the post-buckled specimen was under clamped-clamped-free-free boundary conditions: clamped at $x = 0,\ 228.6$ mm but free at $y = 0,\ 127.0$ mm. The mounting frame provided the clamped boundaries. The initially-flat specimen was mechanically buckled by setting the boundary at $x = 228.6$ mm free to move along the x-axis and applying mechanical pressure to the plate. The specimen had random speckles of white and black on its surface for DIC measurement.

2.2.2 Equipment setup

The equipment setup for the dynamic tests is shown in Fig 2.2. The frame was mounted onto the slip table of an electrodynamic shaker, which inertially applied harmonic loading

[2]For the layup $[45]_4$, the weave prepreg layers used in this work had fibers oriented in ± 45 degrees (i.e., generally orthotropic laminae, see Appendix B).

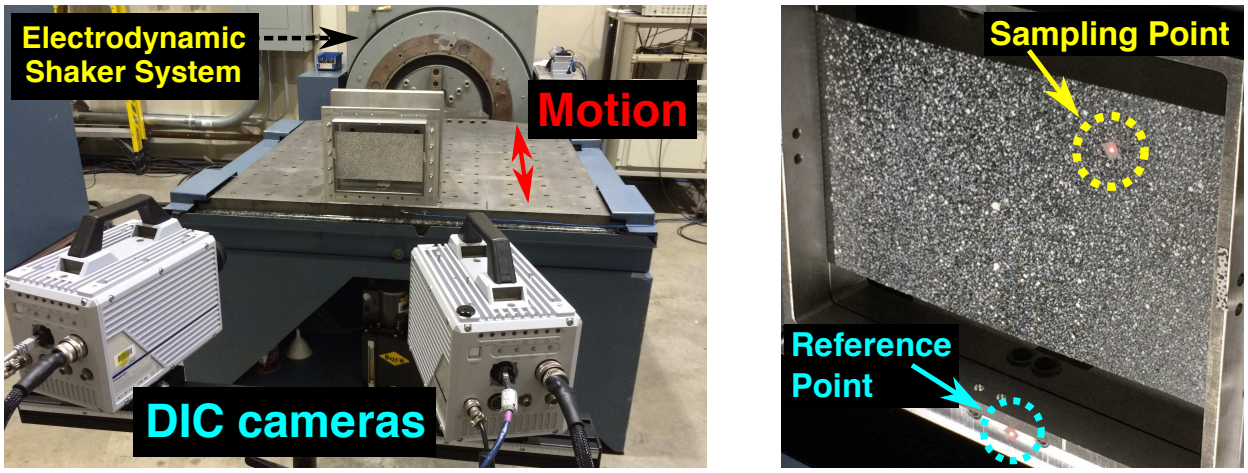

(a) (b)

Figure 2.2: The experimental setup for: (a) the DIC measurement, and (b) the vibrometer measurement.

to the specimen. Two DIC cameras, Photron FASTCAM SA5 (see Fig 2.2a), were used for full-field measurement. For frequency-sweep tests, a double-point laser Doppler vibrometer, Polytec OFV 512, was used. As shown in Fig 2.2b, one of the vibrometer's laser points (the sampling point) was pointed on the specimen, while the other point (the reference point) was pointed on the bottom of the frame to allow for measurement of the specimen's velocity relative to the frame.

2.2.3 Static measurement of the post-buckled specimen

The initially-buckled shape of the specimen prior to dynamic tests (i.e., at time $t = 0$) was captured by the DIC cameras with 13475 sampling points. The resolution of the static images was 1024×1024 pixels. The static images were processed with a facet (or subset [28]) size of 20×20 pixels with a 5-pixel overlap. The z-axis resolution was 8.4 μm.

The reconstructed shape is illustrated in Fig 2.3. A part of the shape near the boundary at $x = 228.6$ mm was not captured since the speckle pattern was not painted on this region to ensure smooth movement and adjustments of the boundary between the clamps during

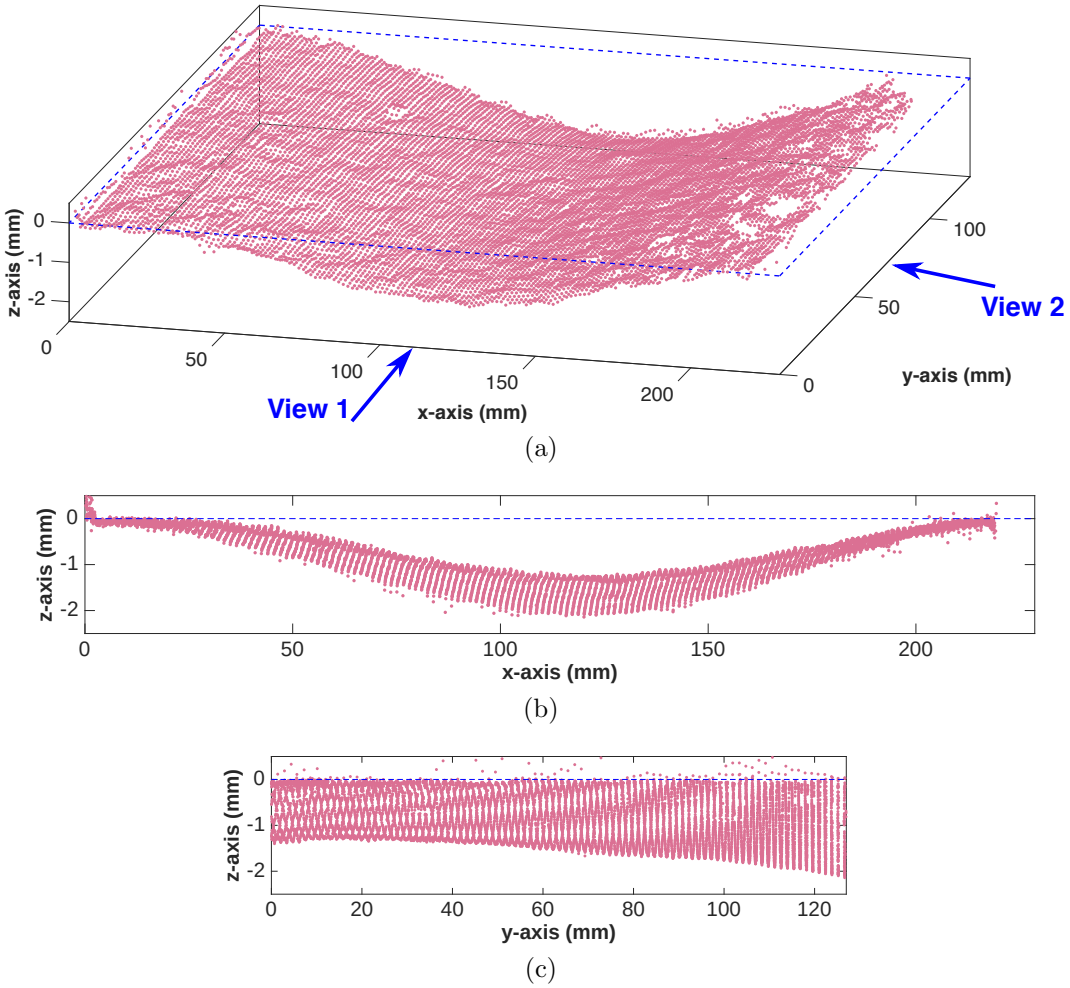

Figure 2.3: The static DIC measurement of the initially-buckled shape of the specimen prior to dynamic tests. The z-axes are exaggerated for interpretation of the depth measurement. The blue dotted rectangle indicates the position of the initially-flat specimen. (a) The 3-D buckled shape of the specimen. (b) View 1: the shape along the x-axis. (c) View 2: the shape along the y-axis.

the buckling process. It can be observed from View 1 (see Fig 2.3b) that the buckled shape was slightly asymmetric along the x-axis. In addition, View 2 (see Fig 2.3c) shows that the buckled depth (i.e., transverse displacement along the z-axis) was asymmetric along the y-axis and the largest buckled depth varied from 1.3 to 2.1 mm along this axis. It is suspected that these phenomena occurred because the pressure applied to buckle the specimen could not

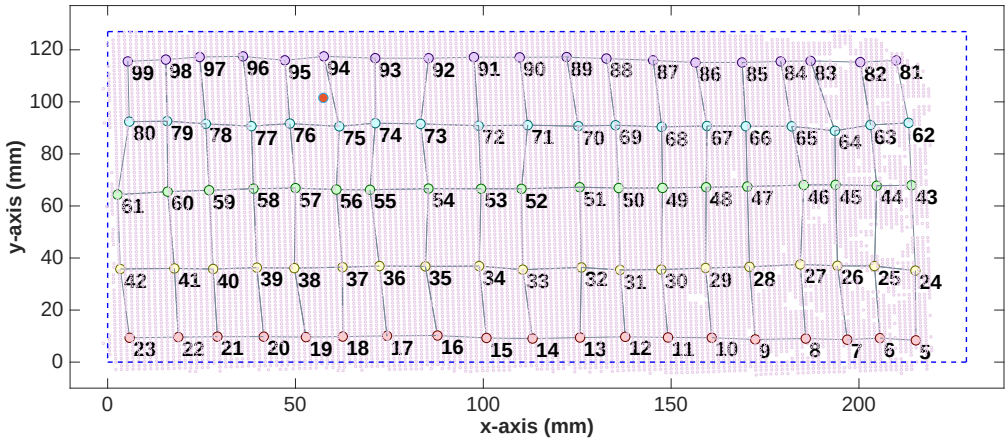

Figure 2.4: The dynamic DIC sampling points are superimposed on the static measurement (red hollow circles) illustrated in Fig 2.3. The points numbered 1 to 4 are the reference points on the frame and are not drawn here. The red-circular point between the points number 75 and 94 is the vibrometer sampling point.

be carefully controlled. This spatial complexity made modeling more challenging; however, buckling is hardly expected to occur perfectly or symmetrically in reality and thus analysis of dynamic behaviors exhibited by this asymmetrically-buckled specimen can provide a better insight into realistic problems.

2.2.4 Methodology for dynamic DIC measurement

The number of DIC sampling points used for the static measurement could not be maintained for dynamic tests due to a drastic increase of data size with time. Instead, 99 points were chosen as shown in Fig 2.4; however, those points were enough to capture the 3-D deflected shapes of the specimen with a 2000 Hz sampling frequency. The points numbered 1 to 4 are the reference points tracing the movement of the frame (i.e., the base motion) to allow for measurement of the relative displacement of the specimen. The resolution of the dynamic images was 1024×1024 pixels. The images were processed with a facet size of 20×20 pixels. For the dynamic DIC measurement, overlap was not implemented due to a large number of images. The z-axis resolution was 8.4 μm.

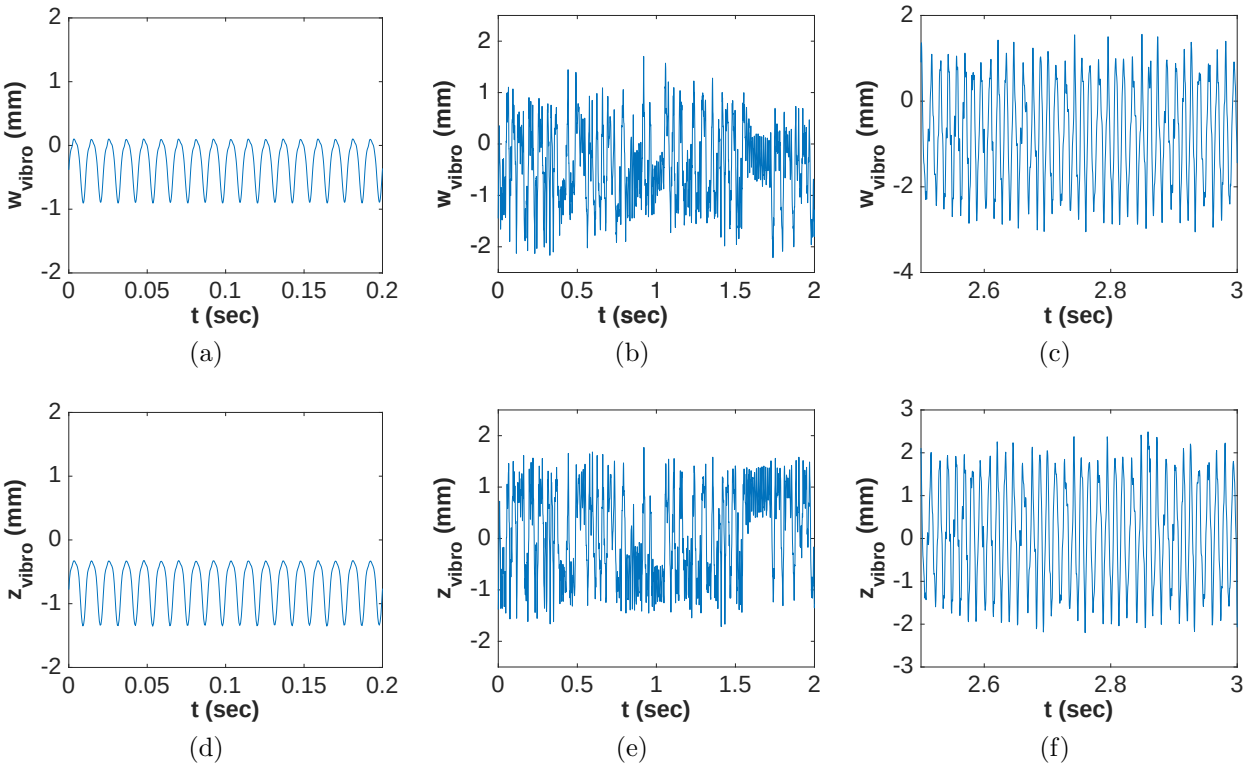

Figure 2.5: Comparison between the vibrometer and DIC measurements of the vibrometer sampling point (w_{vibro} and z_{vibro}, respectively) under the harmonic loading cases: (a, d) 4 g–180 Hz, (b, e) 5 g–85 Hz, and (c, f) 7 g–75 Hz.

2.2.5 Methodology for vibrometer measurement

The potential for intermittent snap-through leads to challenges in integrating laser vibrometer velocities to obtain displacements which are needed to identify snap-through (see Ref [18] for discussion on this issue).

The relative displacement of the vibrometer sampling point (see Fig 2.2b) was obtained by numerically integrating its relative velocity (sampled at 5000 Hz). To provide some level of mutual validation of both sensing methods, the integrated displacement w_{vibro}, which was obtained using the vibrometer data collected during the dynamic DIC tests, was compared

to the corresponding DIC measurement z_{vibro}[3] of three characteristic response types: single-well, c-snap, and p-snap, as shown in Fig 2.5. The DIC measurement of the response of the vibrometer sampling point was obtained by interpolating the data of the DIC sampling points number 75 and 95 (see Fig 2.4).

In the singe-well (see Figs 2.5a and 2.5d) and p-snap (see Figs 2.5c and 2.5f) cases, w_{vibro} and z_{vibro} were precisely synchronized showing the identical curves and peak-to-peak displacement although the datum of the vibrometer data was arbitrary. For the c-snap case (see Figs 2.5b and 2.5e), the vibrometer measurement appeared less dependable because the bi-stability of the intermittent snap-through could not be captured in the integrated displacement due to the local drift of the mean caused by irregular transitions between cross-well and single-well responses, as shown in Fig 2.5b. However, w_{vibro} and z_{vibro} were nevertheless synchronized, demonstrating the same trend (i.e., large or small oscillations), and crucially, the same peak-to-peak displacements. Therefore, the peak-to-peak displacement obtained from the vibrometer measurement could be used as an important indication of the occurrence of snap-through.

2.2.6 Methodology for frequency-sweep tests

For investigation of parameter sensitivity and characterization of snap-through boundaries, forcing frequency-sweep tests were conducted. The vibrometer was used in these tests to measure the dynamic response of the specimen under various harmonic forcing amplitudes: 0.5, 1, 2, 3, 4, 5, 6, and 7 g. For all of these forcing cases, the target forcing frequency range was 50–200 Hz. The forcing frequency increased (or swept up) from 50 to 200 Hz.

[3]The vibrometer measurement is labeled w_{vibro} because the displacement w of the vibrometer sampling point along z axis was obtained using the vibrometer data. On the other hand, the DIC measurement is named z_{vibro} because the DIC data provided the z-coordinate of the position vector of the vibrometer sampling point (along with the other two (x and y) coordinates).

2.3 Experimental results and discussions

This section presents the full-field measurement of the dynamic response of the post-buckled specimen under harmonic loading scenarios to discuss the spatio-temporal complexity of this response. In addition, based on the frequency-sweep test results, the sensitivity of the dynamic response to forcing parameters is explored and the experimental snap-through boundaries of the specimen are characterized in the HFP space. Finally, free-decay tests of the specimen in the pre- and post-buckled states are introduced and the damping parameters of the post-buckled specimen are characterized.

2.3.1 Spatio-temporal complexity

Using the DIC system for full-field measurement, the post-buckled specimen was tested under three harmonic loading scenarios: 4 g–180 Hz, 5 g–85 Hz, and 7 g–75 Hz. These cases were chosen to investigate characteristic response types such as single-well, c-snap, and p-snap. The time series of the response near the midpoint of the specimen ($x = 114.3$ mm, $y = 63.5$ mm) and phase projections for the time series are illustrated in Fig 2.6.

4 g–180 Hz case (single-well)

For the first loading scenario (4 g–180 Hz), snap-through was not observed (see Fig 2.6a). As shown in the projected phase portrait (i.e., z_{52} vs. v_{52}, see Fig 2.6b), z_{52} settled down in one of the stable equilibria and oscillated around the point in a periodic manner. Consequently, z_{52} showed periodic single-well response in the phase space; that is, z_{52} traveled inside one of the two attracting wells tracing an elliptical and hollow shape.

For 3-D spatial analysis of this phenomenon, some snapshots of the deflected shapes of the specimen are illustrated in Fig 2.7. For investigation of the impact of the asymmetrically buckled shape, a DIC sampling point slightly away from the midpoint of the specimen was chosen for Figs 2.7a and 2.7b. Therefore, the time series of transverse response and its projected phase portrait shown in Fig 2.7 are different from Figs 2.6a and 2.6b. The specimen

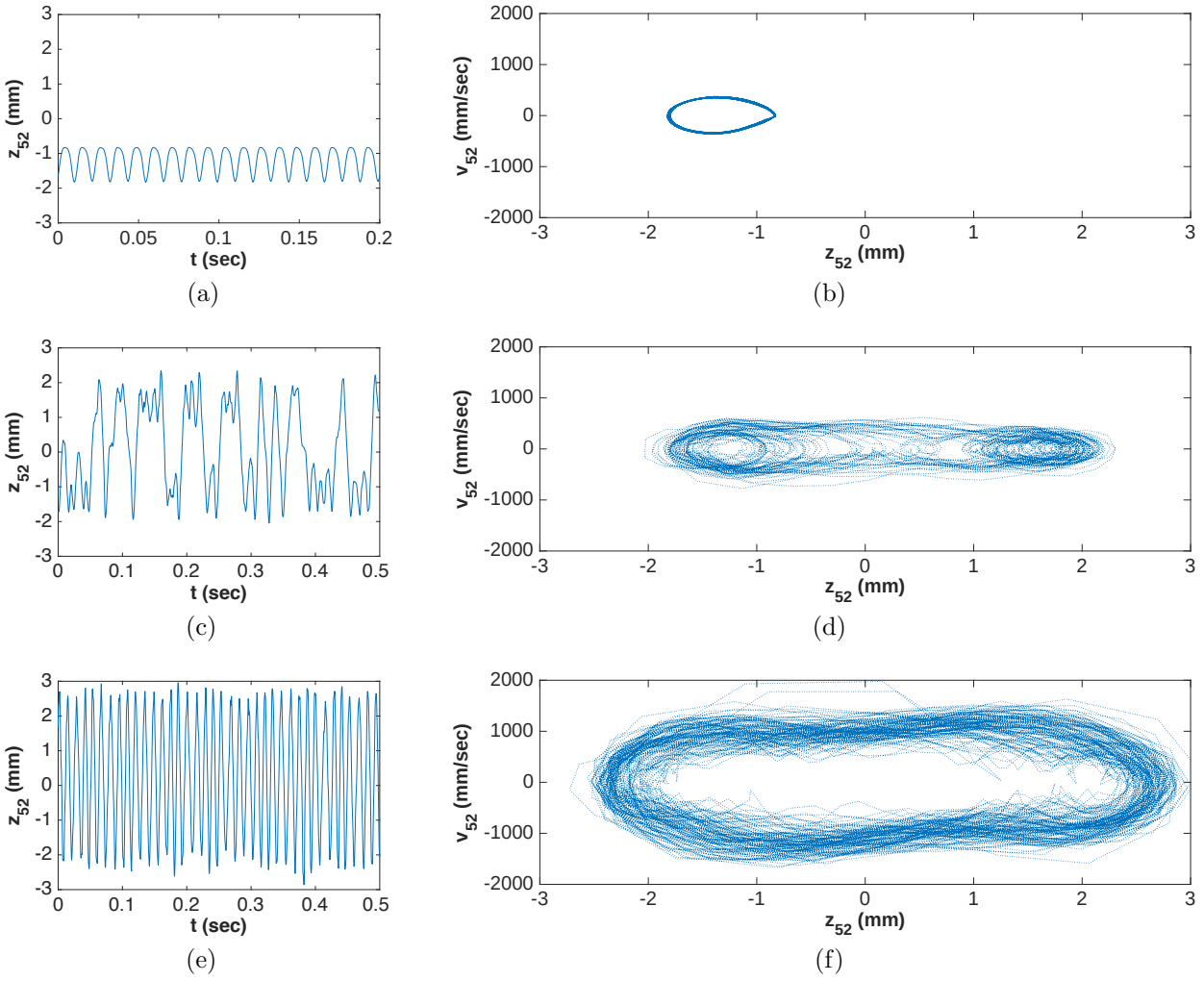

Figure 2.6: The DIC measurement of the response near the midpoint of the specimen and phase projections for the time series under the harmonic loading cases: (a, b) 4 g–180 Hz, (c, d) 5 g–85 Hz, and (e, f) 7 g–75 Hz. The response and velocity of the DIC sampling point number 52 (see Fig 2.4) are represented by z_{52} and v_{52}, respectively.

experienced the (local) maximum bending about the positive y-axis at point (1) (see Figs 2.7c and 2.7d). The influence of twisting (or torsional) deformation about the negative x-axis began growing at point (2). The twisting deformation reached the maximum at point (3) (see Figs 2.7e and 2.7f) and started decreasing by rotating about the other direction (the positive x-axis). At point (4), z_{50} escaped from the small inner trajectory of the projected

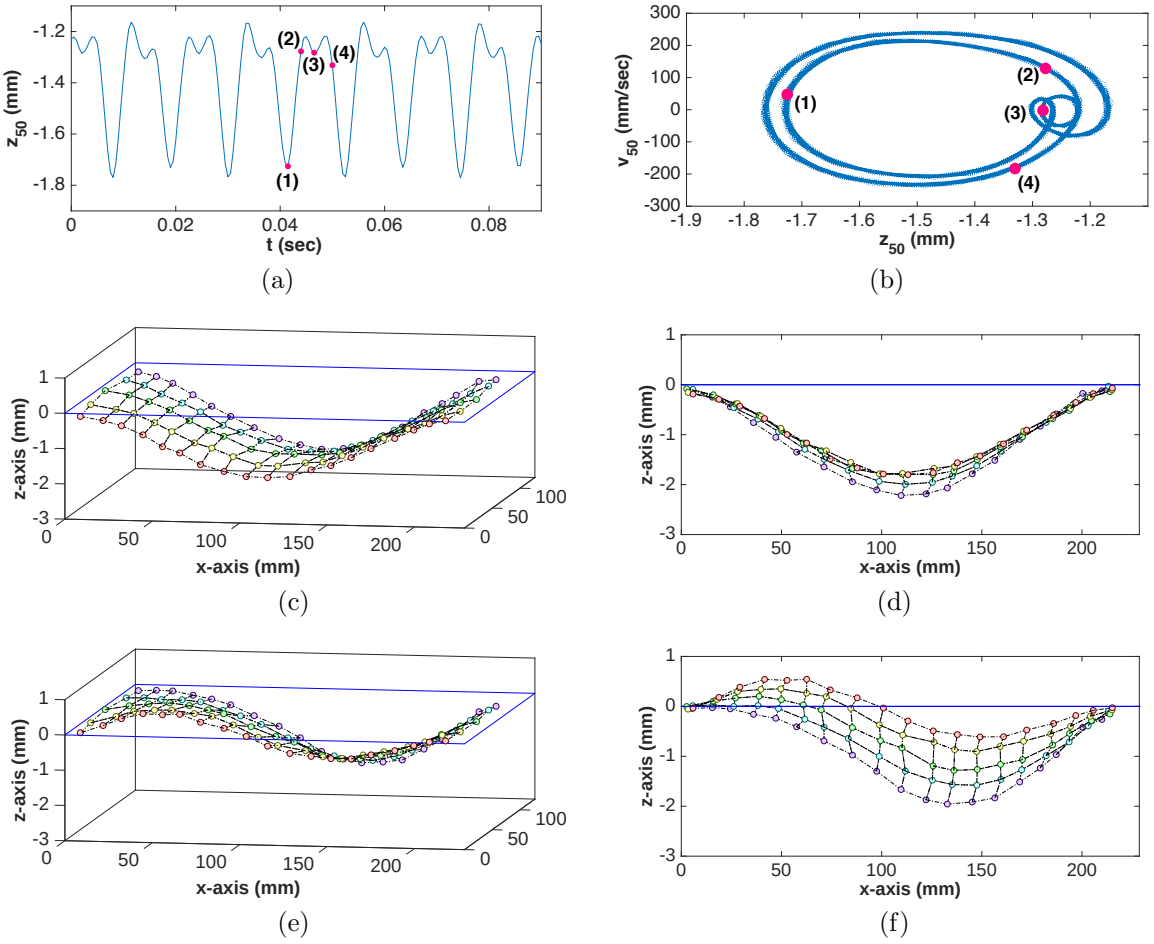

Figure 2.7: The dynamic DIC measurement (single-well) under 4 g–180 Hz harmonic loading. (a) The time series of z_{50}. (b) The projected phase portrait of the time series. The response and velocity of the DIC sampling point number 50 (see Fig 2.4) are represented by z_{50} and v_{50}, respectively. The snapshots of the deflected shapes of the specimen were taken: (c, d) at (1), and (e, f) at (3).

phase portrait (i.e., z_{50} vs. v_{50}, see Fig 2.7b) and bending dominated the specimen's response again. This cycle was continuously repeated along the orbit of the phase portrait under this loading case. Somewhat surprisingly, despite the presence of noise in the applied forcing and measurement of the response, the time series of z_{50} (see Fig 2.7a) shows an intricate response type (Period 4) that might be the result of a period-doubling cascade.

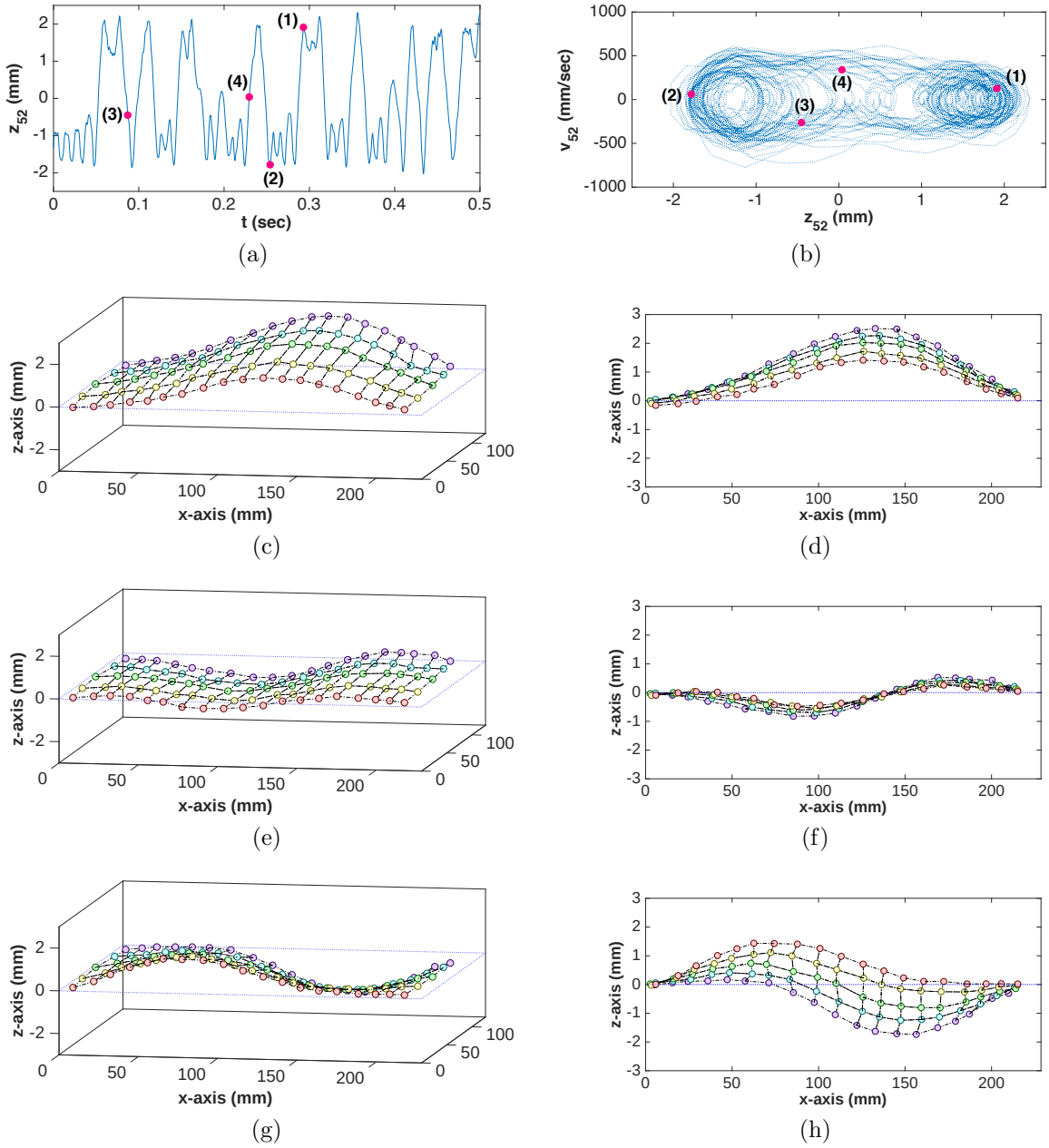

Figure 2.8: The dynamic DIC measurement (c-snap) under 5 g–85 Hz harmonic loading. (a) The time series of z_{52}. (b) The projected phase portrait of the time series. The snapshots of the deflected shapes of the specimen were taken: (c, d) at (1), (e, f) at (3), and (g, h) at (4).

5 g–85 Hz case (c-snap)

For the second loading scenario (5 g–85 Hz), steady-state c-snap was observed (see Fig 2.6c); that is, the specimen occasionally jumped between the stable equilibria in a chaotic manner. As shown in the projected phase portrait (see Fig 2.6d), the orbit of z_{52} inside one of the two attracting wells traced small inner ellipses, while its cross-well response (i.e., the occasional snap-through) appeared as the large characteristic 'peanut' shapes encompassing the small ones. The c-snap response showed a significantly larger peak-to-peak displacement and phase portrait than did the previous single-well case.

Some snapshots of the deflected shapes under this loading case are illustrated in Fig 2.8. The specimen showed the (local) maximum negative and positive bending about the y-axis at points (1) and (2), respectively (see Figs 2.8c and 2.8d). These points are located at the opposite ends of the projected phase portrait shown in Fig 2.8b. At point (3), the specimen was about to snap through the neutral plane (i.e., the position of the initially-flat specimen at $z = 0$) and a strong influence of the higher modes on the response of the specimen was observed (see Figs 2.8e and 2.8f). The dominance of the higher modes near the neutral plane is not surprising since these modes have lower potential energy. At point (4), a large twisting deformation was observed (see Figs 2.8g and 2.8h).

7 g–75 Hz case (p-snap)

Finally, for the third loading scenario (7 g–75 Hz), steady-state p-snap was observed (see Fig 2.6e); that is, the specimen continuously snapped between the two stable equilibria in a nearly periodic manner. As shown in the projected phase portrait (see Fig 2.6f), since z_{52} periodically traveled 'above' the two attracting wells, the trajectory traced a thick and hollow ellipse in the phase space. The p-snap response showed a larger peak-to-peak displacement and phase portrait than did the previous c-snap case. In addition, the p-snap case demonstrated a significantly higher number of snap-through events than did the c-snap case in the same time window. Therefore, such high-frequency p-snap cases could possi-

bly accelerate damage growth in composite structures due to large-amplitude deformations (consequently, high strains and stresses) occurring during snap-through events along with quickly increasing fatigue cycles. The deflected shapes of the p-snap case (not presented) showed similar patterns as observed in the c-snap case.

2.3.2 Parameter sensitivity

For analysis of the frequency-sweep test data obtained using the vibrometer, the peak-to-peak response of the numerically integrated displacement was taken due to the presence of c-snap (see the discussion in Section 2.2.5).

The peak-to-peak displacement $w_{\text{p-p}}$ of the vibrometer sampling point (see Fig 2.4) is illustrated in Fig 2.9. The frequency-sweep rate was not constant; however, the frequency axes of the figures were continuously defined only for the purpose of visualization. The vibrometer occasionally failed to trace the sampling point when the point exhibited large-amplitude snap-through (see Figs 2.9g and 2.9h). The corresponding $w_{\text{p-p}}$ extended beyond the figure frames. The peak-to-peak static buckled depth $z_{\text{p-p}}$ of the sampling point, which was measured as $z_{\text{p-p}} = 1.69$ mm from the reconstructed buckled shape, is demarcated as red dotted lines in the figures. The lines could potentially be used as a threshold to determine occurrence of snap-through. In this context, snap-through is taken as the sampling point passing beyond its remote stable equilibrium; however, this definition can be deemed somewhat inadequate given the response complexity. Moreover, as observed from the full-field measurement of the single-well response (see Fig 2.7f), some DIC sampling points exceeded their peak-to-peak buckled depths without obvious snap-through due to the twisting deformation.

To define a reasonable threshold of snap-through, the sensitivity of the snap-through boundaries to changes in the threshold level of snap-through was investigated as shown in Figs 2.10 and 2.11. The frequency-response plots (see Figs 2.10a to 2.10d and 2.11a to 2.11d) show the maximum $w_{\text{p-p}}$ under discrete forcing frequencies. The threshold sensitivity plots (see Figs 2.10e and 2.11e) illustrate the relationship between the threshold level and the number of snap-through points which form snap-through regions in the HFP space.

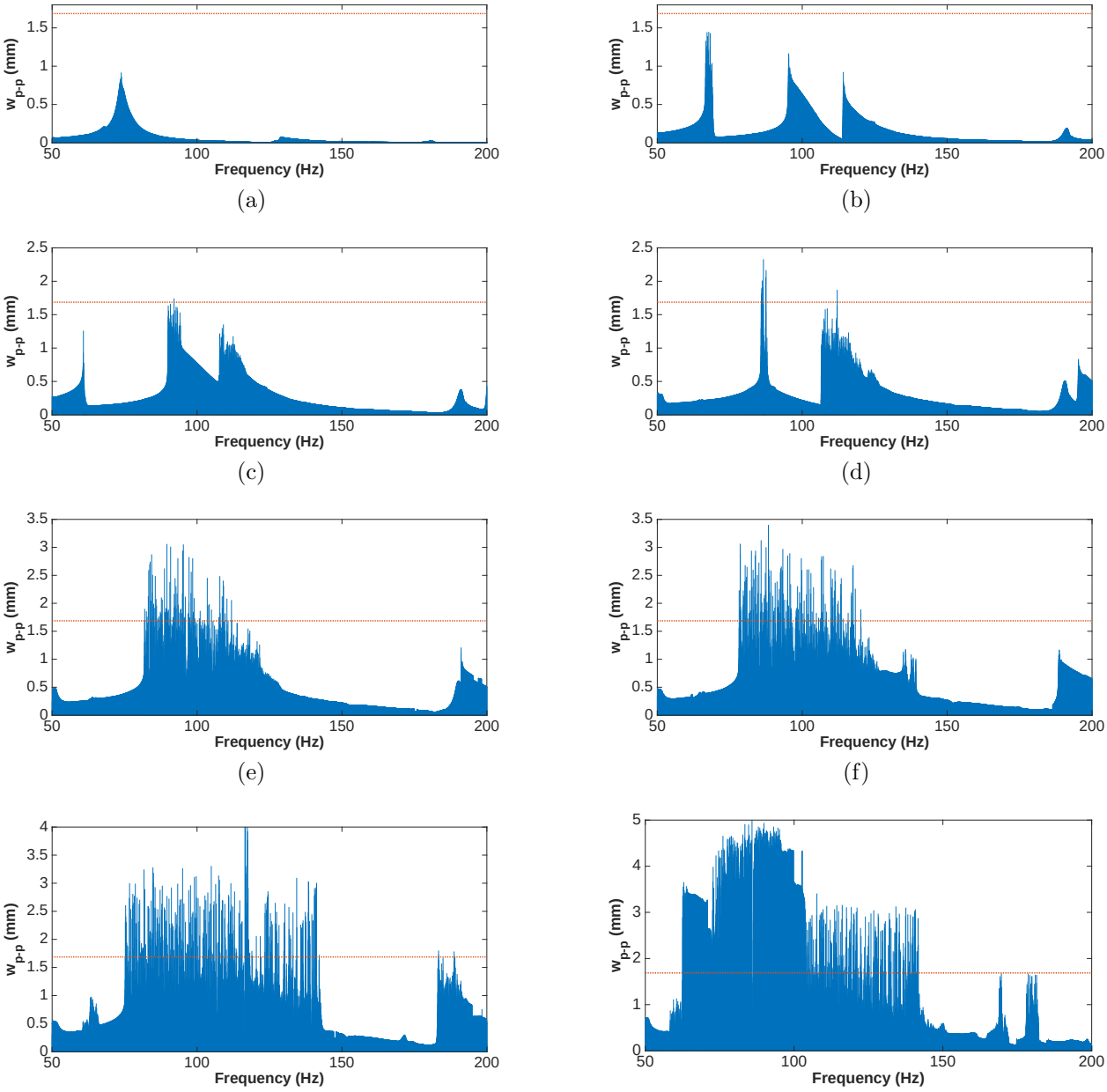

Figure 2.9: The peak-to-peak displacement $w_{\text{p-p}}$ of the vibrometer sampling point under the forcing amplitudes: (a) 0.5 g, (b) 1 g, (c) 2 g, (d) 3 g, (e) 4 g, (f) 5 g, (g) 6 g, and (h) 7 g. The vertical axes of the figures are not all the same. The red dotted lines indicate the peak-to-peak buckled depth $z_{\text{p-p}}$ of the sampling point.

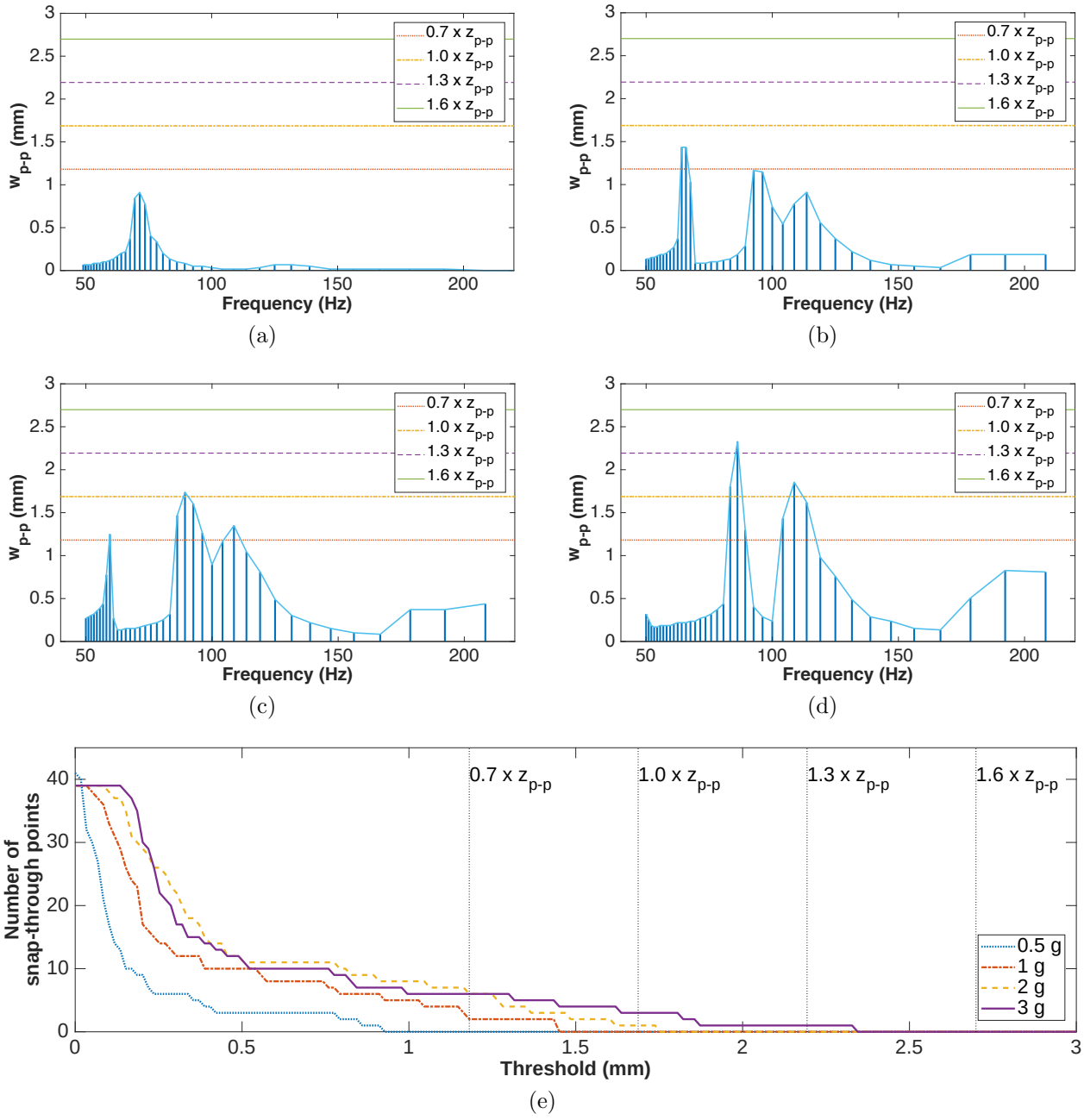

Figure 2.10: The frequency-response plots of the vibrometer measurement under the forcing amplitudes: (a) 0.5 g, (b) 1 g, (c) 2 g, and (d) 3 g. (e) The threshold sensitivity plots under these forcing amplitudes.

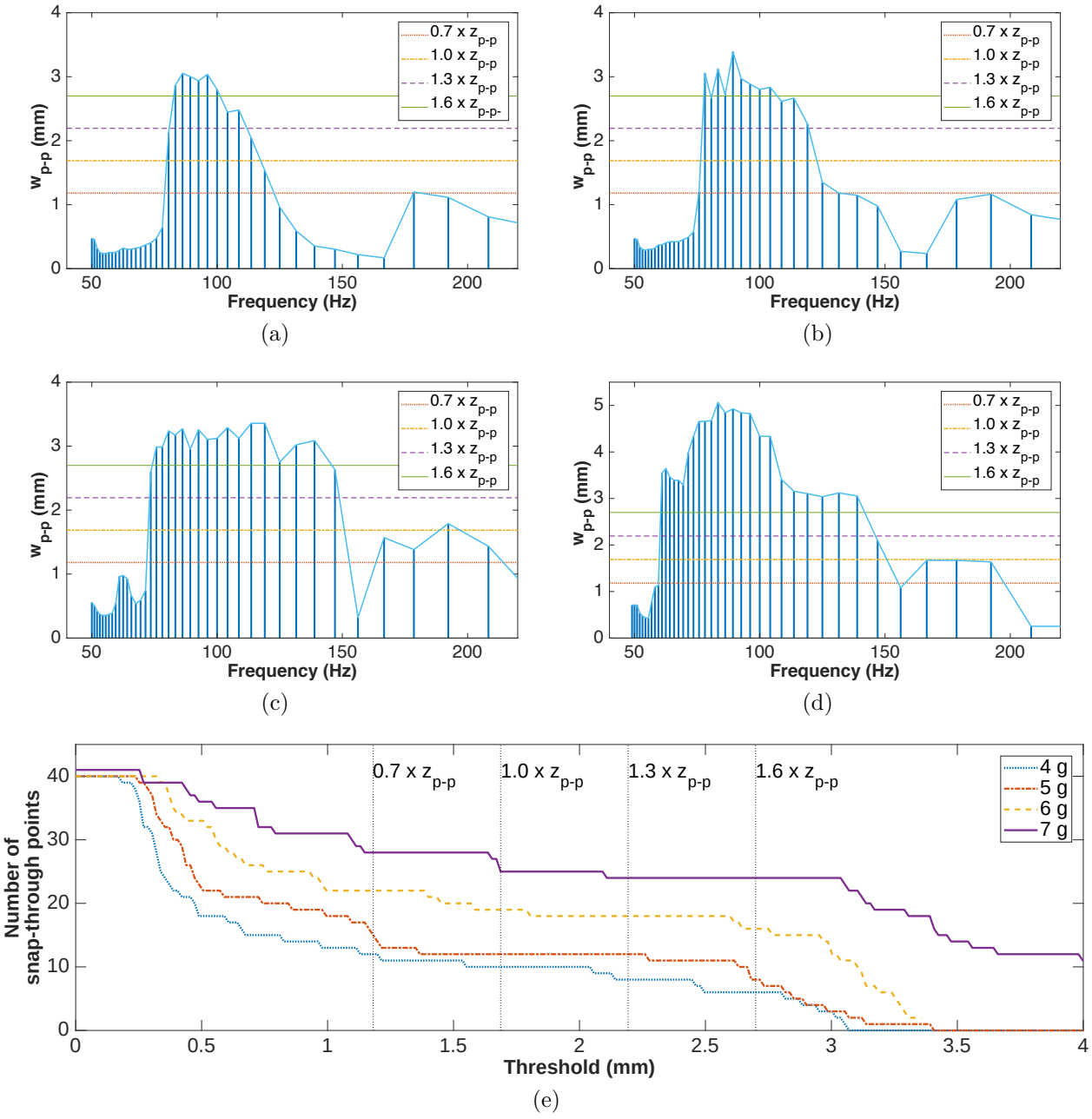

Figure 2.11: The frequency-response plots of the vibrometer measurement under the forcing amplitudes: (a) 4 g, (b) 5 g, (c) 6 g, and (d) 7 g. (e) The threshold sensitivity plots under these forcing amplitudes.

The snap-through boundaries at forcing amplitudes 0.5–3 g were very sensitive to a marginal increase from the zero threshold. Consequently, the number of snap-through points significantly dropped with such increase and most of the snap-through points vanished before the threshold level reached $1.0\times z_{\text{p-p}}$. Fortunately, the number of snap-through points at larger amplitudes 4–7 g was relatively constant at the thresholds between $0.7\times z_{\text{p-p}}$ and $1.6\times z_{\text{p-p}}$. This indicates that the responses at these forcing amplitudes are either small or large since the responses are filtered by the unstable potential energy barrier. The frequency-response plots at these amplitudes first formed steep cliffs at 60–80 Hz and then gradual descending slopes at 120–160 Hz.

Therefore, as dictated by the observed responses, thresholds between $0.7\times z_{\text{p-p}}$ and $1.6\times z_{\text{p-p}}$ appear to represent snap-through. In this more general definition, snap-through is a natural 'shelf' in the threshold sensitivity plots (see Fig 2.11e). The consequence of snap-through in this context is a disproportionate increase in mean response amplitude under small parameter changes.

2.3.3 Experimental snap-through boundaries

The experimental snap-through boundaries of the post-buckled specimen were generated in the HFP space based on the frequency-sweep test results, as illustrated in Fig 2.12. Four layers of snap-through boundaries were formed using four thresholds of snap-through: $0.7\times z_{\text{p-p}}$ (a lower bound), $1.0\times z_{\text{p-p}}$, $1.3\times z_{\text{p-p}}$, and $1.6\times z_{\text{p-p}}$ (an upper bound). The edges of the discrete snap-through points were connected to visualize the snap-through regions.

In Region 1, the left boundary (or the low-frequency boundary) at 4–7 g consistently appeared in the almost identical position on every layer due to an abrupt change in the response amplitude across the boundary as observed in the sensitivity study of the boundaries. However, there was wide variance in the right boundaries (or the high-frequency boundaries) defined by the thresholds due to a gradual change in the response amplitude near the boundary. In Region 2, a single snap-through point appeared in the $1.0\times z_{\text{p-p}}$ level. In Regions 3 and 4, the snap-through boundaries appeared only in the lower bound.

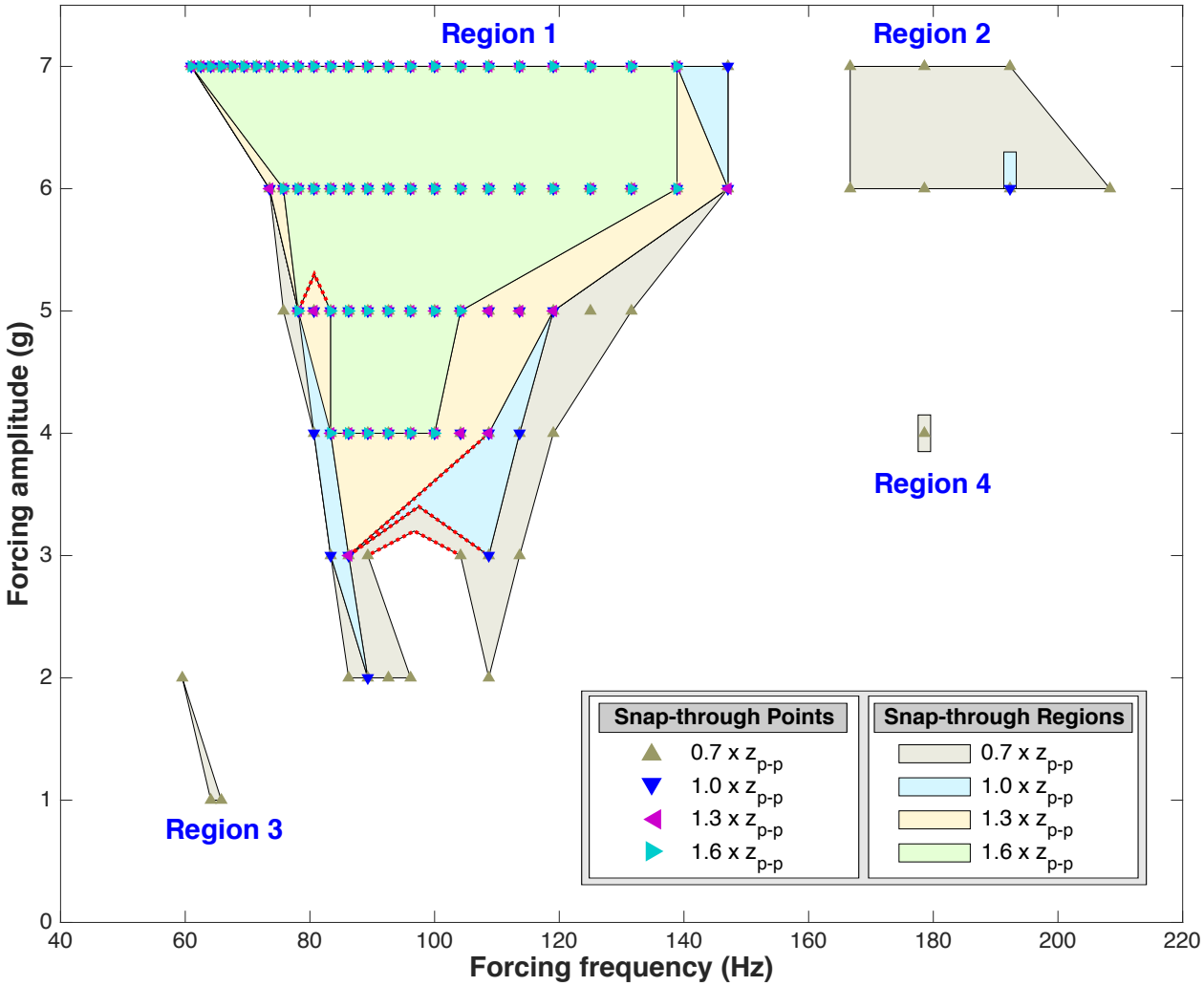

Figure 2.12: The experimental snap-through boundaries of the post-buckled plate specimen in the HFP space.

It would not be simple to define one of these snap-through boundaries as a true boundary of the specimen; however, the range can be narrowed. From the visual inspection during the test, a single snap-through event was observed at 1 g, several snap-through events at 2 g, and many snap-through events at 3 g. These events were observed as violent excursions. Therefore, the actual snap-through boundaries at 1–3 g were possibly located at somewhere between the layers defined by the thresholds $0.7\times z_{\text{p-p}}$ and $1.0\times z_{\text{p-p}}$.

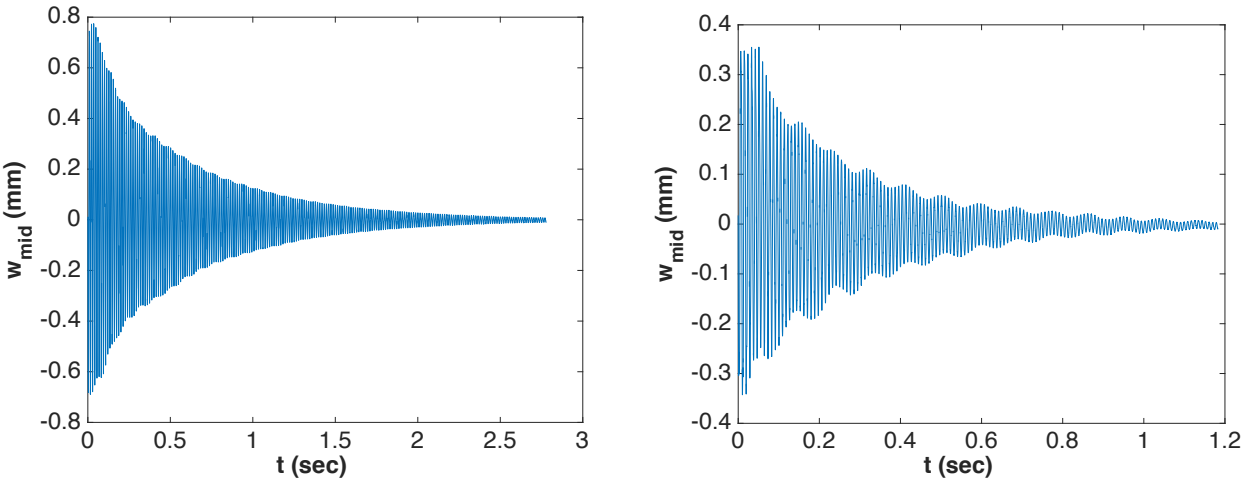

Figure 2.13: The free-vibration response of the midpoint of the specimen for the first mode. (a) The flat (or pre-buckled) case. (b) The post-buckled case.

2.3.4 Experimental measurement of damping ratio

For characterization of the damping parameters of the specimen, free-decay tests were conducted using a single-point displacement-sensing laser sensor, Micro-Epsilon optoNCDT 2300-20 (not used in the forced vibration tests). The free-vibration response of the midpoint of the specimen was measured with a 20000-Hz sampling frequency as shown in Fig 2.13. The post-buckled state of the specimen was reconstructed to approximately match the full-field measurement shown in Fig 2.3.

The natural frequencies of the first mode were obtained as 73 Hz for the flat case and 113 Hz for the post-buckled case. This result indicates that the system was well into the post-buckled regime, as near buckling the frequency drops.

Based on the logarithmic decrement [20, 58], the damping ratio ζ was determined from

$$\zeta = \frac{1}{2\pi j}\ln\left(\frac{u_i}{u_{i+j}}\right), \tag{2.4}$$

where u_i and u_{i+j} are the ith and $(i+j)$th peak displacements (maxima), respectively. Using

the peak-to-peak displacements of the response shown in Fig 2.13, ζ was estimated as 0.32 % for the flat case and 0.45 % for the post-buckled case. This result shows that ζ of the specimen grew indicating stiffness dependence.

2.4 Summary

In this chapter, the experimental results of an asymmetrically-buckled composite plate under inertially-applied harmonic loading were presented. The nonlinear dynamics and snap-through boundaries of the specimen were experimentally investigated in order to understand the nonlinear dynamic behaviors of post-buckled composite plates and obtain experimental data for robust validation of numerical models.

The static full-field measurement of the post-buckled specimen prior to the dynamic tests revealed the spatial complexity of its asymmetrically-buckled shape, making modeling more challenging. Given that buckling is hardly expected to happen perfectly or symmetrically in reality, however, the experimental and simulation results obtained in this work can provide a better insight into real-world problems than those of symmetric cases. In addition, the static full-field measurement provides geometric data required for calibration of the initial static equilibrium of numerical models.

The dynamic response of the specimen captured in the full-field measurement showed its spatio-temporal complexity. The analysis of these nonlinear dynamic behaviors showed that the previous discussions on bi-stable metallic structures such as single DOF linkage systems, shallow arches, and post-buckled beams can be extended to composite structures such as post-buckled laminated plates and shells. In addition, based on the frequency-sweep test results, the sensitivity of the dynamic response of the specimen to forcing parameters was investigated and the experimental snap-through boundaries were characterized in the HFP space. These snap-through boundaries provide extensive benchmark data for robust validation of numerical models.

Finally, damping of the specimen in the pre- and post-buckled states was characterized through the free-decay tests. The damping parameters obtained from these tests enable

damping calibration of numerical models.

In the following chapters, various types of numerical models of the post-buckled specimen are developed and their simulation results are compared to the experimental data for validation.

Part I

MODELING AND SIMULATION: DISPLACEMENT-BASED APPROACH

Chapter 3

CLPT MODEL AND SIMULATION RESULTS

3.1 Introduction

In the previous chapter, the spatial complexity of the asymmetrically-buckled specimen was observed from the static full-field measurement of its initially-buckled shape (see Fig 2.1). Numerical models of the specimen are required to reproduce this complexity to accurately capture the spatio-temporal complexity and parameter sensitivity of the specimen's dynamic response. In this section, the first numerical model of this work is introduced and its simulation results are presented.

Various types of laminated composite plate theories have been proposed and their performance has been discussed in the literature. Generally, the theories can be categorized as either equivalent single-layer (ESL) or 3-D elasticity theories (e.g., layerwise theories [52, 67]). In ESL theories, 3-D elasticity problems are reduced to 2-D ones based on assumptions on the kinematics of deformations through the thickness of laminated plates [68]. Geometric nonlinearity can be included in ESL theories by employing von Kármán strains [90]. Commonly-used ESL theories are the classical laminated plate theory (CLPT), the first-order shear deformation theory (FSDT), and higher-order shear deformation theories (HSDTs). As an extension of the Kirchhoff plate theory into laminated plates, CLPT is based on the well-known Kirchhoff hypothesis and thus disregards transverse shear deformations in its kinematics. The transverse shear stress field of CLPT, however, can be computed using the equilibrium equations of 3-D elasticity [17, 26]. The exclusion of transverse shear deformations makes the applications of CLPT limited to thin laminated plates. On the other hand, FSDT is an extension of the Reissner-Mindlin theory [51, 72] to laminated plates and thus incorporates transverse shear deformations in its kinematics [68]. Therefore, FSDT is

applicable to moderately thick plates and its transverse shear stress field can be obtained directly through constitutive equations [68]. The uniform distribution of its transverse shear strain field through thickness, however, requires a shear correction factor, which affects the accuracy of FSDT [35]. More accurate and realistic transverse shear strains and stresses can be obtained from HSDTs and 3-D elasticity theories; however, the numerical implementation of these theories incurs significantly higher computational cost than that of FSDT [68].

As the first attempt, this work adopted CLPT to model the specimen (its length-to-thickness ratio: 3.15×10^{-3}) because CLPT can accurately determine the global response of thin laminated composite plates at a relatively low computational cost [35, 68]. In addition, the numerical implementation of CLPT has an enormous advantage over that of the other theories in that CLPT models are free of shear locking.

In this chapter, the nonlinear equations of motion and the finite element models (FEMs) for CLPT are introduced. In addition, the numerical implementation of the FEMs to generate a CLPT model of the specimen is presented with its simulation results and numerical snap-through boundaries. The numerical boundaries are compared with the experimental ones for robust validation of the model.

3.2 Nonlinear equations of motion and FEM for CLPT

The detailed derivation of the nonlinear equations of motion and FEMs for CLPT are presented in previous work [37] based on the work of Reddy [68]. Therefore, only the results are introduced with the distinctive characteristics of CLPT in this chapter.

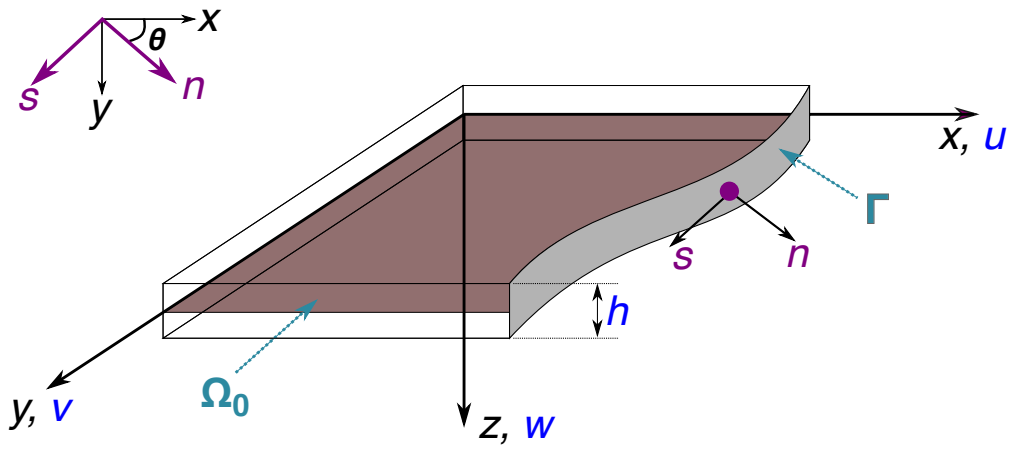

Figure 3.1: The coordinate system of plates. The displacements along the x, y, and z axes are denoted by u, v, and w, respectively. The unit normal and tangential vectors of a point on the boundary Γ are given by $\mathbf{n}$ and $\mathbf{s}$, respectively. The undeformed midplane is denoted by Ω_0. This figure was drawn based on the work of Reddy [68].

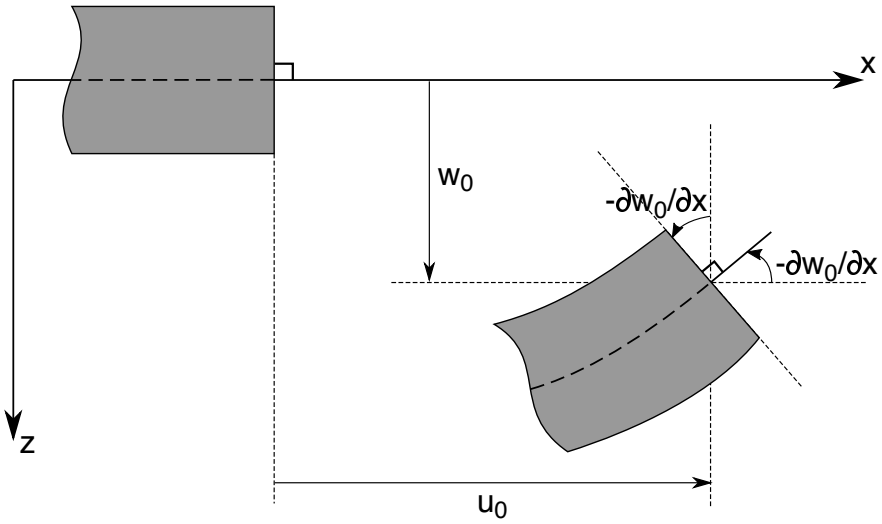

Figure 3.2: The undeformed and deformed configurations of CLPT on the x-z plane. This figure was drawn based on the work of Reddy [68].

3.2.1 Nonlinear equations of motion for CLPT

Following the coordinate system of plates illustrated in Fig 3.1, the displacement field of CLPT is given by

$$\begin{aligned} u(x,y,z,t) &= u_0(x,y,t) - z\frac{\partial w_0}{\partial x}, \\ v(x,y,z,t) &= v_0(x,y,t) - z\frac{\partial w_0}{\partial y}, \\ w(x,y,z,t) &= w_0(x,y,t), \end{aligned} \tag{3.1}$$

where (u_0, v_0, w_0) are midplane displacements along the x, y, and z axes, respectively. The deformations induced by this displacement field are illustrated in Fig 3.2.

This work adopted von Kármán strains to include geometric nonlinearity in CLPT. More details about the von Kármán nonlinear strains are introduced in Appendix C. Using the displacement field in Eq (3.1), the von Kármán nonlinear strains for CLPT are given by

$$\varepsilon_{xx} = \frac{\partial u}{\partial x} + \frac{1}{2}\left(\frac{\partial w}{\partial x}\right)^2 = \frac{\partial u_0}{\partial x} + \frac{1}{2}\left(\frac{\partial w_0}{\partial x}\right)^2 - z\frac{\partial^2 w_0}{\partial x^2} = \varepsilon_{xx}^{(0)} + z\varepsilon_{xx}^{(1)}, \tag{3.2}$$

$$\varepsilon_{yy} = \frac{\partial v}{\partial y} + \frac{1}{2}\left(\frac{\partial w}{\partial y}\right)^2 = \frac{\partial v_0}{\partial y} + \frac{1}{2}\left(\frac{\partial w_0}{\partial y}\right)^2 - z\frac{\partial^2 w_0}{\partial y^2} = \varepsilon_{yy}^{(0)} + z\varepsilon_{yy}^{(1)}, \tag{3.3}$$

$$\varepsilon_{zz} = \frac{\partial w}{\partial z} = \frac{\partial w_0}{\partial z} = 0, \tag{3.4}$$

$$\begin{aligned} \gamma_{xy} = 2\varepsilon_{xy} &= \frac{\partial u}{\partial y} + \frac{\partial v}{\partial x} + \frac{\partial w}{\partial x}\frac{\partial w}{\partial y} \\ &= \frac{\partial u_0}{\partial y} + \frac{\partial v_0}{\partial x} + \frac{\partial w_0}{\partial x}\frac{\partial w_0}{\partial y} - 2z\frac{\partial^2 w_0}{\partial x \partial y} = \gamma_{xy}^{(0)} + z\gamma_{xy}^{(1)}, \end{aligned} \tag{3.5}$$

$$\gamma_{yz} = 2\varepsilon_{yz} = \frac{\partial v}{\partial z} + \frac{\partial w}{\partial y} = -\frac{\partial w_0}{\partial y} + \frac{\partial w_0}{\partial y} = 0, \tag{3.6}$$

$$\gamma_{xz} = 2\varepsilon_{xz} = \frac{\partial u}{\partial z} + \frac{\partial w}{\partial x} = -\frac{\partial w_0}{\partial x} + \frac{\partial w_0}{\partial x} = 0, \tag{3.7}$$

where (ε_{xx}, ε_{yy}, ε_{zz}) are normal strains and (γ_{xy}, γ_{xz}, γ_{yz}) are shear strains. The in-plane

strains (ε_{xx}, ε_{yy}, γ_{xy}) can be divided into membrane strains ($\varepsilon^{(0)}_{xx}$, $\varepsilon^{(0)}_{yy}$, $\gamma^{(0)}_{xy}$) and bending strains ($\varepsilon^{(1)}_{xx}$, $\varepsilon^{(1)}_{yy}$, $\gamma^{(1)}_{xy}$).

Using the typical displacement-based variational principle[1], the governing equations of motion for CLPT can be obtained as

$$\frac{\partial N_{xx}}{\partial x} + \frac{\partial N_{xy}}{\partial y} = I_0 \frac{\partial^2 u_0}{\partial t^2} - I_1 \frac{\partial^2}{\partial t^2}(\frac{\partial w_0}{\partial x}), \tag{3.8}$$

$$\frac{\partial N_{xy}}{\partial x} + \frac{\partial N_{yy}}{\partial y} = I_0 \frac{\partial^2 v_0}{\partial t^2} - I_1 \frac{\partial^2}{\partial t^2}(\frac{\partial w_0}{\partial y}), \tag{3.9}$$

$$\begin{aligned} &\frac{\partial^2 M_{xx}}{\partial x^2} + 2\frac{\partial^2 M_{xy}}{\partial y \partial x} + \frac{\partial^2 M_{yy}}{\partial y^2} + \frac{\partial}{\partial x}(N_{xx}\frac{\partial w_0}{\partial x} + N_{xy}\frac{\partial w_0}{\partial y}) + \frac{\partial}{\partial y}(N_{xy}\frac{\partial w_0}{\partial x} \\ &+ N_{yy}\frac{\partial w_0}{\partial y}) + q = I_0 \frac{\partial^2 w_0}{\partial t^2} - I_2 \frac{\partial^2}{\partial t^2}(\frac{\partial^2 w_0}{\partial x^2} + \frac{\partial^2 w_0}{\partial y^2}) + I_1 \frac{\partial^2}{\partial t^2}(\frac{\partial u_0}{\partial x} + \frac{\partial v_0}{\partial y}), \end{aligned} \tag{3.10}$$

where q is distributed transverse (i.e., along the z-axis) loading, (I_0, I_1, I_2) are mass moments of inertia, (N_{xx}, N_{yy}, N_{xy}) are in-plane stress resultants, and (M_{xx}, M_{yy}, M_{xy}) are bending stress resultants. The details about these stress resultants are described in Appendix B. The mass moments of inertia are given by

$$\begin{Bmatrix} I_0 \\ I_1 \\ I_2 \end{Bmatrix} = \int_{-h/2}^{h/2} \begin{Bmatrix} 1 \\ z \\ z^2 \end{Bmatrix} \rho_0 dz, \tag{3.11}$$

where ρ_0 is the material density.

---

[1] Another type of variational principle is discussed in Chapter 5

3.2.2 FEMs for CLPT

Applying the gradient and divergence theorems [69], the modified weak forms of Eqs (3.8) to (3.10) are given by

$$\begin{aligned} 0 = &\int_{\Omega^e} \Big[\frac{\partial \delta u_0}{\partial x} N_{xx} + \frac{\partial \delta u_0}{\partial y} N_{xy} + I_0 \delta u_0 \frac{\partial^2 u_0}{\partial t^2} - I_1 \delta u_0 \frac{\partial^2}{\partial t^2}\Big(\frac{\partial w_0}{\partial x}\Big)\Big] dxdy \\ &- \oint_{\Gamma^e} (N_{xx} n_x + N_{xy} n_y) \delta u_0 ds, \end{aligned} \tag{3.12}$$

$$\begin{aligned} 0 = &\int_{\Omega^e} \Big[\frac{\partial \delta v_0}{\partial x} N_{xy} + \frac{\partial \delta v_0}{\partial y} N_{yy} + I_0 \delta v_0 \frac{\partial^2 v_0}{\partial t^2} - I_1 \delta v_0 \frac{\partial^2}{\partial t^2}\Big(\frac{\partial w_0}{\partial y}\Big)\Big] dxdy \\ &- \oint_{\Gamma^e} (N_{xy} n_x + N_{yy} n_y) \delta v_0 ds, \end{aligned} \tag{3.13}$$

$$\begin{aligned} 0 = &\int_{\Omega^e} \Big[- \frac{\partial^2 \delta w_0}{\partial x^2} M_{xx} - 2\frac{\partial^2 \delta w_0}{\partial y \partial x} M_{xy} - \frac{\partial^2 \delta w_0}{\partial y^2} M_{yy} \\ &+ \frac{\partial \delta w_0}{\partial x}\Big(N_{xx}\frac{\partial w_0}{\partial x} + N_{xy}\frac{\partial w_0}{\partial y}\Big) + \frac{\partial \delta w_0}{\partial y}\Big(N_{xy}\frac{\partial w_0}{\partial x} + N_{yy}\frac{\partial w_0}{\partial y}\Big) \\ &- \delta w_0 q + I_0 \delta w_0 \frac{\partial^2 w_0}{\partial t^2} + I_2\Big(\frac{\partial \delta w_0}{\partial x}\frac{\partial^3 w_0}{\partial x \partial t^2} + \frac{\partial \delta w_0}{\partial y}\frac{\partial^3 w_0}{\partial y \partial t^2}\Big) \\ &- I_1\Big(\frac{\partial \delta w_0}{\partial x}\frac{\partial^2 u_0}{\partial t^2} + \frac{\partial \delta w_0}{\partial y}\frac{\partial^2 v_0}{\partial t^2}\Big)\Big] dxdy - \oint_{\Gamma^e} Q_n \delta w_0 ds \\ + \oint_{\Gamma^e} &\Big[\frac{\partial \delta w_0}{\partial x}(M_{xx} n_x + M_{xy} n_y) + \frac{\partial \delta w_0}{\partial y}(M_{xy} n_x + M_{yy} n_y)\Big] ds, \end{aligned} \tag{3.14}$$

where Ω^e is the element domain, Γ^e is the closed boundary of Ω^e, ($n_x = \cos\theta$, $n_y = \sin\theta$) are the direction cosines of the unit outward normal vector $\mathbf{n}$ on Γ^e (see Fig 3.1), and Q_n is given by

$$\begin{aligned} Q_n = &\Big(\frac{\partial M_{xx}}{\partial x} + \frac{\partial M_{xy}}{\partial y} + N_{xx}\frac{\partial w_0}{\partial x} + N_{xy}\frac{\partial w_0}{\partial y}\Big) n_x \\ &+ \Big(\frac{\partial M_{xy}}{\partial x} + \frac{\partial M_{yy}}{\partial y} + N_{xy}\frac{\partial w_0}{\partial x} + N_{yy}\frac{\partial w_0}{\partial y}\Big) n_y \\ &+ \Big(I_1\frac{\partial^2 u_0}{\partial t^2} - I_2\frac{\partial^3 w_0}{\partial x \partial t^2}\Big) n_x + \Big(I_1\frac{\partial^2 v_0}{\partial t^2} - I_2\frac{\partial^3 w_0}{\partial y \partial t^2}\Big) n_y. \end{aligned} \tag{3.15}$$

The midplane displacements u_0, v_0, and w_0 can be expressed in terms of the nodal

displacements u_j^e, v_j^e, and Δ_j^e, respectively:

$$u_0(x,y,t) = \sum_{j=1}^{m} u_j^e(t)\psi_j^e(x,y), \tag{3.16}$$

$$v_0(x,y,t) = \sum_{j=1}^{m} v_j^e(t)\psi_j^e(x,y), \tag{3.17}$$

$$w_0(x,y,t) = \sum_{k=1}^{n} \Delta_k^e(t)\varphi_k^e(x,y), \tag{3.18}$$

where ψ_j^e are Lagrange interpolation functions, and φ_j^e are Hermite interpolation functions satisfying C^1 continuity of w_0. Substituting these equations into Eqs (3.12) to (3.14), the weak forms can be expressed in terms of the nodal displacements. Rearranging the weak forms in a coupled matrix form, a nonlinear FEM based on CLPT is given by

$$\mathbf{M}\ddot{\mathbf{u}} + \mathbf{K}\mathbf{u} = \mathbf{F}, \tag{3.19}$$

where $\boldsymbol{u}$ is a nodal displacement vector, $\boldsymbol{K}$ is a geometrically nonlinear stiffness matrix (i.e., $\boldsymbol{K} = \boldsymbol{K}(\boldsymbol{u})$), $\boldsymbol{M}$ is a mass matrix, and $\boldsymbol{f}$ is a force vector. The components of $\boldsymbol{K}$, $\boldsymbol{M}$, and $\boldsymbol{f}$ are presented in Ref [37]. Including a damping term in this equation results in

$$\mathbf{M}\ddot{\mathbf{u}} + \mathbf{C}\dot{\mathbf{u}} + \mathbf{K}\mathbf{u} = \mathbf{F}, \tag{3.20}$$

where $\mathbf{C}$ is a damping matrix, which is discussed in Section 3.4.

For four-node elements, $m = 4$ in Eqs (3.16) and (3.17) and the bilinear Lagrange interpolation functions ψ_j^e in the reference (or isoparametric) element are given by [36]

$$\begin{aligned} \psi_1^e &= \frac{1}{4}(1-\xi)(1-\eta), \qquad \psi_2^e = \frac{1}{4}(1+\xi)(1-\eta), \\ \psi_3^e &= \frac{1}{4}(1+\xi)(1+\eta), \qquad \psi_4^e = \frac{1}{4}(1-\xi)(1+\eta). \end{aligned} \tag{3.21}$$

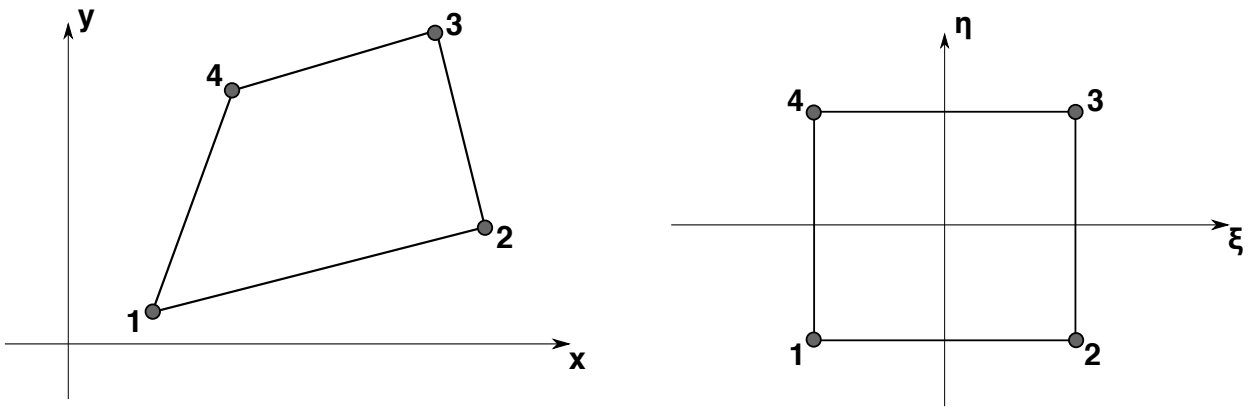

Figure 3.3: Nodal DOFs for CLPT on: (a) a real element, and (b) a reference element.

There are two types of four-node Hermite elements for w_0 in Eq (3.18) [22, 68]: conforming [15] and nonconforming [50, 103] elements. The conforming element satisfies complete C^1 continuity of w_0 while the nonconforming element does not guarantee the continuity of $\frac{\partial^2 w_0}{\partial x \partial y}$ (i.e., semi-C^1 continuity of w_0) [22]. The advantage of using the nonconforming element, however, is that it allows quadrilateral discretization of structures, while the application of the conforming element is confined to only rectangular discretization. As a result, the models composed of the conforming elements are incapable of reproducing the asymmetric buckled shape of the specimen (see Refs [37, 39] for discussion on this issue). Therefore, this work employed the nonconforming elements in conjunction with the associated Hermite interpolation functions.

Applying the nonconforming elements into w_0 in Eq (3.18), the nodal displacements Δ_k^e for $k = 1, 2, ..., 12$ ($n = 12$) are given by

$$\Delta_{3i-2}^e = (w_0)_i, \quad \Delta_{3i-1}^e = \left(\frac{\partial w_0}{\partial x}\right)_i, \quad \Delta_{3i}^e = \left(\frac{\partial w_0}{\partial y}\right)_i, \tag{3.22}$$

where the node numbers $i = 1, 2, 3, 4$. The corresponding Hermite interpolation functions

φ_k^e are given in the reference element [22]:

$$\begin{Bmatrix}\varphi_1^e\\ \varphi_2^e\\ \varphi_3^e\end{Bmatrix}=\begin{Bmatrix}\frac{1}{8}a(\alpha-\xi-\eta)\\ \frac{1}{8}a(1-\xi^2)\\ \frac{1}{8}a(1-\eta^2)\end{Bmatrix},\quad \begin{Bmatrix}\varphi_4^e\\ \varphi_5^e\\ \varphi_6^e\end{Bmatrix}=\begin{Bmatrix}\frac{1}{8}b(\alpha+\xi-\eta)\\ -\frac{1}{8}b(1-\xi^2)\\ \frac{1}{8}b(1-\eta^2)\end{Bmatrix},$$
$$\begin{Bmatrix}\varphi_7^e\\ \varphi_8^e\\ \varphi_9^e\end{Bmatrix}=\begin{Bmatrix}\frac{1}{8}c(\alpha+\xi+\eta)\\ -\frac{1}{8}c(1-\xi^2)\\ -\frac{1}{8}c(1-\eta^2)\end{Bmatrix},\quad \begin{Bmatrix}\varphi_{10}^e\\ \varphi_{11}^e\\ \varphi_{12}^e\end{Bmatrix}=\begin{Bmatrix}\frac{1}{8}d(\alpha-\xi+\eta)\\ \frac{1}{8}d(1-\xi^2)\\ -\frac{1}{8}d(1-\eta^2)\end{Bmatrix}, \tag{3.23}$$

where

$$a=(1-\xi)(1-\eta),\quad b=(1+\xi)(1-\eta),\quad c=(1+\xi)(1+\eta),$$
$$d=(1-\xi)(1+\eta),\quad \alpha=2-\xi^2-\eta^2. \tag{3.24}$$

The nodal DOFs of the nonconforming elements are illustrated in Fig 3.3. The implementation of the nonconforming elements requires transformation of the nodal DOFs $\frac{\partial w_0}{\partial x}$ and $\frac{\partial w_0}{\partial y}$ between the real and reference elements (see Refs [22, 37] for discussion on this issue).

3.3 Modeling of the post-buckled specimen

Using an in-house FEM code written in MATLAB [49], the post-buckled plate specimen was modeled with 200 nonconforming elements as illustrated in Fig 3.4. To reproduce the asymmetrically-buckled shape of the specimen, the elements surrounded by the nodes number 210 to 231 were trapezoidal but the others were rectangular. To buckle the initially-flat model, the boundary at $x=0$ (along the nodes number 1 to 11) was set clamped while the other boundary along the nodes number 221 to 231 (the blue dashed lines shown in Fig 3.4b) was made free to move along the x-axis. Axial loading was applied to the moving boundary until the deformed boundary (the red solid lines) matched the physical boundary used in the experiment at $x=228.6$ mm. This numerical buckling process is illustrated in Fig 3.5. In

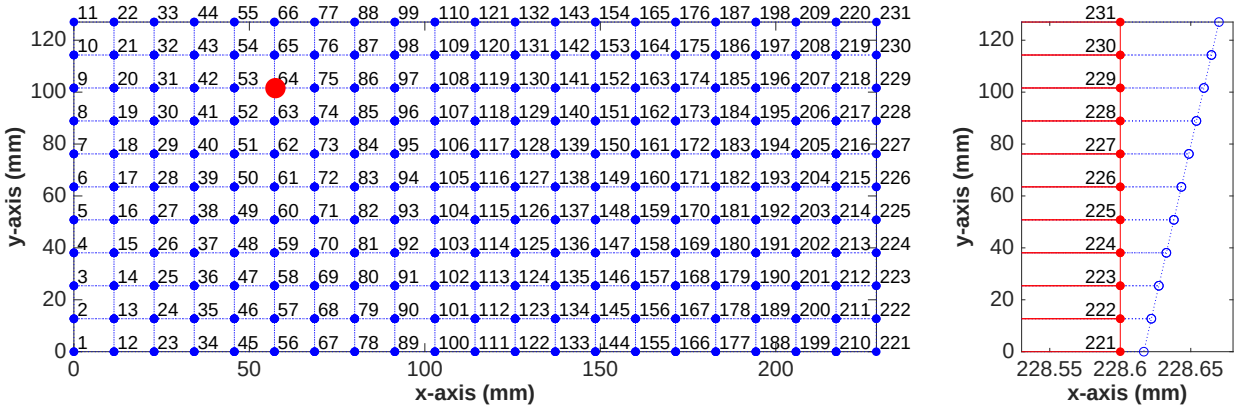

Figure 3.4: The element mesh of the CLPT model. (a) The red circular point at around the node number 64 corresponds to the vibrometer sampling point. (b) A part of the mesh around the moving boundary is illustrated with the exaggerated x-axis. The blue dashed lines illustrate the undeformed trapezoidal elements of the initially-flat model. The deformed elements of the post-buckled model are drawn with red solid lines.

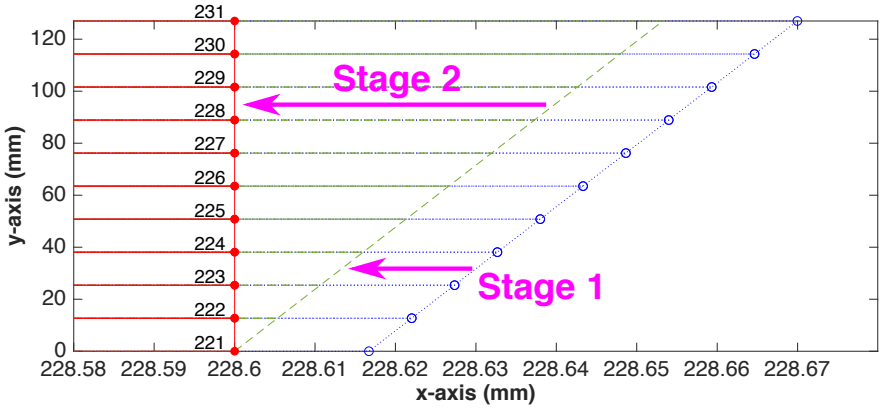

Figure 3.5: Numerical buckling process. A part of the mesh shown in Fig 3.4b is redrawn with the extremely exaggerated x-axis for illustration of the process.

Stage 1, uniformly distributed loads were applied to the moving boundary using a linearized arc-length method [78] (i.e., a force-displacement control). In Stage 2, unevenly distributed loads were indirectly applied to the boundary by implementing a displacement control using the Newton-Raphson method; that is, larger-amplitude loads were applied to higher node

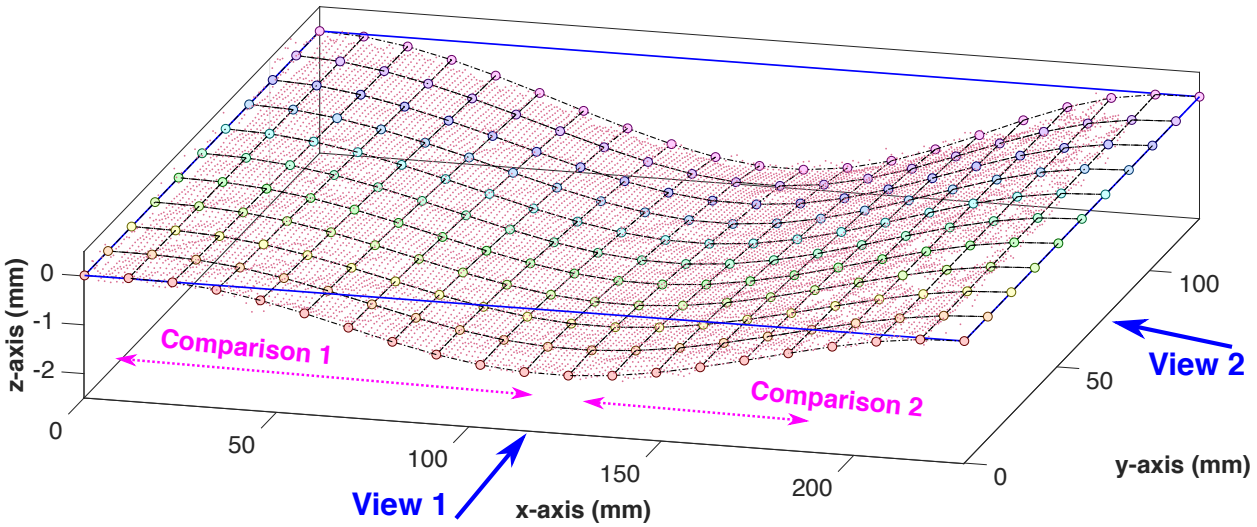

Figure 3.6: The CLPT model of the post-buckled specimen is superimposed on the DIC measurement shown in Fig. 2.3. The z-axis is exaggerated for interpretation of the buckled depth. The blue rectangle indicates the position of the initially-flat model.

numbers. This stage was intended to reproduce the asymmetricity of the specimen and to match the physical boundary at $x = 228.6$ mm.

The CLPT model of the post-buckled specimen is illustrated in Fig 3.6. The boundaries at $x = 0$ and $x = 228.6$ mm were clamped whereas the boundaries at $y = 0$ and $y = 127.0$ mm were set free as in the experiment.

The buckled shapes of the specimen and CLPT model are compared as shown in Fig 3.7. It can be observed from Views 1 and 2 that the model successfully reproduced the asymmetric buckled shape of the specimen showing the identical largest buckled depth 1.3–2.1 mm along the y-axis.

The quantitative analysis of the comparison is shown in Fig 3.8. The DIC data were interpolated to obtain the depth values at the location of the nodes of the model. The DIC measurement obtained around the free boundaries was irregular and thus the interpolated values on the boundaries were not reliable. Therefore, the buckled depths near the boundaries were indicated but were not used for comparison (e.g., the DIC marker between the nodes

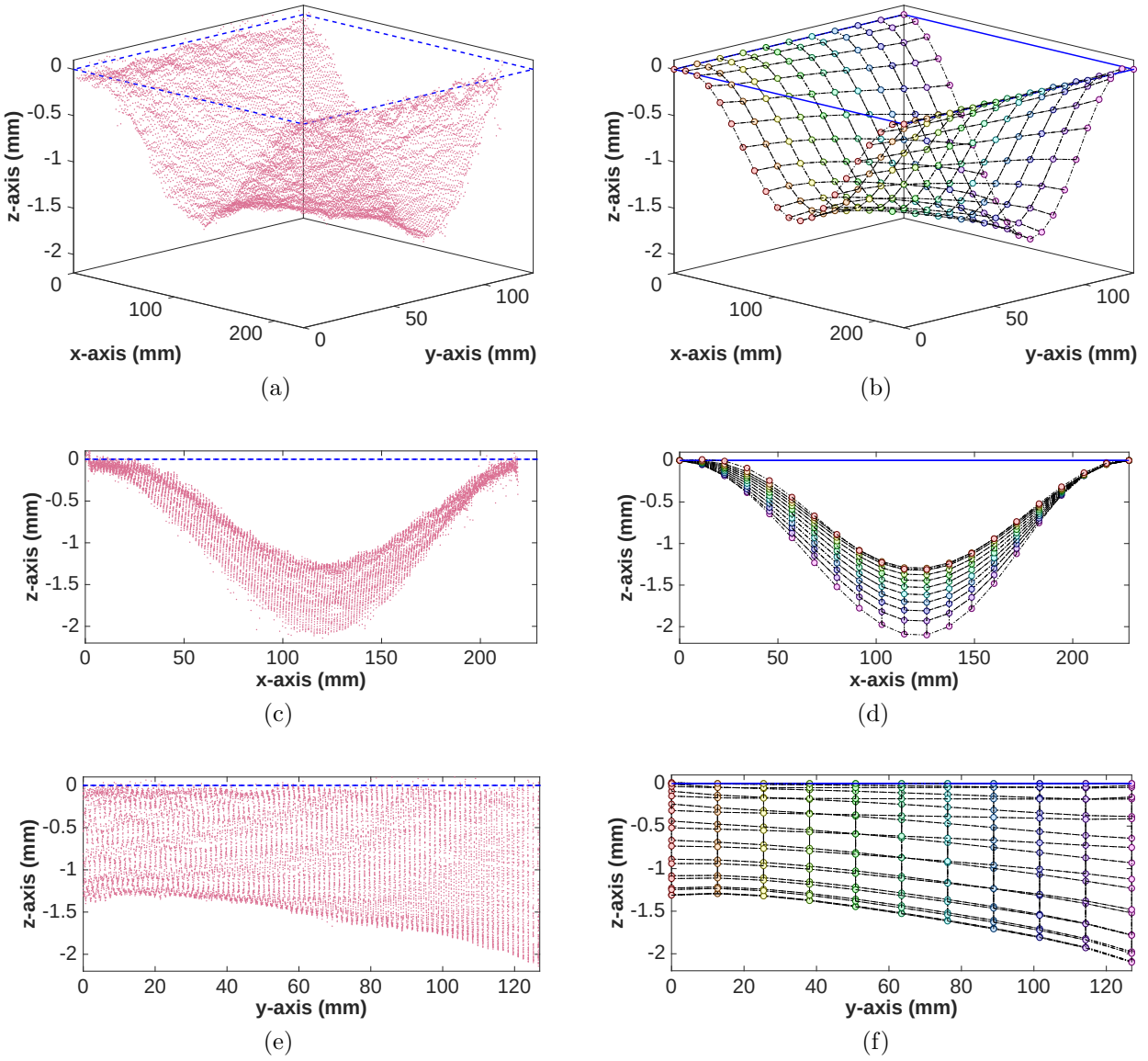

Figure 3.7: Comparison between the buckled shapes of the specimen (a, c, e) and CLPT model (b, d, f). The z-axes are extremely exaggerated for comparison. The blue rectangles indicate the position of the initially-flat plate. (a, b) The 3-D buckled shapes. (c, d) View 1: the shapes along the x-axis. (e, f) View 2: the shapes along the y-axis. Views 1 and 2 are indicated in Fig. 3.6.

number 111 and 112 in Fig 3.8a). In addition, a part of the buckled shape of the specimen at x = 190.0–228.6 mm could not be captured in the DIC measurement as mentioned in

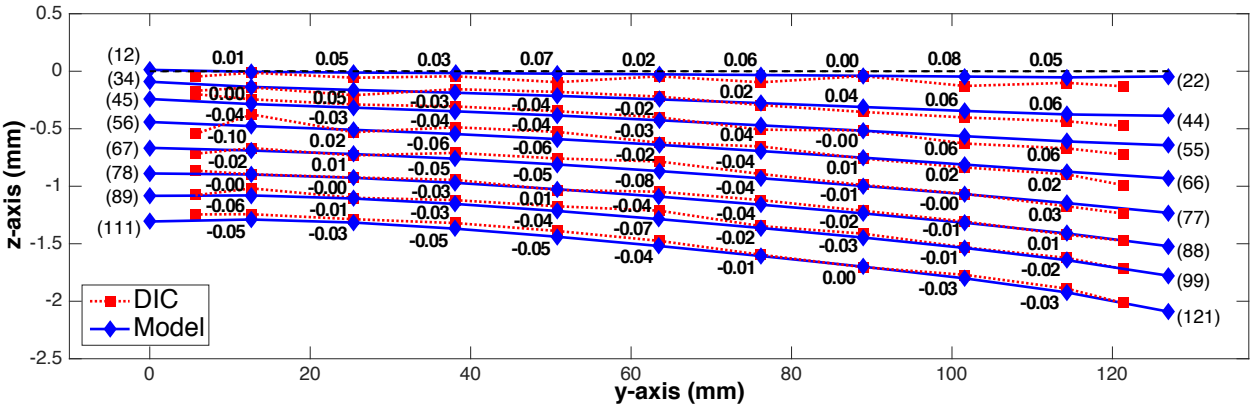

(a)

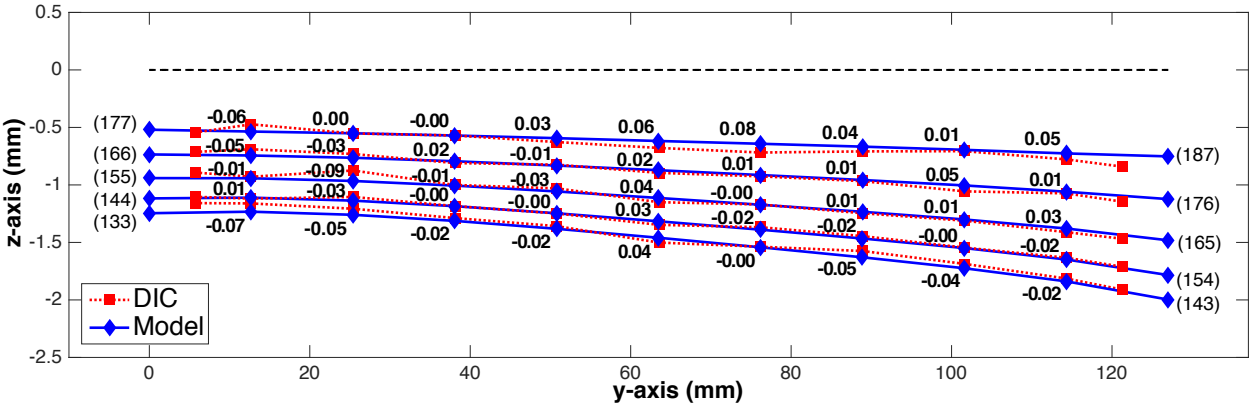

(b)

Figure 3.8: The quantitative analysis of the comparison between the buckled shapes of the CLPT model and specimen in View 2. (a) Comparison 1: the nodes number 12 to 121. (b) Comparison 2: the nodes number 133 to 187. The numbers in brackets indicate the node numbers of the model. The discrepancies (the nodal values minus the DIC measurements) are written in a millimeter unit (mm) around the nodes. View 2 and Comparisons 1 and 2 are indicated in Fig. 3.6.

Section 2.2.3 and thus comparison could not be made at the nodes number 188 to 220. Despite the irregularity of some of the DIC measurements, the model showed an excellent agreement with the buckled shape of the specimen.

Therefore, these comparison results confirm that the CLPT model successfully captured the spatial complexity of the post-buckled specimen.

3.4 Damping

In this section, damping calibration of the CLPT model based on the free-decay tests of the specimen (see Section 2.3.4) is introduced. In addition, the performance of several damping options is investigated.

3.4.1 Natural frequencies and modes of the CLPT model

The first six modes of the post-buckled model and the corresponding natural frequencies were analyzed for damping calibration. The natural frequency of the first mode (post-buckled), 107.92 Hz, showed a reasonable agreement with the experimental measurement (4.5 % error). The natural frequencies of the second through the sixth modes are 164.97, 197.01, 316.53, 387.42, and 398.54 Hz, respectively.

3.4.2 Impact of damping on dynamic simulation

To investigate the impact of damping on the performance of the CLPT model, the dynamic response under 5 g–85 Hz harmonic loading was simulated with three damping scenarios: no-damping, mass-proportional damping, and Rayleigh damping. The simulation results showed c-snap in all of these damping cases.

As illustrated in Fig 3.9, the fast Fourier transform (FFT) analysis of the simulation results was compared to the FFT of the corresponding DIC measurement (c-snap, see Fig 2.6c). The node number 116 of the model (see Fig 3.4) corresponds to the DIC sampling point number 52 (see Fig 2.4). The sampling frequency of the DIC measurement was 2000 Hz and thus the FFT plot of the measurement (see Fig 3.9) does not extend beyond 1000 Hz.

Damping options 1 and 2: no-damping and mass-proportional damping

The mass-proportional damping $\mathbf{C}$ [20, 58] is given by

$$\mathbf{C} = a\mathbf{M}, \text{ where } a = 2\zeta\omega_1. \tag{3.25}$$

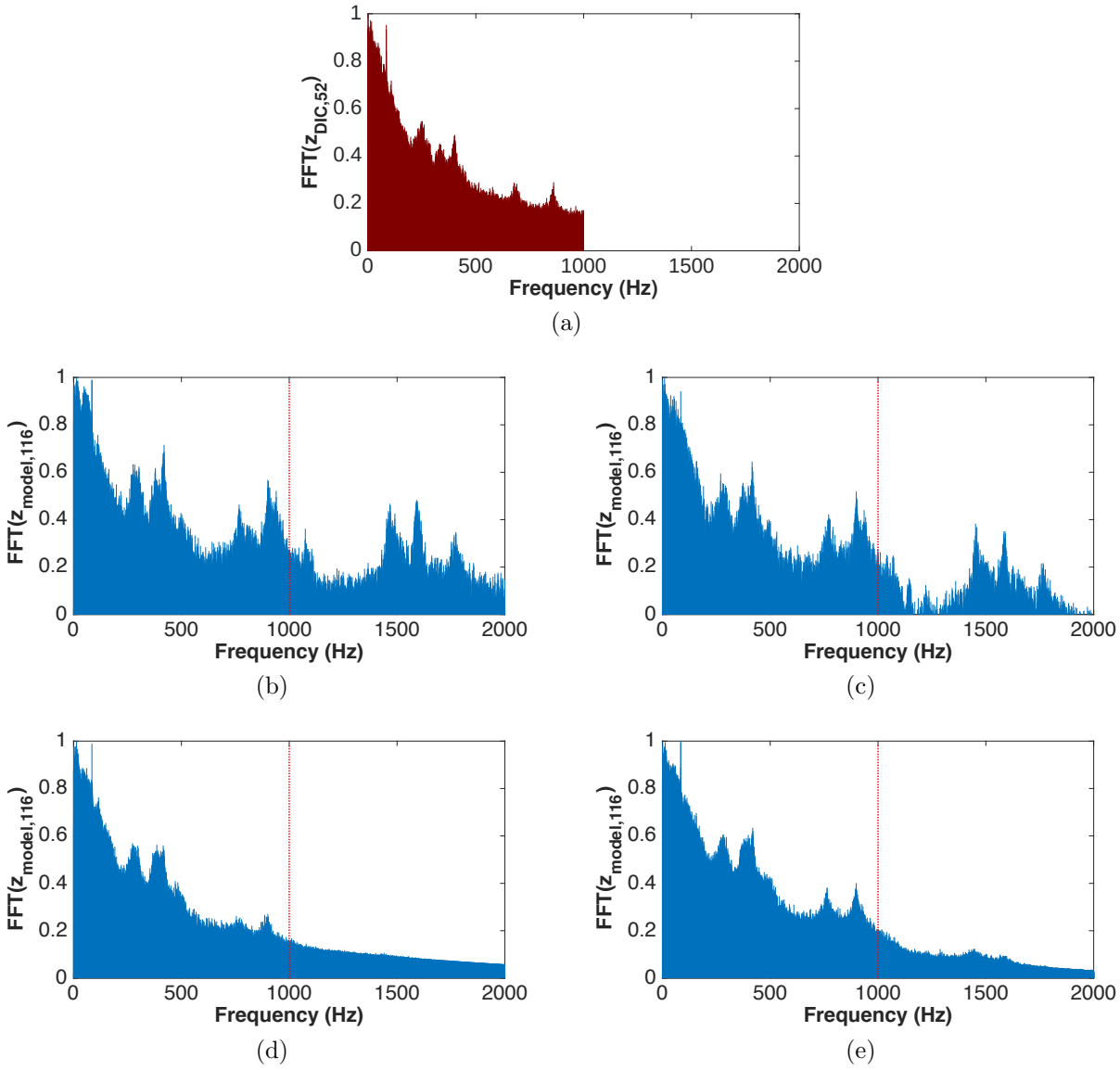

Figure 3.9: The FFT analysis of the dynamic response of the specimen and CLPT model under 5 g-85 Hz harmonic loading. (a) The DIC measurement of the response of the specimen. (b) The simulation result for no-damping. (c) The simulation result for mass-proportional damping. (d) The simulation result for Rayleigh damping with $\omega_j = \omega_3$. (e) The simulation result for Rayleigh damping with $\omega_j = \omega_6$. The FFT values are written in a normalized log-scale. The transverse displacements of the DIC sampling point number 52 (see Fig 2.4) and model node number 116 (see Fig 3.4) are represented by $z_{\text{DIC},52}$ and $z_{\text{model},116}$, respectively.

The coefficient a was determined using the experimental damping ratio for the post-buckled case ($\zeta = 0.45$ %) along with the first-mode natural frequency of the CLPT model ($f_1 = 107.92$ Hz or $\omega_1 = 678.08$ rad/sec).

For the no-damping case (see Fig 3.9b), a significant impact of high-frequency modes on the response was observed. Such a strong influence of high-frequency modes was not shown in the FFT of the DIC measurement (see Fig 3.9a). The mass-proportional damping (see Fig 3.9c) marginally subdued the high-frequency modes, whose strong influence was still observed. The simulations under both damping scenarios consequently encountered convergence issues and failed to converge during the Newton-Raphson iterations within a time step after 220 loading cycles ($t = 2.60$ sec) and 480 loading cycles ($t = 5.65$ sec) for the no-damping and mass-proportional damping cases, respectively.

Damping option 3: Rayleigh damping

In order to obtain physically-realistic dynamic response, address the convergence issue, and include the stiffness-proportional damping as observed from the experiment, Rayleigh damping was employed in the CLPT model. The Rayleigh damping matrix $\mathbf{C}$ [20, 58] is given by

$$\mathbf{C} = a_0\mathbf{M} + a_1\mathbf{K}. \tag{3.26}$$

The coefficients a_0 and a_1 can be determined from

$$a_0 = \zeta\frac{2\omega_1\omega_j}{\omega_1 + \omega_j}, \quad a_1 = \zeta\frac{2}{\omega_1 + \omega_j}, \tag{3.27}$$

where $\zeta = 0.45$ % and $\omega_1 = 678.08$ rad/sec. The natural frequencies of the third and sixth modes of the model (corresponding to the typical second and third beam modes, respectively) were tried for ω_j.

During the simulation for both cases, no convergence issues were observed. Furthermore,

as shown in Figs 3.9d and 3.9e, the FFT of the simulation results demonstrated a similar trend as shown in the FFT of the DIC measurement (see Fig 3.9a). However, it was observed that the Rayleigh damping with $\omega_j = \omega_3$ excessively controlled high-frequency modes at 700–900 Hz. On the other hand, the Rayleigh damping with $\omega_j = \omega_6$ showed a reasonable agreement with the experimental measurement.

Based on the evaluation of the damping options, Rayleigh damping with $\omega_j = \omega_6$ was finally adopted in the CLPT model. While only a single loading case was discussed in this section, Rayleigh damping with $\omega_j = \omega_6$ performed well over a broad range of forcing parameters.

3.5 Dynamic simulation results

This section presents the simulation results obtained using the CLPT model. In addition, the spatio-temporal complexity and parameter sensitivity of the model are assessed by comparing the simulation results to the experimental observations. In the nonlinear regime, model validation using only one or a small set of experimental tests is not sufficient. To address this issue, the numerical snap-through boundaries were characterized in the HFP space and were compared to the experimental results for robust validation of the model.

3.5.1 Simulation method

For time integration, the Newmark-beta method [53], particularly the average acceleration method $\beta = \frac{1}{4}$ [58], was applied to the FEM shown in Eq (3.20). Within each time step t_n, the Newton-Raphson method was used to solve the nonlinear equation. These steps were processed using MATLAB.

The time step size Δt for each loading scenario was determined by

$$\Delta t = \frac{1}{b \times f} = \frac{1}{320 \times f} \text{ sec}, \tag{3.28}$$

where f is a forcing frequency and b is the number of time steps per loading cycle (for this

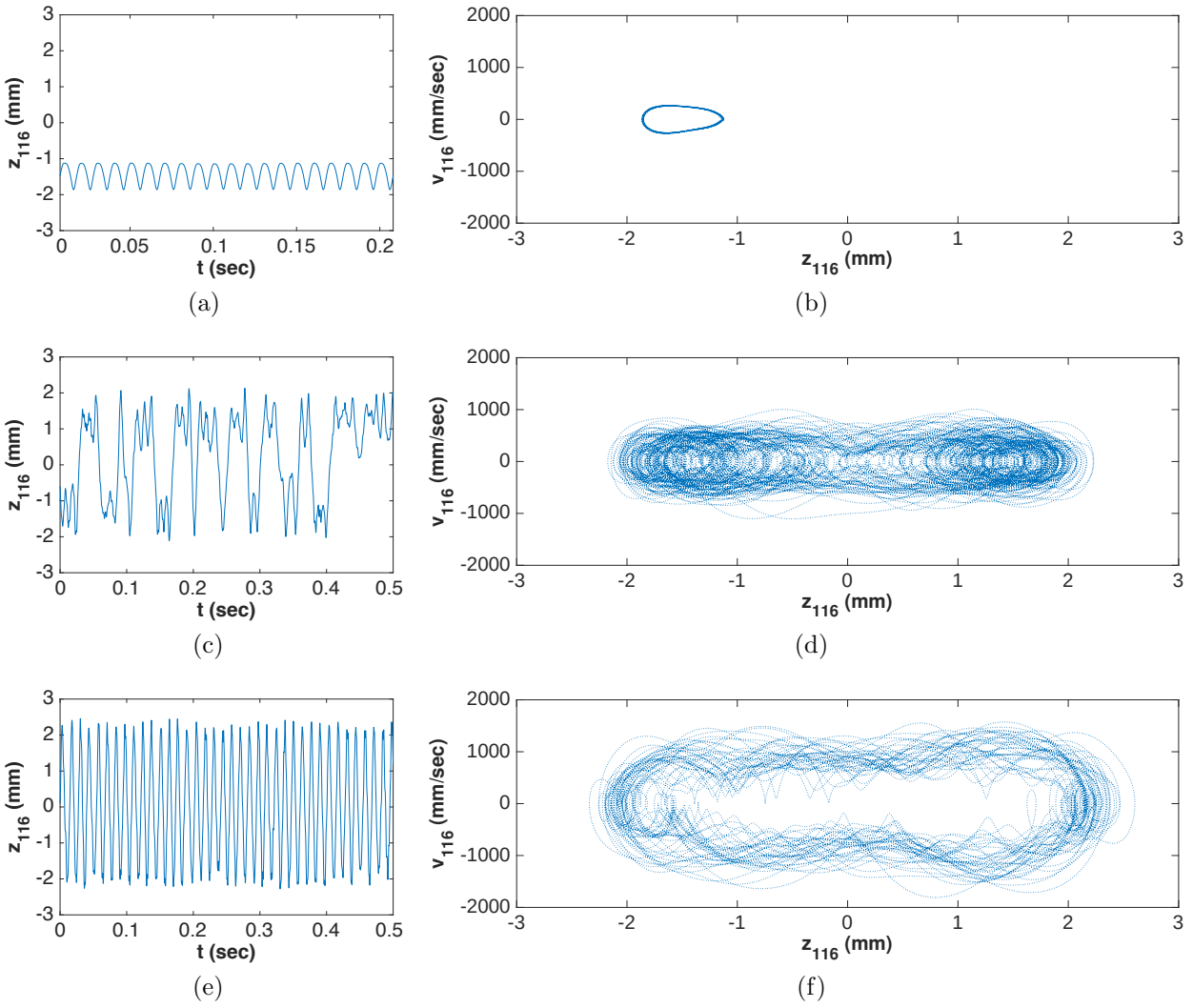

Figure 3.10: The simulated midpoint response of the CLPT model and phase projections for the time series under the harmonic loading cases: (a) 4 g–200 Hz, (b) 5 g–85 Hz, and (c) 7 g–75 Hz. The response and velocity of the node number 116 (see Fig 3.6) are represented by z_{116} and v_{116}, respectively.

work, $b = 320$). For the 85 Hz forcing frequency case, for example, $\Delta t = 1/(320 \times 85 \text{ Hz}) = 3.6765 \times 10^{-5}$ sec.

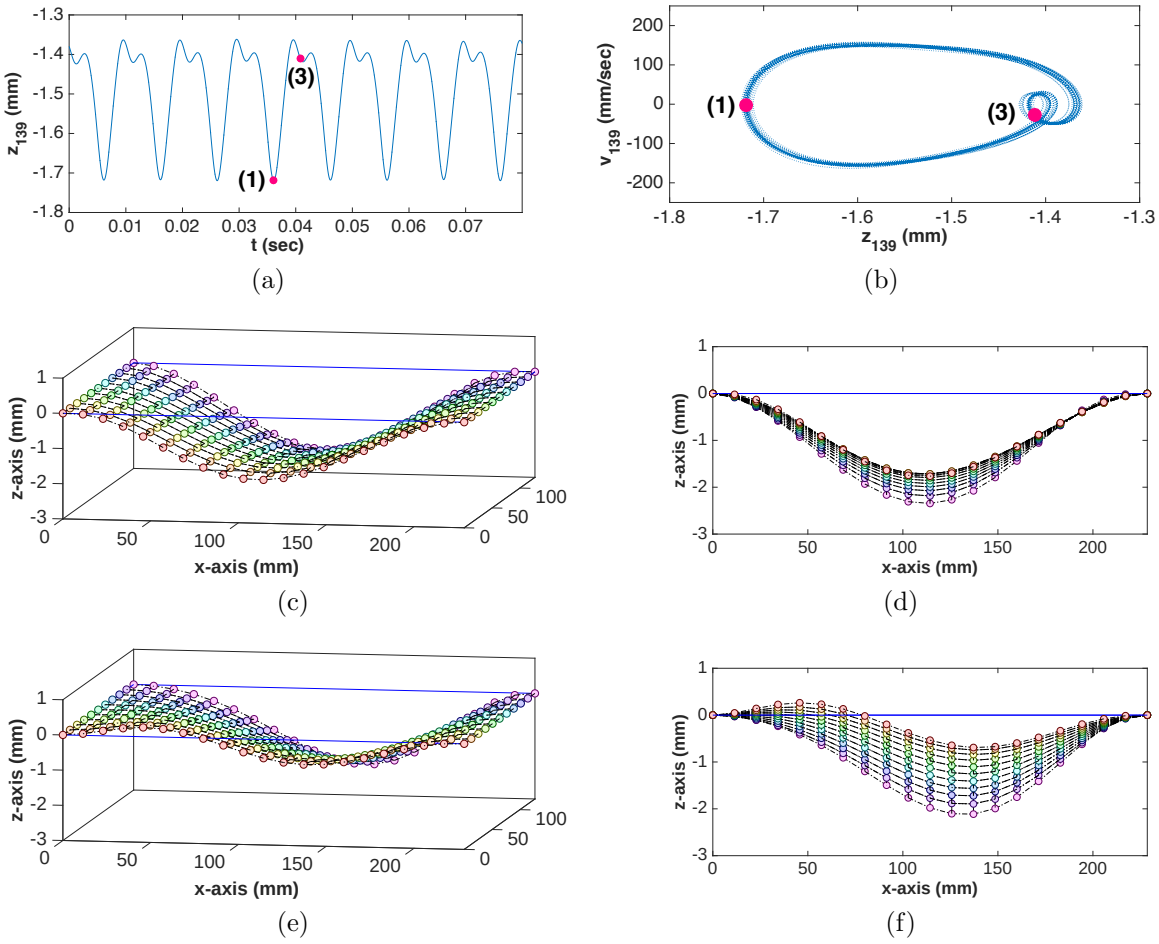

Figure 3.11: The simulation result (single-well) of the CLPT model under 4 g–200 Hz harmonic loading. (a) The time series of z_{139}. (b) The projected phase portrait of the time series. The response and velocity of the node number 139 (see Fig 3.6) are represented by z_{139} and v_{139}, respectively. The snapshots of the deflected shapes were taken: (c, d) at (1), and (e, f) at (3).

3.5.2 Simulation of the spatio-temporal complexity

The dynamic response of the CLPT model was obtained through dynamic simulations under the same harmonic loading scenarios as used in the dynamic DIC tests. The simulation results showed the same characteristic response types as observed from the experiment: steady-state single-well, c-snap, and p-snap responses for the 4 g–180 Hz, 5 g–85 Hz, and

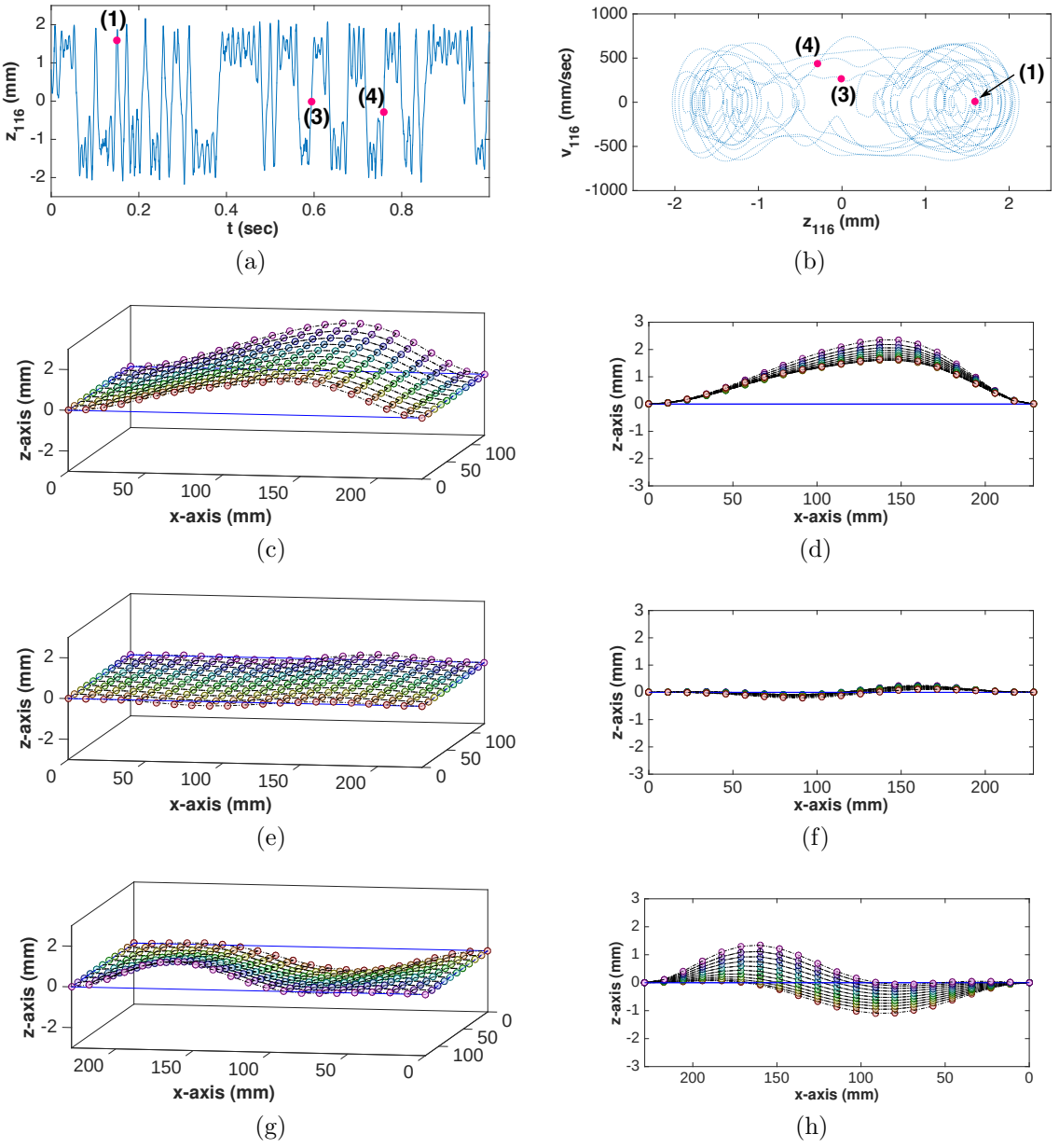

Figure 3.12: The simulation result (c-snap) of the CLPT model under 5 g–85 Hz harmonic loading. (a) The time series of z_{116}. (b) The projected phase portrait of the time series. The snapshots of the deflected shapes were taken: (c, d) at (1), (e, f) at (3), and (g, h) at (4). The angle of the snapshots taken at (4) was rotated 180° for comparison with the DIC snapshots taken at the corresponding point.

7 g–75 Hz loading cases, respectively. However, while 4 g–180 Hz did produce a single-well response, the response of the model under 4 g–200 Hz loading was more comparable to the experimental observation at 4 g–180 Hz; thus, these two cases were compared in this section. Shifts in behaviors are not surprising given the system complexity.

The time series of the midpoint response of the model and phase projections for the time series are illustrated in Fig 3.10. The node number 116 of the model (see Fig 3.6) corresponds to the DIC sampling point number 52 (see Fig 2.4). In all of the three loading scenarios, the response and projected phase portraits of the CLPT model showed a reasonable agreement with the corresponding DIC measurement shown in Fig 2.6.

For 3-D spatio-temporal comparison, some snapshots of the deflected shapes of the CLPT model under the 4 g–200 Hz and 5 g–85 Hz harmonic loading cases are illustrated in Figs 3.11 and 3.12, respectively. These snapshots well match the snapshots of the experimentally measured deflected shapes of the specimen taken at the corresponding points (see Figs 2.7 and 2.8).

Therefore, these comparisons confirm that the model successfully captures the spatio-temporal complexity of the dynamic response of the specimen. While there was some shift in the HFP for the single-well response, the overall agreement over a broad range of HFPs, which is discussed in the following section, was excellent.

3.5.3 Simulation of the parameter sensitivity

The simulation of the forcing frequency-sweep tests involves a high computational cost. To address this issue, the dynamic response of the CLPT model under various HFPs (or discrete points in the HFP space) was separately simulated with at-rest (or zero-energy) initial conditions. In this section, some of the simulation results which were used to form the numerical snap-through boundaries of the CLPT model in the HFP space are presented in the form of the time series of z_{64}, which denotes the transverse displacement of the node number 64 (see Fig 3.6). The node number 64 of the model corresponding to the vibrometer sampling point (see Fig 2.4) was chosen because the parameter sensitivity of the specimen's

dynamic response (see Fig 2.9) was investigated using the vibrometer data.

Simulation results at 4–7 g

For the 7 g loading case (see Fig 3.13a), steady-state p-snap and c-snap were observed at 70–90 Hz and at 90–145 Hz, respectively. At the interface (90 Hz) between the two regions, transitions between c-snap and p-snap were observed: the response started with c-snap, switched to p-snap at $t = 0.7$ sec, and reverted to c-snap at $t = 1.8$ sec. At the end of the c-snap region (145 Hz), the number of snap-through occurrences significantly decreased. In the high frequency range, another c-snap region was observed at 195–197 Hz, where a single snap-through event occurred at a time interval of two seconds. Similarly, for the 6 g loading case (see Fig 3.13b), steady-state p-snap and c-snap were observed at 75–80 Hz and at 80–140 Hz, respectively; in addition, transitions between the two responses (p-snap to c-snap at $t = 1.0$ sec and the reverse transition at $t = 1.7$ sec) occurred at the interface, 80 Hz. In contrast to the 7 g case, snap-through was not observed in the high frequency range at 6 g while large-amplitude responses were observed at 193–200 Hz.

The 5 g loading case (see Fig 3.13c) demonstrated a different response pattern from the previous two cases. Steady-state p-snap did not appear but steady-state c-snap was observed in the two regions: at 78 Hz and at 82–130 Hz. At the interface (80 Hz) between the two c-snap regions, the start-up transient c-snap response settled down in the steady-state single-well response at $t = 1.0$ sec. The start-up transient c-snap was observed again at the interface (135 Hz) between the c-snap and single-well regions. Similarly, the 4 g loading case (see Fig 3.13d) showed the two c-snap regions (at 83–105 Hz and at 115–125 Hz) and the start-up transient c-snap at the interface (110 Hz).

Simulation results at 0.5–3 g

For the 3 g loading case (see Fig 3.14a), steady-state c-snap was observed at 87–100 Hz. At 102 Hz, after the start-up transient c-snap stopped at $t = 1.3$ sec, the model experienced extremely chaotic response and finally settled down into the nearly-periodic response at

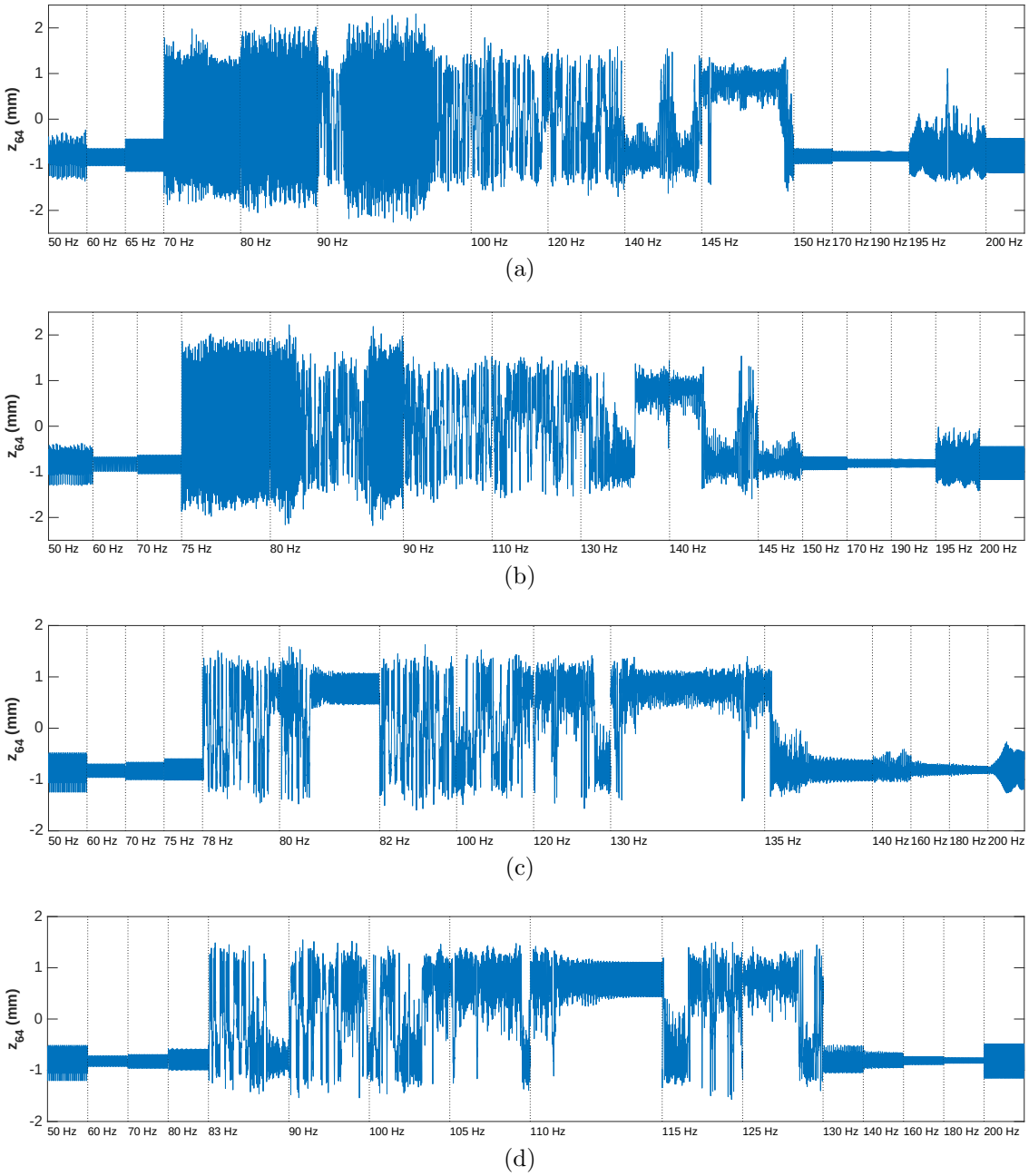

Figure 3.13: The simulated time series of the response of the CLPT model under the forcing amplitudes: (a) 7 g, (b) 6 g, (c) 5 g, and (d) 4 g. The transverse displacement of the node number 64 (see Fig 3.6) is represented by z_{64}.

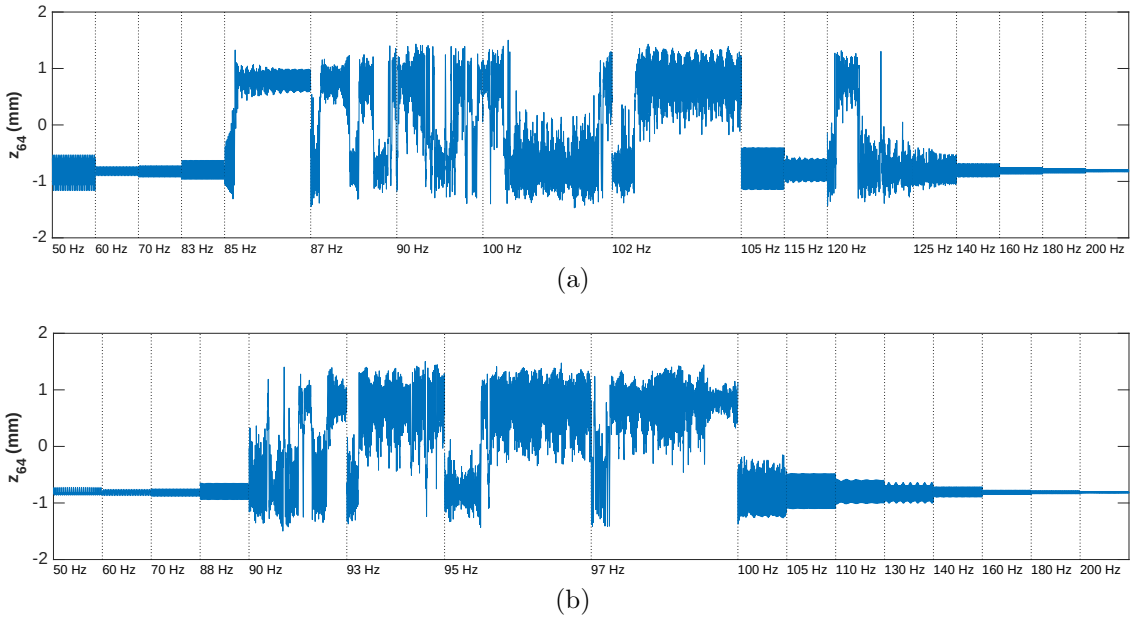

Figure 3.14: The simulated time series of the response of the CLPT model under the forcing amplitudes: (a) 3 g, and (b) 2 g. The transverse displacement of the node number 64 (see Fig 3.6) is represented by z_{64}.

$t = 2.6$ sec. The start-up transient c-snap was also observed at 85 and 120 Hz. The 2 g loading case (see Fig 3.14b) demonstrated steady-state c-snap at 90–93 Hz and start-up transient c-snap at 95–97 Hz. For the 0.5 and 1 g loading cases, snap-through was not observed through simulation.

3.5.4 Numerical snap-through boundaries of the CLPT model

Based on the simulation results, the numerical snap-through boundaries were characterized in the HFP space as illustrated in Fig 3.15. The occurrence of steady-state snap-through was determined by analyzing the responses at all of the nodes. The HFPs at 2, 3, 4, 5, 6, and 7 g are the primary data points, where the dynamic response was simulated for longer than two seconds for the snap-through cases and one second for the single-well cases. The investigation of the other HFPs (the secondary points) was exploratory and thus the simulation for the secondary points was run for not as long as done for the primary cases. It was assumed that

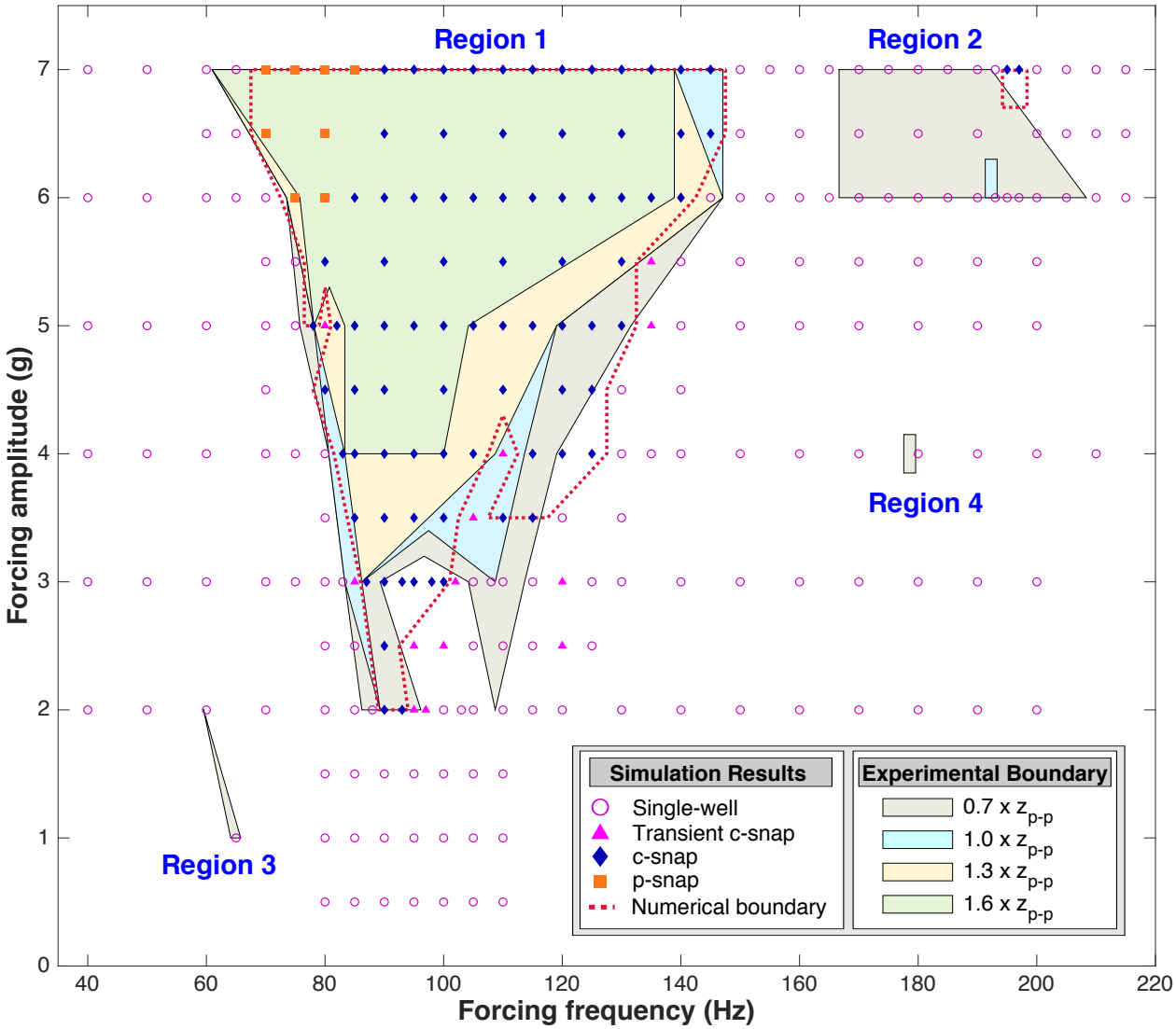

Figure 3.15: The dynamic simulation results and numerical snap-through boundaries of the CLPT model in the HFP space. The experimental snap-through boundaries were replicated from Fig 2.12.

the numerical boundaries existed between the single-well and snap-through regions.

In Region 1, the left boundary (or the low-frequency boundary) of the CLPT model well matched the experimental boundaries at all of the threshold levels. Along the left boundary, the response of the model displayed an extreme sensitivity to frequency changes.

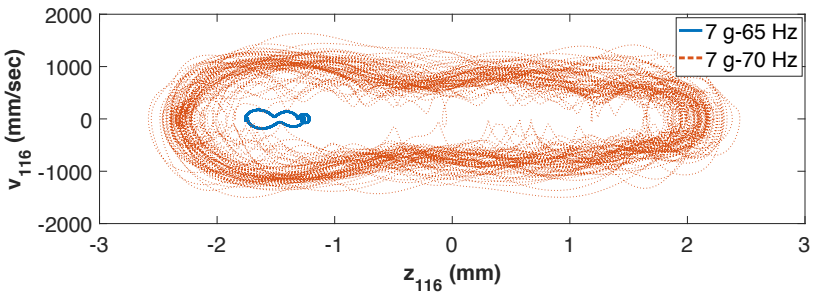

Figure 3.16: Phase projection for the simulated time series of z_{116} under 7 g–65 Hz and 7 g–70 Hz harmonic loading (see Fig 3.13a).

For example, as illustrated in Fig 3.16, a marginal frequency increase (5 Hz) across the boundary at 7 g resulted in the two extremely different projected phase portraits: a single-well response at 65 Hz and p-snap at 70 Hz. Furthermore, co-existing responses of the model were observed in the vicinity of the left boundary at 5–7 g as shown in Fig 3.17. In all of the three cases, the model showed steady-state single-well response with at-rest initial conditions and steady-state p-snap that could be 'found' by using high-energy initial conditions. In contrast to the left boundary, characterization of the right boundary (or the high-frequency boundary) of the model was complicated due to the long time interval between snap-through events (e.g., at 7 g–145 Hz in Fig 3.13a) and the prolonged chaotic response (e.g., at 3 g–102 Hz in Fig 3.14a) along the boundary. The numerical right boundary nonetheless showed a reasonable agreement with the lower bound ($0.7 \times z_{\text{p-p}}$) at 3.5–5.5 g and with all of the threshold levels at 5.5–7 g.

In Region 2, the model exhibited large-amplitude response (close to $z_{\text{p-p}}$) at 193–200 Hz but snap-through was observed only at 7 g (195–197 Hz), which possibly corresponds to the experimental snap-through boundary of the threshold $1.0 \times z_{\text{p-p}}$ at 6 g–193 Hz. Snap-through of the model was not observed in Regions 3 and 4, where the experimental snap-through boundaries appeared only in the lower bound. However, the simulation results showed significantly larger amplitude single-well response in these regions than the response observed in the vicinity of the regions.

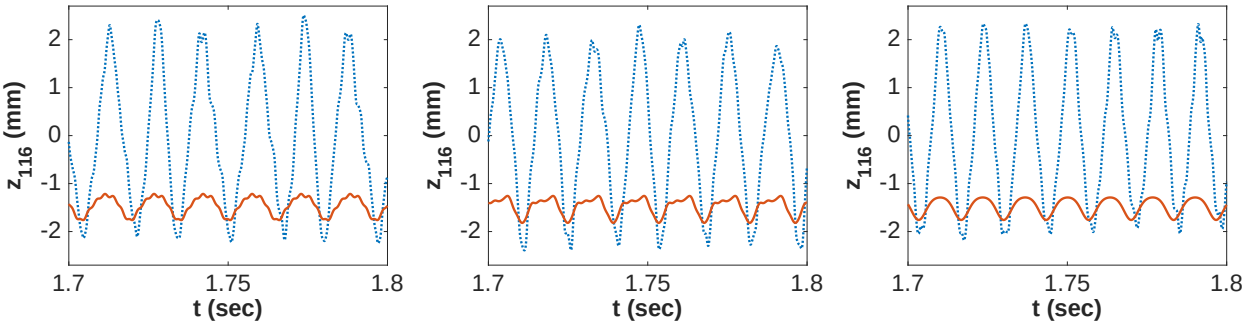

Figure 3.17: The simulated time series of co-existing responses z_{116} under (a) 7 g–65 Hz, (b) 6 g–70 Hz, and (c) 5 g–75 Hz harmonic loading with at-rest (red solid lines) and high-energy (blue dotted lines) initial conditions.

Therefore, the CLPT model successfully captured the parameter sensitivity of the dynamic response of the specimen. Furthermore, given the difficulties in identifying the exact experimental boundaries, the numerical snap-through boundaries showed a remarkable agreement with the experimental ones, thereby providing robust validation of the CLPT model.

3.6 Summary

In this chapter, the CLPT model and its simulation results were presented. The CLPT model of the post-buckled specimen was generated by calibrating only its initial static equilibrium to match the initially buckled shape of the specimen. It should be highlighted that the simulations of the forced dynamic response using the model required neither modification nor curve-fitting to match the experimental data. The model adopted Rayleigh damping with the damping parameters obtained from the free-decay tests of the specimen. The simulation results confirmed that the model successfully captured the spatio-temporal complexity and parameter sensitivity observed in the dynamic response of the specimen. In addition, the model demonstrated complex co-existing responses along its snap-through boundary. Finally, the comparison between the numerical and experimental snap-through boundaries in the HFP space provided robust validation of the CLPT model.

Given that CLPT has not been a preferred choice over shear deformation theories to investigate nonlinear dynamics and snap-through, this work provided a new perspective on the capabilities of CLPT models. Furthermore, the numerical data obtained through extensive dynamic simulations using the CLPT model provide a useful benchmark for validation of computationally-demanding models (e.g., models involve high computational costs or locking issues).

Chapter 4

FSDT MODEL AND NUMERICAL LOCKING

4.1 Introduction

In the previous chapter, the simulation results of the CLPT model showed excellent agreement with the experimental data including snap-through boundaries and thus robust validation of the model was achieved for thin plates. This successful characterization of the nonlinear dynamic response and snap-through of the post-buckled specimen in the displacement fields naturally leads to another objective of this work: analysis of stress fields induced by these phenomena and their impact on fatigue of composite structures. For accurate and direct computation of transverse shear stress fields, the CLPT model is extended to shear deformation models, which are applicable to both thin and moderately thick plates.

This work adopted FSDT as the first step in developing reliable simulation tools for stress analysis because numerical implementation and validation of FSDT models are easily achieved compared to the other shear deformation models. In addition, once a reliable implementation of FSDT models including accurate prediction of displacement and stress fields is validated, the formulation can be readily extended to higher-order shear deformation and layerwise models.

This chapter presents in detail the nonlinear equations of motion for FSDT and the FEM formulation for an FSDT model. The performance of the FSDT model is investigated through linear analysis of cylindrical bending problems and relevant issues are discussed.

4.2 Nonlinear equations of motion for FSDT

This section presents the equations of motion for FSDT based on the work of Reddy [68].

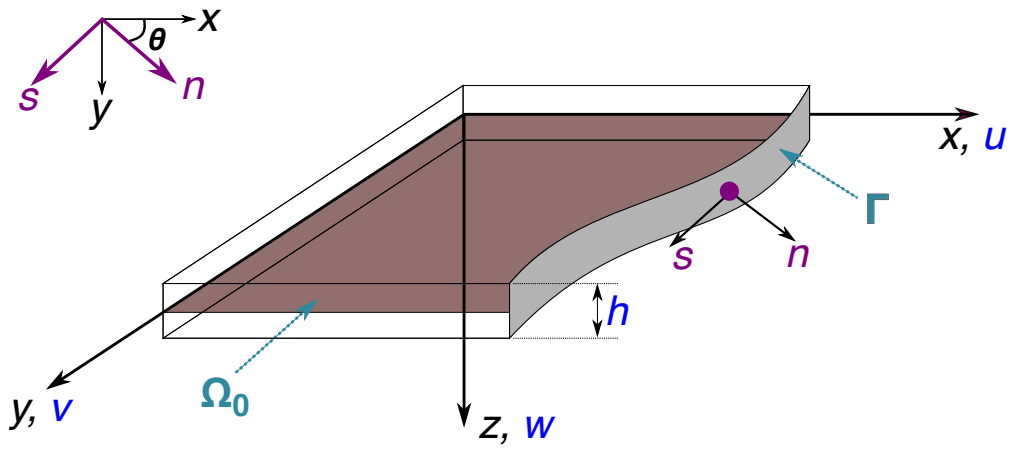

Figure 4.1: The figure illustrated in Fig 3.1 is replicated for convenience. The coordinate system of plates. The displacements along the x, y, and z axes are given by u, v, and w, respectively. The unit normal and tangential vectors of a point on the boundary Γ are given by $\mathbf{n}$ and $\mathbf{s}$, respectively. The undeformed midplane is denoted by Ω_0.

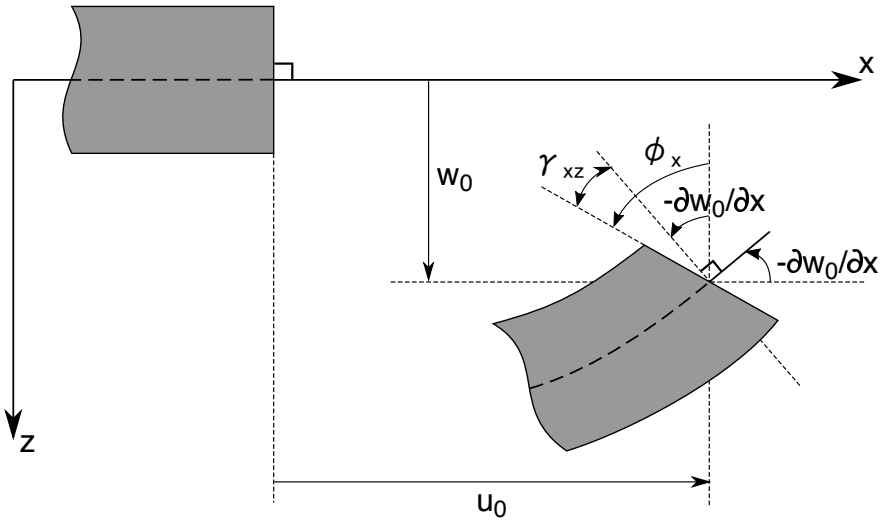

Figure 4.2: The undeformed and deformed configurations of FSDT on the x-z plane. This figure was drawn based on the work of Reddy [68].

4.2.1 Displacement and strain fields

In FSDT, constant transverse shear strain distribution through the plate thickness is assumed; thus, the Kirchhoff hypothesis for the normality of transverse planes[1] is relaxed. Following the coordinate system of plates illustrated in Fig 4.1, the displacement field of FSDT is given by

$$\begin{aligned} u(x,y,z,t) &= u_0(x,y,t) + z\phi_x(x,y,t), \\ v(x,y,z,t) &= v_0(x,y,t) + z\phi_y(x,y,t), \\ w(x,y,z,t) &= w_0(x,y,t), \end{aligned} \tag{4.1}$$

where (u_0, v_0, w_0) are midplane displacements along the x-, y-, and z-axes, respectively, and (ϕ_x, ϕ_y) are the rotations of transverse normal planes about the y- and x-axes as illustrated in Fig 4.2 for ϕ_x.

The rotations ϕ_x and ϕ_y are defined as

$$\frac{\partial u}{\partial z} = \phi_x, \quad \frac{\partial v}{\partial z} = \phi_y. \tag{4.2}$$

As an alternative, the rotations about the x- and y-axes (θ_x and θ_y, respectively) following the right-hand rule are also frequently used for the Reissner-Mindlin theory. The relationship between the two definitions is given by

$$\theta_x = -\phi_y, \quad \theta_y = \phi_x. \tag{4.3}$$

This work adopted von Kármán strains[2] to include geometric nonlinearity in FSDT following the works of Timoshenko and Reddy in Refs [89] and [68], respectively. Using the

[1] A straight line which is initially perpendicular to the midplane of the plate remains straight and perpendicular to the midplane of the plate after deformation [90].

[2] More details about the von Kármán nonlinear strains are discussed in Appendix C.

displacement field in Eq (4.1), the von Kármán nonlinear strains for FSDT are given by

$$\varepsilon_{xx} = \frac{\partial u}{\partial x} + \frac{1}{2}\Big(\frac{\partial w}{\partial x}\Big)^2 = \frac{\partial u_0}{\partial x} + \frac{1}{2}\Big(\frac{\partial w_0}{\partial x}\Big)^2 + z\frac{\partial \phi_x}{\partial x} = \varepsilon_{xx}^{(0)} + z\varepsilon_{xx}^{(1)}, \tag{4.4}$$

$$\varepsilon_{yy} = \frac{\partial v}{\partial y} + \frac{1}{2}\Big(\frac{\partial w}{\partial y}\Big)^2 = \frac{\partial v_0}{\partial y} + \frac{1}{2}\Big(\frac{\partial w_0}{\partial y}\Big)^2 + z\frac{\partial \phi_y}{\partial y} = \varepsilon_{yy}^{(0)} + z\varepsilon_{yy}^{(1)}, \tag{4.5}$$

$$\varepsilon_{zz} = \frac{\partial w}{\partial z} = \frac{\partial w_0}{\partial z} = 0, \tag{4.6}$$

$$\begin{aligned}\gamma_{xy} = 2\varepsilon_{xy} &= \frac{\partial u}{\partial y} + \frac{\partial v}{\partial x} + \frac{\partial w}{\partial x}\frac{\partial w}{\partial y} \\ &= \frac{\partial u_0}{\partial y} + \frac{\partial v_0}{\partial x} + \frac{\partial w_0}{\partial x}\frac{\partial w_0}{\partial y} + z\Big[\frac{\partial \phi_x}{\partial y} + \frac{\partial \phi_y}{\partial x}\Big] = \gamma_{xy}^{(0)} + z\gamma_{xy}^{(1)},\end{aligned} \tag{4.7}$$

$$\gamma_{yz} = 2\varepsilon_{yz} = \frac{\partial v}{\partial z} + \frac{\partial w}{\partial y} = \phi_y + \frac{\partial w_0}{\partial y}, \tag{4.8}$$

$$\gamma_{xz} = 2\varepsilon_{xz} = \frac{\partial u}{\partial z} + \frac{\partial w}{\partial x} = \phi_x + \frac{\partial w_0}{\partial x}, \tag{4.9}$$

where (ε_{xx}, ε_{yy}, ε_{zz}) are normal strains, (γ_{xy}, γ_{xz}, γ_{yz}) are shear strains, ($\varepsilon_{xx}^{(0)}$, $\varepsilon_{yy}^{(0)}$, $\gamma_{xy}^{(0)}$) are membrane strains, and ($\varepsilon_{xx}^{(1)}$, $\varepsilon_{yy}^{(1)}$, $\gamma_{xy}^{(1)}$) are bending strains.

4.2.2 Equations of motion

Using the typical displacement-based variational principle[3], the governing equations of motion for FSDT can be derived from the principle of virtual work:

$$0 = \int_0^T (\delta U + \delta V - \delta K)dt, \tag{4.10}$$

where the virtual strain energy, the virtual work done by applied forces, and the virtual kinetic energy are denoted by δU, δV, and δK, respectively. Following the coordinate system

[3]Another type of variational principle is discussed in Chapter 5

of plates illustrated in Fig 4.1, δU, δK, and δV can be expressed as

$$\delta U = \int_{\Omega_0} \int_{-\frac{h}{2}}^{\frac{h}{2}} \Big[\sigma_{xx}\delta\varepsilon_{xx} + \sigma_{yy}\delta\varepsilon_{yy} + \tau_{xy}\delta\gamma_{xy} + \tau_{xz}\delta\gamma_{xz} + \tau_{yz}\delta\gamma_{yz}\Big] dzdxdy, \tag{4.11}$$

$$\delta K = \int_{\Omega_0} \int_{-\frac{h}{2}}^{\frac{h}{2}} \rho_0 \Big[\dot{u}\delta\dot{u} + \dot{v}\delta\dot{v} + \dot{w}\delta\dot{w}\Big] dzdxdy, \tag{4.12}$$

$$\begin{aligned} \delta V = &- \int_{\Omega_0} \Big[q_b(x,y)\delta w\Big(x,y,-\frac{h}{2}\Big) + q_t(x,y)\delta w\Big(x,y,\frac{h}{2}\Big)\Big] dxdy \\ &- \int_{\Gamma_\sigma} \int_{-\frac{h}{2}}^{\frac{h}{2}} \Big[\hat{\sigma}_{nn}\delta u_n + \hat{\sigma}_{ns}\delta u_s + \hat{\sigma}_{nz}\delta w\Big] dzds, \end{aligned} \tag{4.13}$$

where h is the plate thickness, ρ_0 is the material density, (q_b, q_t) are transverse load applied to the bottom and top surface, respectively, and $q = q_b + q_t$ is the total transverse load. The closed boundary and undeformed midplane of the total domain Ω are denoted by Γ and Ω_0, respectively. The portion of Γ on which applied stress components ($\hat{\sigma}_{nn}$, $\hat{\sigma}_{ns}$, $\hat{\sigma}_{nz}$) are specified is denoted by Γ_σ, while the portion of Γ whose displacements are prescribed is denoted by Γ_u. The stress resultants applied on Γ_σ are given by

$$\begin{aligned} &\hat{N}_{nn} = \int_{-\frac{h}{2}}^{\frac{h}{2}} \hat{\sigma}_{nn} dz, \quad \hat{N}_{ns} = \int_{-\frac{h}{2}}^{\frac{h}{2}} \hat{\sigma}_{ns} dz, \quad \hat{Q}_{nz} = \int_{-\frac{h}{2}}^{\frac{h}{2}} \hat{\sigma}_{nz} dz, \\ &\hat{M}_{nn} = \int_{-\frac{h}{2}}^{\frac{h}{2}} z\hat{\sigma}_{nn} dz, \quad \hat{M}_{ns} = \int_{-\frac{h}{2}}^{\frac{h}{2}} z\hat{\sigma}_{ns} dz. \end{aligned} \tag{4.14}$$

The nonlinear equations of motion for FSDT can be derived[4] from Eqs (4.10) to (4.13) and are given by

$$\frac{\partial N_{xx}}{\partial x} + \frac{\partial N_{xy}}{\partial y} = I_0\ddot{u}_0 + I_1\ddot{\phi}_x, \tag{4.15}$$

$$\frac{\partial N_{yy}}{\partial y} + \frac{\partial N_{xy}}{\partial x} = I_0\ddot{v}_0 + I_1\ddot{\phi}_y, \tag{4.16}$$

[4]The detailed derivation is presented in Appendix D.

$$\frac{\partial}{\partial x}\left(N_{xx}\frac{\partial w_0}{\partial x}+N_{xy}\frac{\partial w_0}{\partial y}\right)+\frac{\partial}{\partial y}\left(N_{xy}\frac{\partial w_0}{\partial x}+N_{yy}\frac{\partial w_0}{\partial y}\right)+\frac{\partial Q_{xz}}{\partial x}+\frac{\partial Q_{yz}}{\partial y}+q=I_0\ddot{w}_0, \quad (4.17)$$

$$\frac{\partial M_{xx}}{\partial x}+\frac{\partial M_{xy}}{\partial y}-Q_{xz}=I_1\ddot{u}_0+I_2\ddot{\phi}_x, \quad (4.18)$$

$$\frac{\partial M_{yy}}{\partial y}+\frac{\partial M_{xy}}{\partial x}-Q_{yz}=I_1\ddot{v}_0+I_2\ddot{\phi}_y. \quad (4.19)$$

The in-plane stress resultants (N_{xx}, N_{yy}, N_{xy}), bending stress resultants (M_{xx}, M_{yy}, M_{xy}), and shear stress resultants (Q_{xz}, Q_{yz}) are given in Eqs (4.20), (4.21), and (4.22), respectively, with respect to the displacement fields and laminate stiffness[5].

$$\begin{Bmatrix} N_{xx} \\ N_{yy} \\ N_{xy} \end{Bmatrix} = \Big[A_{ij}\Big] \begin{Bmatrix} \frac{\partial u_0}{\partial x}+\frac{1}{2}(\frac{\partial w_0}{\partial x})^2 \\ \frac{\partial v_0}{\partial y}+\frac{1}{2}(\frac{\partial w_0}{\partial y})^2 \\ \frac{\partial u_0}{\partial y}+\frac{\partial v_0}{\partial x}+\frac{\partial w_0}{\partial x}\frac{\partial w_0}{\partial y} \end{Bmatrix} + \mathbf{B} \begin{Bmatrix} \frac{\partial \phi_x}{\partial x} \\ \frac{\partial \phi_y}{\partial y} \\ \frac{\partial \phi_x}{\partial y}+\frac{\partial \phi_y}{\partial x} \end{Bmatrix}, \text{ where } i,j=1,2,6. \quad (4.20)$$

$$\begin{Bmatrix} M_{xx} \\ M_{yy} \\ M_{xy} \end{Bmatrix} = \mathbf{B} \begin{Bmatrix} \frac{\partial u_0}{\partial x}+\frac{1}{2}(\frac{\partial w_0}{\partial x})^2 \\ \frac{\partial v_0}{\partial y}+\frac{1}{2}(\frac{\partial w_0}{\partial y})^2 \\ \frac{\partial u_0}{\partial y}+\frac{\partial v_0}{\partial x}+\frac{\partial w_0}{\partial x}\frac{\partial w_0}{\partial y} \end{Bmatrix} + \mathbf{D} \begin{Bmatrix} \frac{\partial \phi_x}{\partial x} \\ \frac{\partial \phi_y}{\partial y} \\ \frac{\partial \phi_x}{\partial y}+\frac{\partial \phi_y}{\partial x} \end{Bmatrix}. \quad (4.21)$$

$$\begin{Bmatrix} Q_{yz} \\ Q_{xz} \end{Bmatrix} = K\Big[A_{mn}\Big] \begin{Bmatrix} \phi_y+\frac{\partial w_0}{\partial y} \\ \phi_x+\frac{\partial w_0}{\partial x} \end{Bmatrix}, \text{ where } m,n=4,5. \quad (4.22)$$

The coefficient K in front of the shear stiffness in Eq (4.22) is the well-known shear correction factor for FSDT. As shown in Eqs (4.8) and (4.9), FSDT assumes that the transverse shear strains are constant through the laminate thickness and thus the corresponding transverse shear stress fields are also constant through the thickness. To correct the discrepancy between the actual stress distribution and the one based on the FSDT assumption, the shear correction factor is introduced to compute the transverse shear stress resultants Q_{xz} and Q_{yz} of FSDT [68, 92]. The shear correction factor for homogeneous, isotropic plates can be evaluated using the 3-D elasticity theory. However, it is difficult to obtain the shear

[5]The laminate stiffness is discussed in Appendix B.

correction factor of composite structures because it depends on the lamination scheme, geometry, and material properties [68, 92]. This work adopted $K = 5/6$, which is derived from homogeneous, isotropic plates. This issue will be further investigated in future work.

For the laminated composite specimen used in this work (see Eq (2.3)), $A_{16} = A_{26} = A_{45} = D_{16} = D_{26} = 0$, and $\mathbf{B} = \mathbf{0}$; thus, Eqs (4.20) to (4.22) can be reduced into Eqs (4.23) to (4.25), respectively.

$$\begin{Bmatrix} N_{xx} \\ N_{yy} \\ N_{xy} \end{Bmatrix} = \begin{bmatrix} A_{11} & A_{12} & 0 \\ A_{12} & A_{22} & 0 \\ 0 & 0 & A_{66} \end{bmatrix} \begin{Bmatrix} \frac{\partial u_0}{\partial x} + \frac{1}{2}(\frac{\partial w_0}{\partial x})^2 \\ \frac{\partial v_0}{\partial y} + \frac{1}{2}(\frac{\partial w_0}{\partial y})^2 \\ \frac{\partial u_0}{\partial y} + \frac{\partial v_0}{\partial x} + \frac{\partial w_0}{\partial x}\frac{\partial w_0}{\partial y} \end{Bmatrix}. \tag{4.23}$$

$$\begin{Bmatrix} M_{xx} \\ M_{yy} \\ M_{xy} \end{Bmatrix} = \begin{bmatrix} D_{11} & D_{12} & 0 \\ D_{12} & D_{22} & 0 \\ 0 & 0 & D_{66} \end{bmatrix} \begin{Bmatrix} \frac{\partial \phi_x}{\partial x} \\ \frac{\partial \phi_y}{\partial y} \\ \frac{\partial \phi_x}{\partial y} + \frac{\partial \phi_y}{\partial x} \end{Bmatrix}. \tag{4.24}$$

$$\begin{Bmatrix} Q_{yz} \\ Q_{xz} \end{Bmatrix} = K \begin{bmatrix} A_{44} & 0 \\ 0 & A_{55} \end{bmatrix} \begin{Bmatrix} \phi_y + \frac{\partial w_0}{\partial y} \\ \phi_x + \frac{\partial w_0}{\partial x} \end{Bmatrix}. \tag{4.25}$$

4.3 FEM formulation for an FSDT model

To generate an FEM based on FSDT, the weak forms of Eqs (4.15) to (4.19) were taken as shown in Eqs (4.26) to (4.30).

$$\begin{aligned} 0 = &\int_{\Omega^e} \Big\{ N_{xx}\frac{\partial \delta u_0}{\partial x} + N_{xy}\frac{\partial \delta u_0}{\partial y} + \Big(I_0\ddot{u}_0 + I_1\ddot{\phi}_x\Big)\delta u_0 \Big\} dxdy \\ &- \oint_{\Gamma^e} \delta u_0 \Big\{ n_x N_{xx} + n_y N_{xy} \Big\} ds. \end{aligned} \tag{4.26}$$

$$\begin{aligned} 0 = &\int_{\Omega^e} \Big\{ N_{yy}\frac{\partial \delta v_0}{\partial y} + N_{xy}\frac{\partial \delta v_0}{\partial x} + \Big(I_0\ddot{v}_0 + I_1\ddot{\phi}_y\Big)\delta v_0 \Big\} dxdy \\ &- \oint_{\Gamma^e} \delta v_0 \Big(n_x N_{xy} + n_y N_{yy} \Big) ds. \end{aligned} \tag{4.27}$$

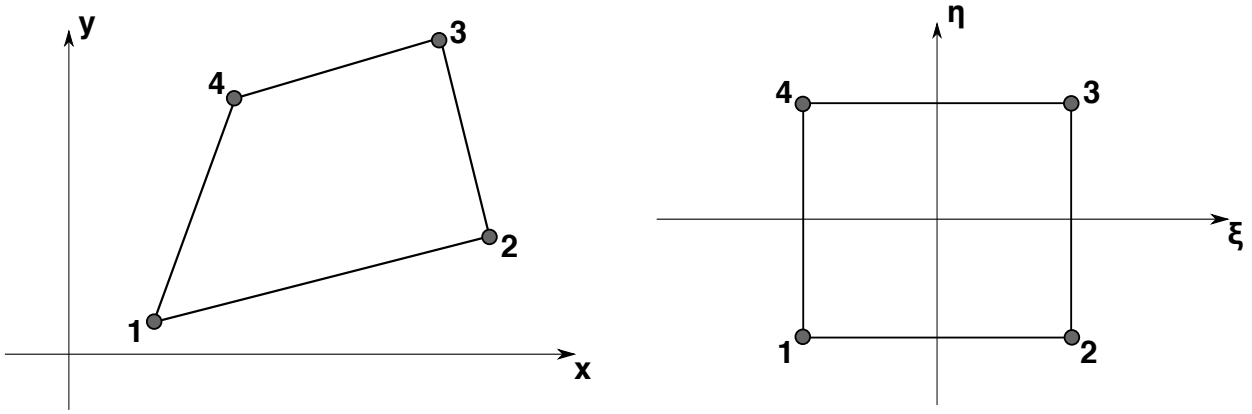

(a) (b)

Figure 4.3: Nodal DOFs for FSDT on: (a) a real element, and (b) a reference element.

$$
\begin{aligned}
0 = \int_{\Omega^e} \Big\{ & \frac{\partial \delta w_0}{\partial x}\Big(N_{xx}\frac{\partial w_0}{\partial x} + N_{xy}\frac{\partial w_0}{\partial y} + Q_{xz}\Big) \\
& + \frac{\partial \delta w_0}{\partial y}\Big(N_{xy}\frac{\partial w_0}{\partial x} + N_{yy}\frac{\partial w_0}{\partial y} + Q_{yz}\Big) + \delta w_0 I_0 \ddot{w}_0 - \delta w_0 q \Big\} dxdy \\
& - \oint_{\Gamma^e} \delta w_0 Q_{nz} ds.
\end{aligned} \tag{4.28}
$$

$$
\begin{aligned}
0 = \int_{\Omega^e} & \Big\{ \frac{\partial \delta \phi_x}{\partial x} M_{xx} + \frac{\partial \delta \phi_x}{\partial y} M_{xy} + \delta \phi_x Q_{xz} + \delta \phi_x \Big(I_1 \ddot{u}_0 + I_2 \ddot{\phi}_x \Big) \Big\} dxdy \\
& - \oint_{\Gamma^e} \delta \phi_x \Big(n_x M_{xx} + n_y M_{xy} \Big) ds.
\end{aligned} \tag{4.29}
$$

$$
\begin{aligned}
0 = \int_{\Omega^e} & \Big\{ \frac{\partial \delta \phi_y}{\partial x} M_{xy} + \frac{\partial \delta \phi_y}{\partial y} M_{yy} + \delta \phi_y Q_{yz} + \delta \phi_y \Big(I_1 \ddot{v}_0 + I_2 \ddot{\phi}_y \Big) \Big\} dxdy \\
& - \oint_{\Gamma^e} \delta \phi_y \Big(n_y M_{yy} + n_x M_{xy} \Big) ds.
\end{aligned} \tag{4.30}
$$

The midplane displacements (u_0, v_0, w_0) and rotations (ϕ_x, ϕ_x) can be expressed in terms of the nodal displacements (u_j^e, v_j^e, w_j^e) and rotations (X_j^e, Y_j^e), respectively, as shown in Eqs (4.31) to (4.35).

$$
u_0(x, y, t) = \sum_{j=1}^{m} u_j^e(t) \psi_j^e(x, y), \tag{4.31}
$$

$$v_0(x,y,t) = \sum_{j=1}^{m} v_j^e(t)\psi_j^e(x,y), \tag{4.32}$$

$$w_0(x,y,t) = \sum_{j=1}^{n} w_j^e(t)\psi_j^e(x,y), \tag{4.33}$$

$$\phi_x(x,y,t) = \sum_{j=1}^{m} X_j^e(t)\psi_j^e(x,y), \tag{4.34}$$

$$\phi_y(x,y,t) = \sum_{j=1}^{m} Y_j^e(t)\psi_j^e(x,y), \tag{4.35}$$

where $m = 4$ for four-node elements and ψ_j^e denotes the bilinear Lagrange interpolation functions. The nodal displacements and rotations on the real and reference elements are illustrated in Fig 4.3. In contrast to the nonconforming elements of the CLPT model (see Fig 3.3), the nodal variables in both the real and reference elements are identical for the FSDT elements. The bilinear interpolation functions in the reference element (see Fig 4.3b) are given by

$$\begin{aligned} \psi_1^e &= \frac{1}{4}(1-\xi)(1-\eta), \qquad \psi_2^e = \frac{1}{4}(1+\xi)(1-\eta), \\ \psi_3^e &= \frac{1}{4}(1+\xi)(1+\eta), \qquad \psi_4^e = \frac{1}{4}(1-\xi)(1+\eta). \end{aligned} \tag{4.36}$$

Finally, the nonlinear FEM of FSDT is obtained by applying the displacement fields in Eqs (4.31) to (4.35) into the weak forms in Eqs (4.26) to (4.30) and rearranging them in a coupled matrix form. The FEM is given in a compact form by

$$\mathbf{M}\ddot{\mathbf{u}} + \mathbf{K}\mathbf{u} = \mathbf{F}, \tag{4.37}$$

where $\mathbf{u}$ is a nodal displacement and rotation vector, $\mathbf{K}$ is a geometrically nonlinear stiffness matrix (i.e., $\mathbf{K} = \mathbf{K}(\mathbf{u})$), $\mathbf{M}$ is a mass matrix, and $\mathbf{F}$ is a force vector. The components of $\mathbf{K}$,

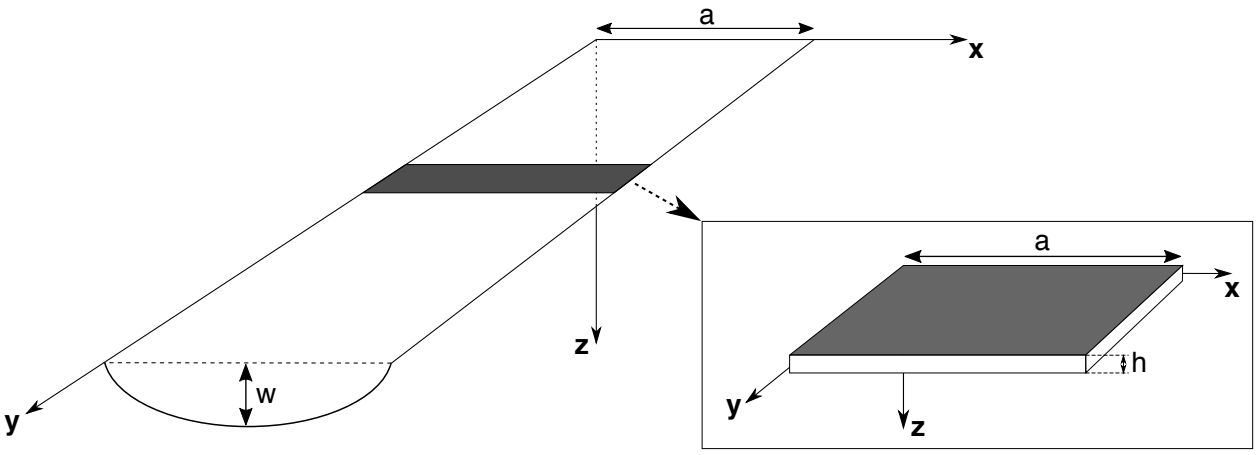

Figure 4.4: A long rectangular plate and its elemental strip cut, which is colored gray. The elemental strip cut demonstrates cylindrical bending.

M, and **F** are presented in Appendix E. Including a damping term in the equation results in

$$\mathbf{M}\ddot{\mathbf{u}} + \mathbf{C}\dot{\mathbf{u}} + \mathbf{K}\mathbf{u} = \mathbf{F}, \tag{4.38}$$

where **C** is a damping matrix, which is discussed in Section 3.4.

4.4 Demonstration of locking issues for cylindrical bending problems

This section investigates the performance of FSDT models which are generated using four-node elements with bilinear interpolations. The numerical, linear static analysis of cylindrical bending problems is presented and is compared to the analytical solutions of FSDT. Finally, the relevant locking issues and their impact on the global behaviors of plates are discussed.

4.4.1 Analytical solutions

A long rectangular plate, which is long along the y-axis and has a significantly shorter dimension along the x-axis, is illustrated in Fig 4.4. In the event that the plate is subject to a transverse load $q(x)$ that is uniform at any section parallel to the x-axis, the deflected surface of an elemental strip cut from the plate at a considerable distance from the ends

can be assumed cylindrical [89]. In such a case, the displacements and rotations of the plate strip are functions of only x and thus all derivatives with respect to y are zero [68]. Based on these assumptions, the equations of motion for FSDT can be reduced to solve cylindrical bending problems.

For a plate strip clamped at both ends and subject to a uniformly distributed transverse load q_0, the analytical solutions are derived in detail in Appendix F, by following the work of Reddy in Ref [68]. As shown in Eqs (F.13) and (F.14), the transverse midplane displacement w_0 and rotation ϕ_x are given by

$$w_0(x) = \frac{q_0 a^4}{24D}\Big[\Big(\frac{x}{a}\Big)^2 - \Big(\frac{x}{a}\Big)\Big]^2 + \frac{q_0 a^2}{2KA_{55}}\Big[\Big(\frac{x}{a}\Big) - \Big(\frac{x}{a}\Big)^2\Big], \tag{4.39}$$

$$\phi_x(x) = -\frac{q_0 a^3}{12D}\Big[2\Big(\frac{x}{a}\Big)^3 - 3\Big(\frac{x}{a}\Big)^2 + \Big(\frac{x}{a}\Big)\Big]. \tag{4.40}$$

In addition, as shown in Eq (F.22), the buckling load N_{cr} for the first mode is given by

$$N_{\text{cr}} = \Big(\frac{2\pi}{a}\Big)^2 D\Big[1 - \frac{D(2\pi/a)^2}{KA_{55} + D(2\pi/a)^2}\Big]. \tag{4.41}$$

4.4.2 FEM analysis and comparison

For linear, numerical analysis of the cylindrical bending problem, a long rectangular plate was modeled as illustrated in Fig 4.5. The plate was clamped along $x = 0, a$ (black, solid lines) and free along $y = 0, b$ (black, dotted lines) while a uniformly distributed transverse load q_0 =-7 g was applied. The material properties and geometric dimensions (except for length b) of the laminated composite specimen (see Section 2.2.1) were used for modeling.

An FSDT model was generated using four-node rectangular elements with bilinear interpolations as illustrated Fig 4.6. The element size is 11.43×12.70 mm and 20×50 elements were used to mesh the plate. As shown in the deformed shape of the model illustrated in Fig 4.7, the deflected surface away from the free boundaries $y = 0, 635.0$ mm is cylindrical.

As illustrated in Fig 4.8, the FEM model considerably underestimates the transverse

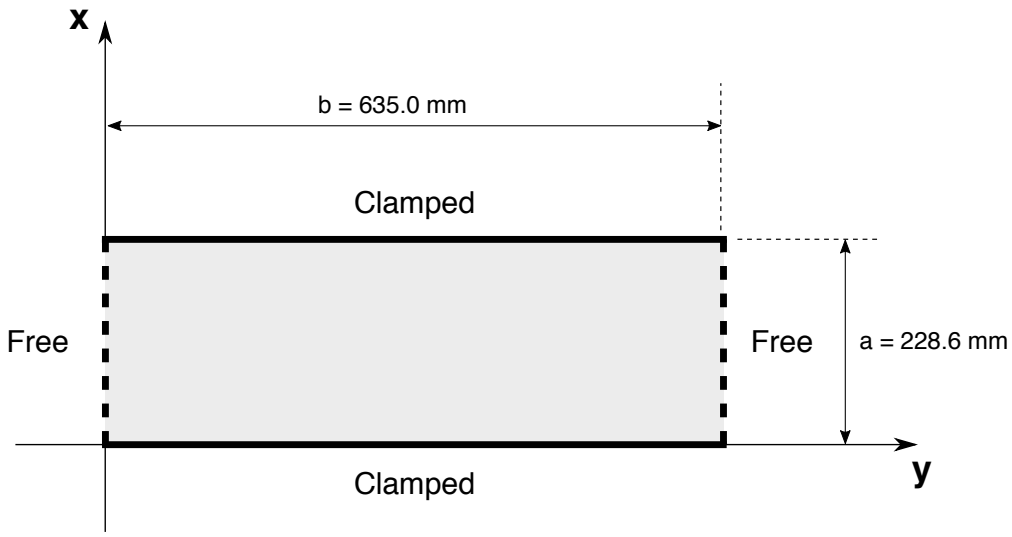

Figure 4.5: The geometric dimensions and boundary conditions of a cylindrical bending problem.

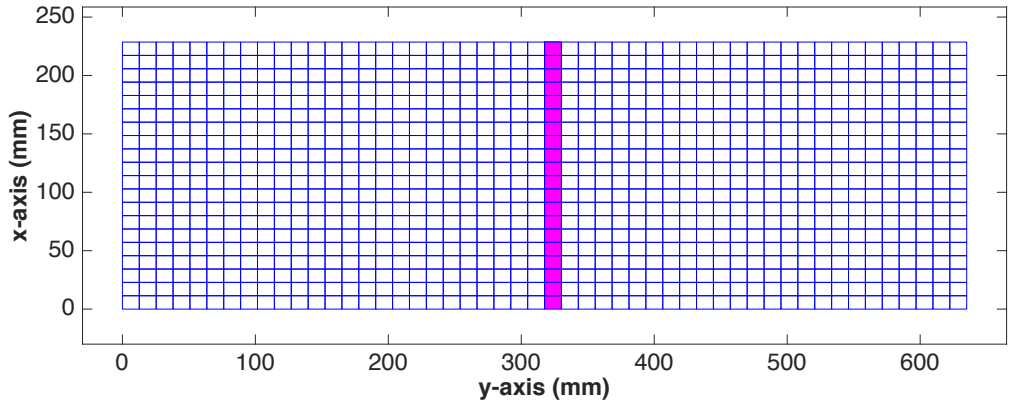

Figure 4.6: The element mesh of the FSDT model for the cylindrical bending problem (see Fig 4.5). The displacement and stress fields of the model were obtained on the pink elements.

displacement w_0 and rotation ϕ_x compared to the analytical solution. This kind of over-stiffening phenomenon of FEMs based on shear deformation theories is named shear locking. Shear locking occurs when numerical elements cannot represent physical deformation in which transverse shear strain should vanish and consequent spurious shear absorbs a large part of the energy generated by external forces [14]. The maximum transverse displacement

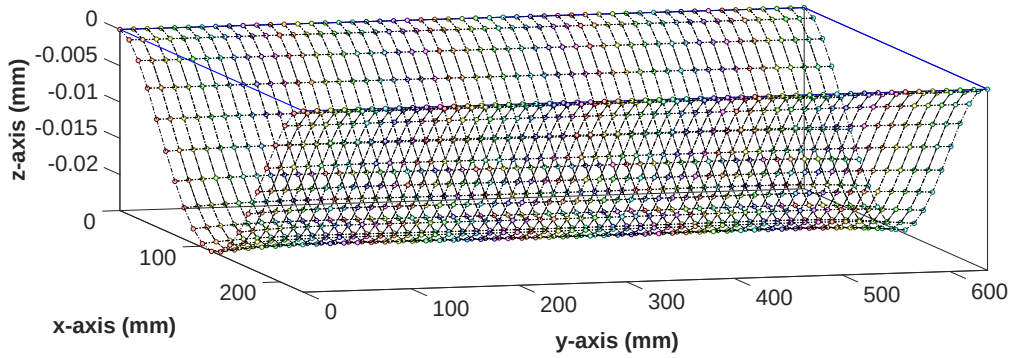

Figure 4.7: The deformed shape of the FSDT model (see Fig 4.6) under q_0 =-7 g. The z-axis is extremely exaggerated for interpretation of deflection. The colored circles indicate the nodes of the element mesh. The blue rectangle indicates the position of the initially-flat model.

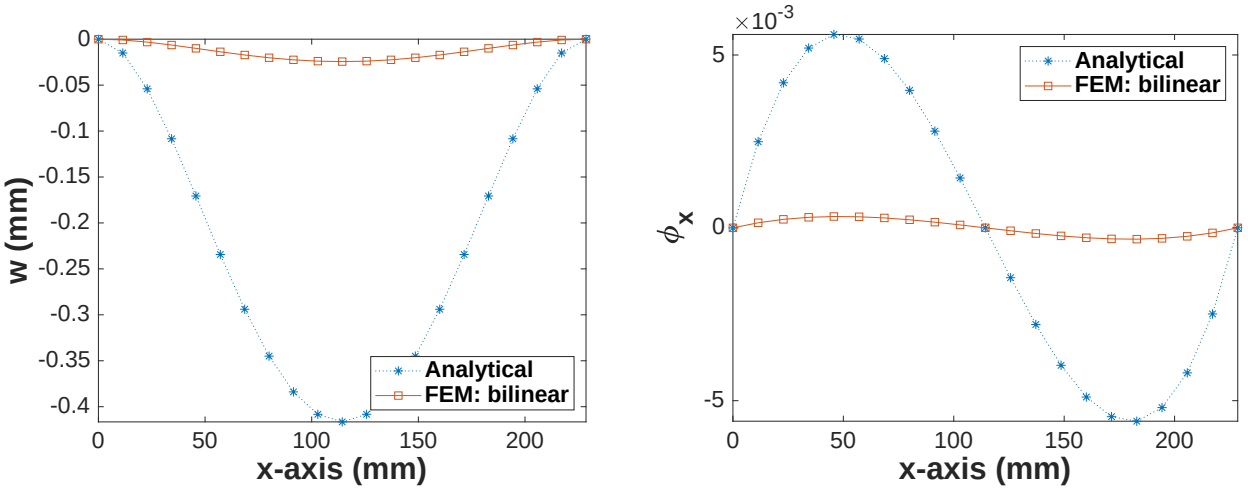

Figure 4.8: The transverse displacement w_0 and rotation ϕ_x of the FSDT model using the mesh shown in Fig 4.6 for the cylindrical bending plate (see Fig 4.5) under q_0 =-7 g. (a) The transverse displacement w_0. (b) The transverse rotation ϕ_x

w_0 and rotation ϕ_x, and the first-mode buckling load N_{CR} of the analytical solution and FSDT model are tabulated in Table 4.1. The buckling load N_{cr} of the FSDT model is significantly overestimated due to the over-stiffening phenomenon induced by shear locking.

Field	Analytical	FEM: bilinear
$\lvert w_0 \rvert_{\max}$ (mm)	0.4165	0.02439 (94.14 %)
$\lvert \phi_x \rvert_{\max} \times 10^3$ (rad)	5.463	0.3199 (94.14 %)
$\lvert \sigma_{xx} \rvert_{\max}$ (MPa)	3.413	0.1993 (94.16 %)
N_{CR} (N/m)	1018.5	17533.4 (1621.5 %)

Table 4.1: The maximum transverse displacement w_0, rotation ϕ_x, and bending stress σ_{xx}, and the first-mode buckling load N_{CR} of the FSDT model using the mesh illustrated in Fig 4.6. The values in the parentheses indicate the percent error of the numerical predictions.

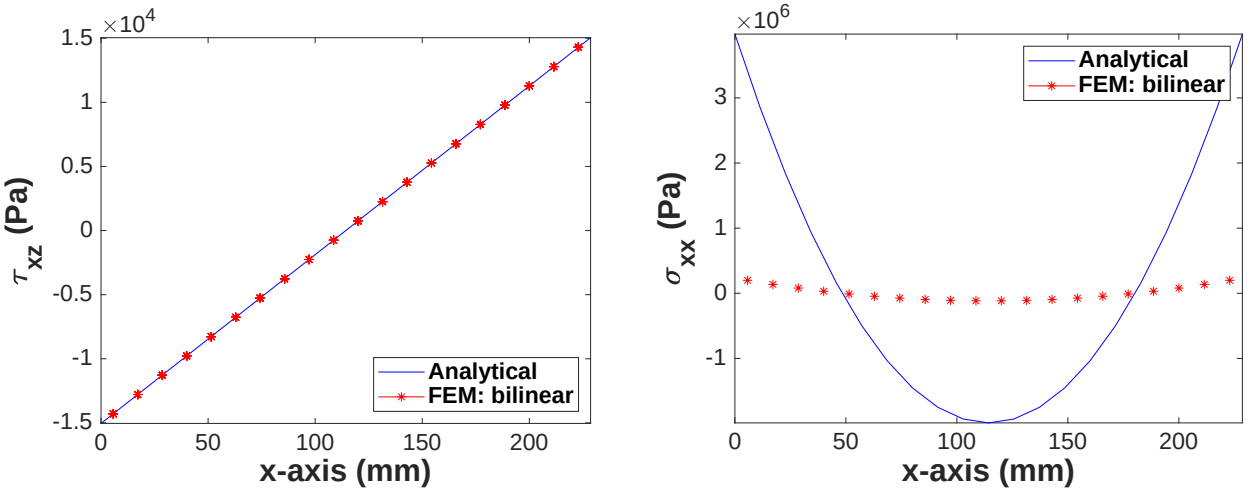

Figure 4.9: The stress fields analyzed at the Barlow points of the FSDT model using the mesh shown in Fig 4.6 for the cylindrical bending problem. (a) The transverse shear stress τ_{xz}. (b) The bending stress σ_{xx} at the top of the plate.

To explain this phenomenon, the stress fields of the FSDT model were analyzed at the Barlow points [9], which is a common method for stress analysis and has been adopted in many commercial FEM packages. As shown in Fig 4.9, the transverse shear stress τ_{xz} of the model agrees with the analytical solution at the Barlow points. On the other hand, the bending stress σ_{xx} of the model at the top of the plate is significantly smaller than the

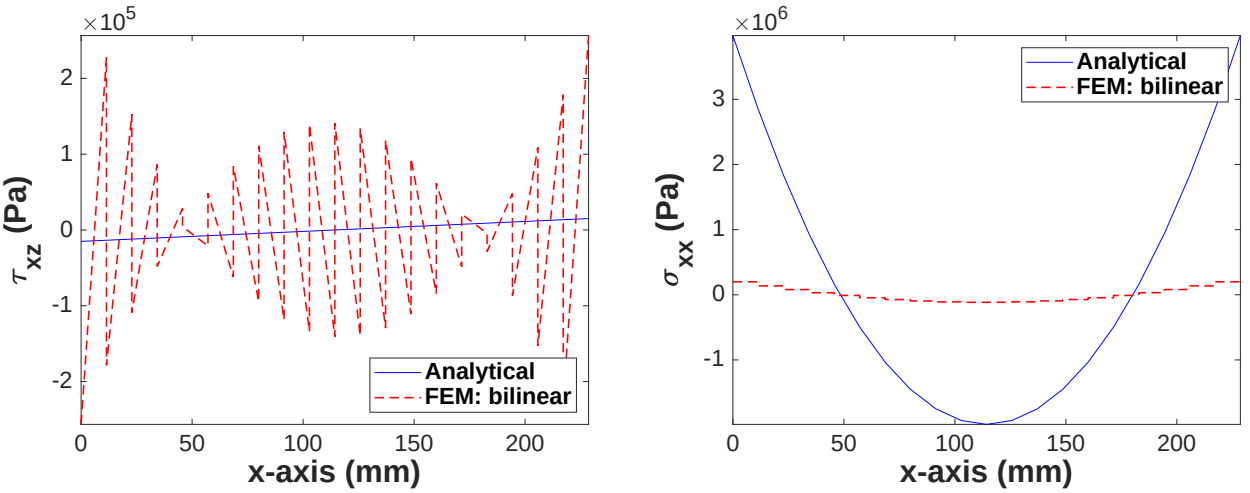

Figure 4.10: The full-field stress over the elements of the FSDT model using the mesh shown in Fig 4.6 for the cylindrical bending problem. (a) The transverse shear stress τ_{xz}. (b) The bending stress σ_{xx} at the top of the plate.

analytical solution. The maximum bending stress σ_{xx} of the model is tabulated in Table 4.1. Considering the substantially underestimated displacement and rotation of the model, the agreement between τ_{xz} of the model and analytical solution seems surprising.

For a better explanation of the phenomenon, the stress fields were analyzed along the entire length (along x-axis) of the elements as presented in Fig 4.10. While the bending stress is constant on each element, the shear stress exhibits violent stress oscillation [63]. Considering the shear energy term in Eq (4.11), that is,

$$\frac{1}{2}\gamma_{xz}\tau_{xz} = \frac{1}{2\bar{C}_{55}}\tau_{xz}^2, \tag{4.42}$$

spurious shear induced by the stress oscillation absorbs a large part of the external energy input, and consequently the rest of the energy input generates significantly underestimated bending strain and stress fields (as shown in Fig 4.9b for the bending stress). Thus, the stress fields obtained at the Barlow points can be accurate when there are no violent stress

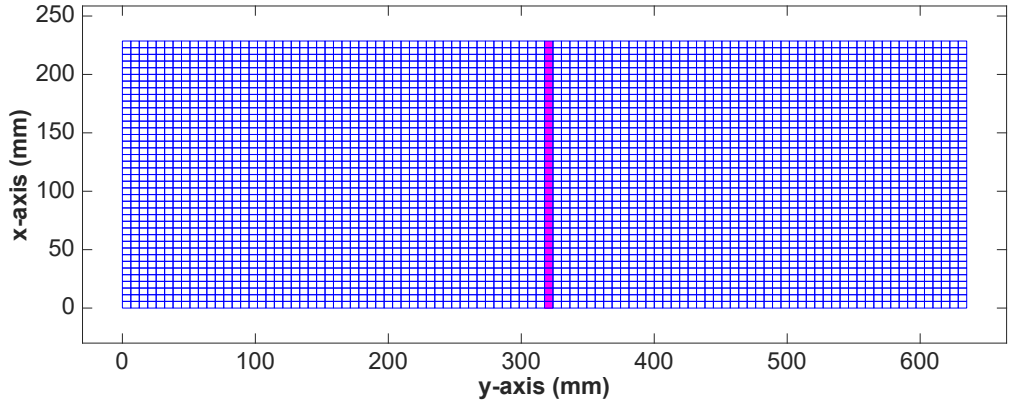

Figure 4.11: The refined element mesh of the FSDT model for the cylindrical bending problem. The displacement and stress fields of the model were obtained on the pink elements.

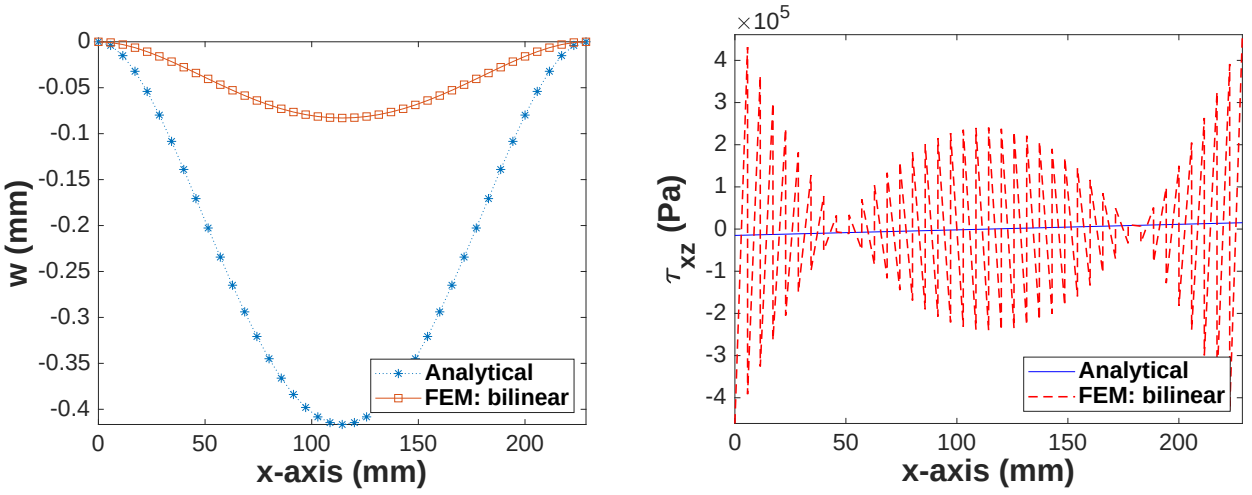

(a) (b)

Figure 4.12: The transverse displacement w_0 and stress τ_{xz} fields of the FSDT model using the refined mesh (see Fig 4.11) for the cylindrical bending problem. (a) The transverse displacement fields w_0. (b) The transverse shear stress fields τ_{xz}.

oscillations. In cases where stress oscillations are present over elements, however, the stress analysis method relying on the Barlow points can disguise the occurrence of locking.

To investigate the impact of mesh refinement on shear locking, the element mesh illustrated in Fig 4.6 was refined as shown in Fig 4.11. The simulation using the refined mesh

Field	Analytical	FEM: bilinear
$\lvert w_0 \rvert_{\max}$ (mm)	0.4165	0.08297 (80.08 %)
$\lvert \phi_x \rvert_{\max} \times 10^3$ (rad)	5.463	1.0881 (80.08 %)
$\lvert \sigma_{xx} \rvert_{\max}$ (MPa)	3.413	0.7343 (80.09 %)
N_{CR} (N/m)	1018.5	5107.9 (401.5 %)

Table 4.2: The maximum transverse displacement w_0, rotation ϕ_x, and bending stress σ_{xx}, and the first-mode buckling load N_{CR} of the FSDT model using the refined mesh (see Fig 4.11). The values in the parentheses indicate the percent error of the numerical predictions.

substantially increased the computational cost. The simulation results of the model using the refined mesh are illustrated in Fig 4.12 and are tabulated in Table 4.2. The mesh refinement improved the results; however, serious errors remain. As shown in Fig 4.12b, the stress oscillations were not resolved by the mesh refinement; furthermore, the oscillations were intensified with the increase of the transverse displacement (i.e., the increase of the external energy input).

4.5 Summary

In this chapter, the nonlinear equations of motion and corresponding FEM were presented. To investigate the performance of FSDT models, cylindrical bending problems were analytically and numerically analyzed. The analysis results showed that a shear locking phenomenon of FSDT models leads to a significant underestimate of deflections and an overestimate of buckling loads. Such an overestimate of structural capacity from numerical analysis can cause a serious problem in structural design if the occurrence of locking phenomenon fails to be identified. However, the full-field stress analysis revealed that the common stress analysis method using the Barlow points can disguise shear locking occurrence in case of stress oscillations over elements. Moreover, it was shown that mesh refinement is not effective in resolving this shear locking issue. In the following chapter, remedies for shear locking are discussed and their performance is investigated.

Part II

MODELING AND SIMULATION: ASSUMED STRAIN-BASED APPROACH

Chapter 5

ASSUMED STRAIN THEORIES

5.1 Introduction

The previous chapter discussed shear locking phenomena and their impact on the global behaviors of FSDT models. It was shown that mesh refinement does not resolve the issue.

Various theories and techniques have been proposed to alleviate shear locking. They can be broadly categorized as reduced/selective integration, assumed strain and stress, and enhanced strain methods. Reduced/selective integration methods are the simplest among them. This method reduces the number of integration (or Gauss) points for shear stiffness terms to achieve consistent interpolation over elements. This method can resolve shear locking without increasing the matrix size; however, instability and spurious zero-energy modes of models can occur. Assumed strain and stress methods provide more stable solutions to locking issues. These methods include the incompatible modes introduced by Wilson [99] and Taylor [88] and the Hellinger-Reissner element of Pian-Sumihara [62]. These methods had been labeled a 'variational crime' for many years until Simo and Hughes [80] provided the variational foundations of these methods. One of the most popular assumed strain theories was proposed by Hughes and Tezduyar [32]. Their theory successfully alleviates shear locking of the four-node Reissner-Mindlin plate element using full integration. Bathe and Dvorkin [11, 23] formulated the theory of Hughes and Tezduyar using tensor components, which is called the MITC4 (Mixed Interpolation of Tensorial Components) method. Commercial FEM packages such as Abaqus [87] and ADINA [66] still use this method to manage shear locking. However, this method cannot handle membrane locking. To address this issue, Bathe et al. [41, 42, 43, 44] have been making efforts to improve the MITC4 method to resolve membrane locking. Finally, the enhanced assumed strain (EAS) method of Simo and

Rifai [81] is capable of managing overall (e.g., shear, membrane, and volumetric) locking issues and is adopted in the commercial FEM packages for membrane locking. The EAS method can incorporate the aforementioned methods by selecting appropriate interpolation functions for the enhanced strains.

In this chapter, the MITC4 and EAS theories are introduced and FEM formulations for MITC4 and EAS models are presented. The performance of these models is investigated through linear analysis of the cylindrical bending problem introduced in the previous chapter. The detailed descriptions of the numerical implementation of the MITC4 and EAS methods are not available in the literature or textbooks to the best of the author's knowledge. Therefore, in order to contribute to the future works of researchers using these methods, this work provides the complete formulation of the MITC4 and EAS models by presenting the components of their stiffness matrices.

5.2 MITC4 method

The MITC4 method focuses on alleviating shear locking. In the method, transverse shear strains (γ_{xz}, γ_{yz}) are interpolated based on an assumed strain method, while typical bilinear interpolation is applied to bending strains ($\varepsilon_{xx}^{(0)}$, $\varepsilon_{yy}^{(0)}$, $\gamma_{xy}^{(0)}$) and transverse displacement and rotation fields (w_0, ϕ_x, ϕ_y). Thus, MITC4 employs mixed interpolation, which the first two letters of the acronym originated from. In addition, MITC4 is formulated using tensor components, which make up the last two letters of the acronym. In this section, MITC4 is presented based on the work of Bathe and Dvorkin [11] and the FSDT model is improved by incorporating the MITC4 method.

5.2.1 Tensor components of transverse shear strains

In a Cartesian coordinate system, the position and displacement vectors ($\mathbf{P}$, $\mathbf{u}$, respectively) of a particle can be expressed as

$$\mathbf{P} = x\mathbf{i} + y\mathbf{j} + z\mathbf{k}, \tag{5.1}$$

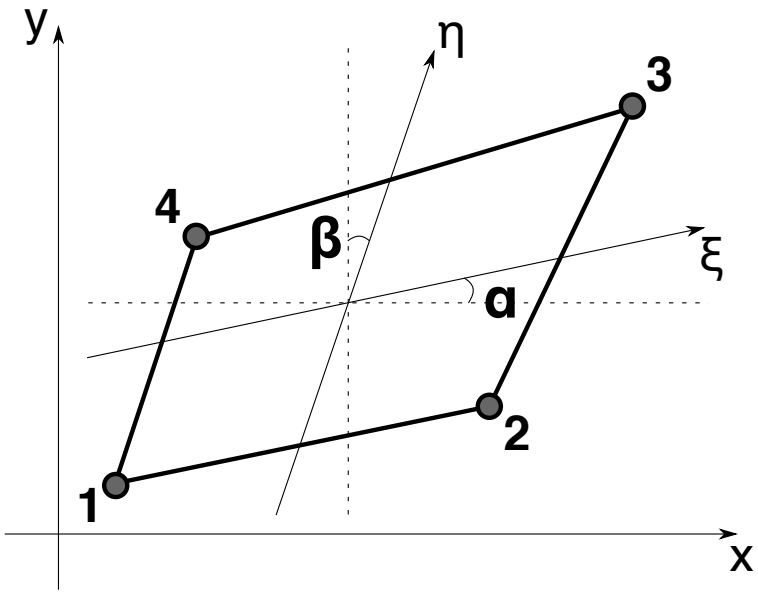

Figure 5.1: An MITC4 element in Cartesian (x, y) and natural (ξ, η) coordinate systems. The angles between these coordinate systems are denoted by (α, β). The two systems share the same z-axis.

$$\mathbf{u} = u\mathbf{i} + v\mathbf{j} + w\mathbf{k}. \tag{5.2}$$

In the reference (or natural) coordinate system, a strain tensor is given by

$$\boldsymbol{\varepsilon} = \tilde{\varepsilon}_{ij} g^i \otimes g^j \quad \text{for } i, j = \xi, \eta, z, \tag{5.3}$$

where g^i is the contravariant basis vector set and $\tilde{\varepsilon}_{ij}$ represents the tensor components measured in the natural coordinate system, which are given by

$$\tilde{\varepsilon}_{ij} = \frac{1}{2}\Big[{}^1g_i \cdot {}^1g_j - {}^0g_i \cdot {}^0g_j\Big], \tag{5.4}$$

where ${}^0g_i$ and ${}^1g_i$ are the covariant base vectors of initial (undeformed) and deformed con-

figurations, respectively. The base vectors for the undeformed configuration are given by

$$ {}^{0}g_{\xi} = \frac{\partial \mathbf{P}}{\partial \xi} = \frac{\partial x}{\partial \xi}\mathbf{i} + \frac{\partial y}{\partial \xi}\mathbf{j}, \tag{5.5} $$

$$ {}^{0}g_{\eta} = \frac{\partial \mathbf{P}}{\partial \eta} = \frac{\partial x}{\partial \eta}\mathbf{i} + \frac{\partial y}{\partial \eta}\mathbf{j}, \tag{5.6} $$

$$ {}^{0}g_{z} = \frac{\partial \mathbf{P}}{\partial z} = \mathbf{k}. \tag{5.7} $$

The basis vectors for the deformed configuration are given by

$$ {}^{1}g_{\xi} = \frac{\partial(\mathbf{P}+\mathbf{u})}{\partial \xi} = \Big(\frac{\partial x}{\partial \xi} + \frac{\partial u}{\partial \xi}\Big)\mathbf{i} + \Big(\frac{\partial y}{\partial \xi} + \frac{\partial v}{\partial \xi}\Big)\mathbf{j} + \frac{\partial w}{\partial \xi}\mathbf{k}, \tag{5.8} $$

$$ {}^{1}g_{\eta} = \frac{\partial(\mathbf{P}+\mathbf{u})}{\partial \eta} = \Big(\frac{\partial x}{\partial \eta} + \frac{\partial u}{\partial \eta}\Big)\mathbf{i} + \Big(\frac{\partial y}{\partial \eta} + \frac{\partial v}{\partial \eta}\Big)\mathbf{j} + \frac{\partial w}{\partial \eta}\mathbf{k}, \tag{5.9} $$

$$ {}^{1}g_{z} = \frac{\partial(\mathbf{P}+\mathbf{u})}{\partial z} = \frac{\partial u}{\partial z}\mathbf{i} + \frac{\partial v}{\partial z}\mathbf{j} + \mathbf{k} = \phi_x\mathbf{i} + \phi_y\mathbf{j} + \mathbf{k}. \tag{5.10} $$

Using the assumptions for the von Kármán strains, the transverse shear strains in the natural coordinate system are given by

$$ \tilde{\varepsilon}_{\xi z} = \frac{1}{2}\Big[{}^{1}g_{\xi}\cdot{}^{1}g_{z} - {}^{0}g_{\xi}\cdot{}^{0}g_{z}\Big] = \frac{1}{2}\Big[\frac{\partial x}{\partial \xi}\phi_x + \frac{\partial y}{\partial \xi}\phi_y + \frac{\partial w}{\partial \xi}\Big], \tag{5.11} $$

$$ \tilde{\varepsilon}_{\eta z} = \frac{1}{2}\Big[{}^{1}g_{\eta}\cdot{}^{1}g_{z} - {}^{0}g_{\eta}\cdot{}^{0}g_{z}\Big] = \frac{1}{2}\Big[\frac{\partial x}{\partial \eta}\phi_x + \frac{\partial y}{\partial \eta}\phi_y + \frac{\partial w}{\partial \eta}\Big]. \tag{5.12} $$

The strain tensor components in the real and natural coordinates can be related by

$$ \boldsymbol{\varepsilon} = \tilde{\varepsilon}_{ij} g_i \otimes g_j = \varepsilon_{kl} e_k \otimes e_l \quad \text{for } k,l = x,y,z, \tag{5.13} $$

where ε_{kl} is the tensor components measured in the real coordinate system and e_k represents the unit normal base vectors of the real coordinates. Using tensor calculus, ε_{kl} can be

expressed as

$$\varepsilon_{kl} = \tilde{\varepsilon}_{ij}(g^i \cdot e_l)(g^j \cdot e_k). \tag{5.14}$$

Thus, the shear strains in the real coordinates can be obtained as

$$\varepsilon_{xz} = \tilde{\varepsilon}_{ij}(g^i \cdot e_z)(g^j \cdot e_x) = \tilde{\varepsilon}_{zj}(g^z \cdot e_z)(g^j \cdot e_x) = \tilde{\varepsilon}_{z\xi}(g^\xi \cdot e_x) + \tilde{\varepsilon}_{z\eta}(g^\eta \cdot e_x), \tag{5.15}$$

$$\varepsilon_{zx} = \tilde{\varepsilon}_{ij}(g^i \cdot e_x)(g^j \cdot e_z) = \tilde{\varepsilon}_{iz}(g^i \cdot e_x)(g^z \cdot e_z) = \tilde{\varepsilon}_{\xi z}(g^\xi \cdot e_x) + \tilde{\varepsilon}_{\eta z}(g^\eta \cdot e_x), \tag{5.16}$$

$$\varepsilon_{yz} = \tilde{\varepsilon}_{ij}(g^i \cdot e_z)(g^j \cdot e_y) = \tilde{\varepsilon}_{zj}(g^z \cdot e_z)(g^j \cdot e_y) = \tilde{\varepsilon}_{z\xi}(g^\xi \cdot e_y) + \tilde{\varepsilon}_{z\eta}(g^\eta \cdot e_y), \tag{5.17}$$

$$\varepsilon_{zy} = \tilde{\varepsilon}_{ij}(g^i \cdot e_y)(g^j \cdot e_z) = \tilde{\varepsilon}_{iz}(g^i \cdot e_y)(g^z \cdot e_z) = \tilde{\varepsilon}_{\xi z}(g^\xi \cdot e_y) + \tilde{\varepsilon}_{\eta z}(g^\eta \cdot e_y), \tag{5.18}$$

$$\begin{aligned} \gamma_{xz} = \varepsilon_{xz} + \varepsilon_{zx} =& (\tilde{\varepsilon}_{z\xi} + \tilde{\varepsilon}_{\xi z})(g^\xi \cdot e_x) + (\tilde{\varepsilon}_{z\eta} + \tilde{\varepsilon}_{\eta z})(g^\eta \cdot e_x) \\ =& \tilde{\gamma}_{\xi z}(g^\xi \cdot e_x) + \tilde{\gamma}_{\eta z}(g^\eta \cdot e_x), \end{aligned} \tag{5.19}$$

$$\begin{aligned} \gamma_{yz} = \varepsilon_{yz} + \varepsilon_{zy} =& (\tilde{\varepsilon}_{z\xi} + \tilde{\varepsilon}_{\xi z})(g^\xi \cdot e_y) + (\tilde{\varepsilon}_{z\eta} + \tilde{\varepsilon}_{\eta z})(g^\eta \cdot e_y) \\ =& \tilde{\gamma}_{\xi z}(g^\xi \cdot e_y) + \tilde{\gamma}_{\eta z}(g^\eta \cdot e_y), \end{aligned} \tag{5.20}$$

where the following relations are used:

$$g^\xi \cdot e_z = 0, \quad g^\eta \cdot e_z = 0, \quad g^z \cdot e_z = 1. \tag{5.21}$$

The unit covariant base vectors of the natural coordinates are given by

$$\hat{e}_\xi = \frac{g_\xi}{\sqrt{g_{\xi\xi}}} = \cos\alpha \mathbf{i} + \sin\alpha \mathbf{j}, \tag{5.22}$$

$$\hat{e}_\eta = \frac{g_\eta}{\sqrt{g_{\eta\eta}}} = \cos\beta \mathbf{i} + \sin\beta \mathbf{j}, \tag{5.23}$$

$$\hat{e}_z = \mathbf{k}, \tag{5.24}$$

while the unit contravariant base vectors of the natural coordinates are given by

$$\hat{e}^{\xi} = \frac{g^{\xi}}{\sqrt{g^{\xi\xi}}} = \sin\beta\mathbf{i} - \cos\beta\mathbf{j}, \tag{5.25}$$

$$\hat{e}^{\eta} = \frac{g^{\eta}}{\sqrt{g^{\eta\eta}}} = -\sin\alpha\mathbf{i} + \cos\alpha\mathbf{j}, \tag{5.26}$$

$$\hat{e}^{z} = \mathbf{k}. \tag{5.27}$$

Thus, the contravariant base vectors can be expressed as

$$g^{\xi} = \sqrt{g^{\xi\xi}}\hat{e}^{\xi} = \sqrt{g^{\xi\xi}}(\sin\beta\mathbf{i} - \cos\beta\mathbf{j}), \tag{5.28}$$

$$g^{\eta} = \sqrt{g^{\eta\eta}}\hat{e}^{\eta} = \sqrt{g^{\eta\eta}}(-\sin\alpha\mathbf{i} + \cos\alpha\mathbf{j}), \tag{5.29}$$

$$g^{z} = \sqrt{g^{zz}}\hat{e}^{k} = \sqrt{g^{zz}}\mathbf{k}, \tag{5.30}$$

where

$$g^{ij} = \frac{D^{ij}}{g}, \tag{5.31}$$

D^{ij} and g are the cofactor and determinant of the matrix $[g_{ij}]$.

$$g_{11} = g_{\xi\xi} = g_{\xi} \cdot g_{\xi} = \left(\frac{\partial x}{\partial \xi}\right)^2 + \left(\frac{\partial y}{\partial \xi}\right)^2, \tag{5.32}$$

$$g_{12} = g_{\xi\eta} = g_{\xi} \cdot g_{\eta} = \frac{\partial x}{\partial \xi}\frac{\partial x}{\partial \eta} + \frac{\partial y}{\partial \xi}\frac{\partial y}{\partial \eta}, \tag{5.33}$$

$$g_{13} = g_{\xi z} = g_{\xi} \cdot g_{z} = 0, \tag{5.34}$$

$$g_{22} = g_{\eta\eta} = g_{\eta} \cdot g_{\eta} = \left(\frac{\partial x}{\partial \eta}\right)^2 + \left(\frac{\partial y}{\partial \eta}\right)^2, \tag{5.35}$$

$$g_{23} = g_{\eta z} = g_{\eta} \cdot g_{z} = 0, \tag{5.36}$$

$$g_{33} = g_{zz} = g_z \cdot g_z = 1. \tag{5.37}$$

Thus, the determinant g is given by

$$g = g_{11}D^{11} + g_{12}D^{12} + g_{13}D^{13}, \tag{5.38}$$

where

$$D^{11} = \Big(\frac{\partial x}{\partial \eta}\Big)^2 + \Big(\frac{\partial y}{\partial \eta}\Big)^2, \tag{5.39}$$

$$D^{12} = -\Big[\frac{\partial x}{\partial \xi}\frac{\partial x}{\partial \eta} + \frac{\partial y}{\partial \xi}\frac{\partial y}{\partial \eta}\Big], \tag{5.40}$$

$$D^{13} = 0. \tag{5.41}$$

The Jacobian matrix for the transformation can be defined as

$$\boldsymbol{J} = \begin{bmatrix} \frac{\partial x}{\partial \xi} & \frac{\partial x}{\partial \eta} \\ \frac{\partial y}{\partial \xi} & \frac{\partial y}{\partial \eta} \end{bmatrix}. \tag{5.42}$$

Thus, the determinant g can be expressed as

$$g = \Big[\frac{\partial x}{\partial \xi}\frac{\partial y}{\partial \eta} - \frac{\partial x}{\partial \eta}\frac{\partial y}{\partial \xi}\Big]^2 = (\det \boldsymbol{J})^2. \tag{5.43}$$

$$g^{\xi\xi} = \frac{D^{11}}{g} = \frac{\Big(\frac{\partial x}{\partial \eta}\Big)^2 + \Big(\frac{\partial y}{\partial \eta}\Big)^2}{(\det J)^2} = \frac{J_{21}^2 + J_{22}^2}{(\det J)^2}, \tag{5.44}$$

$$g^{\eta\eta} = \frac{D^{22}}{g} = \frac{\Big(\frac{\partial x}{\partial \xi}\Big)^2 + \Big(\frac{\partial y}{\partial \xi}\Big)^2}{(\det J)^2} = \frac{J_{11}^2 + J_{12}^2}{(\det J)^2}, \tag{5.45}$$

$$g^{zz} = \frac{D^{33}}{g} = \frac{\Big[\Big(\frac{\partial x}{\partial \xi}\Big)^2 + \Big(\frac{\partial y}{\partial \xi}\Big)^2\Big]\Big[\Big(\frac{\partial x}{\partial \eta}\Big)^2 + \Big(\frac{\partial y}{\partial \eta}\Big)^2\Big] - \Big(\frac{\partial x}{\partial \xi}\frac{\partial y}{\partial \eta} + \frac{\partial y}{\partial \xi}\frac{\partial y}{\partial \eta}\Big)^2}{(\det J)^2} = \frac{(\det J)^2}{(\det J)^2} = 1. \tag{5.46}$$

Substituting Eqs (5.28) to (5.30) into Eqs (5.44) to (5.46), the contravariant base vectors can be expressed as

$$g^{\xi} = \sqrt{g^{\xi\xi}}(\sin\beta\mathbf{i} - \cos\beta\mathbf{j}) = \frac{\sqrt{J_{21}^2 + J_{22}^2}}{|\det J|}(\sin\beta\mathbf{i} - \cos\beta\mathbf{j}), \tag{5.47}$$

$$g^{\eta} = \sqrt{g^{\eta\eta}}(-\sin\alpha\mathbf{i} + \cos\alpha\mathbf{j}) = \frac{\sqrt{J_{11}^2 + J_{12}^2}}{|\det J|}(-\sin\alpha\mathbf{i} + \cos\alpha\mathbf{j}), \tag{5.48}$$

$$g^{z} = \sqrt{g^{zz}}\mathbf{k} = \mathbf{k}, \tag{5.49}$$

Finally, Eqs (5.19) and (5.20) can be expanded as

$$\begin{aligned}\gamma_{xz} =& \tilde{\gamma}_{\xi z}(g^{\xi} \cdot e_x) + \tilde{\gamma}_{\eta z}(g^{\eta} \cdot e_x) \\ =& \tilde{\gamma}_{\xi z}\frac{\sqrt{J_{21}^2 + J_{22}^2}}{|\det J|}\sin\beta - \tilde{\gamma}_{\eta z}\frac{\sqrt{J_{11}^2 + J_{12}^2}}{|\det J|}\sin\alpha,\end{aligned} \tag{5.50}$$

$$\begin{aligned}\gamma_{yz} =& \tilde{\gamma}_{\xi z}(g^{\xi} \cdot e_y) + \tilde{\gamma}_{\eta z}(g^{\eta} \cdot e_y) \\ =& -\tilde{\gamma}_{\xi z}\frac{\sqrt{J_{21}^2 + J_{22}^2}}{|\det J|}\cos\beta + \tilde{\gamma}_{\eta z}\frac{\sqrt{J_{11}^2 + J_{12}^2}}{|\det J|}\cos\alpha.\end{aligned} \tag{5.51}$$

5.2.2 Mixed interpolations for transverse shear strains

In the MITC4 method, transverse shear strains are interpolated using the strains at tying points in the natural coordinates (see Fig 5.2):

$$\tilde{\gamma}_{\xi z}(\xi, \eta) = \frac{1}{2}\Big[(1 - \eta)\tilde{\gamma}_{\xi z}^{\mathrm{A}} + (1 + \eta)\tilde{\gamma}_{\xi z}^{\mathrm{C}}\Big], \tag{5.52}$$

$$\tilde{\gamma}_{\eta z}(\xi, \eta) = \frac{1}{2}\Big[(1 - \xi)\tilde{\gamma}_{\eta z}^{\mathrm{D}} + (1 + \xi)\tilde{\gamma}_{\eta z}^{\mathrm{B}}\Big], \tag{5.53}$$

where ($\tilde{\gamma}_{\xi z}^{\mathrm{A}}$, $\tilde{\gamma}_{\xi z}^{\mathrm{C}}$) and ($\tilde{\gamma}_{\eta z}^{\mathrm{B}}$, $\tilde{\gamma}_{\eta z}^{\mathrm{D}}$) are transverse shear strains at typing points (A, C) and (B, D), respectively. This interpolation method was originally proposed by Hughes and Tezduyar [32].

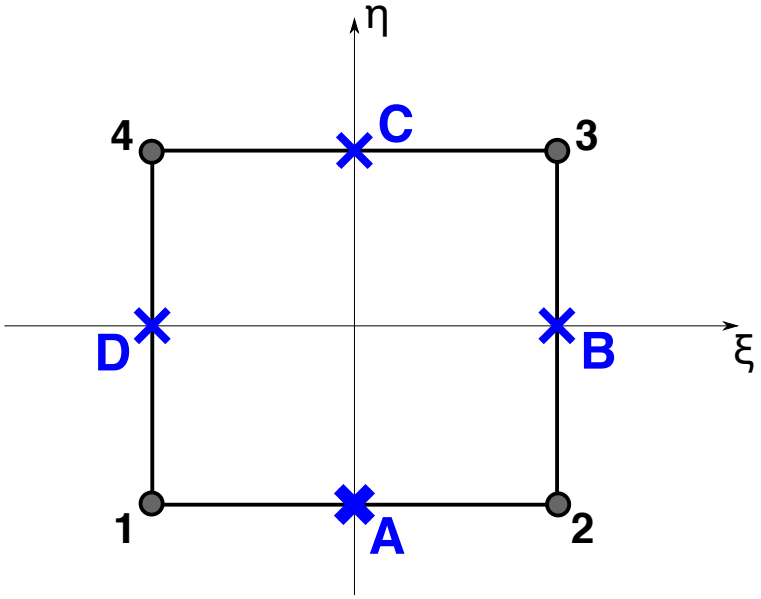

Figure 5.2: An MITC4 reference element in the natural ($\xi\eta$) coordinate system. The tying points of MITC4 elements for the interpolation of transverse shear strains are denoted by (A, B, C, D).

Using nodal variables (w_j^e, X_j^e, Y_j^e, see Eqs (4.33) to (4.35)) and the bilinear interpolations (ψ_j^e, see Eq (4.36)), the transverse shear strains in the natural coordinates (see Eqs (5.11) and (5.12)) can be expressed as

$$\begin{aligned}\tilde{\gamma}_{\xi z} = 2\tilde{\varepsilon}_{\xi z} =& \frac{\partial x}{\partial \xi}\phi_x + \frac{\partial y}{\partial \xi}\phi_y + \frac{\partial w}{\partial \xi} \\ =& \Big(\sum_{j=1}^{4} \frac{\partial \psi_j^e(\xi,\eta)}{\partial \xi} x_j^e\Big)\Big(\sum_{k=1}^{4} \psi_k^e(\xi,\eta) X_k^e\Big) \\ &+ \Big(\sum_{j=1}^{4} \frac{\partial \psi_j^e(\xi,\eta)}{\partial \xi} y_j^e\Big)\Big(\sum_{k=1}^{4} \psi_k^e(\xi,\eta) Y_k^e\Big) + \sum_{j=1}^{4} \frac{\partial \psi_j^e(\xi,\eta)}{\partial \xi} w_j^e,\end{aligned} \tag{5.54}$$

$$\begin{aligned}\tilde{\gamma}_{\xi z} = 2\tilde{\varepsilon}_{\eta z} =& \frac{\partial x}{\partial \eta}\phi_x + \frac{\partial y}{\partial \eta}\phi_y + \frac{\partial w}{\partial \eta} \\ =& \Big(\sum_{j=1}^{4} \frac{\partial \psi_j^e(\xi,\eta)}{\partial \eta} x_j^e\Big)\Big(\sum_{k=1}^{4} \psi_k^e(\xi,\eta) X_k^e\Big) \\ &+ \Big(\sum_{j=1}^{4} \frac{\partial \psi_j^e(\xi,\eta)}{\partial \eta} y_j^e\Big)\Big(\sum_{k=1}^{4} \psi_k^e(\xi,\eta) Y_k^e\Big) + \sum_{j=1}^{4} \frac{\partial \psi_j^e(\xi,\eta)}{\partial \eta} w_j^e.\end{aligned} \tag{5.55}$$

Thus, the transverse shear strains at tying points can be expressed as

$$\tilde{\gamma}_{\xi z}^{\mathrm{A}} = \tilde{\gamma}_{\xi z}(0,-1) = \Big(\frac{x_2^e - x_1^e}{2}\Big)\Big(\frac{X_2^e + X_1^e}{2}\Big) + \Big(\frac{y_2^e - y_1^e}{2}\Big)\Big(\frac{Y_2^e + Y_1^e}{2}\Big) + \frac{w_2^e - w_1^e}{2}, \tag{5.56}$$

$$\tilde{\gamma}_{\xi z}^{\mathrm{C}} = \tilde{\gamma}_{\xi z}(0,1) = \Big(\frac{x_3^e - x_4^e}{2}\Big)\Big(\frac{X_3^e + X_4^e}{2}\Big) + \Big(\frac{y_3^e - y_4^e}{2}\Big)\Big(\frac{Y_3^e + Y_4^e}{2}\Big) + \frac{w_3^e - w_4^e}{2}, \tag{5.57}$$

$$\tilde{\gamma}_{\eta z}^{\mathrm{B}} = \tilde{\gamma}_{\eta z}(1,0) = \Big(\frac{x_3^e - x_2^e}{2}\Big)\Big(\frac{X_3^e + X_2^e}{2}\Big) + \Big(\frac{y_3^e - y_2^e}{2}\Big)\Big(\frac{Y_3^e + Y_2^e}{2}\Big) + \frac{w_3^e - w_2^e}{2}, \tag{5.58}$$

$$\tilde{\gamma}_{\eta z}^{\mathrm{D}} = \tilde{\gamma}_{\eta z}(-1,0) = \Big(\frac{x_4^e - x_1^e}{2}\Big)\Big(\frac{X_4^e + X_1^e}{2}\Big) + \Big(\frac{y_4^e - y_1^e}{2}\Big)\Big(\frac{Y_4^e + Y_1^e}{2}\Big) + \frac{w_4^e - w_1^e}{2}. \tag{5.59}$$

Thus, Eqs (5.52) and (5.53) can be expanded as

$$\begin{aligned}\tilde{\gamma}_{\xi z}(\eta) =& \frac{1-\eta}{2}\Big[\Big(\frac{x_2^e - x_1^e}{2}\Big)\Big(\frac{X_2^e + X_1^e}{2}\Big) + \Big(\frac{y_2^e - y_1^e}{2}\Big)\Big(\frac{Y_2^e + Y_1^e}{2}\Big) + \frac{w_2^e - w_1^e}{2}\Big] \\ &+ \frac{1+\eta}{2}\Big[\Big(\frac{x_3^e - x_4^e}{2}\Big)\Big(\frac{X_3^e + X_4^e}{2}\Big) + \Big(\frac{y_3^e - y_4^e}{2}\Big)\Big(\frac{Y_3^e + Y_4^e}{2}\Big) + \frac{w_3^e - w_4^e}{2}\Big],\end{aligned} \tag{5.60}$$

$$\begin{aligned}\tilde{\gamma}_{\eta z}(\xi) =& \frac{1-\xi}{2}\Big[\Big(\frac{x_4^e - x_1^e}{2}\Big)\Big(\frac{X_4^e + X_1^e}{2}\Big) + \Big(\frac{y_4^e - y_1^e}{2}\Big)\Big(\frac{Y_4^e + Y_1^e}{2}\Big) + \frac{w_4^e - w_1^e}{2}\Big] \\ &+ \frac{1+\xi}{2}\Big[\Big(\frac{x_3^e - x_2^e}{2}\Big)\Big(\frac{X_3^e + X_2^e}{2}\Big) + \Big(\frac{y_3^e - y_2^e}{2}\Big)\Big(\frac{Y_3^e + Y_2^e}{2}\Big) + \frac{w_3^e - w_2^e}{2}\Big].\end{aligned} \tag{5.61}$$

Finally, substituting Eqs (5.60) and (5.61) into Eqs (5.50) and (5.51), the transverse shear

strains in the real coordinates are given by

$$\begin{aligned}\gamma_{xz} = &\Big\{\frac{1-\eta}{2}\Big[\Big(\frac{x_2^e-x_1^e}{2}\Big)\Big(\frac{X_2^e+X_1^e}{2}\Big)+\Big(\frac{y_2^e-y_1^e}{2}\Big)\Big(\frac{Y_2^e+Y_1^e}{2}\Big)+\frac{w_2^e-w_1^e}{2}\Big]\\ &+\frac{1+\eta}{2}\Big[\Big(\frac{x_3^e-x_4^e}{2}\Big)\Big(\frac{X_3^e+X_4^e}{2}\Big)+\Big(\frac{y_3^e-y_4^e}{2}\Big)\Big(\frac{Y_3^e+Y_4^e}{2}\Big)+\frac{w_3^e-w_4^e}{2}\Big]\Big\}\\ &\times\frac{\sqrt{J_{21}^2+J_{22}^2}}{|\det J|}\sin\beta\\ -&\Big\{\frac{1-\xi}{2}\Big[\Big(\frac{x_4^e-x_1^e}{2}\Big)\Big(\frac{X_4^e+X_1^e}{2}\Big)+\Big(\frac{y_4^e-y_1^e}{2}\Big)\Big(\frac{Y_4^e+Y_1^e}{2}\Big)+\frac{w_4^e-w_1^e}{2}\Big]\\ &+\frac{1+\xi}{2}\Big[\Big(\frac{x_3^e-x_2^e}{2}\Big)\Big(\frac{X_3^e+X_2^e}{2}\Big)+\Big(\frac{y_3^e-y_2^e}{2}\Big)\Big(\frac{Y_3^e+Y_2^e}{2}\Big)+\frac{w_3^e-w_2^e}{2}\Big]\Big\}\\ &\times\frac{\sqrt{J_{11}^2+J_{12}^2}}{|\det J|}\sin\alpha,\end{aligned} \tag{5.62}$$

$$\begin{aligned}\gamma_{yz} = -&\Big\{\frac{1-\eta}{2}\Big[\Big(\frac{x_2^e-x_1^e}{2}\Big)\Big(\frac{X_2^e+X_1^e}{2}\Big)+\Big(\frac{y_2^e-y_1^e}{2}\Big)\Big(\frac{Y_2^e+Y_1^e}{2}\Big)+\frac{w_2^e-w_1^e}{2}\Big]\\ &+\frac{1+\eta}{2}\Big[\Big(\frac{x_3^e-x_4^e}{2}\Big)\Big(\frac{X_3^e+X_4^e}{2}\Big)+\Big(\frac{y_3^e-y_4^e}{2}\Big)\Big(\frac{Y_3^e+Y_4^e}{2}\Big)+\frac{w_3^e-w_4^e}{2}\Big]\Big\}\\ &\times\frac{\sqrt{J_{21}^2+J_{22}^2}}{|\det J|}\cos\beta\\ +&\Big\{\frac{1-\xi}{2}\Big[\Big(\frac{x_4^e-x_1^e}{2}\Big)\Big(\frac{X_4^e+X_1^e}{2}\Big)+\Big(\frac{y_4^e-y_1^e}{2}\Big)\Big(\frac{Y_4^e+Y_1^e}{2}\Big)+\frac{w_4^e-w_1^e}{2}\Big]\\ &+\frac{1+\xi}{2}\Big[\Big(\frac{x_3^e-x_2^e}{2}\Big)\Big(\frac{X_3^e+X_2^e}{2}\Big)+\Big(\frac{y_3^e-y_2^e}{2}\Big)\Big(\frac{Y_3^e+Y_2^e}{2}\Big)+\frac{w_3^e-w_2^e}{2}\Big]\Big\}\\ &\times\frac{\sqrt{J_{11}^2+J_{12}^2}}{|\det J|}\cos\alpha.\end{aligned} \tag{5.63}$$

5.2.3 FEM formulation for an MITC4 model

Because MITC4 employs the same interpolation method as the FSDT model for bending strains but a special interpolation for transverse shear strains, an MITC4 model can be obtained by simply manipulating only shear stiffness terms of the FSDT model. To be specific, the shear stiffness terms in the stiffness matrices $\mathbf{K}^{33}$, $\mathbf{K}^{34}$, $\mathbf{K}^{35}$, $\mathbf{K}^{43}$, $\mathbf{K}^{44}$, $\mathbf{K}^{45}$, $\mathbf{K}^{53}$, $\mathbf{K}^{54}$, and $\mathbf{K}^{55}$ (see Eq (E.1)) need to be calculated based on the shear strain formulation in Eq (5.63). These stiffness components are presented in Appendix G.

The MITC4 model does not require additional DOF or stiffness components to allevi-

ate shear locking; consequently, the model is computationally efficient and thus has been employed in many FEM packages for linear numerical analysis.

5.3 EAS method

It is well-known that the MITC4 method successfully handles shear locking. However, geometrically nonlinear models can suffer membrane locking, which the application of the MITC4 method is not sufficient to alleviate. Thus, this issue necessitates more general remedies for locking, one of which is the EAS method [79, 81]. In this section, the EAS method is presented and the FSDT model is modified to embrace the method.

5.3.1 Assumed strain fields

In the EAS method, an assumed strain field $\boldsymbol{\varepsilon}$ is defined as

$$\boldsymbol{\varepsilon} = \nabla^{\mathrm{s}}\boldsymbol{u} + \tilde{\boldsymbol{\varepsilon}}, \tag{5.64}$$

where $\nabla^{\mathrm{s}}\boldsymbol{u}$ is a symmetric gradient of a displacement field $\boldsymbol{u}$ and $\tilde{\boldsymbol{\varepsilon}}$ is the enhanced part of the strain field. The enhanced strain $\tilde{\boldsymbol{\varepsilon}}$ is not subject to any interelement continuity requirement, while the symmetric gradient $\nabla^{\mathrm{s}}\boldsymbol{u}$ forms a compatible strain field.

This work employs von Kármán strains[1]; thus, $\nabla^{\mathrm{s}}\boldsymbol{u}$ is replaced with $\boldsymbol{B}^{\mathrm{NL}}(\boldsymbol{u})$ for the compatible nonlinear strain field in Eqs (4.4) to (4.9). Therefore, the assumed strain field $\boldsymbol{\varepsilon}$ is given by

$$\boldsymbol{\varepsilon} = \boldsymbol{B}^{\mathrm{NL}}(\boldsymbol{u}) + \tilde{\boldsymbol{\varepsilon}}, \tag{5.65}$$

where

$$\varepsilon_{xx} = \varepsilon_{xx}^{(0)} + \tilde{\varepsilon}_{xx}^{(0)} + z\left[\varepsilon_{xx}^{(1)} + \tilde{\varepsilon}_{xx}^{(1)}\right] = \frac{\partial u_0}{\partial x} + \frac{1}{2}\left(\frac{\partial w_0}{\partial x}\right)^2 + \tilde{\varepsilon}_{xx}^{(0)} + z\left[\frac{\partial \phi_x}{\partial x} + \tilde{\varepsilon}_{xx}^{(1)}\right], \tag{5.66}$$

[1]The symmetric gradient of displacements field can form only the linear part of von Kármán strains.

$$\varepsilon_{yy} = \varepsilon_{yy}^{(0)} + \tilde{\varepsilon}_{yy}^{(0)} + z\Big[\varepsilon_{yy}^{(1)} + \tilde{\varepsilon}_{yy}^{(1)}\Big] = \frac{\partial v_0}{\partial y} + \frac{1}{2}\Big(\frac{\partial w_0}{\partial y}\Big)^2 + \tilde{\varepsilon}_{yy}^{(0)} + z\Big[\frac{\partial \phi_y}{\partial y} + \tilde{\varepsilon}_{yy}^{(1)}\Big], \tag{5.67}$$

$$\begin{aligned}\gamma_{xy} =& \gamma_{xy}^{(0)} + \tilde{\gamma}_{xy}^{(0)} + z\Big[\gamma_{xy}^{(1)} + \tilde{\gamma}_{yy}^{(1)}\Big] \\ =& \frac{\partial u_0}{\partial y} + \frac{\partial v_0}{\partial x} + \frac{\partial w_0}{\partial x}\frac{\partial w_0}{\partial y} + \tilde{\gamma}_{xy}^{(0)} + z\Big[\frac{\partial \phi_x}{\partial y} + \frac{\partial \phi_y}{\partial x} + \tilde{\gamma}_{xy}^{(1)}\Big],\end{aligned} \tag{5.68}$$

$$\gamma_{yz} = \gamma_{yz}^{(0)} + \tilde{\gamma}_{yz}^{(0)} = \phi_y + \frac{\partial w_0}{\partial y} + \tilde{\gamma}_{yz}^{(0)} \tag{5.69}$$

$$\gamma_{xz} = \gamma_{xz}^{(0)} + \tilde{\gamma}_{xz}^{(0)} = \phi_x + \frac{\partial w_0}{\partial x} + \tilde{\gamma}_{xz}^{(0)}. \tag{5.70}$$

Thus, the stress resultants of the compatible strains in Eqs (B.10), (B.12) and (B.14) are modified for the assumed strain field as

$$\begin{Bmatrix} N_{xx} \\ N_{yy} \\ N_{xy} \end{Bmatrix} = \begin{bmatrix} A_{11} & A_{12} & A_{16} \\ A_{12} & A_{22} & A_{26} \\ A_{16} & A_{26} & A_{66} \end{bmatrix} \begin{Bmatrix} \varepsilon_{xx}^{(0)} + \tilde{\varepsilon}_{xx}^{(0)} \\ \varepsilon_{yy}^{(0)} + \tilde{\varepsilon}_{yy}^{(0)} \\ \gamma_{xy}^{(0)} + \tilde{\gamma}_{xy}^{(0)} \end{Bmatrix} + \begin{bmatrix} B_{11} & B_{12} & B_{16} \\ B_{12} & B_{22} & B_{26} \\ B_{16} & B_{26} & B_{66} \end{bmatrix} \begin{Bmatrix} \varepsilon_{xx}^{(1)} + \tilde{\varepsilon}_{xx}^{(1)} \\ \varepsilon_{yy}^{(1)} + \tilde{\varepsilon}_{yy}^{(1)} \\ \gamma_{xy}^{(1)} + \tilde{\gamma}_{xy}^{(1)} \end{Bmatrix}, \tag{5.71}$$

$$\begin{Bmatrix} M_{xx} \\ M_{yy} \\ M_{xy} \end{Bmatrix} = \begin{bmatrix} B_{11} & B_{12} & B_{16} \\ B_{12} & B_{22} & B_{26} \\ B_{16} & B_{26} & B_{66} \end{bmatrix} \begin{Bmatrix} \varepsilon_{xx}^{(0)} + \tilde{\varepsilon}_{xx}^{(0)} \\ \varepsilon_{yy}^{(0)} + \tilde{\varepsilon}_{yy}^{(0)} \\ \gamma_{xy}^{(0)} + \tilde{\gamma}_{xy}^{(0)} \end{Bmatrix} + \begin{bmatrix} D_{11} & D_{12} & D_{16} \\ D_{12} & D_{22} & D_{26} \\ D_{16} & D_{26} & D_{66} \end{bmatrix} \begin{Bmatrix} \varepsilon_{xx}^{(1)} + \tilde{\varepsilon}_{xx}^{(1)} \\ \varepsilon_{yy}^{(1)} + \tilde{\varepsilon}_{yy}^{(1)} \\ \gamma_{xy}^{(1)} + \tilde{\gamma}_{xy}^{(1)} \end{Bmatrix}, \tag{5.72}$$

$$\begin{Bmatrix} Q_{yz} \\ Q_{xz} \end{Bmatrix} = \begin{bmatrix} A_{44} & A_{45} \\ A_{45} & A_{55} \end{bmatrix} \begin{Bmatrix} \gamma_{yz}^{(0)} + \tilde{\gamma}_{yz}^{(0)} \\ \gamma_{xz}^{(0)} + \tilde{\gamma}_{xz}^{(0)} \end{Bmatrix}. \tag{5.73}$$

5.3.2 Transformation and interpolation of enhanced strain fields

Using the Jacobian matrix $\boldsymbol{J}(\xi,\eta)$[2] (see Eq (5.42)), Simo and Rifai defined in Ref [81] a transformation matrix of enhanced strains between real and reference elements (see Fig 4.3):

$$\tilde{\boldsymbol{E}}(\xi,\eta) = \frac{j(\xi,\eta)}{j_0}\boldsymbol{F}_0^T\tilde{\boldsymbol{\varepsilon}}(\xi,\eta), \tag{5.74}$$

[2]Simo and Rifai used deformation (ϕ) gradient for the Jacobain matrix: $\boldsymbol{J}_{\alpha\beta}^{\text{Simo}} = \frac{\partial \phi_\alpha}{\partial \xi_\beta}$. Thus, $\boldsymbol{J} = [\boldsymbol{J}^{\text{Simo}}]^T$.

where

$$\boldsymbol{J}_0 = \boldsymbol{J}(0,0), \quad j(\xi,\eta) = \det\boldsymbol{J}(\xi,\eta), \quad j_0 = \det\boldsymbol{J}_0, \tag{5.75}$$

and $\tilde{\boldsymbol{\varepsilon}}$ and $\tilde{\boldsymbol{E}}$ are enhanced strain fields in real and reference elements, respectively. For enhanced in-plane strains $\tilde{\boldsymbol{\varepsilon}} = [\tilde{\varepsilon}_{xx}, \tilde{\varepsilon}_{yy}, \tilde{\gamma}_{xx}]^T$, $\boldsymbol{F}_0$ is given by

$$\boldsymbol{F}_0 = \begin{bmatrix} J_{11}^2 & J_{21}^2 & 2J_{11}J_{21} \\ J_{12}^2 & J_{22}^2 & 2J_{12}J_{22} \\ J_{11}J_{12} & J_{21}J_{22} & J_{11}J_{22} + J_{12}J_{21} \end{bmatrix}_{(\xi,\eta)=(0,0)} . \tag{5.76}$$

For enhanced transverse shear strains $\tilde{\boldsymbol{\varepsilon}} = [\tilde{\gamma}_{xz}, \tilde{\gamma}_{yz}]^T$, $\boldsymbol{F}_0$ is given by

$$\boldsymbol{F}_0 = \boldsymbol{J}_0. \tag{5.77}$$

The interpolation matrix $\mathbb{E}(\xi,\eta)$ for enhanced strains $\tilde{\boldsymbol{E}}$ in reference elements can be defined [81] as

$$\tilde{\boldsymbol{E}}(\xi,\eta) = \mathbb{E}(\xi,\eta)\boldsymbol{\alpha}^e, \tag{5.78}$$

where $\mathbb{E}$ is an $m \times n$ matrix[3], and $\boldsymbol{\alpha}^e$ is an $n \times 1$ column vector. The elemental variable $\boldsymbol{\alpha}^e$ is free of interelement continuity requirements as is $\tilde{\boldsymbol{E}}$. Thus, the interpolation matrix $\mathbb{G}(\xi,\eta)$ for enhanced strains $\tilde{\boldsymbol{\varepsilon}}$ in real elements is given by

$$\mathbb{G}(\xi,\eta) = \frac{j_0}{j(\xi,\eta)}\boldsymbol{F}_0^{-T}\mathbb{E}(\xi,\eta). \tag{5.79}$$

For enhanced in-plane strains $\tilde{\boldsymbol{\varepsilon}}_{xy} = [\tilde{\varepsilon}_{xx}, \tilde{\varepsilon}_{yy}, \tilde{\gamma}_{xx}]^T$, Andelfinger and Ramm [3] proposed

[3]For enhanced in-plane strains, m is equal to 3, while m is equal to 2 for enhanced transverse shear strains.

the seven-parameter (or seven-mode) interpolation:

$$\mathbb{E}_m^7(\xi,\eta) = \begin{bmatrix} \xi & 0 & 0 & 0 & \xi\eta & 0 & 0 \\ 0 & \eta & 0 & 0 & 0 & \xi\eta & 0 \\ 0 & 0 & \xi & \eta & 0 & 0 & \xi\eta \end{bmatrix}, \tag{5.80}$$

and the eleven-parameter (or eleven-mode) interpolation:

$$\mathbb{E}_m^{11}(\xi,\eta) = \begin{bmatrix} \xi & 0 & 0 & 0 & \xi\eta & 0 & 0 & 3\xi^2-1 & 0 & 0 & 0 \\ 0 & \eta & 0 & 0 & 0 & \xi\eta & 0 & 0 & 3\eta^2-1 & 0 & 0 \\ 0 & 0 & \xi & \eta & 0 & 0 & \xi\eta & 0 & 0 & 3\xi^2-1 & 3\eta^2-1 \end{bmatrix}. \tag{5.81}$$

For enhanced transverse shear strains $\tilde{\boldsymbol{\varepsilon}}_{xy} = [\tilde{\gamma}_{xz}, \tilde{\gamma}_{yz}]^T$, Simo and Rifai [81] proposed the four-parameter interpolation:

$$\mathbb{E}_s^4(\xi,\eta) = \begin{bmatrix} \xi & 0 & \xi\eta & 0 \\ 0 & \eta & 0 & \xi\eta \end{bmatrix}, \tag{5.82}$$

which generates the transverse shear strain field identical to the one of MITC4.

This work applied the EAS method to all of the three strain fields (membrane, bending, and shear strains):

$$\begin{Bmatrix} \tilde{\varepsilon}_{xx}^{(0)} \\ \tilde{\varepsilon}_{yy}^{(0)} \\ \tilde{\gamma}_{xy}^{(0)} \end{Bmatrix} = \mathbb{G}_m(\xi,\eta)\boldsymbol{\alpha}_m^e, \quad \text{where } \mathbb{G}_m(\xi,\eta) = \frac{j_0}{j(\xi,\eta)}\boldsymbol{F}_0^{-T}\mathbb{E}_m(\xi,\eta), \tag{5.83}$$

$$\begin{Bmatrix} \tilde{\varepsilon}_{xx}^{(1)} \\ \tilde{\varepsilon}_{yy}^{(1)} \\ \tilde{\gamma}_{xy}^{(1)} \end{Bmatrix} = \mathbb{G}_b(\xi,\eta)\boldsymbol{\alpha}_b^e, \quad \text{where } \mathbb{G}_b(\xi,\eta) = \frac{j_0}{j(\xi,\eta)}\boldsymbol{F}_0^{-T}\mathbb{E}_m(\xi,\eta), \tag{5.84}$$

$$\begin{Bmatrix} \tilde{\gamma}_{xz}^{(0)} \\ \tilde{\gamma}_{yz}^{(0)} \end{Bmatrix} = \mathbb{G}_s(\xi,\eta)\boldsymbol{\alpha}_s^e, \quad \text{where } \mathbb{G}_s(\xi,\eta) = \frac{j_0}{j(\xi,\eta)}\boldsymbol{J}_0^{-T}\mathbb{E}_s(\xi,\eta). \tag{5.85}$$

5.3.3 Three-field variational formulation

The EAS theory is based on the Hu-Washizu three-field variational principle [93, 94]. The principle is presented in detail in Appendix H. Substituting the assumed strain field into the variational principle in Eqs (H.7) to (H.9), the three-field variational formulation for the EAS theory is obtained as

$$\int_{\Omega_0}\int_{-\frac{h}{2}}^{\frac{h}{2}} \Big[\boldsymbol{B}^{\mathrm{NL}}(\delta\boldsymbol{u})\cdot\boldsymbol{\sigma}\Big] dzdxdy + F_{\mathrm{ext}}(\delta\boldsymbol{u}) = 0, \tag{5.86}$$

$$\int_{\Omega_0}\int_{-\frac{h}{2}}^{\frac{h}{2}} \Big[\Big(\frac{\partial A(\boldsymbol{B}^{\mathrm{NL}}(\boldsymbol{u})+\tilde{\boldsymbol{\varepsilon}})}{\partial\boldsymbol{\varepsilon}} - \boldsymbol{\sigma}\Big)\cdot\delta\Big(\boldsymbol{B}^{\mathrm{NL}}(\boldsymbol{u})+\tilde{\boldsymbol{\varepsilon}}\Big)\Big] dzdxdy = 0, \tag{5.87}$$

$$\int_{\Omega_0}\int_{-\frac{h}{2}}^{\frac{h}{2}} \tilde{\boldsymbol{\varepsilon}}\cdot\delta\boldsymbol{\sigma} dzdxdy = 0, \tag{5.88}$$

where $F_{\mathrm{ext}}(\delta\boldsymbol{u})$ is the virtual work done by external loading (i.e., $F_{\mathrm{ext}} = \delta V$, see Eq (D.3)), a state function A is given in Eq (H.3), and

$$\boldsymbol{u} = \begin{Bmatrix} u \\ v \\ w \\ \phi_x \\ \phi_y \end{Bmatrix}, \quad \boldsymbol{\sigma} = \begin{Bmatrix} \sigma_{xx} \\ \sigma_{yy} \\ \tau_{xy} \\ \tau_{xz} \\ \tau_{yz} \end{Bmatrix}, \quad \boldsymbol{\varepsilon} = \begin{Bmatrix} \varepsilon_{xx} \\ \varepsilon_{yy} \\ \gamma_{xy} \\ \gamma_{xz} \\ \gamma_{yz} \end{Bmatrix}. \tag{5.89}$$

Equation (5.87) can be expanded as

$$\int_{\Omega_0}\int_{-\frac{h}{2}}^{\frac{h}{2}} \Big[\Big(\frac{\partial A}{\partial\boldsymbol{\varepsilon}} - \boldsymbol{\sigma}\Big)\cdot\boldsymbol{B}^{\mathrm{NL}}(\boldsymbol{\delta u})\Big] dzdxdy + \int_{\Omega_0}\int_{-\frac{h}{2}}^{\frac{h}{2}} \Big[\Big(\frac{\partial A}{\partial\boldsymbol{\varepsilon}} - \boldsymbol{\sigma}\Big)\cdot\delta\tilde{\boldsymbol{\varepsilon}}\Big] dzdxdy = 0. \tag{5.90}$$

Setting the first integral term zero as shown in Eq (5.91), two new equations arise:

$$\int_{\Omega_0}\int_{-\frac{h}{2}}^{\frac{h}{2}}\Big[\Big(\frac{\partial A(\boldsymbol{B}^{\mathrm{NL}}(\boldsymbol{u})+\tilde{\boldsymbol{\varepsilon}})}{\partial \boldsymbol{\varepsilon}}-\boldsymbol{\sigma}\Big)\cdot \boldsymbol{B}^{\mathrm{NL}}(\boldsymbol{\delta u})\Big]dzdxdy=0, \tag{5.91}$$

$$\int_{\Omega_0}\int_{-\frac{h}{2}}^{\frac{h}{2}}\boldsymbol{\sigma}\cdot\delta\tilde{\boldsymbol{\varepsilon}}dzdxdy=\int_{\Omega_0}\int_{-\frac{h}{2}}^{\frac{h}{2}}\frac{\partial A(\boldsymbol{B}^{\mathrm{NL}}(\boldsymbol{u})+\tilde{\boldsymbol{\varepsilon}})}{\partial \boldsymbol{\varepsilon}}\cdot\delta\tilde{\boldsymbol{\varepsilon}}dzdxdy. \tag{5.92}$$

Substituting Eq (5.92) into Eq (5.86) and replacing Eq (5.87) with Eq (5.91), a modified three-field varational formulation [81] is obtained as

$$\int_{\Omega_0}\int_{-\frac{h}{2}}^{\frac{h}{2}}\Big[\boldsymbol{B}^{\mathrm{NL}}(\delta\boldsymbol{u})\cdot\frac{\partial A(\boldsymbol{B}^{\mathrm{NL}}(\boldsymbol{u})+\tilde{\boldsymbol{\varepsilon}})}{\partial \boldsymbol{\varepsilon}}\Big]dzdxdy+F_{\mathrm{ext}}(\delta\boldsymbol{u})=0, \tag{5.93}$$

$$\int_{\Omega_0}\int_{-\frac{h}{2}}^{\frac{h}{2}}\Big[\Big(\frac{\partial A(\boldsymbol{B}^{\mathrm{NL}}(\boldsymbol{u})+\tilde{\boldsymbol{\varepsilon}})}{\partial \boldsymbol{\varepsilon}}-\boldsymbol{\sigma}\Big)\cdot\delta\tilde{\boldsymbol{\varepsilon}}\Big]dzdxdy=0, \tag{5.94}$$

$$\int_{\Omega_0}\int_{-\frac{h}{2}}^{\frac{h}{2}}\tilde{\boldsymbol{\varepsilon}}\cdot\delta\boldsymbol{\sigma}dzdxdy=0. \tag{5.95}$$

The stress field $\boldsymbol{\sigma}$ can be eliminated from the three-field ($\boldsymbol{u}$-$\boldsymbol{\epsilon}$-$\boldsymbol{\sigma}$) formulation by enforcing the orthogonality between $\boldsymbol{\sigma}$ and $\tilde{\boldsymbol{\varepsilon}}$ [80]:

$$\int_{\Omega_0}\int_{-\frac{h}{2}}^{\frac{h}{2}}\boldsymbol{\sigma}\cdot\tilde{\boldsymbol{\varepsilon}}dzdxdy=0. \tag{5.96}$$

Thus, Eqs (5.81) to (5.83) can be reduced to a two-field ($\boldsymbol{u}$-$\boldsymbol{\varepsilon}$) formulation [81]:

$$\int_{\Omega_0}\int_{-\frac{h}{2}}^{\frac{h}{2}}\Big[\boldsymbol{B}^{\mathrm{NL}}(\delta\boldsymbol{u})\cdot\frac{\partial A(\boldsymbol{B}^{\mathrm{NL}}(\boldsymbol{u})+\tilde{\boldsymbol{\varepsilon}})}{\partial \boldsymbol{\varepsilon}}\Big]dzdxdy+F_{\mathrm{ext}}(\delta\boldsymbol{u})=0, \tag{5.97}$$

$$\int_{\Omega_0}\int_{-\frac{h}{2}}^{\frac{h}{2}}\Big[\frac{\partial A(\boldsymbol{B}^{\mathrm{NL}}(\boldsymbol{u})+\tilde{\boldsymbol{\varepsilon}})}{\partial \boldsymbol{\varepsilon}}\cdot\delta\tilde{\boldsymbol{\varepsilon}}\Big]dzdxdy=0. \tag{5.98}$$

5.3.4 FEM formulation for an EAS model

Using Eqs (5.66) to (5.73) and Eqs (5.83) to (5.85), the first term of Eq (5.91) can be expanded:

$$
\begin{aligned}
&\int_{\Omega_0}\int_{-\frac{h}{2}}^{\frac{h}{2}}\Big[\boldsymbol{B}^{\mathrm{NL}}(\delta\boldsymbol{u})\cdot\frac{\partial A(\boldsymbol{B}^{\mathrm{NL}}(\boldsymbol{u})+\tilde{\boldsymbol{\varepsilon}})}{\partial\boldsymbol{\varepsilon}}\Big]dzdxdy\\
&=\int_{\Omega_0}\int_{-\frac{h}{2}}^{\frac{h}{2}}\Big[\sigma_{xx}\Big\{\Big(\frac{\partial\delta u_0}{\partial x}+\frac{\partial\delta w_0}{\partial x}\frac{\partial w_0}{\partial x}\Big)+z\frac{\partial\delta\phi_x}{\partial x}\Big\}\\
&\qquad+\sigma_{yy}\Big\{\Big(\frac{\partial\delta v_0}{\partial y}+\frac{\partial\delta w_0}{\partial y}\frac{\partial w_0}{\partial y}\Big)+z\frac{\partial\delta\phi_y}{\partial y}\Big\}\\
&\qquad+\sigma_{xy}\Big\{\Big(\frac{\partial\delta u_0}{\partial y}+\frac{\partial\delta v_0}{\partial x}+\frac{\partial\delta w_0}{\partial x}\frac{\partial w_0}{\partial y}+\frac{\partial w_0}{\partial x}\frac{\partial\delta w_0}{\partial y}\Big)+z\Big(\frac{\partial\delta\phi_x}{\partial y}+\frac{\partial\delta\phi_y}{\partial x}\Big)\Big\}\\
&\qquad+\sigma_{xz}\Big(\delta\phi_x+\frac{\partial\delta w_0}{\partial x}\Big)+\sigma_{yz}\Big(\delta\phi_y+\frac{\partial\delta w_0}{\partial y}\Big)\Big]dzdxdy\\
&=\int_{\Omega_0}\Big[N_{xx}\Big(\frac{\partial\delta u_0}{\partial x}+\frac{\partial\delta w_0}{\partial x}\frac{\partial w_0}{\partial x}\Big)+M_{xx}\frac{\partial\delta\phi_x}{\partial x}\\
&\qquad+N_{yy}\Big(\frac{\partial\delta v_0}{\partial y}+\frac{\partial\delta w_0}{\partial y}\frac{\partial w_0}{\partial y}\Big)+M_{yy}\frac{\partial\delta\phi_y}{\partial y}\\
&\qquad+N_{xy}\Big(\frac{\partial\delta u_0}{\partial y}+\frac{\partial\delta v_0}{\partial x}+\frac{\partial\delta w_0}{\partial x}\frac{\partial w_0}{\partial y}+\frac{\partial w_0}{\partial x}\frac{\partial\delta w_0}{\partial y}\Big)+M_{xy}\Big(\frac{\partial\delta\phi_x}{\partial y}+\frac{\partial\delta\phi_y}{\partial x}\Big)\\
&\qquad+Q_{xz}\Big(\delta\phi_x+\frac{\partial\delta w_0}{\partial x}\Big)+Q_{yz}\Big(\delta\phi_y+\frac{\partial\delta w_0}{\partial y}\Big)\Big]dxdy,
\end{aligned}
\tag{5.99}
$$

and thus Eq (5.97) yields

$$
\boldsymbol{k}_{\mathrm{uu}}\boldsymbol{u}+\boldsymbol{k}_{\mathrm{u}\alpha}\boldsymbol{\alpha}=\boldsymbol{f},
\tag{5.100}
$$

where $\boldsymbol{k}_{\mathrm{uu}}$ and $\boldsymbol{f}$ are identical to the stiffness matrix $\boldsymbol{K}$ and force vector $\boldsymbol{F}$ of the FSDT model (see Eq (4.37)), respectively. Similarly, Eq (5.92) can be expanded:

$$\begin{aligned}
&\int_{\Omega_0}\int_{-\frac{h}{2}}^{\frac{h}{2}}\left[\boldsymbol{B}^{\mathrm{NL}}(\delta\boldsymbol{u})\cdot\frac{\partial A(\boldsymbol{B}^{\mathrm{NL}}(\boldsymbol{u})+\tilde{\boldsymbol{\varepsilon}})}{\partial\boldsymbol{\varepsilon}}\right]dzdxdy\\
&=\int_{\Omega_0}\int_{-\frac{h}{2}}^{\frac{h}{2}}\Big[\sigma_{xx}\Big(\mathbb{G}_m^{xx}\delta\boldsymbol{\alpha}_e^m+z\mathbb{G}_b^{xx}\delta\boldsymbol{\alpha}_e^b\Big)+\sigma_{yy}\Big(\mathbb{G}_m^{yy}\delta\boldsymbol{\alpha}_e^m+z\mathbb{G}_b^{yy}\delta\boldsymbol{\alpha}_e^b\Big)\\
&\qquad+\sigma_{xy}\Big(\mathbb{G}_m^{xy}\delta\boldsymbol{\alpha}_e^m+z\mathbb{G}_b^{xy}\delta\boldsymbol{\alpha}_e^b\Big)+\sigma_{xz}\mathbb{G}_s^{xz}\delta\boldsymbol{\alpha}_e^s+\sigma_{yz}\mathbb{G}_s^{yz}\delta\boldsymbol{\alpha}_e^s\Big]dzdxdy\\
&=\int_{\Omega_0}\Big[N_{xx}\mathbb{G}_m^{xx}\delta\boldsymbol{\alpha}_e^m+M_{xx}\mathbb{G}_b^{xx}\delta\boldsymbol{\alpha}_e^b+N_{yy}\mathbb{G}_m^{yy}\delta\boldsymbol{\alpha}_e^m+M_{yy}\mathbb{G}_b^{yy}\delta\boldsymbol{\alpha}_e^b\\
&\qquad+N_{xy}\mathbb{G}_m^{xy}\delta\boldsymbol{\alpha}_e^m+M_{xy}\mathbb{G}_b^{xy}\delta\boldsymbol{\alpha}_e^b+Q_{xz}\mathbb{G}_s^{xz}\delta\boldsymbol{\alpha}_e^s+Q_{yz}\mathbb{G}_s^{yz}\delta\boldsymbol{\alpha}_e^s\Big]dxdy.
\end{aligned}\tag{5.101}$$

and gives

$$\boldsymbol{k}_{\alpha\mathrm{u}}\boldsymbol{u}+\boldsymbol{k}_{\alpha\alpha}\boldsymbol{\alpha}=0,\tag{5.102}$$

where the components of $\boldsymbol{k}_{\mathrm{u}\alpha}$, $\boldsymbol{k}_{\alpha\mathrm{u}}$, and $\boldsymbol{k}_{\alpha\alpha}$ are presented in Appendix I.

Equations (5.100) and (5.102) can be written in a matrix form:

$$\begin{bmatrix}\boldsymbol{k}_{\mathrm{uu}} & \boldsymbol{k}_{\mathrm{u}\alpha}\\ \boldsymbol{k}_{\alpha\mathrm{u}} & \boldsymbol{k}_{\alpha\alpha}\end{bmatrix}\begin{Bmatrix}\boldsymbol{u}\\ \boldsymbol{\alpha}\end{Bmatrix}=\begin{Bmatrix}\boldsymbol{f}\\ \boldsymbol{0}\end{Bmatrix}.\tag{5.103}$$

The variable $\boldsymbol{\alpha}$ can be removed from this matrix through static condensation [81]:

$$\bar{\boldsymbol{K}}\boldsymbol{u}=\boldsymbol{f},\tag{5.104}$$

where

$$\boldsymbol{\alpha}=-\boldsymbol{k}_{\alpha\alpha}^{-1}\boldsymbol{k}_{\alpha\mathrm{u}}\boldsymbol{u},\tag{5.105}$$

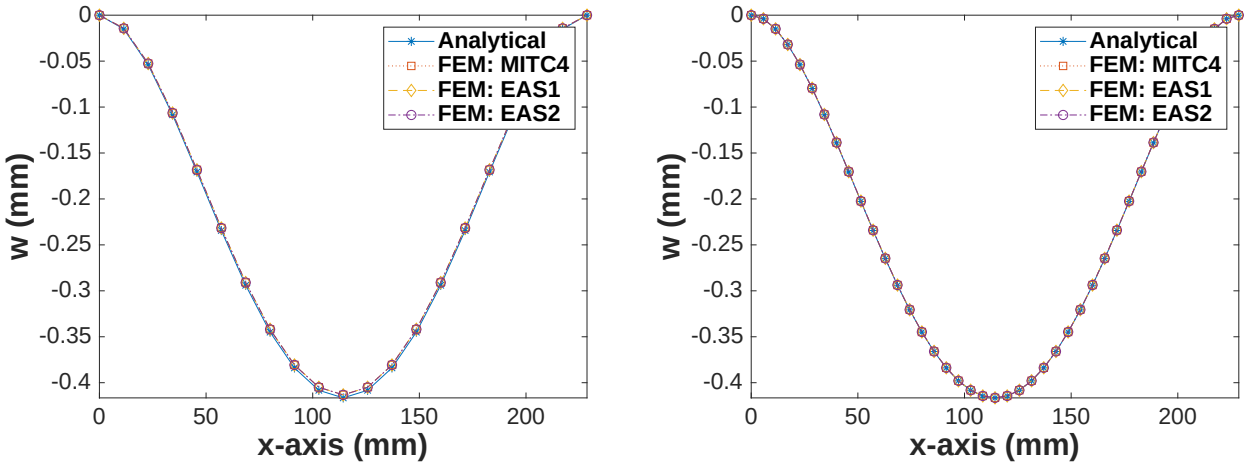

(a) (b)

Figure 5.3: The transverse displacement w_0 of the MITC4 and EAS models for the cylindrical bending plate problem (see Fig 4.5) using (a) the normal mesh (see Fig 4.6) and (b) the refined mesh (Fig 4.11).

and

$$\bar{\boldsymbol{K}} = \boldsymbol{k}_{\mathrm{uu}} - \boldsymbol{k}_{\mathrm{u}\alpha}\boldsymbol{k}_{\alpha\alpha}^{-1}\boldsymbol{k}_{\alpha\mathrm{u}}. \tag{5.106}$$

This static condensation process can be performed at the element level because $\boldsymbol{\alpha}$ is not subject to any interelement continuity requirement.

5.4 Linear static analysis using MITC4 and EAS models

Based on the FEM formulation introduced in the previous sections, in-house FEM codes were written using MATLAB to generate MITC4 and EAS models. In this section, the performance of the MITC4 and EAS models is investigated by simulating the cylindrical bending problem introduced in Section 4.4. The same element size, applied load, and boundary conditions of the FSDT models were adopted for these models (see Figs 4.6 and 4.11). The EAS model having only enhanced transverse shear strain field is named 'EAS1' while the

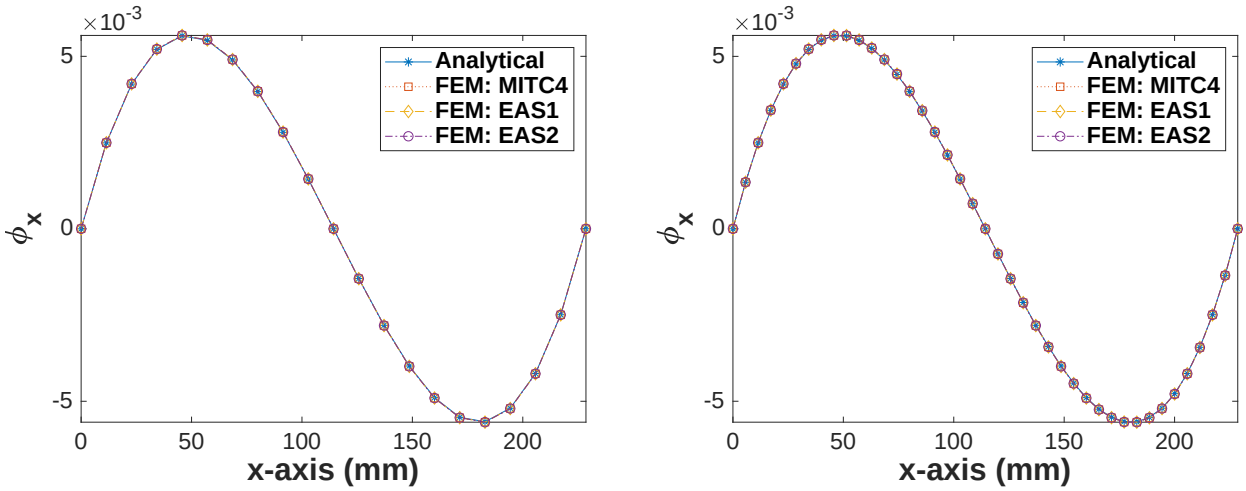

Figure 5.4: The rotation ϕ_x of the MITC4 and EAS models for the cylindrical bending plate problem using (a) the normal mesh and (b) the refined mesh.

one employing both enhanced transverse shear and bending strain fields is named 'EAS2'.

The transverse displacement and rotation fields of the MITC4, EAS1, and EAS2 models are illustrated in Figs 5.3 and 5.4. The simulation results showed good agreement with the analytical solution on both the normal and refined meshes and the over-stiffening phenomenon of the FSDT model is not observed in the results. Therefore, the models can be deemed free of shear locking (in the linear case). The maximum transverse displacement w_0 and rotation ϕ_x, and the first-mode buckling load N_{CR} of the MITC4 and EAS models on the normal and refined meshes are tabulated in Table 5.1. The MITC4 and EAS1 models demonstrate identical results as expected; however, the EAS2 model shows a slightly better $|w_0|_{\max}$ with negligibly worse $|\phi_x|_{\max}$ and N_{CR}. Therefore, these comparisons do not clarify the impact of the enhanced bending strain of the EAS2 model. The comparison between the results of the normal and refined meshes reveals that the mesh refinement makes a marginal impact on the simulation results of these models with a substantially higher computational cost.

For stress analysis using assumed strain methods, Simo and Rifai [81] proposed a stress

Field	Mesh	Analytical	FEM: MITC4 & EAS1	FEM: EAS2
$\lvert w_0\rvert_{\max}$ (mm)	Normal	0.41653	0.41323 (0.792 %)	0.41328 (0.778 %)
	Refined	0.41653	0.41648 (0.012 %)	0.41650 (0.008 %)
$\lvert\phi_x\rvert_{\max}$ $\times 10^3$ (rad)	Normal	5.463	5.475 (0.220 %)	5.476 (0.235 %)
	Refined	5.463	5.477 (0.251 %)	5.477 (0.256 %)
N_{CR} (N/m)	Normal	1018.53	987.65 (3.032 %)	986.20 (3.174 %)
	Refined	1018.53	973.22 (4.449 %)	972.80 (4.490 %)

Table 5.1: The maximum transverse displacement w_0 and rotation ϕ_x, and the first-mode buckling load N_{CR} of the MITC4 and EAS models on the normal and refined meshes for the cylindrical bending problem. The values in the parentheses indicate the percent error of the numerical predictions.

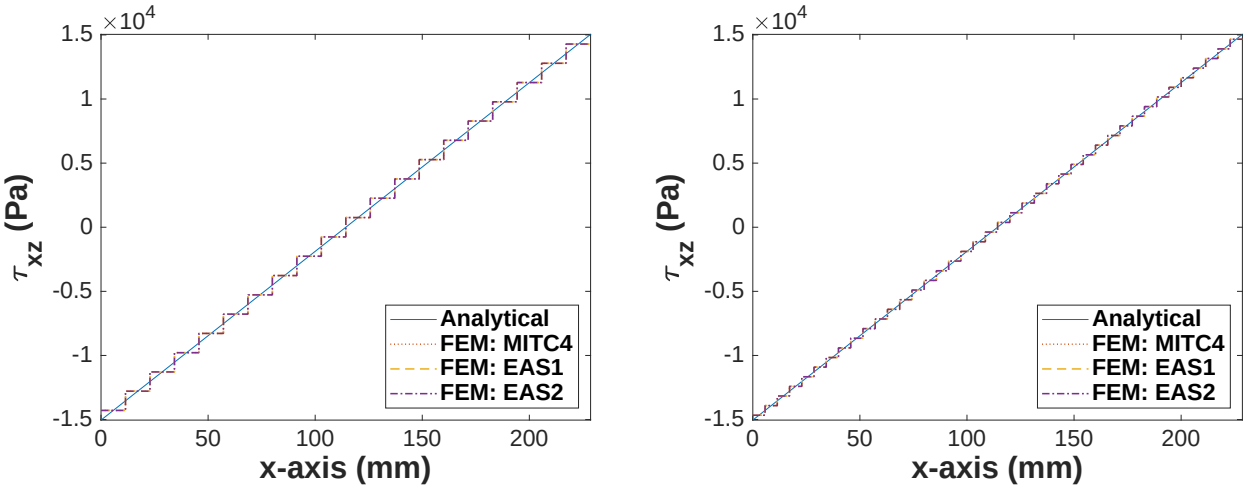

Figure 5.5: The transverse shear stress τ_{xz} of the MITC4 and EAS models for the cylindrical bending plate problem using (a) the normal mesh and (b) the refined mesh.

recovery method based on the orthogonality condition in Eq (5.96) and demonstrated that the recovered stress $\boldsymbol{\sigma}^{\mathrm{R}}$ shows good agreement with the true solution at the center of elements but not over the entire elements. They pointed out that the stress field evaluated using the

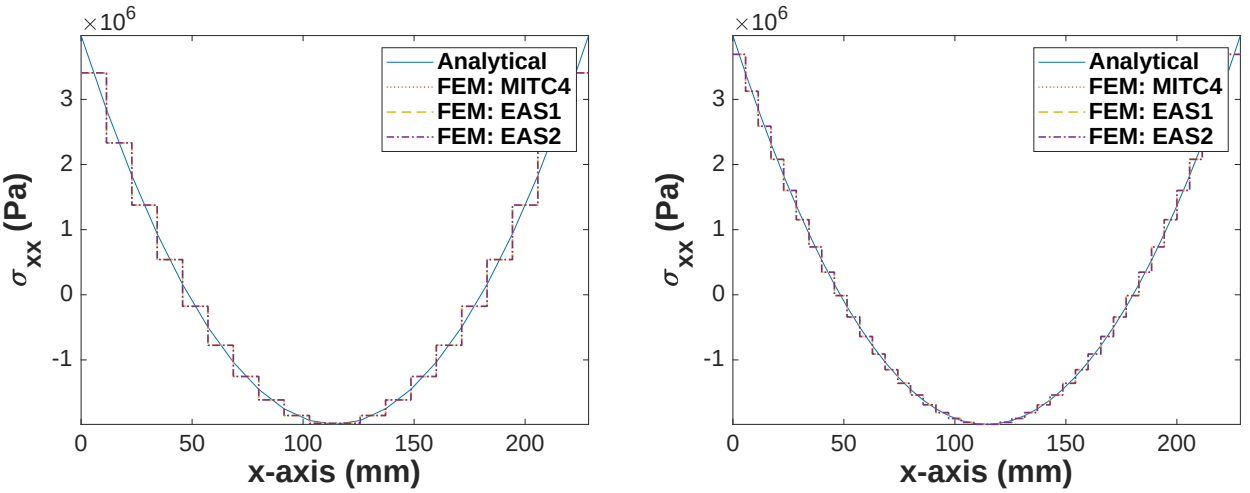

Figure 5.6: The bending stress σ_{xx} of the MITC4 and EAS models at the top of the plate for the cylindrical bending plate problem using (a) the normal mesh and (b) the refined mesh.

assumed strain field (see Eq (5.65)) and lamina constitutive relation (see Eq (B.8)):

$$\boldsymbol{\sigma}^{\mathrm{C}} = \bar{\boldsymbol{C}}\big[\boldsymbol{B}^{\mathrm{NL}}(\boldsymbol{u}) + \tilde{\boldsymbol{\epsilon}}\big], \tag{5.107}$$

does not satisfy the orthogonality condition; however, $\boldsymbol{\sigma}^{\mathrm{C}}$ is identical to $\boldsymbol{\sigma}^{\mathrm{R}}$ obtained at the center of elements. This work evaluated the stress fields of the MITC4 and EAS models using Eq (5.107) over elements (i.e., $\boldsymbol{\sigma}^{\mathrm{C}}$) because the method provides a variationally correct stress at the center of elements and additional information on stress oscillations over elements.

The transverse shear and bending stress fields of the three models for the cylindrical bending problem are plotted in Figs 5.5 and 5.6. Both of the stress fields of the models are constant over each element and show good agreement with the analytical solutions at the center of the elements as intended. Therefore, the models do not exhibit the shear stress oscillations of the FSDT model, which is closely related to shear locking. The stress fields evaluated using the refined mesh are closer to the continuous stress fields of the analytical solutions; however, the fields obtained from the normal mesh provide enough information to

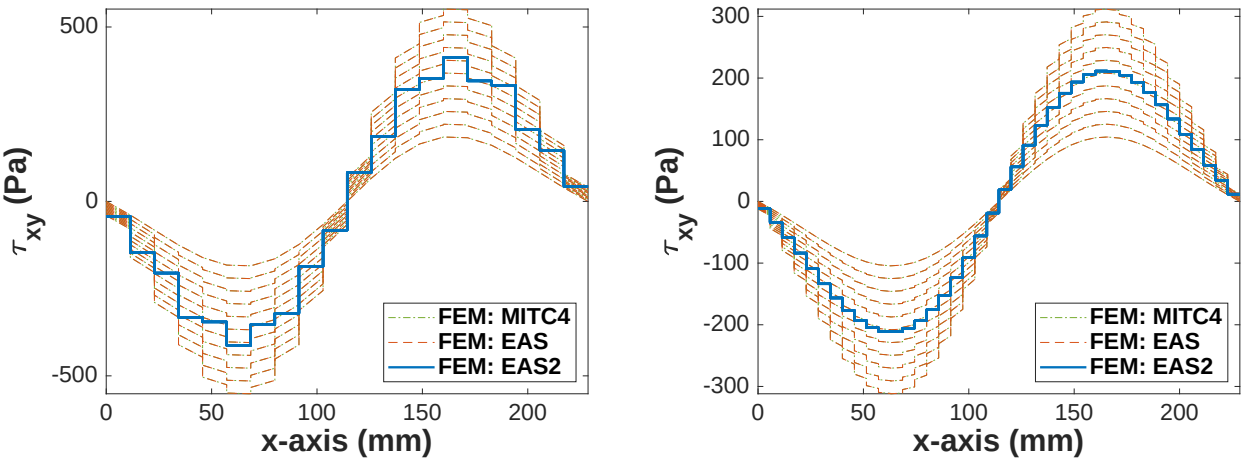

Figure 5.7: The in-plane shear stress τ_{xy} of the MITC4 and EAS models at the top of the plate for the cylindrical bending plate problem using (a) the normal mesh and (b) the refined mesh. The multiple plots of the MITC4 and EAS1 models were generated by changing the y-coordinates of the stress τ_{xy}. The plots of the EAS2 model obtained at these y-coordinates were identical.

interpolate the true solutions at a significantly lower computational cost.

The interpretations of the displacement, rotation, and stress fields of the MITC4 and EAS models confirm that these models are free of shear locking and stress oscillations. However, these do not explain the discrepancy between the results of the MITC4, EAS1, and EAS2 models; thus, other stress fields were explored. The assumptions of the cylindrical bending problem do not allow nonzero in-plane shear stress fields τ_{xy} in the analytical solution; however, the numerical models are not completely free of the influence of the free boundaries (i.e., $\partial/\partial y$ can be nonzero). The in-plane shear stress fields of the models illustrated in Fig 5.7 provide useful information on the impact of the enhanced bending strain. The stress fields of the MITC4 and EAS1 models vary along both the x- and y-axes while the EAS2 model produces constant stress fields over the elements. This explains the reason for the discrepancy of the results between these models and the contribution of the enhanced bending strain. This work employed both enhanced bending and shear strains because constant stress fields

can guarantee the locking-free behaviors of numerical models.

5.5 Summary

In this chapter, the MITC4 and EAS methods were presented and the FSDT model was improved by incorporating these methods. Moreover, the FEM formulations for the MITC4 and EAS models were presented in detail for other researchers to employ the methods for their future works. To investigate the performance of the MITC4 and EAS models, their simulation results for the cylindrical bending problem (linear) were analyzed. The models showed good agreement with the analytical solutions; therefore, their locking-free behaviors were validated in terms of shear locking. In addition, the models produced the constant stress fields over the elements, which prevented the occurrence of stress oscillations and potential shear locking. The following chapter will discuss the effectiveness of these models in simulating geometrically nonlinear problems and alleviating membrane locking.

Chapter 6

NONLINEAR STATIC MODELING AND STRESS FIELDS OF THE POST-BUCKLED SPECIMEN

6.1 Introduction

In the previous chapter, it was demonstrated that the MITC4 and EAS models are capable of successfully alleviating shear locking for the linear static problems. However, geometrically nonlinear problems, in particular for curved structures [84], can engender another locking phenomenon called membrane locking. This chapter discusses the performance of geometrically nonlinear models and relevant locking issues.

There have been recent efforts for geometrically nonlinear static analysis using the EAS method [13, 40, 65, 71]. All of these studies focused on composite structures and investigated locking-free models in displacement fields through patch tests and comparison with numerical results available in the literature. None of them, however, validated their models based on experimental data or evaluated their performance in terms of stress analysis. To address this issue, this work focuses on developing locking-free, geometrically nonlinear models, which are validated by comparing their performance with the experimental results presented in Chapter 2 and by analyzing global stress fields. In addition, the impact of the 11-mode interpolation (see Eq (5.81)) on the nonlinear terms of the membrane strains, which is not covered in the aforementioned works, is investigated.

This chapter presents a methodology for static numerical modeling of the post-buckled plate specimen (see Fig 2.3). The MITC4 and EAS methods are utilized for the modeling and their performance is evaluated in terms of locking by investigating their displacement and stress fields and first-mode buckling load and natural frequency. Using the models, the stress states of the specimen, which were not acquired from the experiment, are predicted

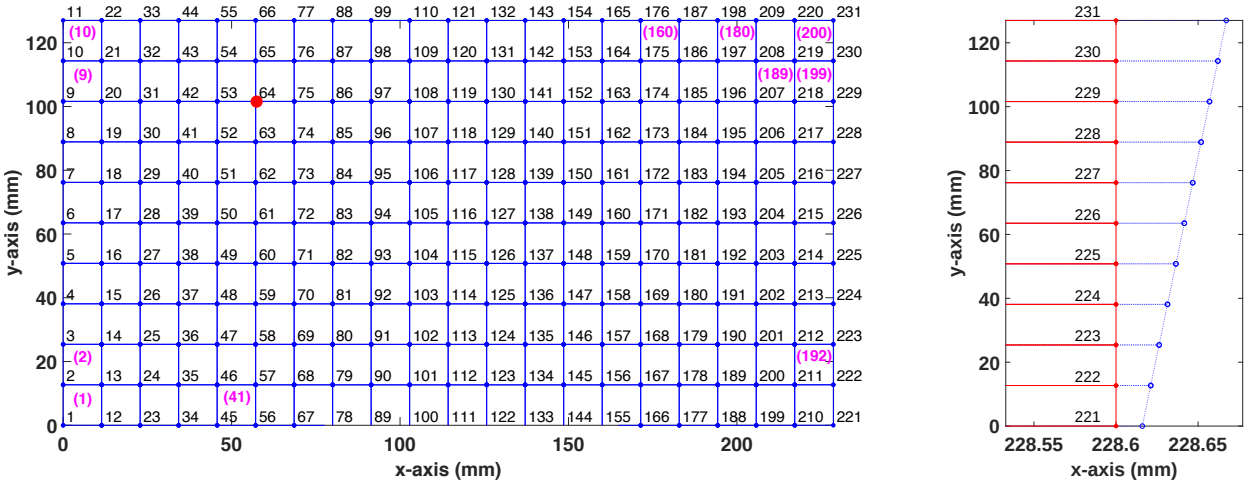

(a) (b)

Figure 6.1: The element mesh of the FSDT, MITC4, and EAS models. (a) The black numbers around the blue solid circles indicate node numbers. The pink numbers in brackets indicate element numbers used for dynamic stress analysis in Chapter 7. The red circular point around at the node number 64 corresponds to the vibrometer sampling point (see Fig 2.2b). (b) A part of the mesh is illustrated. The blue dashed lines illustrate the undeformed trapezoidal elements of the initially-flat models. The deformed elements of the post-buckled models are drawn with red solid lines.

and analyzed.

6.2 Modeling of the post-buckled specimen

6.2.1 Methodology

One of the objectives of this chapter is to develop locking-free, geometrically-nonlinear numerical models which can successfully reproduce the displacement fields of the post-buckled plate specimen (see Fig 2.3) and generate constant stress profiles on elements (but possibly discontinuous at the interfaces between the elements) to satisfy the stress recovery condition of assumed strain methods [80] at the center of each element (see Section 5.4). In addition, the models developed in this chapter are intended to be used to investigate their dynamic response and corresponding stress states; thus, it is important to employ efficient element

meshes, which can capture global displacement and stress fields with reasonable accuracy and computational cost.

For locking-free behaviors, the MITC4 and EAS methods were adopted. Using in-house FEM codes written using MATLAB, nonlinear MITC4 and EAS models were generated. The EAS models adopted the seven- and eleven-parameter interpolations (see Eqs (5.80) and (5.81), respectively) for membrane strains and are named EAS7 and EAS11, respectively. In addition, the interpolation functions in Eqs (5.80) and (5.82) were applied to bending and shear strains, respectively. For comparison, a nonlinear FSDT model also was generated using bilinear elements.

These models adopted the same element mesh as the CLPT model (see Fig 3.4) because the model successfully captured the spatio-temporal complexity of the dynamic response of the post-buckled specimen. In addition, the modeling result of the cylindrical bending problem in Section 5.4 showed that the element size of the CLPT model, which the normal mesh for the problem adopted, was enough to capture the displacement and stress fields (for the first mode) of the plate strip having the same span as the post-buckled specimen (i.e., $a = 228.6$ mm). The element mesh used for the FSDT, MITC4, and EAS models is illustrated in Fig 6.1. Like the CLPT model, the element mesh was composed of rectangular elements; however, the elements surrounded by the nodes number 210 to 231 (see Fig 6.1b) were extended to allow for in-plane displacement during buckling process. These extended lengths were adjusted through a trial-and-error basis to match the DIC measurement of the asymmetrically-buckled shape of the specimen (see Fig 2.3). The resulting lengths of the MITC4 and EAS models were shorter than those of the CLPT model due to additional transverse displacement induced by shear deformation[1]. The FSDT model used for comparison adopted the same mesh. The numerical buckling process described in Section 3.3 was applied to the MITC4, EAS, and FSDT models.

[1]In Fig 6.1b, the extended lengths of the MITC4 and EAS models are 16.03 μm and 67.16 μm for the bottom and top, respectively (i.e., the nodes number 221 and 231, receptively), while those of the CLPT model were 16.70 μm and 69.96 μm for the bottom and top, respectively.

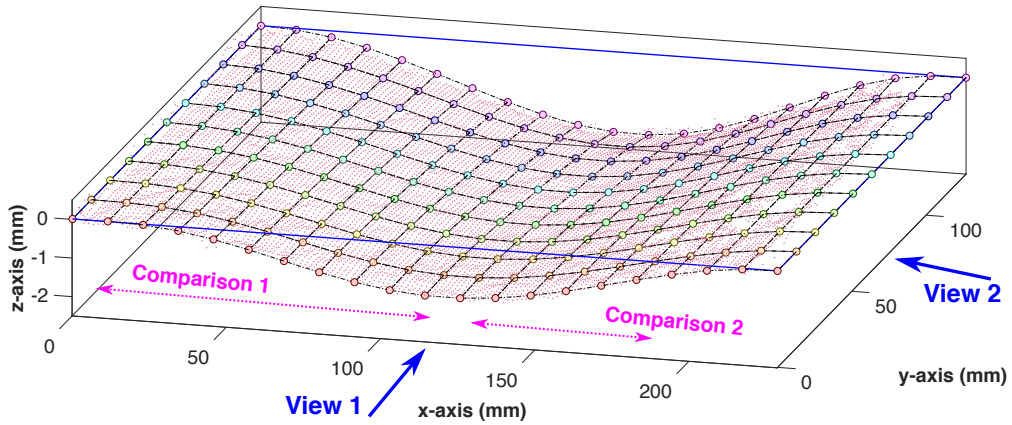

Figure 6.2: The EAS11 model of the post-buckled specimen is superimposed on the DIC measurement shown in Fig 2.3. The z-axis is exaggerated for interpretation of the buckled depth. The blue rectangle indicates the position of the initially-flat model.

6.2.2 Model comparison

The EAS11 model of the post-buckled specimen is illustrated in Fig. 6.2. The MITC4 and EAS7 models look identical to the EAS11 model in this figure scale and thus only the latter is illustrated in the figure. The FSDT model did not buckle with the current geometric configuration and thus the model requires longer extension of the trapezoidal elements to generate larger in-plane stress resultants for buckling.

The displacement fields of the MITC4 and EAS models are quantitatively compared with the DIC measurement of the post-buckled specimen in Figs 6.3 and 6.4. The EAS7 and EAS11 models produced identical results and thus they were illustrated together as a single figure. Despite the irregularity of some of the DIC measurements, all of the models showed an excellent agreement with the specimen's buckled shape. Therefore, the models successfully captured the spatial complexity of the post-buckled specimen.

For further comparison, the first-mode buckling loads and natural frequencies of the models were investigated as tabulated in Table 6.1. The FSDT model incorporating no remedy for locking showed a significantly higher buckling load and natural frequency than the other models due to the over-stiffening phenomena discussed in Section 4.4. The MITC4

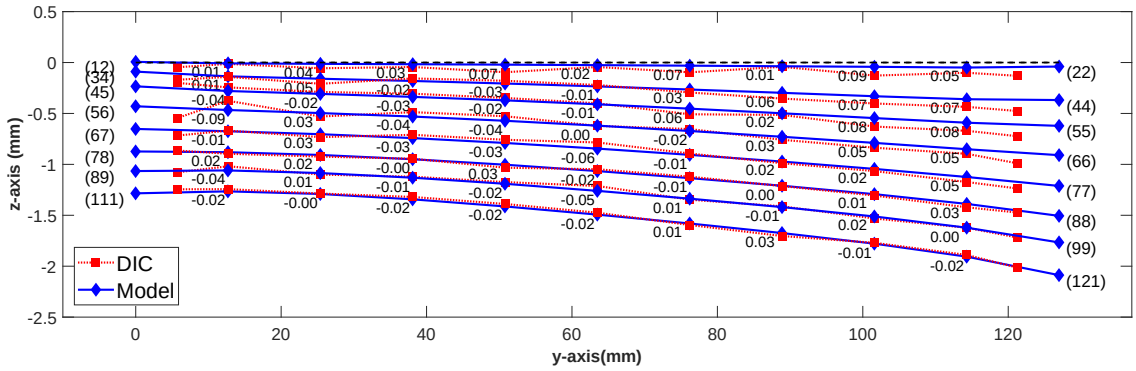

(a)

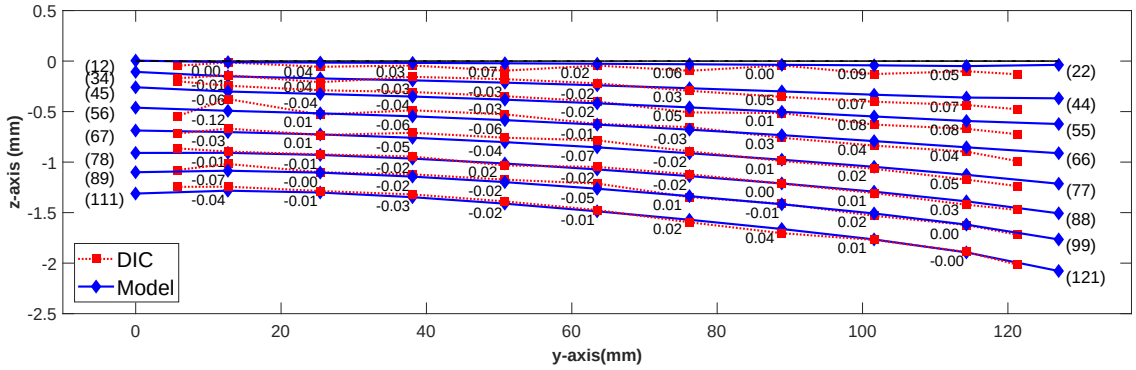

(b)

Figure 6.3: The comparison between the buckled shapes of the models and specimen for the nodes in Comparison 1 in View 2 (see Fig 6.2). The numbers in brackets indicate the node numbers of the model. The discrepancies (the nodal values minus the DIC measurements) are written in a millimeter unit (mm) around the nodes. (a) The MITC4 model. (b) The EAS7 and EAS11 models.

model showed a marginally higher buckling load and natural frequency than the EAS models. This implies that the MITC4 model slightly overestimates its stiffness when compared to the EAS models. The two EAS models exhibited the identical buckling loads and natural frequencies.

To investigate the discrepancies between the results of the MITC4 and EAS models, their stress fields were analyzed as shown in Figs 6.5 to 6.7. The MITC4 model showed no oscillations in transverse shear stress fields (see Fig 6.5a for τ_{xz}) but strong oscillations in

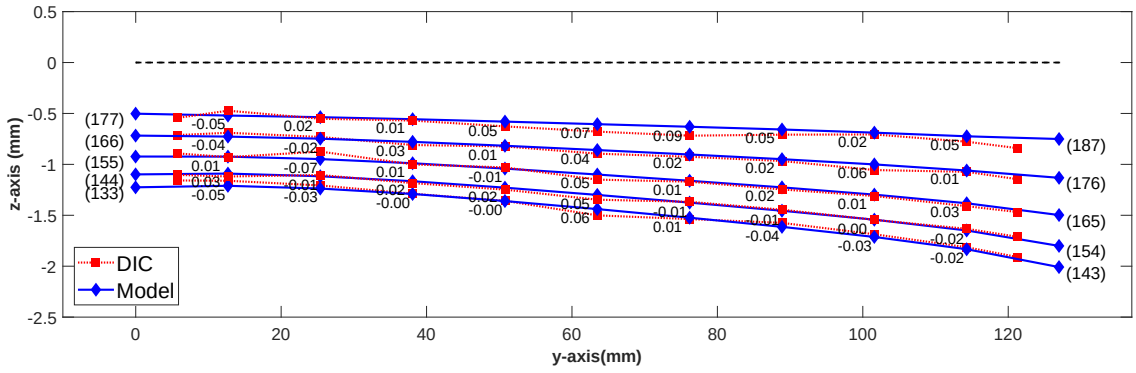

(a)

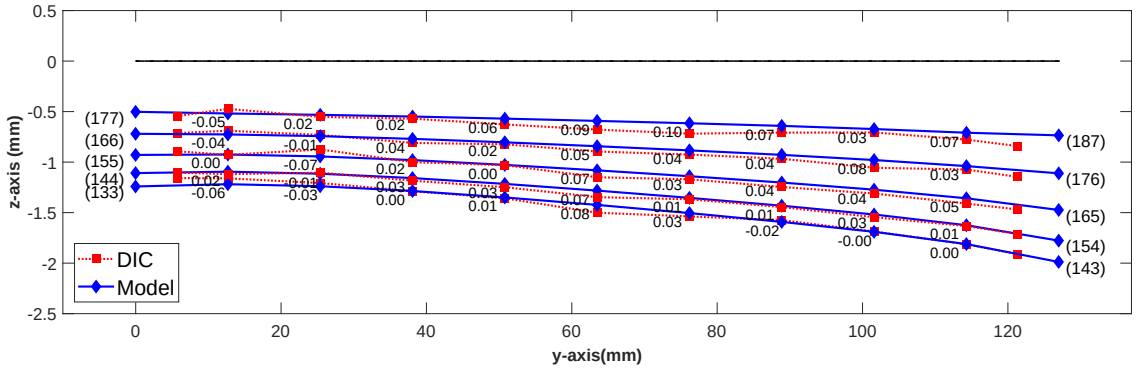

(b)

Figure 6.4: The comparison between the buckled shapes of the models and specimen for the nodes in Comparison 2 in View 2 (see Fig 6.2). The numbers in brackets indicate the node numbers of the model. The discrepancies (the nodal values minus the DIC measurements) are written in a millimeter unit (mm) around the nodes. (a) The MITC4 model. (b) The EAS7 and EAS11 models.

all of the membrane stress fields (σ^0_{xx}, σ^0_{yy}, τ^0_{xy}) as illustrated in Fig 6.5b for σ^0_{yy}. For further investigation of the impact of membrane locking, uniformly distributed transverse loading was applied to the models of the buckled specimen. The resulting load-displacement curves are illustrated in Fig 6.8. The EAS7 and EAS11 models exhibited the identical curves and thus a single curve is drawn for the models in the figure. The transverse displacement w of the midpoint was measured from the buckled position of the plate. At q =-82 g, the transverse displacements of the MITC4 and EAS models were -0.8585 and -0.8705 mm, respectively

Field	Experiment	FEM: FSDT	FEM: MITC4	FEM: EAS7	FEM: EAS11
N_{CR} (N/m)	-	17529	857.4	852.9	852.9
f_{11}^{flat} (Hz)	73	305.6 (318.6 %)	68.3 (6.44 %)	68.1 (6.71 %)	68.1 (6.71 %)
$f_{11}^{\mathrm{buckled}}$ (Hz)	113	-	106.9 (5.40 %)	106.3 (5.93 %)	106.3 (5.93 %)

Table 6.1: The first-mode buckling loads N_{CR} and natural frequencies f_{11} of the FSDT, MITC4, and EAS models. The natural frequencies of the initially-flat and buckled configures are denoted by f_{11}^{flat} and $f_{11}^{\mathrm{buckled}}$, respectively. The values in the parentheses indicate the percent error of the numerical predictions. The experimental value of buckling load N_{CR} was not measured.

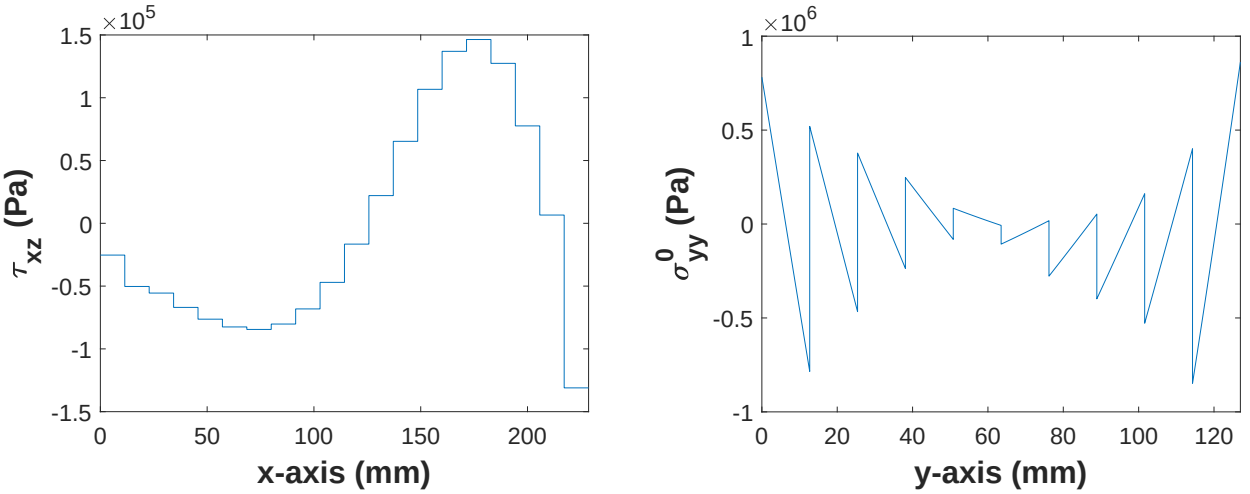

(a) (b)

Figure 6.5: The stress fields of the MITC4 model. (a) The transverse shear stress τ_{xz} at $y = 120.65$ mm along the x-axis. (b) The membrane stress σ_{yy}^{0} at $x = 97.15$ mm along the y-axis.

and thus the MITC4 model demonstrated marginal over-stiffening compared to the EAS models. Therefore, the MITC4 model can be deemed to be subject to membrane locking, which seems to be responsible for the aforementioned over-stiffening phenomena observed in N_{CR}, f_{11}^{flat}, and $f_{11}^{\mathrm{buckled}}$ and the erroneous membrane stress fields. However, the impact

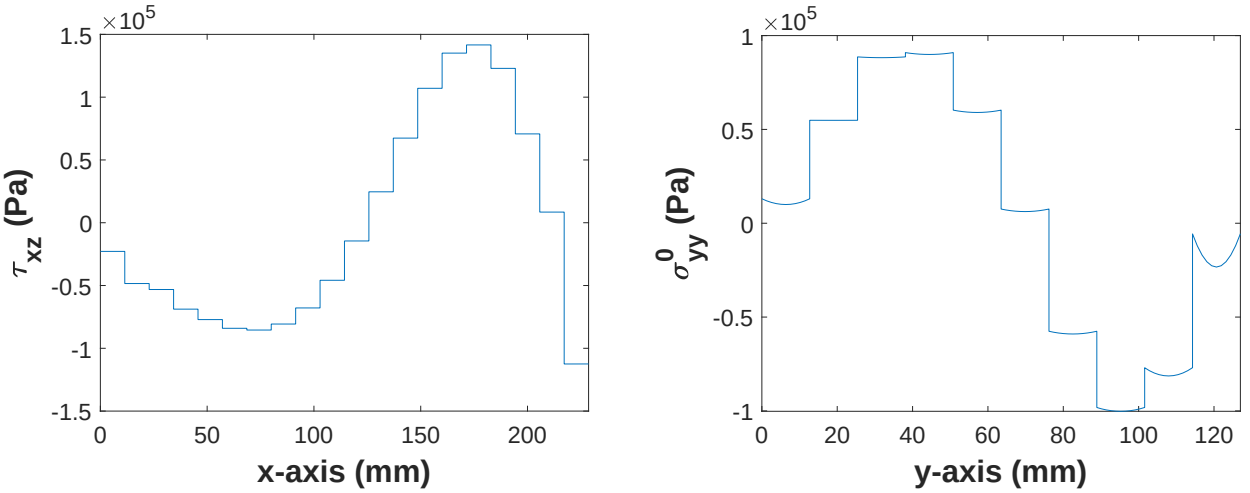

(a) (b)

Figure 6.6: The stress fields of the EAS7 model. (a) The transverse shear stress τ_{xz} at $y = 120.65$ mm along the x-axis. (b) The membrane stress σ^0_{yy} at $x = 97.15$ mm along the y-axis.

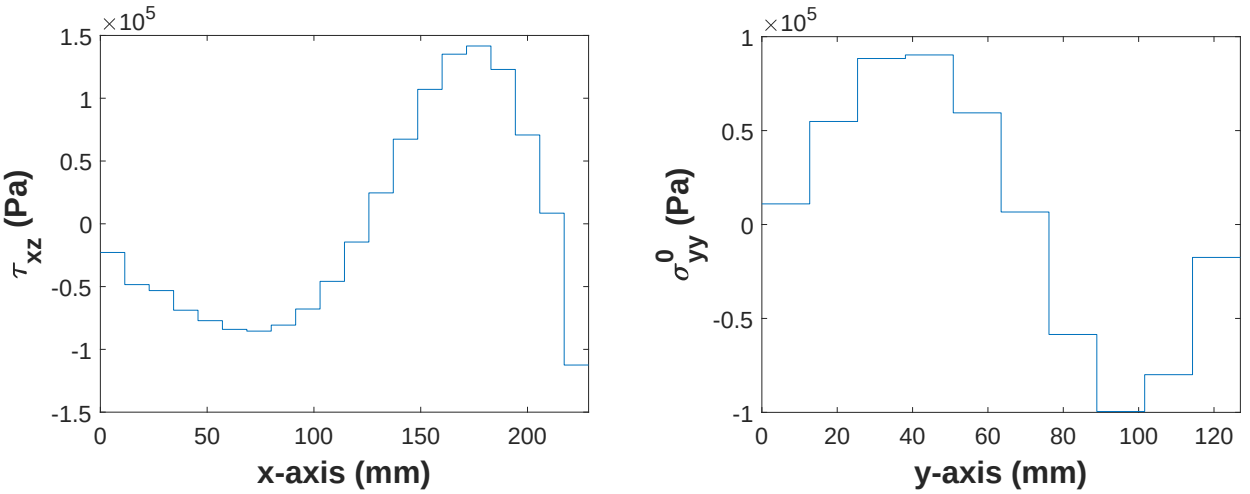

(a) (b)

Figure 6.7: The stress fields of the EAS11 model. (a) The transverse shear stress τ_{xz} at $y = 120.65$ mm along the x-axis. (b) The membrane stress σ^0_{yy} at $x = 97.15$ mm along the y-axis.

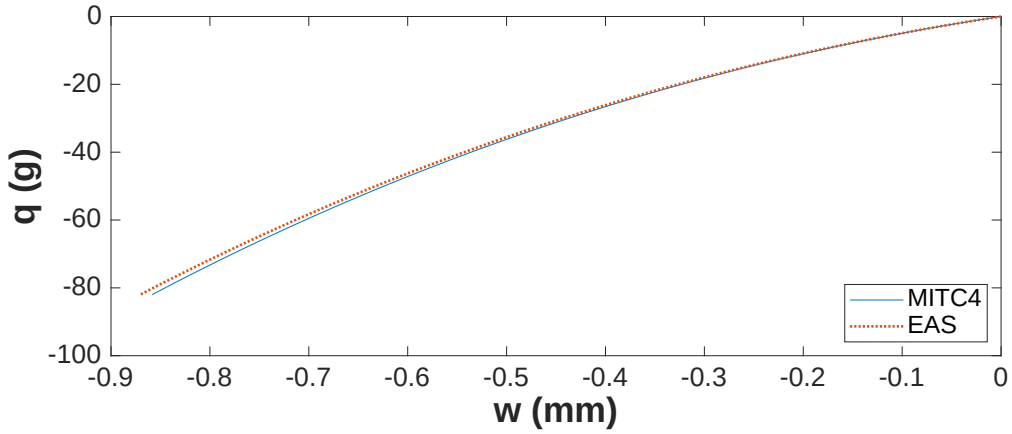

Figure 6.8: The midpoint displacements of the MITC4 and EAS models of the post-buckled specimen under uniformly distributed transverse loading q.

of membrane locking on the global response of the MITC4 model (a shallow arch) is not as significant as the effect of shear locking shown in Section 4.4.2 for a flat (or pre-buckled) plate. For deep arches, on the other hand, membrane locking could possibly make significant impact on their global response.

The EAS7 and EAS11 models generated the identical transverse shear stress fields as shown in Figs 6.6a and 6.7a. However, the in-plane stress fields of the EAS7 model exhibit a strong influence of the quadratic (nonlinear) terms in the von Kármán strains as illustrated in Fig 6.6b for σ^0_{yy}. For example, as shown in Eq (4.5), the membrane strain $\varepsilon^{(0)}_{yy}$ is given by

$$\varepsilon^{(0)}_{yy} = \frac{\partial v_0}{\partial y} + \frac{1}{2}\left(\frac{\partial w_0}{\partial y}\right)^2. \tag{6.1}$$

The 7-mode interpolation successfully enhances the linear term $\frac{\partial v_0}{\partial y}$ but not the quadratic term $\left(\frac{\partial w_0}{\partial y}\right)^2$. This result is not surprising given that the interpolation consists of linear terms. Therefore, the stress profiles are not consistently maintained constant on the elements, making the EAS7 model susceptible to stress oscillations and membrane locking. On the other hand, the EAS11 model produced constant in-plane stress fields on its elements as illustrated in Fig 6.6b for σ^0_{yy}. Therefore, the quadratic terms in the 11-mode interpolation

Model	CLPT	MITC4	EAS7	EAS11
Normalized cost	∼3	∼0.5	∼0.9	1

Table 6.2: The computational costs of the models. The costs were normalized using the cost of the EAS11 model.

adopted in the EAS11 model successfully enhance the membrane strains. The contribution of the 11-mode interpolation to enhancing nonlinear strains is not discussed in the literature to the best of the author's knowledge. As mentioned at the beginning of this section, such constant stress profiles are required to satisfy the stress recovery condition at the center of each element. Therefore, the EAS11 model ensures global behaviors free of shear and membrane locking and thus was chosen over the other models for stress analysis and dynamic simulation.

The computational costs of the models presented herein are compared in Table 6.2. The costs were approximately estimated based on the computation time spent simulating the buckling process to reconstruct the post-buckled specimen using identical computing power. The CLPT model requires the highest cost due to implementation of cubic elements for semi-C^1 continuity and transformation of the nodal DOFs between the real and reference elements (see Section 3.2.2). The MITC4 model shows the lowest cost because the model employs bi-linear elements for C^0 continuity and requires no additional DOF to control shear locking of the FSDT model. The EAS models involve additional DOFs to enhance assumed strains and thus require higher computational costs than the MITC4 model. The extra four modes of the EAS11 model, however, cause a marginal increase in the cost compared to the EAS7 model.

6.3 Results: stress fields of the post-buckled specimen

In this section, the stress states of the post-buckled specimen are predicted with the EAS11 model. Unfortunately, these results are not directly comparable with experimental data. In

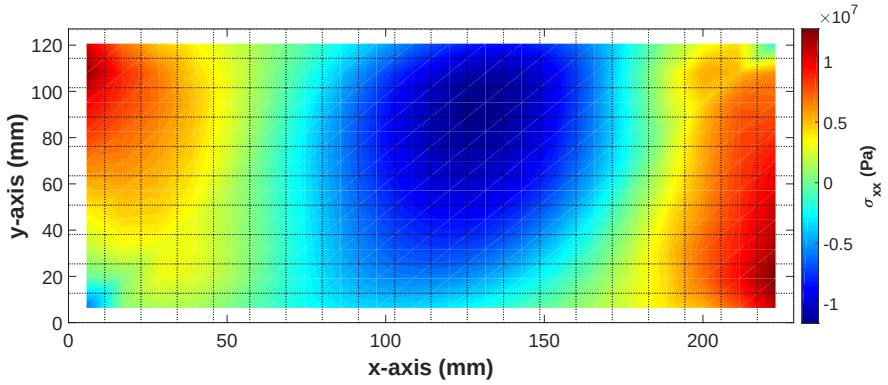

(a)

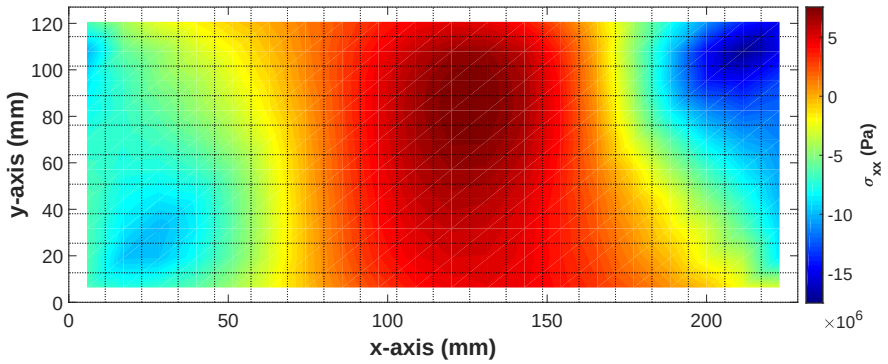

(b)

Figure 6.9: In-plane normal stress field σ_{xx} predicted by the EAS11 model for the post-buckled specimen. (a) σ_{xx} at the top of the plate ($z = \frac{h}{2}$). (b) σ_{xx} at the bottom of the plate ($z =$-$\frac{h}{2}$).

future work, experimental data of strain fields in composite structures will be collected using a DIC system for validation of strain (and stress) fields predicted with the EAS11 model.

As discussed in the previous section, the constant stress fields on the elements of the EAS11 model are expected to coincide with (or closely match) the true values at the center of its elements. Therefore, using the stress fields obtained at the center of the elements, the global stress fields are interpolated as illustrated in Figs 6.9 to 6.13. The stress fields near the boundaries were disregarded (or were not extrapolated). The in-plane strain fields have their maximum and minimum values at the top and bottom of the plate; for example, as

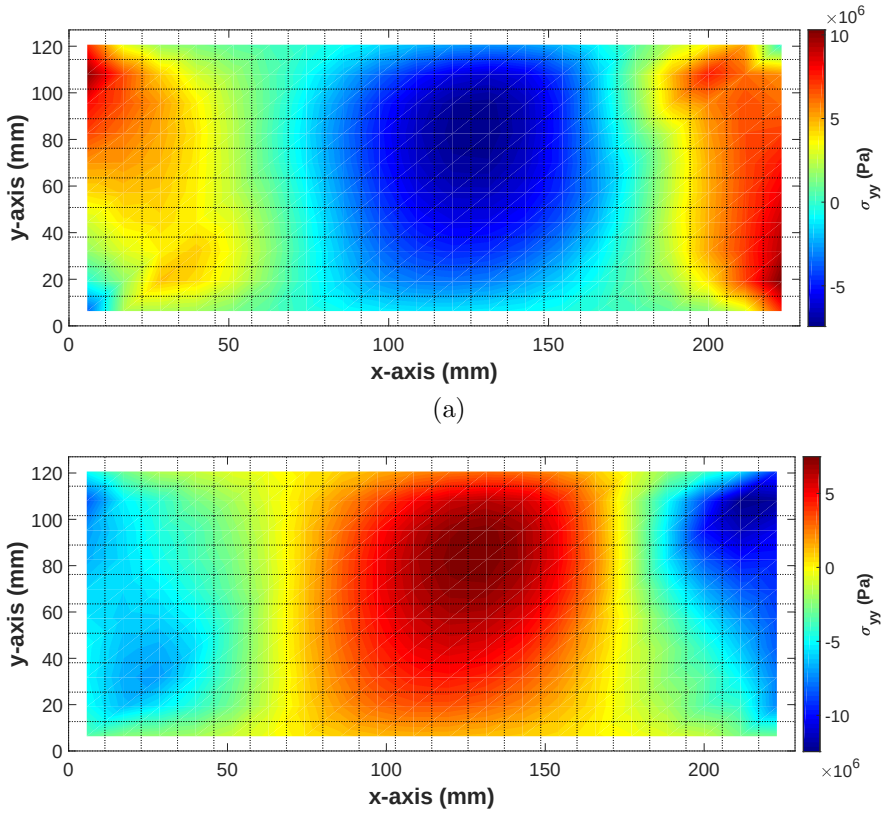

Figure 6.10: In-plane normal stress field σ_{yy} predicted by the EAS11 model for the post-buckled specimen. (a) σ_{yy} at the top of the plate ($z = \frac{h}{2}$). (b) σ_{yy} at the bottom of the plate ($z =$-$\frac{h}{2}$).

shown in Eq (4.4), in-plane normal strain ε_{xx} is given by

$$\varepsilon_{xx} = \varepsilon_{xx}^{(0)} + z\varepsilon_{xx}^{(1)}. \tag{6.2}$$

Therefore, the maxima and minima of the in-plane stress fields, which can be interpreted as the maximum tensile and compressive stresses respectively for the normal stresses σ_{xx} and σ_{yy}, can be obtained on the top and bottom surfaces of the plate as illustrated in Figs 6.9 to 6.11. On the other hand, the transverse shear stress fields of the EAS11 model (see Figs 6.12 and 6.13) are uniform through thickness due to the FSDT assumption on the

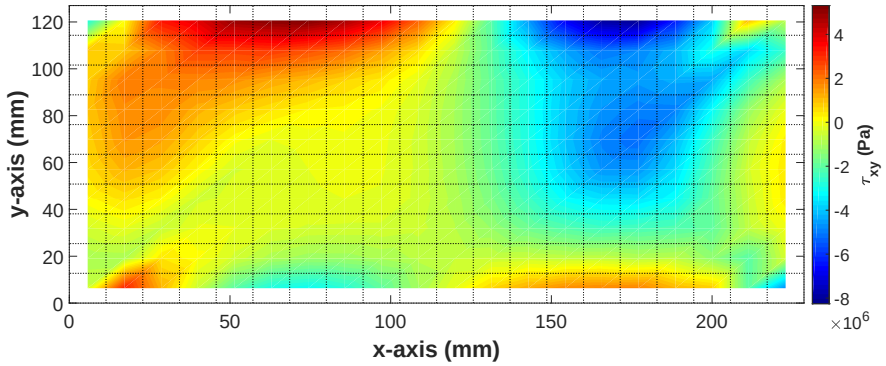

(a)

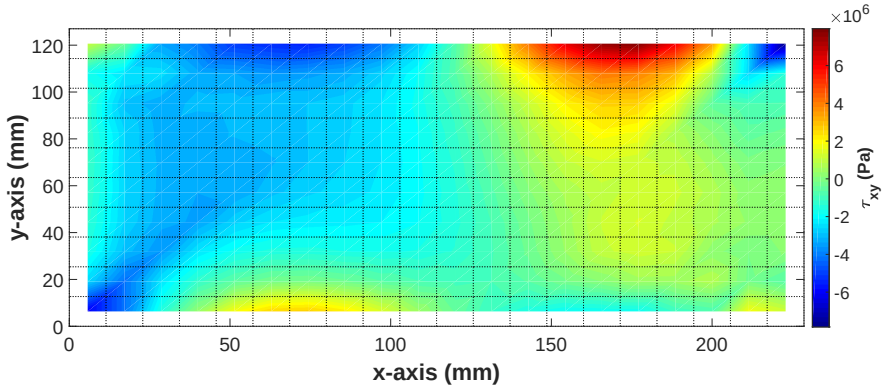

(b)

Figure 6.11: In-plane shear stress field τ_{xy} predicted by the EAS11 model for the post-buckled specimen. (a) τ_{xy} at the top of the plate ($z = \frac{h}{2}$). (b) τ_{xy} at the bottom of the plate ($z =$-$\frac{h}{2}$).

distribution of the transverse shear strain fields through thickness (see Eqs (4.8) and (4.9)). The maximum in-plane tensile and compressive normal stresses were predicted to occur near the midspan and the moving boundary. The maximum in-plane and transverse shear stresses are anticipated along the free boundary at $y = 127.0$ mm where the largest buckled depth is observed from the experimental measurement.

Considering that these maximum stress values are expected to be observed on the surfaces (i.e., the x–y surfaces at $z = \pm\frac{h}{2}$ and the x–z surface at $y = 127.0$ mm) of the post-buckled specimen, once the experimental measurement of strain fields on these surfaces is obtained using DIC, these stress values could be verified.

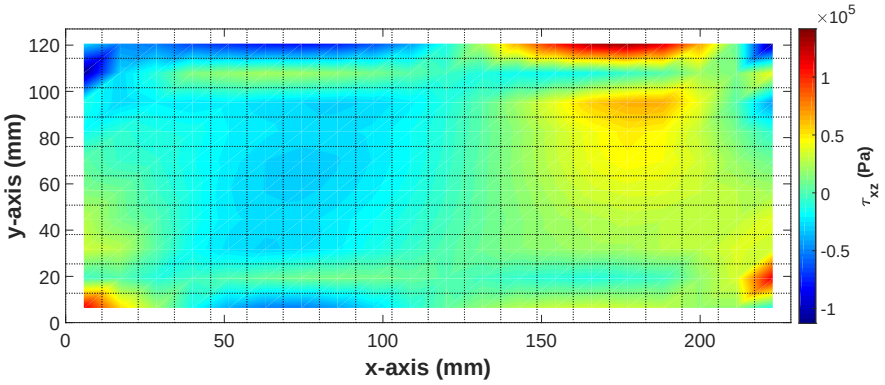

Figure 6.12: Transverse shear stress field τ_{xz} predicted by the EAS11 model for the post-buckled specimen.

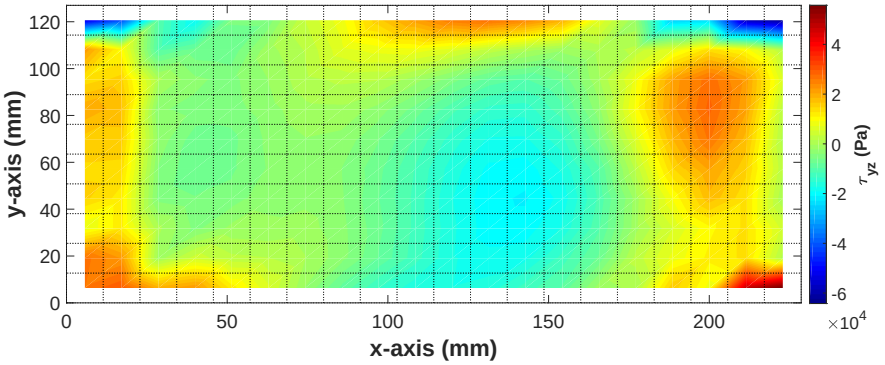

Figure 6.13: Transverse shear stress field τ_{yz} predicted by the EAS11 model for the post-buckled specimen.

6.4 Summary

This chapter presented the performance of geometrically nonlinear MITC4 and EAS models and the relevant locking phenomena.

For validation, the displacement fields, buckling load, and natural frequency of these models were compared to the experimental data. The comparison showed that these models successfully reproduced the post-buckled specimen. However, the MITC4 model, which incorporated no remedy for membrane locking, exhibited strong oscillations of membrane stress fields. This potentially leads to membrane locking of the MITC4 model. Consequently,

the transverse displacement, buckling load, and the natural frequency of the MITC4 model showed the impact of over-stiffening induced by membrane locking. However, it was shown that for shallow arches, membrane locking does not engender locking (or over-stiffening) as severe as shear locking (even though the former still can cause an adverse effect on the accuracy of modeling). In addition, the contribution of the 11-mode interpolation for enhanced assumed strains to nonlinear membrane stress fields was discussed. It was shown that this interpolation is more effective than the commonly-used 7-mode interpolation to achieve constant membrane stress fields on elements. The locking-free behavior ensured by the 11-mode interpolation may be important in cases of extreme deformations involving large membrane strains. Finally, the stress states of the post-buckled specimen were anticipated using the EAS11 model which adopted the 11-mode interpolation for the enhanced membrane strains.

Given that previous works in the literature validated their geometrically-nonlinear EAS models relying only on the displacement fields of numerical data available in the literature, the model validation of this work based on the experimental data can be deemed more robust than that of those works. In addition, this work adds to the literature a new perspective on enhancing nonlinear strains with the 11-mode interpolation and extends the studies of EAS modeling to global stress analysis. In future work, strain and stress fields predicted with the EAS model will be validated through experimental full-field characterization of strain fields in composite structures.

In the following chapter, the dynamic simulation result of the EAS11 model is presented and its spatio-temporal complexity is evaluated in the harmonic forcing parameter space. The impact of the nonlinear dynamic behaviors, in particular that of snap-through, on the stress fields of the post-buckled specimen is of primary interest.

Chapter 7

SIMULATION OF NONLINEAR DYNAMICS AND STRESS FIELDS OF THE POST-BUCKLED SPECIMEN

7.1 Introduction

In the previous chapter, the post-buckled specimen was reproduced using the EAS model and its stress fields were analyzed. In this chapter, the impact of nonlinear dynamics on the stress fields of the specimen is simulated using the model.

Post-buckled composite structures under dynamic loading can experience potentially high strains (and consequent high stresses) due to large deformations, which were observed in the snap-through cases in Chapters 2 and 3. These phenomena can possibly accelerate initiation and propagation of delamination in these structures, thereby posing a potential threat to their structural integrity. However, regarding the impact of nonlinear dynamics on the stress fields of structures, very little research has been done. To address this issue, this work investigates through dynamic simulation the stress fields induced by nonlinear dynamic behaviors of post-buckled structures including snap-through.

In this chapter, the dynamic response of the EAS model is first validated in displacement fields using snap-through boundaries in the HFP space. The stress fields of the post-buckled plate are simulated in single-well and snap-through cases to investigate the impact of large deformations induced by snap-through on the stress fields. In addition, these stress fields are compared to those exhibited by a flat (or pre-buckled) plate to highlight the amplification caused by buckling.

7.2 Dynamic simulation and validation of EAS model

7.2.1 Methodology for dynamic simulation

The EAS11 model introduced in the previous chapter was used for dynamic simulation and is simply called the EAS model in this chapter. For the simulation, the methodology used for the CLPT model (see Section 3.5.1) was adopted. The Newmark-beta method, particularly the average acceleration method $\beta = \frac{1}{4}$, was applied to the model for time integration. Within each time step t_n, the Newton-Raphson method was used to solve a nonlinear equation which resulted from the time integration. These steps were processed using MATLAB. The time step size Δt for each loading scenario was determined by Eq (3.28), which is reproduced here:

$$\Delta t = \frac{1}{b \times f} = \frac{1}{320 \times f} \text{ sec}, \tag{7.1}$$

where f is a forcing frequency and b is the number of time steps per loading cycle (for this work, $b = 320$). To include damping in the model, the Rayleigh damping method was applied to the nonlinear FEM in Eq (4.38). The Rayleigh damping matrix $\mathbf{C}$ for the CLPT model (see Eq (3.26)) was also adopted for the EAS model with $\omega_1 = 668.0$ rad/sec and $\omega_6 = 2536.0$ rad/sec.

7.2.2 Snap-through boundaries of the EAS model

The dynamic response of the EAS model under harmonic loading was simulated with at-rest initial conditions (see Section 3.5.3 for the discussion on the at-rest and high-energy initial conditions). The forcing parameters were chosen to find the low-frequency (or left) snap-through boundary (see Section 3.5.4 for the discussion on the low-frequency snap-through boundary) in the HFP space.

The dynamic simulation results are illustrated in Fig 7.1 with the experimental boundaries and the numerical ones of the CLPT model (see Fig 3.15). Only steady-state response was

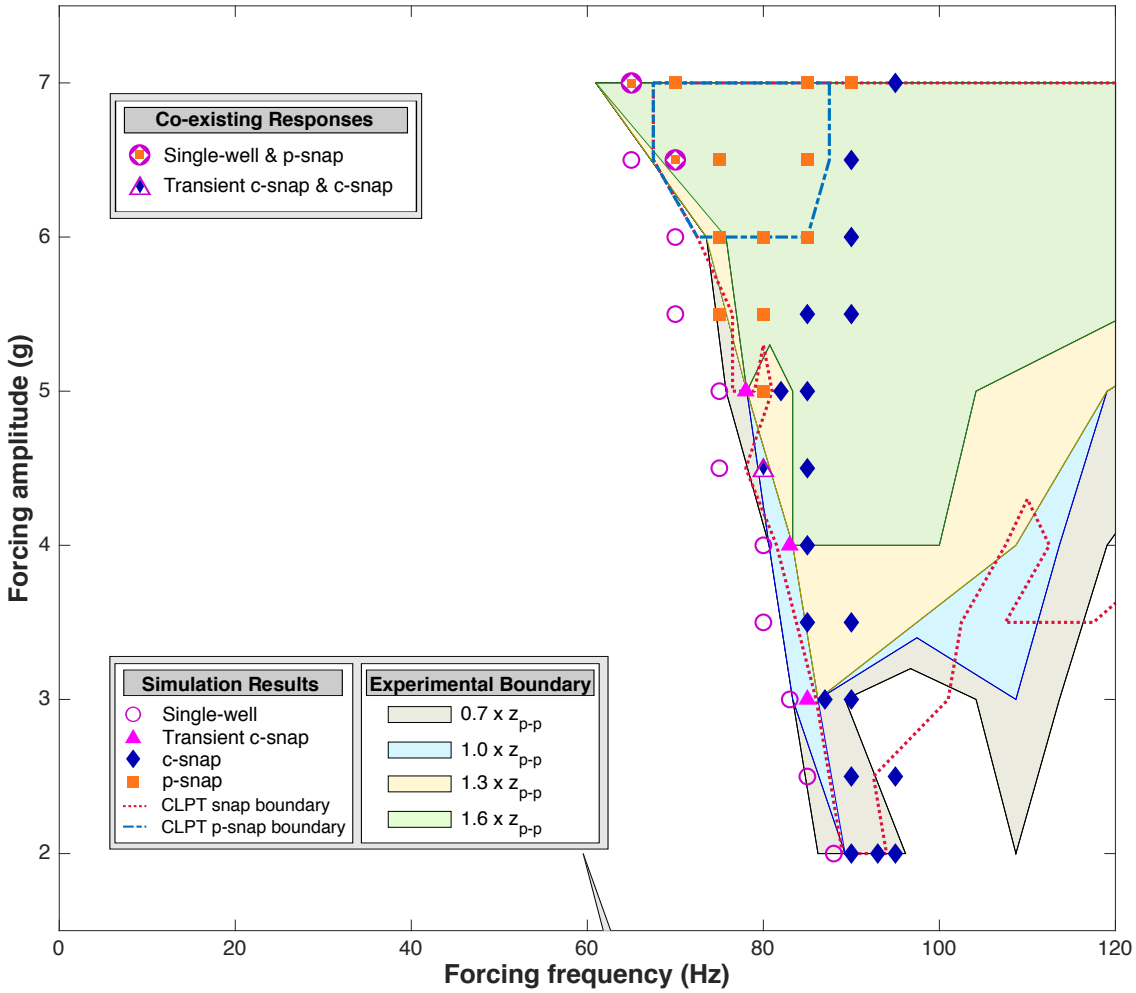

Figure 7.1: The dynamic simulation results of the EAS model with at-rest initial conditions are illustrated in the HFP space. The experimental and CLPT boundaries are reproduced from Fig 3.15.

considered to determine occurrence of snap-through. The response of the EAS model at 3 g–87 Hz switched from c-snap to single-well at $t = 2.3$ sec. However, the response of the CLPT model at the parameter (c-snap) was simulated up to $t = 2.0$ sec and thus the response of the EAS model was marked as c-snap at the parameter for purpose of comparison. The EAS model predicted a larger p-snap region than that of the CLPT model at 5–7 g, while the EAS model exhibited transient c-snap at some parameters at 3–5 g with which

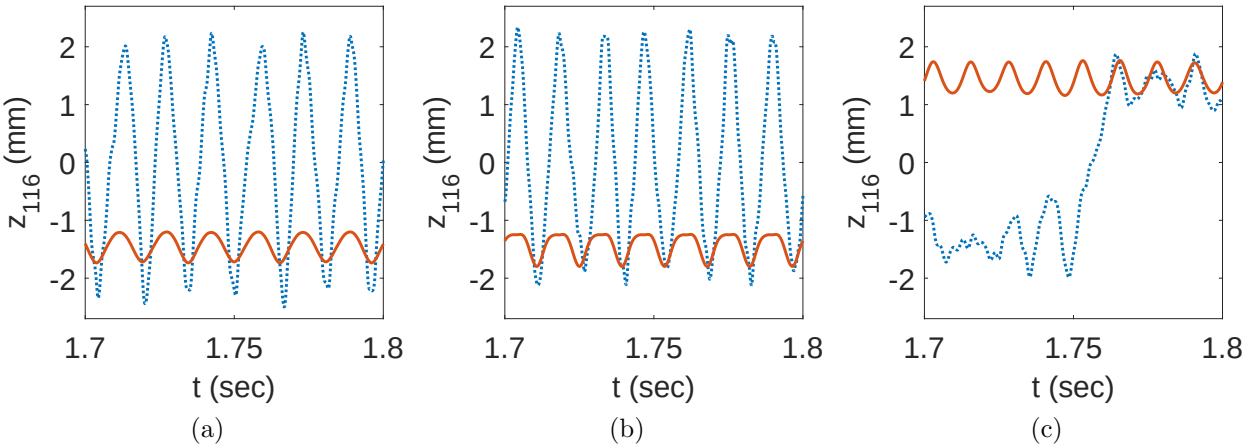

Figure 7.2: The simulated time series of co-existing responses z_{116} of the EAS model under (a) 7 g–65 Hz, (b) 6.5 g–70 Hz, and (c) 4.5 g–80 Hz harmonic loading with at-rest (red solid lines) and high-energy (blue dotted lines) initial conditions.

the CLPT model showed steady-state c-snap. The transient c-snap response of the EAS model is observed on the experimental boundary at the threshold $1.0 \times z_{\text{p-p}}$ where $z_{\text{p-p}}$ is the peak-to-peak static buckled depth of the post-buckled specimen at the vibrometer sampling point and is elaborated in Section 3.5.3. However, this transient c-snap response could have been counted as c-snap in the experimental results (see Fig 2.9) due to the difficulties in identifying transient response from the vibrometer data having short time frames at each forcing frequency. Moreover, as shown in Fig 3.17, single-well and transient c-snap along the low-frequency boundary can switch to steady-state p-snap with high-energy initial conditions. The co-existing responses of the EAS model are illustrated in Fig 7.2. In the loading cases 7 g–65 Hz, 6.5 g–70 Hz, and 4.5 g–80 Hz, the model showed steady-state single-well response with at-rest initial conditions. With high-energy initial conditions, however, the model produced steady-state p-snap at 7 g–65 Hz and 6.5 g–70 Hz and steady-snap c-snap at 4.5 g–80 Hz.

Therefore, the EAS model showed good agreement with the experimental and CLPT results overall and this result provides validation of the model.

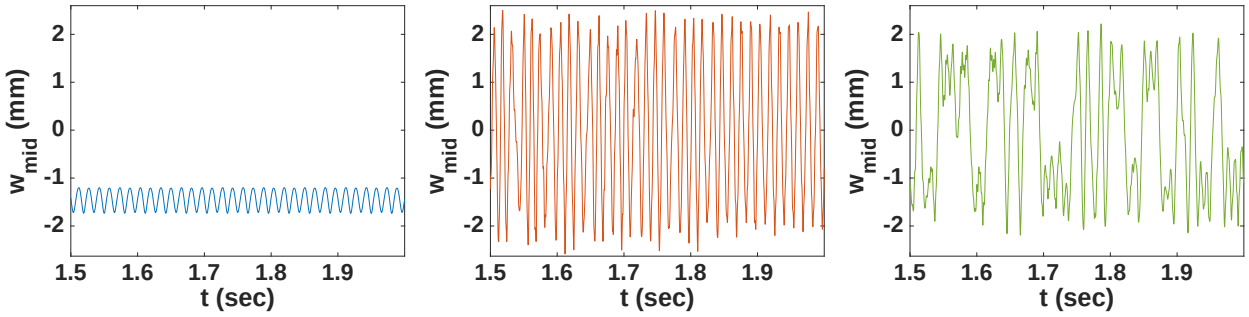

Figure 7.3: The time series of the transverse displacement of the midnode (w_{mid}, the node number 116 in Fig 6.1) under 7 g harmonic loading at: (a) 65 Hz (single-well), (b) 70 Hz (c-snap), and (c) 95 Hz (p-snap).

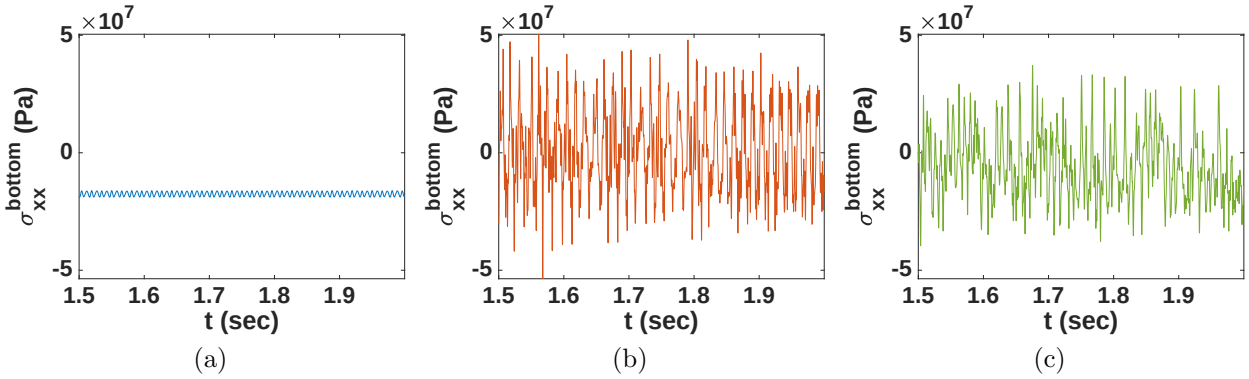

Figure 7.4: The time series of the in-plane normal stress σ_{xx} of the EAS model at the bottom of the plate ($z = -\frac{h}{2}$) under the response illustrated in Fig 7.3. (a) 7 g–65 Hz, Element 189. (b) 7 g–70 Hz, Element 9. (c) 7 g–95 Hz, Element 199.

7.3 Stress analysis: single-well vs. snap-through cases

In this section, the impact of snap-through on stress fields is investigated using the dynamic simulation results. The potential contribution of the amplified stresses to fatigue is also discussed.

Three forcing parameters at 7 g were chosen to obtain the three characteristic response types: 65, 70, and 95 Hz for single-well, c-snap, and p-snap responses, respectively. The

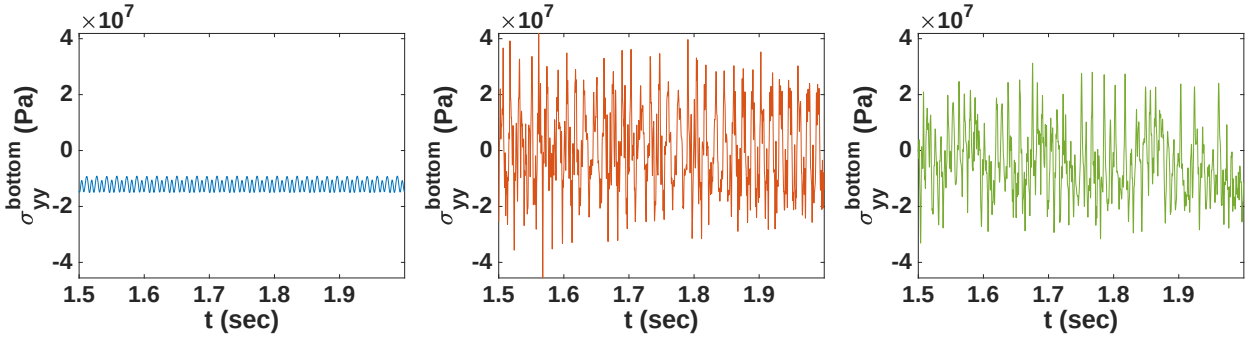

(a) (b) (c)

Figure 7.5: The time series of the in-plane normal stress σ_{yy} of the EAS model at the bottom of the plate ($z = -\frac{h}{2}$) under the response illustrated in Fig 7.3. (a) 7 g–65 Hz, Element 199. (b) 7 g–70 Hz, Element 9. (c) 7 g–95 Hz, Element 199.

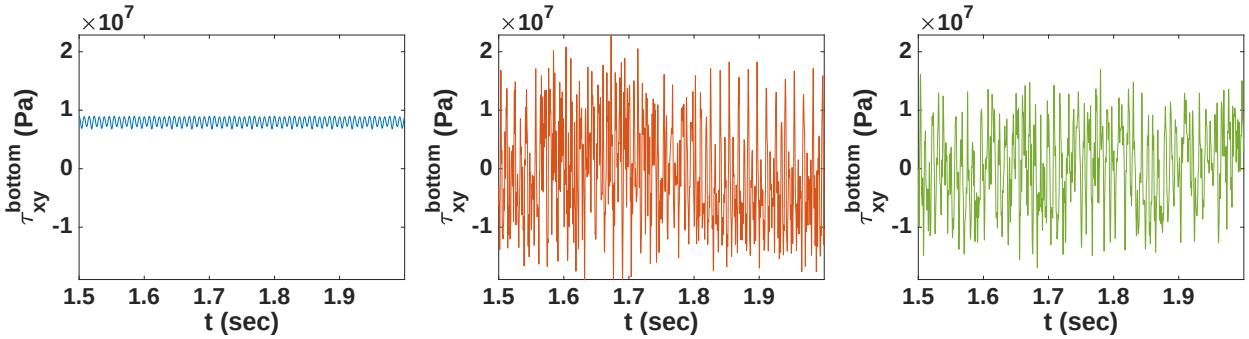

(a) (b) (c)

Figure 7.6: The time series of the in-plane shear stress τ_{xy} of the EAS model at the bottom of the plate ($z = -\frac{h}{2}$) under the response illustrated in Fig 7.3. (a) 7 g–65 Hz, Element 160. (b) 7 g–70 Hz, Element 180. (c) 7 g–95 Hz, Element 180.

transverse displacement and stress fields of the model at these parameters are illustrated in Figs 7.3 to 7.8. These plots were obtained from the steady-state response and demonstrate the maximum stress fields under the parameters. In some of the stress fields, the location of the maximum (magnitude) stresses moved with changes in the forcing parameters. For example, the maximum in-plane normal stresses σ_{yy} at the bottom of the plate at 65, 70, and 90 Hz (see Fig 7.5) were obtained on the elements number 189, 9, and 199, respectively

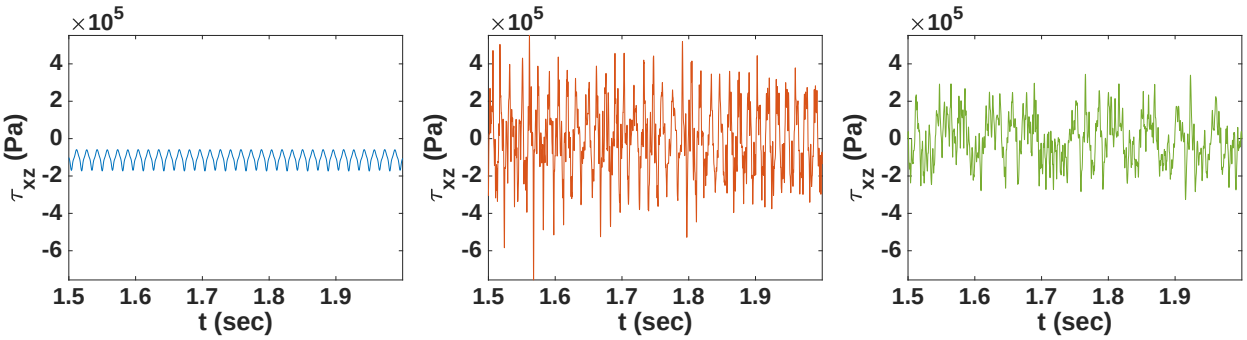

(a) (b) (c)

Figure 7.7: The time series of the transverse shear stress τ_{xz} of the EAS model under the response illustrated in Fig 7.3. (a) 7 g–65 Hz, Element 9. (b) 7 g–70 Hz, Element 9. (c) 7 g–95 Hz, Element 9.

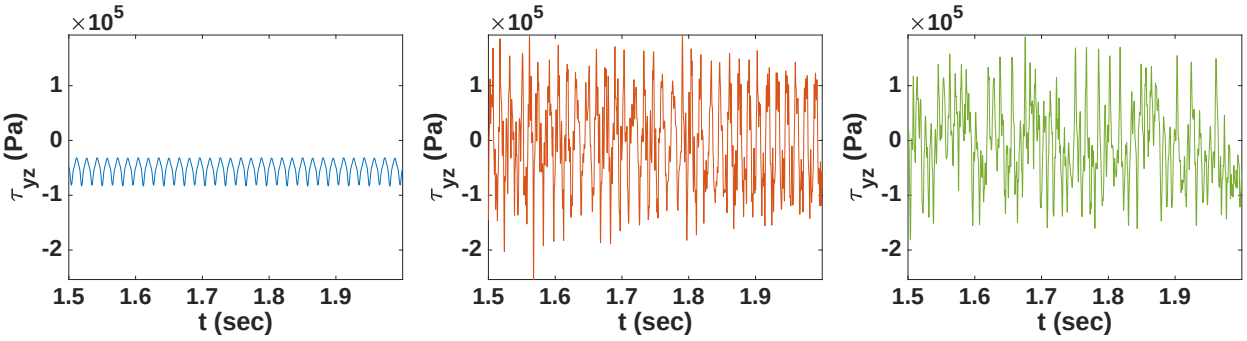

(a) (b) (c)

Figure 7.8: The time series of the transverse shear stress τ_{yz} of the EAS model under the response illustrated in Fig 7.3. (a) 7 g–65 Hz, Element 10. (b) 7 g–70 Hz, Element 10. (c) 7 g–95 Hz, Element 200.

(see Fig 6.1).

The stress fields induced by the single-well response oscillated around the static stress fields of the buckled model with relatively small amplitudes. These stress fields did not change their signs; for example, the in-plane normal stresses at the bottom of the plate (see Figs 7.4 and 7.5) remained compressive under the single-well response.

On the other hand, the p-snap case exhibited significantly larger stress amplitudes and its

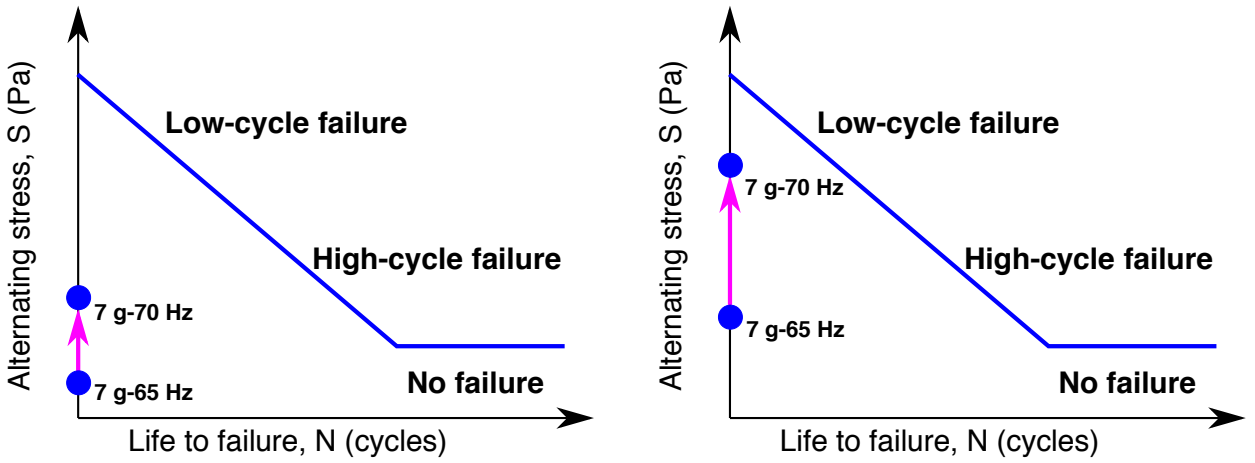

Figure 7.9: Schematic S-N curves for the single-well and p-snap cases at 7 g-65 Hz and 7 g-70 Hz, respectively. (a) Scenario 1: a shift from a no-failure state to high-cycle failure. (b) Scenario 2: a transition from high-cycle failure to low-cycle failure. The S-N curves were drawn based on the work of Bannantine [8].

stress fields changed signs at least once per loading cycle (multiple changes also occurred due to twisting deformations). The transverse displacement induced by p-snap showed nearly periodic response at the midnode. However, the corresponding maximum stress fields, which were obtained near the free boundaries, demonstrated non-periodic stress oscillations due to the strong influence of twisting deformations.

The c-snap case also showed significantly larger stress amplitudes than the single-well case; however, the amplitudes were smaller than those of the p-snap case. In addition, the stress fields of the c-snap case did not alternate sign within every loading cycle. This phenomenon was expected because snap-through occurred in an intermittent manner.

For the variable-amplitude stress fields induced by snap-through, interpreting their impact on fatigue would not be straightforward. Many methods have been proposed to analyze fatigue induced by variable-amplitude stress fields. For example, to reduce a complex load history into a number of constant-amplitude events [8], the ASTM manual [33] presents standard practices for cycle counting in fatigue analysis using rainflow counting.

It is nonetheless obvious that a marginal frequency increase from 65 Hz to 70 Hz across the low-frequency boundary at 7 g can result in significantly higher stresses and consequently larger impact on fatigue. To discuss possible scenarios of this case, schematic stress-life (or S-N) curves [8] are illustrated in Fig 7.9. Based on the initial (static) stress state of post-buckled plates, a small frequency increase (5 Hz) can generate a transition from a no-failure state to high-cycle failure (see Fig 7.9a) or from high-cycle failure to low-cycle failure (see Fig 7.9b). Therefore, along the low-frequency boundary, the fatigue life of the specimen can be extremely sensitive to frequency changes.

The impact of variable-amplitude stress fields induced by snap-through on multiaxial fatigue of laminated composite structures will be further investigated in future work.

7.4 Stress analysis: flat vs. post-buckled plates

In this section, the stress fields of the post-buckled plate are compared to those of a flat (or pre-buckled) plate to characterize the amplification of stresses caused by buckling. For this comparison, an EAS model for a flat plate was generated using a mesh illustrated in Fig 6.1 without extended lengths for the boundary elements (i.e., all elements are rectangular). The comparison was made for the three characteristic response types of the post-buckled plate: single-well, c-snap, and p-snap cases.

7.4.1 Single-well response

In cases where the flat plate switches to the post-buckled state and shows single-well response, the largest amplification of the stress field was observed at 2 g–88 Hz. The transverse displacement and stress fields of the post-buckled and flat models under 2 g–88 Hz are illustrated in Figs 7.10 to 7.15. Among the stress fields obtained on all of the elements, the largest ones were chosen and shown in these figures. As illustrated in Fig 7.10a, the flat plate oscillated around $w_{\text{mid}} = 0$ with the peak-to-peak displacement 0.967 mm, while the post-buckled plate oscillated around w_{mid} =-1.487 mm with the peak-to-peak displacement 0.562 mm. The phase portraits of these time series appeared as single-well response in the

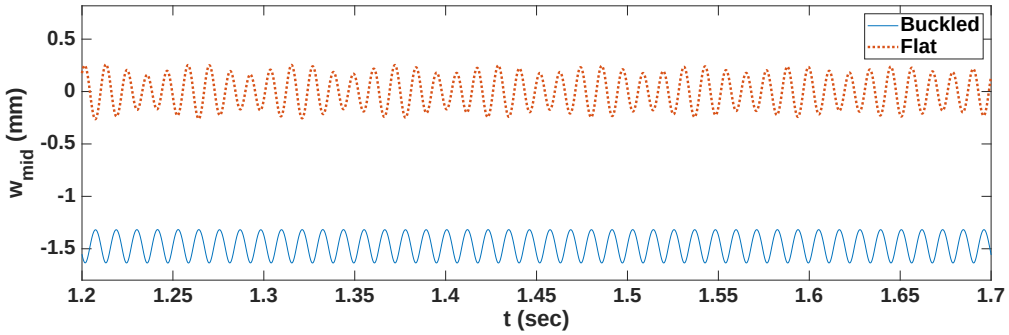

(a)

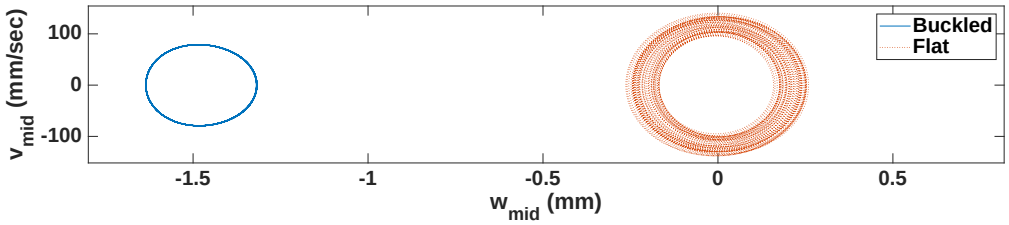

(b)

Figure 7.10: The response of the post-buckled and flat models under 2 g–88 Hz harmonic loading. (a) The time series of the transverse displacement of the midnode (w_{mid}). (b) The projected phase portrait of the time series in the phase space.

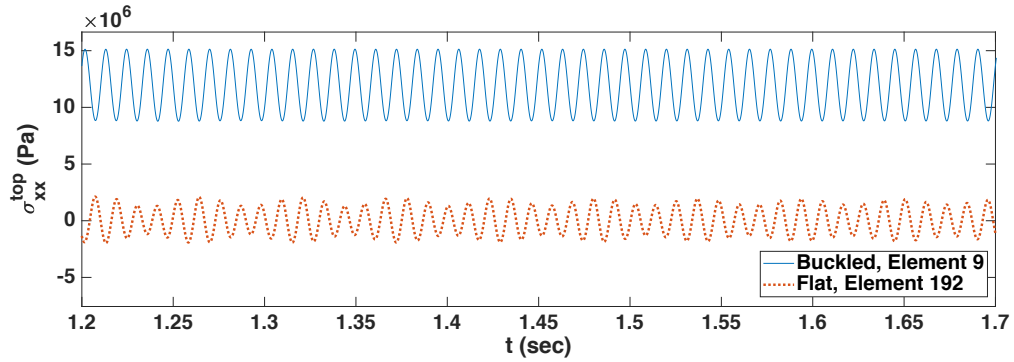

Figure 7.11: The time series of the in-plane normal stress σ_{xx} of the post-buckled and flat models at the top of the plate ($z = \frac{h}{2}$) illustrated in Fig 7.10.

phase space as shown in Fig 7.10b.

This case would be simpler to interpret for fatigue than snap-through cases. For mean

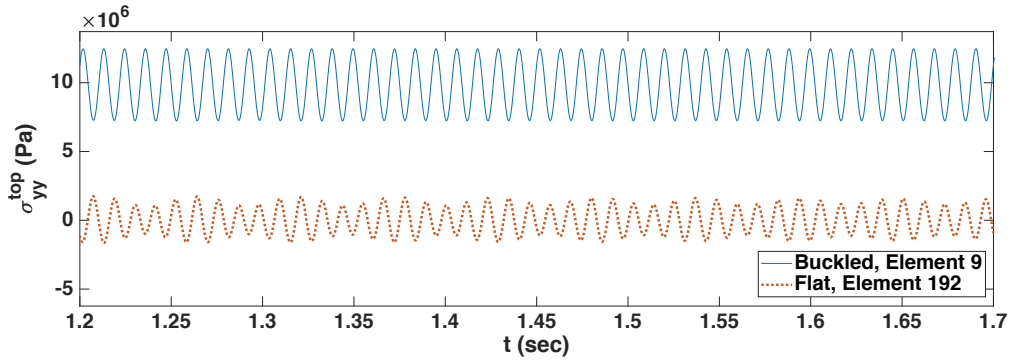

Figure 7.12: The time series of the in-plane normal stress σ_{yy} of the post-buckled and flat models at the top of the plate ($z = \frac{h}{2}$) under the response illustrated in Fig 7.10.

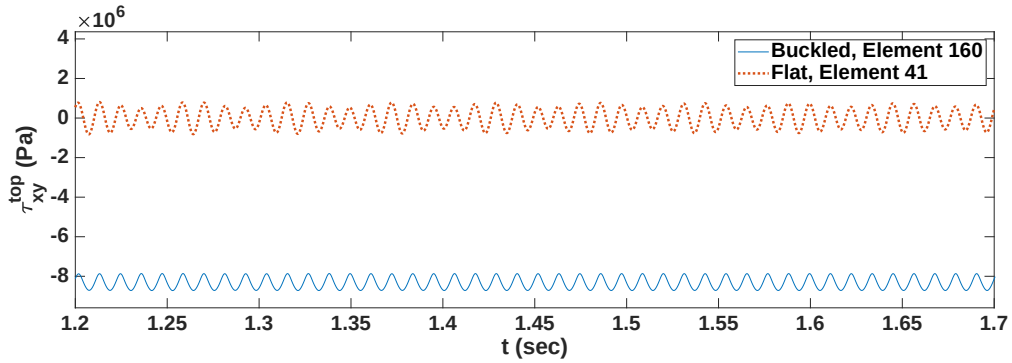

Figure 7.13: The time series of the in-plane shear stress τ_{xy} of the post-buckled and flat models at the top of the plate ($z = \frac{h}{2}$) under the response illustrated in Fig 7.10.

stress effects, alternating stress σ_a, mean stress σ_m, and stress ratio R are required [8]:

$$\sigma_a = \frac{\sigma_{\max} - \sigma_{\min}}{2}, \quad \sigma_m = \frac{\sigma_{\max} + \sigma_{\min}}{2}, \quad R = \frac{\sigma_{\max}}{\sigma_{\min}}. \tag{7.2}$$

Using these equations, alternating and mean stresses, and stress ratio of the in-plane normal stress σ_{yy}^{top} of the post-buckled and flat models are tabulated in table 7.1. These stress fields are not consistent; however, the variations are not significant and acquisition of accurate σ_a, σ_m, and R is outside of the scope of this work. Thus, the maximum and minimum stresses were simply used. The post-buckled model showed seven times higher $\sigma_{\max}$ and significantly

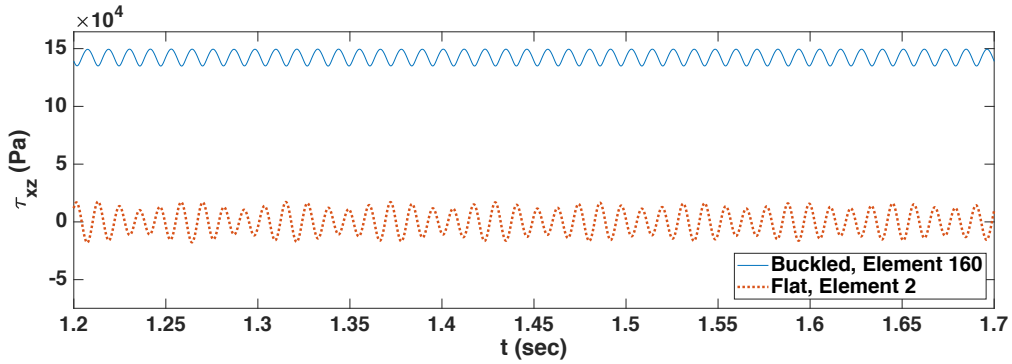

Figure 7.14: The time series of the transverse shear stress τ_{xz} of the post-buckled and flat models under the response illustrated in Fig 7.10.

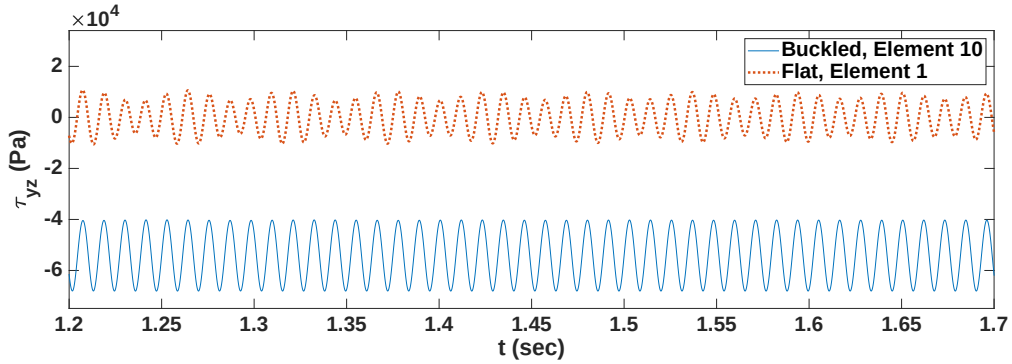

Figure 7.15: The time series of the transverse shear stress τ_{yz} of the post-buckled and flat models under the response illustrated in Fig 7.10.

higher σ_{m} than the flat model. On the other hand, σ_{a} of the post-buckled model was just 1.5 times higher than that of the flat model.

To explore the impact of these values, fatigue life prediction methods for composite materials under constant-amplitude stress fields were considered: for example, Goodman, Gerber, bell-shaped, and anisomorphic diagrams [91]. Kawai and Koizumi [34] proposed an anisomorphic constant fatigue life diagram for a T800H/3631 $[45/90/\text{-}45/0]_{2\mathrm{S}}$ carbon/epoxy laminate with experimental results as illustrated in Fig 7.16. For specimen fabrication, they used the carbon fiber used in this work (T800H). On the other hand, their lamina was unidirectional while this work used woven prepreg and the stacking sequences of the two

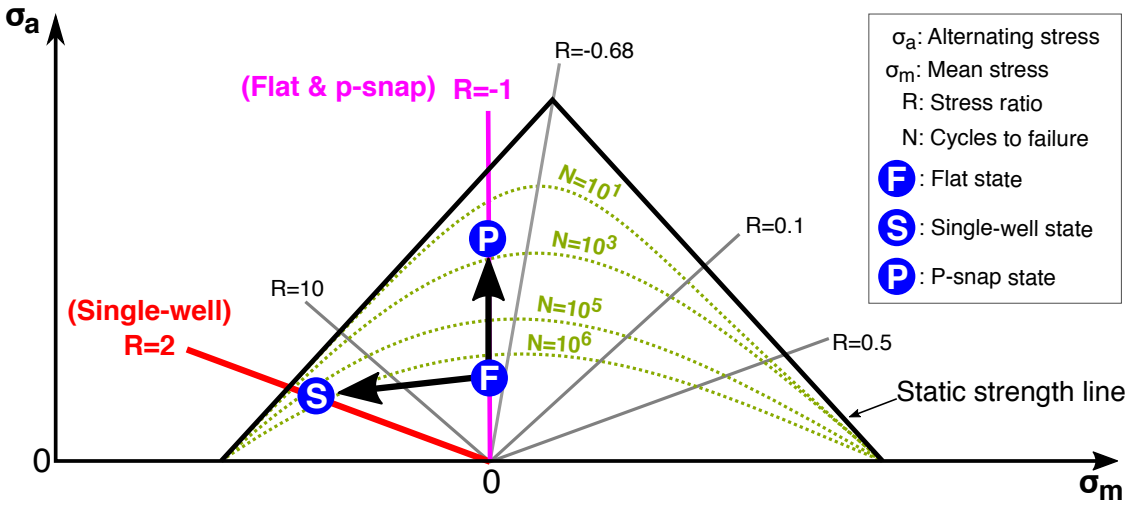

Figure 7.16: Possible scenarios of the impact of stress amplification induced by buckling on fatigue. An anisomorphic constant fatigue life diagram for a T800H/3631 $[45/90/\text{-}45/0]_{2S}$ carbon/epoxy laminate in the work of Kawai and Koizumi [34] is reproduced here.

Stress field	Flat model	Post-buckled model	Ratio (Post-buckled/Flat)
$\sigma_{\max}$ (Pa)	2.125×10^6	1.513×10^7	7.12
$\sigma_{\min}$ (Pa)	-2.003×10^6	8.780×10^6	-4.38
σ_{a} (Pa)	2.064×10^6	3.175×10^6	1.54
σ_{m} (Pa)	6.082×10^4	1.196×10^7	196.57
R	-1.061	1.723	-1.62

Table 7.1: The alternating stress σ_a, mean stress σ_m, and stress ratio R of the in-plane normal stress $\sigma_{\mathrm{xx}}^{\mathrm{top}}$ of the post-buckled and flat models illustrated in Fig 7.11.

works were also different. Therefore, their diagram could not directly be applied to this work. However, the diagram still provides an idea on a possible correlation between the alternating and mean stresses, stress ratio, and fatigue life of the specimen used in this work. Kawai and Koizumi applied in-plane normal cyclic loading (mode I) to their specimens to induce fatigue failure. As shown in the diagram, a rise in alternating or mean stresses induced by buckling can contribute to reducing predicted fatigue life (i.e., failure is expected at fewer

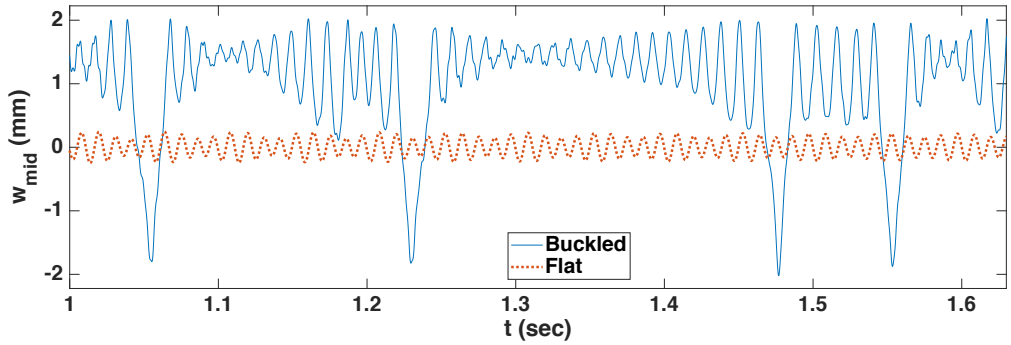

(a)

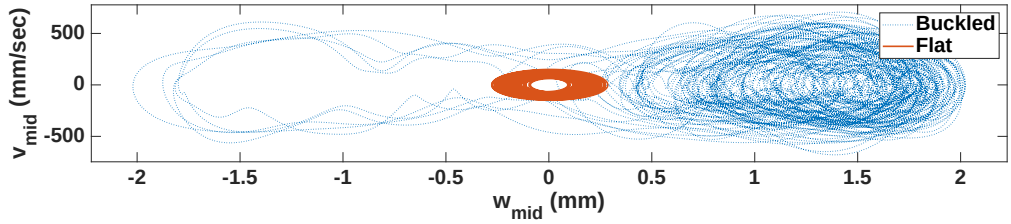

(b)

Figure 7.17: The response of the post-buckled and flat models under 2 g–90 Hz harmonic loading. (a) The time series of the transverse displacement of the midnode (w_{mid}). (b) The projected phase portrait of the time series in the phase space.

cycles). Therefore, the post-buckled model could have a reduced fatigue life compared to the flat model. The figure also illustrates possible scenarios of the impact of stress amplification induced by buckling on fatigue. As shown in Table 7.1, a pre-buckled (or flat) plate would have a stress ratio R close to –1, while a post-buckled plate showing single-well response can have $R \simeq 2$. In cases where the flat plate in a no-failure state experiences buckling and transits into a post-buckled state with single-well response, a consequent increase in mean stresses (with a potential drop in alternating stresses (see Fig 7.14)) could possibly result in high-cycle failure.

7.4.2 Chaotic snap-through

For the transition from the single-well response of the flat plate to the c-snap response of the post-buckled plate, the largest amplification of the stress fields was observed at 2 g–90 Hz.

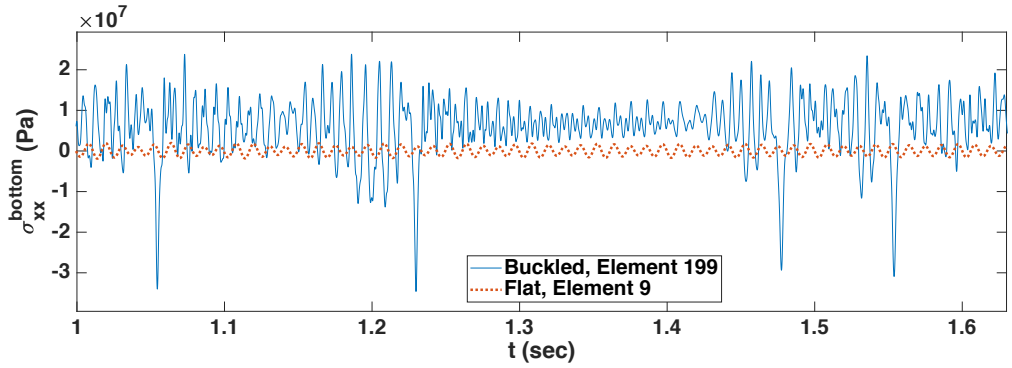

Figure 7.18: The time series of the in-plane normal stress σ_{xx} of the post-buckled and flat models at the bottom of the plate ($z = -\frac{h}{2}$) under the response illustrated in Fig 7.17.

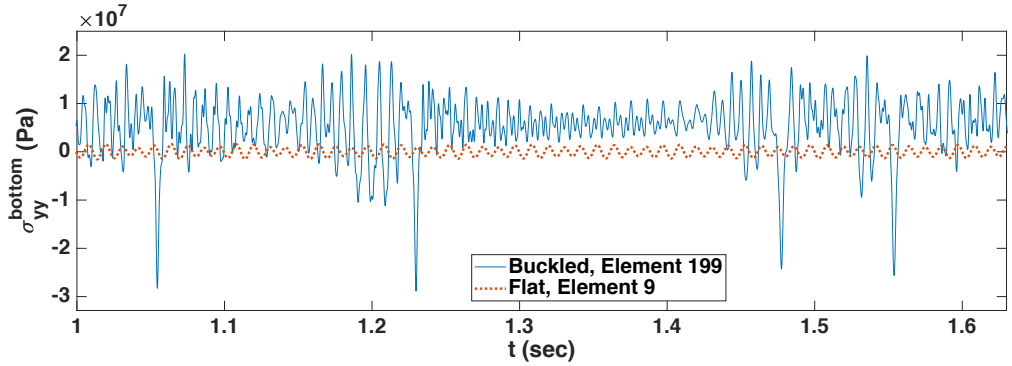

Figure 7.19: The time series of the in-plane normal stress σ_{yy} of the post-buckled and flat models at the bottom of the plate ($z = -\frac{h}{2}$) under the response illustrated in Fig 7.17.

The transverse displacement and stress fields of the post-buckled and flat models under 2 g–90 Hz are illustrated in Figs 7.17 to 7.22. Among the stress fields obtained on all of the elements, the largest ones were chosen and shown in these figures. As illustrated in Fig 7.17a, the flat plate oscillated around $w_{\text{mid}} = 0$ with the peak-to-peak displacement 0.564 mm, while the post-buckled plate exhibited four snap-through events within the time window, which occurred in an intermittent and chaotic manner. In the phase space, the c-snap response of the post-buckled model appeared as a large double-well trajectory encompassing the single-well response of the flat model as shown in Fig 7.17b.

The post-buckled model demonstrated larger-amplitude alternating and mean stresses in

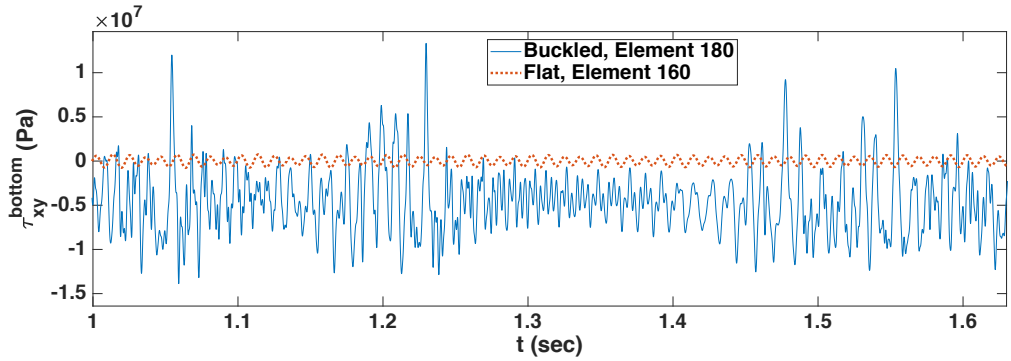

Figure 7.20: The time series of the in-plane shear stress τ_{xy} of the post-buckled and flat models at the bottom of the plate (z =-$\frac{h}{2}$) under the response illustrated in Fig 7.17.

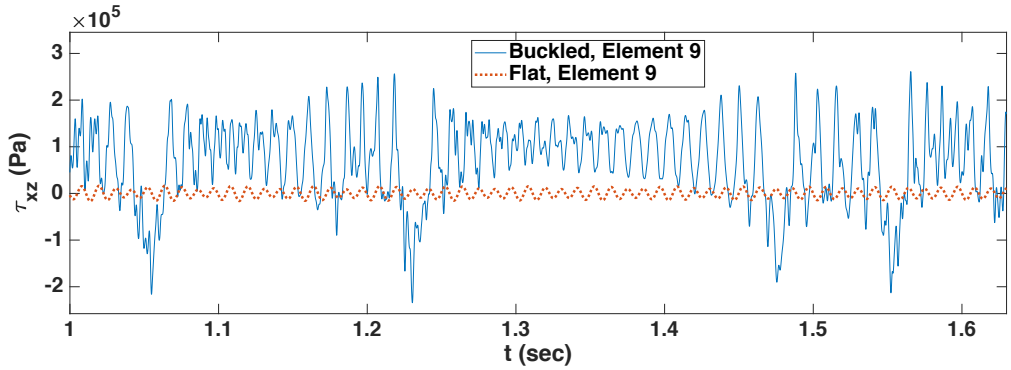

Figure 7.21: The time series of the transverse shear stress τ_{xz} of the post-buckled and flat models under the response illustrated in Fig 7.17.

all the stress fields than the flat model. In the first snap-through case, the alternating in-plane normal stress of the buckled model was $(\sigma_{xx}^{\text{bottom}})_a = 2.60 \times 10^7$ Pa while the corresponding stress of the flat model was $(\sigma_{xx}^{\text{bottom}})_a = 2.22 \times 10^6$ Pa. However, the post-buckled model exhibits wild fluctuation in the alternating and mean stresses and thus it would not be straightforward to compare the impact of the stress fields of the two models on fatigue. Given that c-snap exhibits both single-well response and snap-through in a chaotic manner, the impact of stress amplification induced by buckling with c-snap on fatigue can be a complex combination of the scenarios for single-well and p-snap cases illustrated in Fig 7.16.

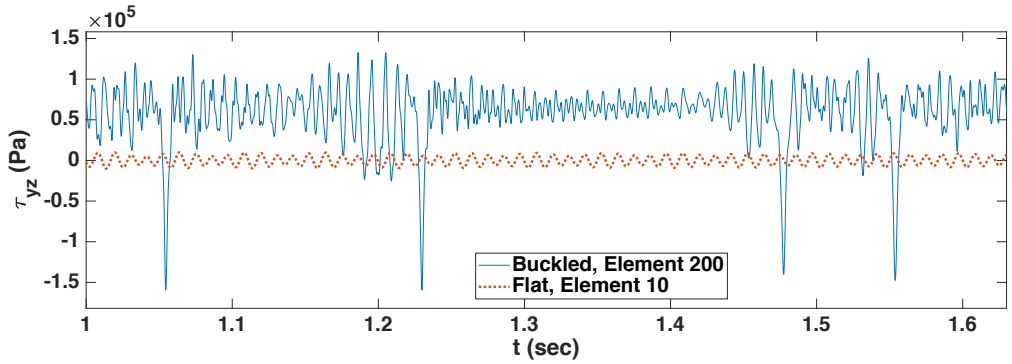

Figure 7.22: The time series of the transverse shear stress τ_{yz} of the post-buckled and flat models under the response illustrated in Fig 7.17.

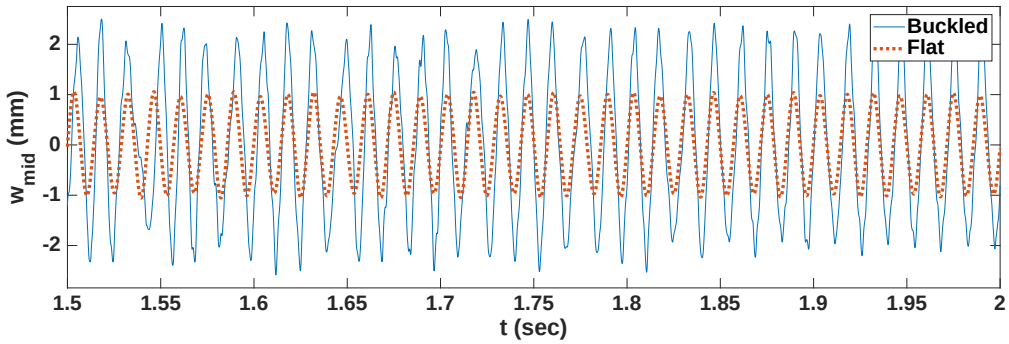

(a)

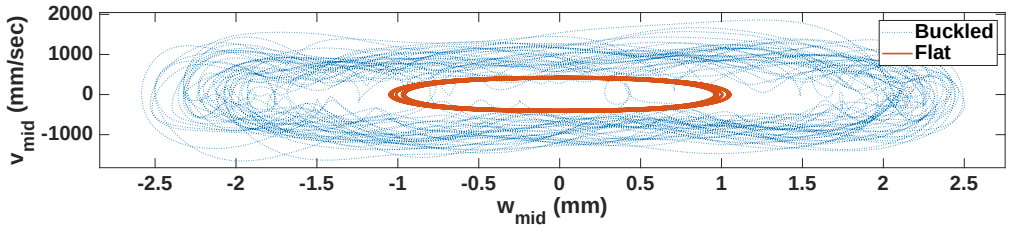

(b)

Figure 7.23: The response of the post-buckled and flat models under 7 g–70 Hz harmonic loading. (a) The time series of the transverse displacement of the midnode (w_{mid}). (b) The projected phase portrait of the time series in the phase space.

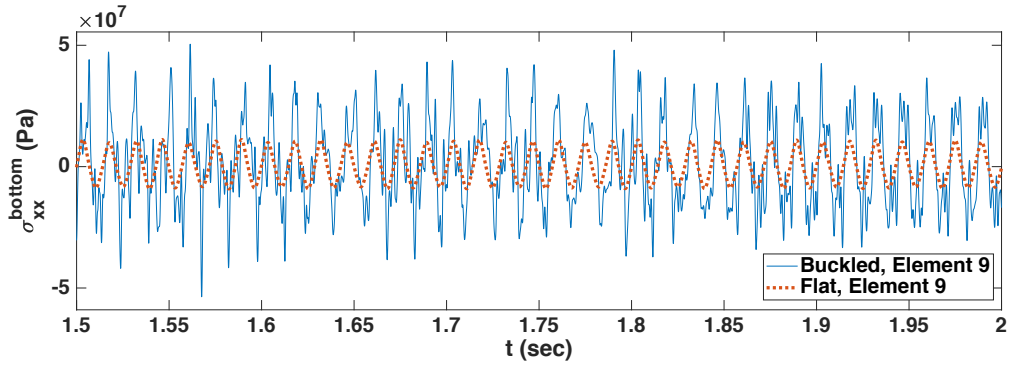

Figure 7.24: The time series of the in-plane normal stress σ_{xx} of the post-buckled and flat models at the bottom of the plate (z =-$\frac{h}{2}$) under the response illustrated in Fig 7.23.

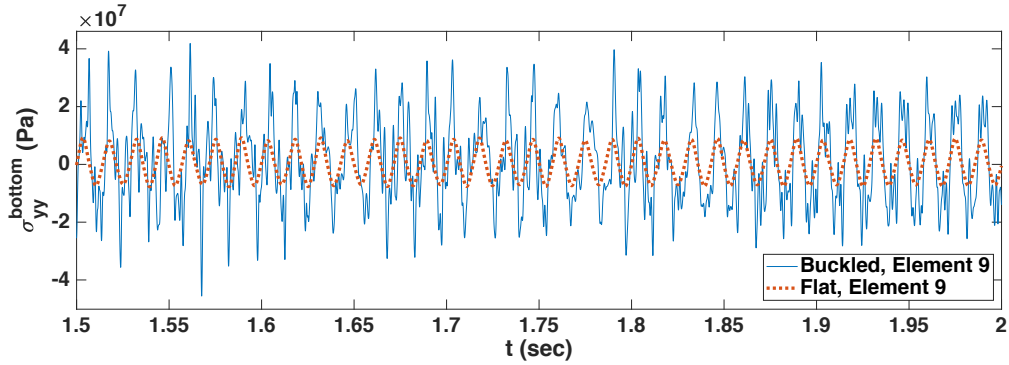

Figure 7.25: The time series of the in-plane normal stress σ_{yy} of the post-buckled and flat models at the bottom of the plate (z =-$\frac{h}{2}$) under the response illustrated in Fig 7.23.

7.4.3 Nearly periodic snap-through

For a shift from the flat plate to the post-buckled one showing p-snap response, the largest amplification of the stress fields values was observed at 7 g–70 Hz. The transverse displacement and stress fields of the post-buckled and flat models under 7 g–70 Hz are illustrated in Figs 7.23 to 7.28. Among the stress fields obtained on all of the elements, the largest ones were chosen and shown in these figures. As illustrated in Fig 7.23a, the flat model showed a significantly higher peak-to-peak displacement (2.114 mm) than in the previous two cases, while the post-buckled plate exhibited snap-through in a nearly periodic manner with the

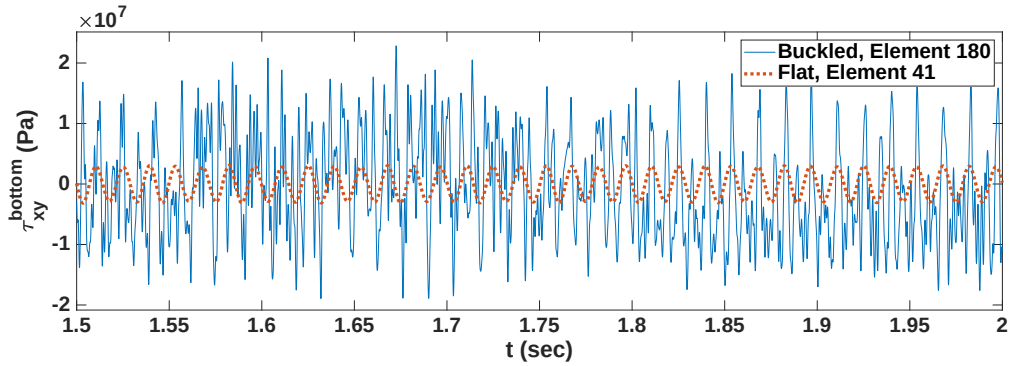

Figure 7.26: The time series of the in-plane shear stress τ_{xy} of the post-buckled and flat models at the bottom of the plate ($z = -\frac{h}{2}$) under the response illustrated in Fig 7.23.

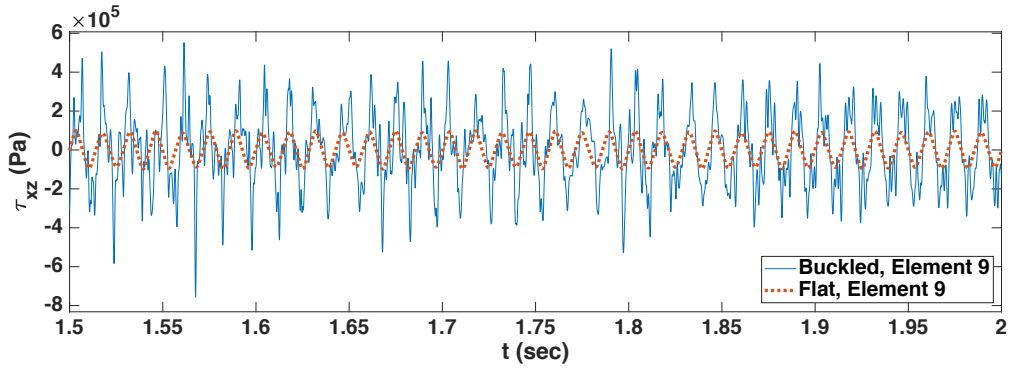

Figure 7.27: The time series of the transverse shear stress τ_{xz} of the post-buckled and flat models under the response illustrated in Fig 7.23.

peak-to-peak displacement 4.0–5.0 mm. Both of the plates oscillated around $w_{\text{mid}} = 0$. As shown in the phase space (see Fig 7.23b), the projected phase portrait of the post-buckled plate formed a nearly single-well response encompassing the phase portrait of the flat model.

The post-buckled model exhibited larger-amplitude (5–7.5 times) peak stresses than the flat model; however, the corresponding alternating and mean stresses are more complex due to wild fluctuations in the stress fields. A possible scenario of the impact of stress amplification induced by buckling with p-snap is illustrated in Fig 7.16. As described in this figure, a consequent increase in alternating stresses could possibly result in low-cycle failure.

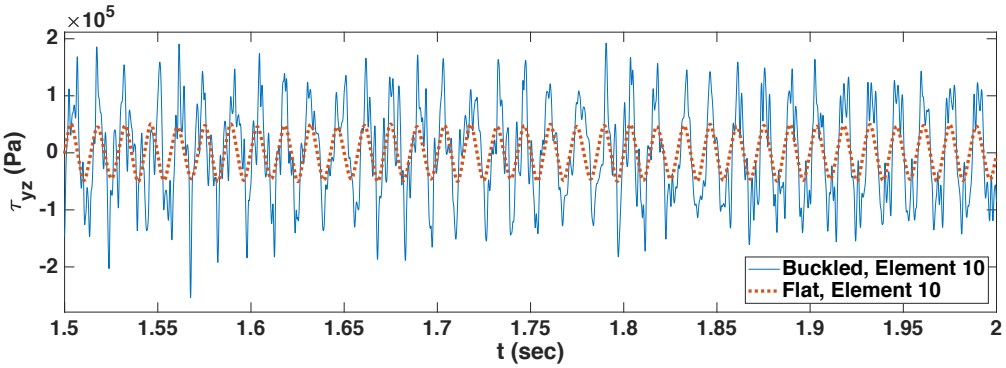

Figure 7.28: The time series of the transverse shear stress τ_{yz} of the post-buckled and flat models under the response illustrated in Fig 7.23.

7.5 Summary

In this chapter, the impact of nonlinear dynamics on the stress fields of the model is investigated in terms of fatigue.

The dynamic response of the EAS model was validated in displacement fields by comparing its simulation results with the experimental results and the numerical data obtained using the CLPT model in the HFP space. The simulation results revealed that the occurrence of snap-through results in a significant increase in stress amplitudes which could affect fatigue life. In addition, it was shown that stress fields (and potentially fatigue life) can be extremely sensitive to frequency changes across low-frequency snap-through boundaries. The comparison between the stress fields of the buckled and flat models showed that a transition from pre-buckled states to post-buckled ones can amplify stress fields and can make changes in alternating and mean stresses, and stress ratio. It was shown that buckling can have different impacts on fatigue depending on post-buckled response types (i.e., single-well, c-snap, or p-snap). The stress fields of the post-buckled model exhibited wild fluctuations with the presence of snap-through. Therefore, for further investigation of the impact of these stress fields on fatigue, the complex stress profiles need to be reduced to simpler ones (e.g., multiple constant-amplitude stress fields) using various methods and experimental results

are required in the form of Goodman, Gerber, bell-shaped, and anisomorphic diagrams.

By investigating the stress fields induced by nonlinear dynamics, particularly snap-through, of post-buckled systems, this work made an important step forward in investigating the impact of the stress fields on fatigue. This work will be further developed to simulate damage growth in composite structures subject to high-frequency dynamic loading using the EAS model.

Chapter 8
SUMMARY AND FUTURE WORK

8.1 Summary

The primary focus of this work was on investigation of nonlinear dynamics and corresponding stress fields which post-buckled composite structures can experience under high-frequency dynamic loading. The potential impact of these phenomena on the structural integrity of composite structures was of particular interest.

For experimental investigation, an asymmetrically-buckled composite plate was tested under inertially-applied harmonic loading. Full-field measurement of the dynamic response of the specimen revealed that post-buckled, bi-stable systems can exhibit spatio-temporally complex behaviors in the nonlinear regime. These behaviors were represented by the three characteristic response types: single-well, chaotic snap-through, and (nearly) periodic snap-through. As shown by frequency-sweep tests, the specimen showed a strong sensitivity to changes in forcing parameters and initial conditions. This phenomenon can be represented by a transition of response from single-well to periodic snap-through with a 5-Hz increase in forcing frequency, and co-existing responses at the identical forcing parameters. These experimental observations showed that the previous discussions on bi-stable metallic structures such as single-degree-of-freedom linkage systems, shallow arches, and post-buckled beams can be extended to more complex composite structures such as post-buckled laminated plates and shells. Finally, the experimental snap-through boundaries of the post-buckled specimen were established in the harmonic forcing parameter space as benchmark data for model validation.

Numerical modeling done in this work was intended to: (i) accurately reproduce the initially-buckled shape of the specimen through numerical buckling process, (ii) produce dy-

namic simulation results matching the experimental data including snap-through boundaries, and (iii) predict the stress fields which the specimen experienced under dynamic loading. To achieve these objectives, different types of finite element models (FEMs) were built using in-house FEM codes written in MATLAB. The models were generated by calibrating only their static equilibrium states to match the full-field geometric data of the initially-buckled shape of the specimen. The dynamic simulation results obtained using these models required neither modification nor curve-fitting to match the experimental results.

The first numerical model was generated based on the classical laminated plate theory (CLPT) and cubic Hermite elements. The theory disregards transverse shear deformation and thus its application is limited to thin laminated composite plates. Its numerical implementation, however, is free of shear locking and thus the CLPT model has an enormous advantage over other models despite its limitations. In addition, the dimension of the specimen was well below the thin-plate limit. The CLPT model developed in this work successfully captured the spatio-temporal complexity and parameter sensitivity observed in the dynamic response of the specimen. In addition, the model demonstrated complex co-existing responses along its snap-through boundary. Robust validation of the model was achieved by excellent agreement between the numerical and experimental snap-through boundaries. Given that CLPT models have not been a preferred choice over shear deformation models to investigate nonlinear dynamics and snap-through boundaries, this work provided a new perspective on the capabilities of CLPT models. Furthermore, the numerical data obtained through extensive dynamic simulation using the CLPT model provide a useful benchmark (displacement fields) and a 'truth' model for validation of other computationally demanding models (e.g., models involving high computational costs or locking issues).

The CLPT model showed impressive performance in predicting displacement fields within the thin-plate limit. One of the principal objectives outlined in this work, however, is to develop reliable simulation tools for stress analysis of both thin and moderately-thick composite structures. To meet this requirement, the CLPT model was extended into a shear-deformable model based on the first-order shear deformation theory (FSDT) and bi-linear elements. The

theory allows for transverse shear deformation and thus can be applied to moderately thick plates. In addition, the theory enables accurate and direct computation of transverse strain and stress fields (as opposed to indirect approaches based on 3-D equilibrium). A simple analysis of cylindrical bending problems using the FSDT model showed that the incorporation of additional shear energy induced by the shear deformation engendered a shear locking phenomenon, which resulted in a significant underestimate of deflections and an overestimate of buckling loads. Such an overestimate of structural capacity from numerical analysis can cause a serious problem in structural design if the occurrence of locking phenomenon fails to be identified. This work showed that a commonly-used stress-analysis method using Barlow points can disguise shear locking occurrence in cases where stress oscillations are present in elements. Moreover, it was shown that mesh refinement is not effective in resolving the shear locking issue.

To address locking, this work applied assumed strain methods to the FSDT model. The performance of two different types of assumed strain methods was explored: the mixed interpolation of tensorial components (MITC4) and the enhanced assumed strain (EAS) method. For linear cylindrical bending problems, these models showed locking-free behaviors. In addition, the models produced a constant stress field within each element, which prevented the occurrence of stress oscillations and consequent shear locking. The numerical implementation of these models is more complicated than that of the conventional CLPT and FSDT models, and is not covered in the literature for laminated composite plate theories. This work presented in detail the nonlinear FEM formulations of the MITC4 and EAS models for other researchers to employ these methods for their future works.

For simulation of the stress fields in the post-buckled plate specimen, geometrically-nonlinear MITC4 and EAS models of the specimen were constructed. The MITC4 model exhibited strong oscillations of a membrane stress field which imply the occurrence of membrane locking. Consequently, the influence of over-stiffening induced by membrane locking was observed in the transverse displacement, buckling load, and natural frequency of the MITC4 model. However, the membrane locking phenomenon did not engender over-stiffening

as severely as did shear locking, even though membrane locking still can damage the accuracy of models. On the other hand, the EAS model produced constant stress fields along elements and thus exhibited neither shear nor membrane locking. This work showed that for nonlinear von Kármán strains, an 11-mode interpolation for enhanced membrane strains is more effective than a commonly-used 7-mode interpolation in obtaining a constant membrane stress field along elements. Given that most of previous works validated their geometrically-nonlinear EAS models relying only on the displacement fields of numerical data available in the literature, the model validation of this work based on the experimental data can be deemed more robust than that of those works. In addition, this work added to the literature a new perspective on enhancing nonlinear strains with the 11-mode interpolation method and extended the studies of EAS modeling into global stress analysis.

Finally, the impact of nonlinear dynamics on the stress field of the post-buckled specimen was simulated using the EAS model. The EAS model was validated by comparing its snap-through boundary with the experimental and CLPT boundaries. The stress-analysis results revealed that snap-through can induce a significant increase in stress amplitudes and possibly affect fatigue life. Therefore, fatigue life could be extremely sensitive to frequency changes along snap-through boundaries. In addition, it was shown that post-buckled states generate larger-amplitude stresses than pre-buckled cases. By simulating the stress fields induced by nonlinear dynamics, particularly snap-through, this work made an important step forward in investigating the impact of these phenomena on the structural integrity of composite structures for supersonic- or hypersonic-speed flight. To the best of the author's knowledge, this work introduced the most robust and complete study of stress fields induced by snap-through.

This work will be further developed to simulate damage growth in composite structures under high-frequency aerodynamic loading (i.e., loads with significant random content) using the models developed in this work with additional fracture and fatigue models.

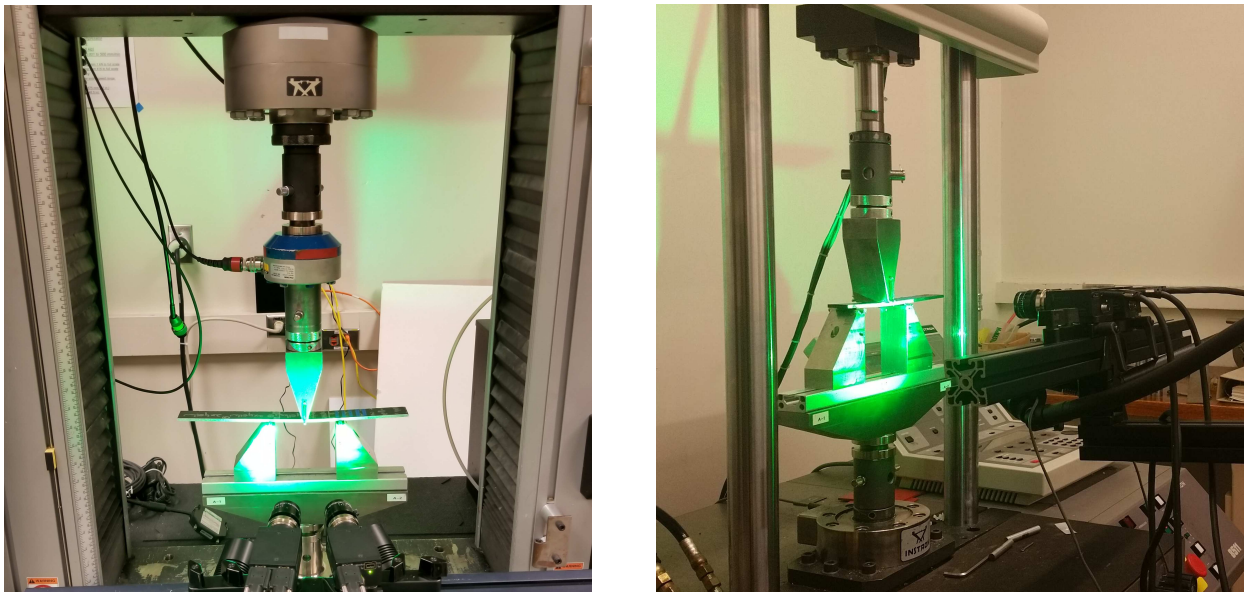

(a) (b)

Figure 8.1: ENF test setup for fracture and fatigue in mode II. (a) Fracture test setup with Instron 5585H and VIC-3D DIC cameras. (b) Fatigue test setup with MTS 8511 and VIC-3D DIC cameras.

8.2 Future work

For further investigation of degradation induced by nonlinear dynamics, the dynamic models developed in this work will need to incorporate fracture and fatigue mechanisms based on experimental characterization of these phenomena. In addition, high computational costs associated with using the current models need to be reduced for extensive simulation of damage growth under various dynamic loading conditions. To address these issues, more experimental and numerical studies are required. Some topics for future work are introduced in this section.

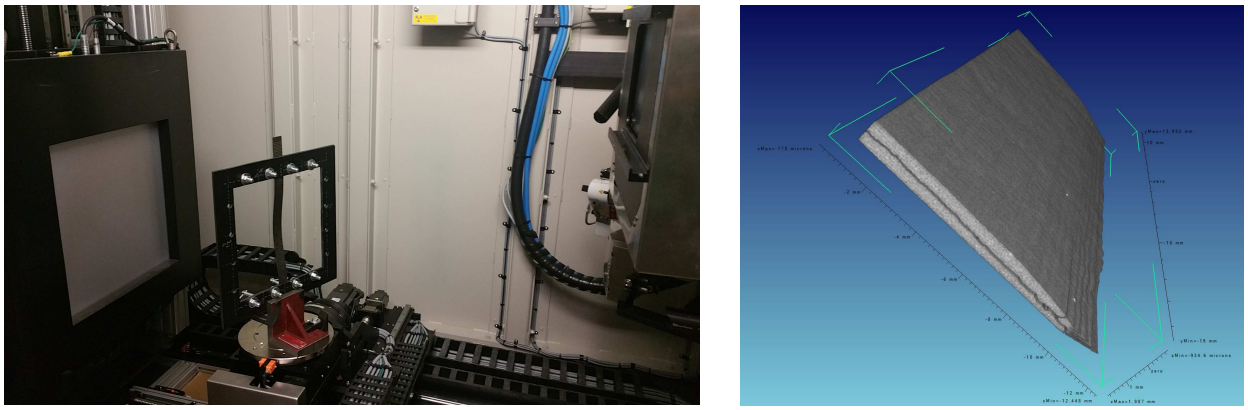

(a) (b)

Figure 8.2: 3-D X-ray CT scan system and scanned delamination. (a) 3-D X-ray CT scan system NSI X5000. (b) A post-processed scanned image of delamination inside a composite beam.

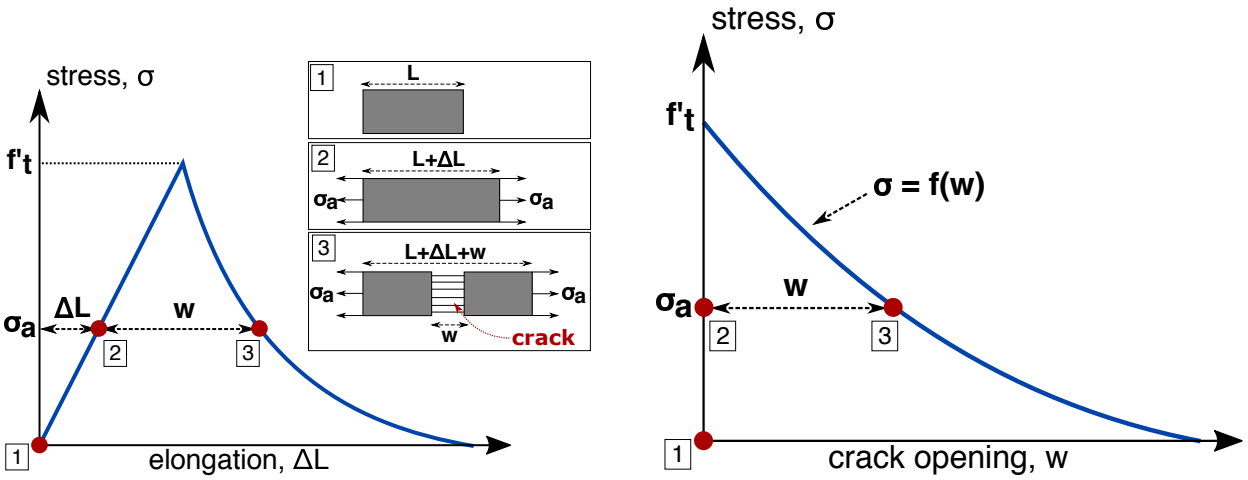

(a) (b)

Figure 8.3: A CZM of mode-I fracture. (a) A stress-elongation curve obtained from a tensile test (assuming the bulk material behavior is linear elastic). The tensile strength of the specimen is denoted by f'_t. (b) A stress-displacement curve under softening (i.e., a cohesive law) corresponding to the stress-elongation curve shown in Fig 8.3a. These curves were drawn based on the work of Bazant [12].

8.2.1 Experimental and numerical characterization of fracture process zones (FPZs)

Composite structures under transverse dynamic loading, as briefly introduced in Section 1.3, can experience fatigue predominantly in mode II depending on loading amplitudes. For experimental characterization of FPZs in mode II, end-notched flexure (ENF) tests (see Fig 1.5) will be conducted following a standard test method instructed in ASTM D7905/D7905M-14 [7]. To overcome difficulties in measuring mode-II delamination, advanced measurement technique such as digital image correlation (DIC) and three-dimensional (3-D) X-ray computed tomography (CT) methods will be employed as shown in Figs 8.1 and 8.2. In addition, size effects on FPZs in composite structures [76, 77] will be studied by testing geometrically-scaled specimens. These tests intend to show the relationship between the size of specimens having the identical dimension ratios and the development of FPZs in mode II.

Based on the experimental data, cohesive zone models (CZMs) will be developed. In CZMs, a fictitious cohesive crack is capable of transferring stresses between adjacent crack surfaces (see Fig 8.3a) and the corresponding FPZ is characterized in the form of a stress-displacement curve under softening (i.e., a cohesive law, see Fig 8.3b) [12]. For characterization of quasi-brittle fracture, CZMs have been widely implemented [101]. Numerical implementation of CZMs requires neither the existence of a precrack nor exact crack-front shapes [100], both of which are the major disadvantages of the linear elastic fracture mechanics represented by the virtual crack closure technique.

8.2.2 Numerical implementation of CZMs with node-dependent variable kinematics (NDVK)

The models developed in this work are based on the laminated plate theories which can be categorized as equivalent single-layer (ESL) theories, in which 3-D elasticity problems are reduced to 2-D ones based on assumptions on the kinematics of deformation through thickness [68]. Numerical implementation of CZMs, however, requires 3-D elasticity formulations (e.g., layerwise (LW) theories [52, 67]). To resolve this issue, NDVK [102] will be employed

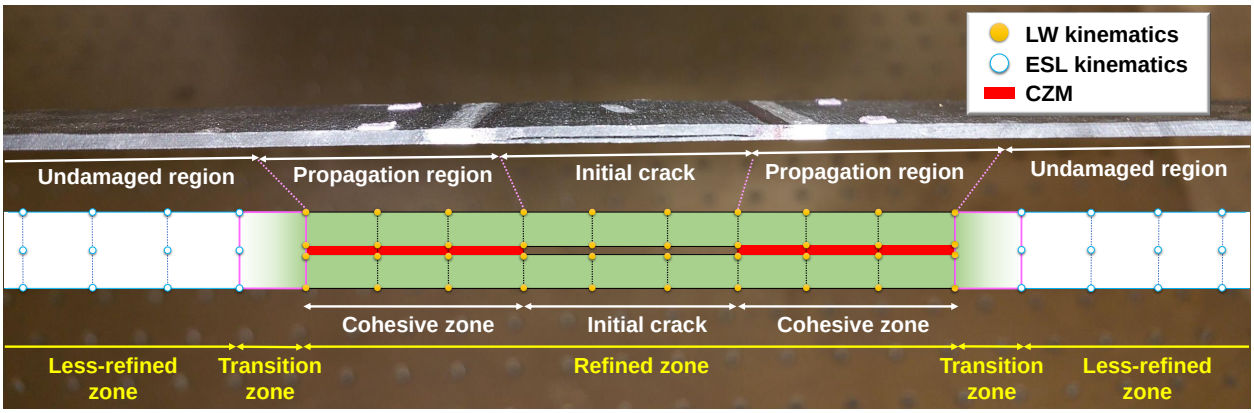

Figure 8.4: Schematic drawings of mesh discretization of a precracked composite specimen using NDVK ESL/LW [102] with CZMs.

in future work.

A variable kinematic global-local model was initially proposed by Robbins and Reddy [74, 75] using hierarchical displacement fields at the element and global levels. In this model, the total displacement field $\boldsymbol{u}$ can be expressed by superposing multiple assumed displacement fields:

$$\boldsymbol{u}(x,y,z,t) = \boldsymbol{u}^{\mathrm{ESL}}(x,y,z,t) + \boldsymbol{u}^{\mathrm{LW}}(x,y,z,t), \tag{8.1}$$

where $\boldsymbol{u}^{\mathrm{ESL}}$ and $\boldsymbol{u}^{\mathrm{LW}}$ are displacement fields obtained using ESL and LW kinematics, respectively. For the global-local analysis of multilayered structures, Zappino et al. [102] recently proposed NDVK by combining node-dependent kinematics of Carrera [16] with variable ESL/LW capabilities shown in Eq (8.1).

In future work, the models developed in this work will be improved by incorporating NDVK ESL/LW and CZMs as illustrated in Fig 8.4. In the model, the regions across which the initial crack could potentially propagate will have CZMs extended from the crack tips between two sublaminates. The zones including the crack and CZMs (named a refined zone) will be discretized by elements having LW kinematic nodes. On the other hand, the other

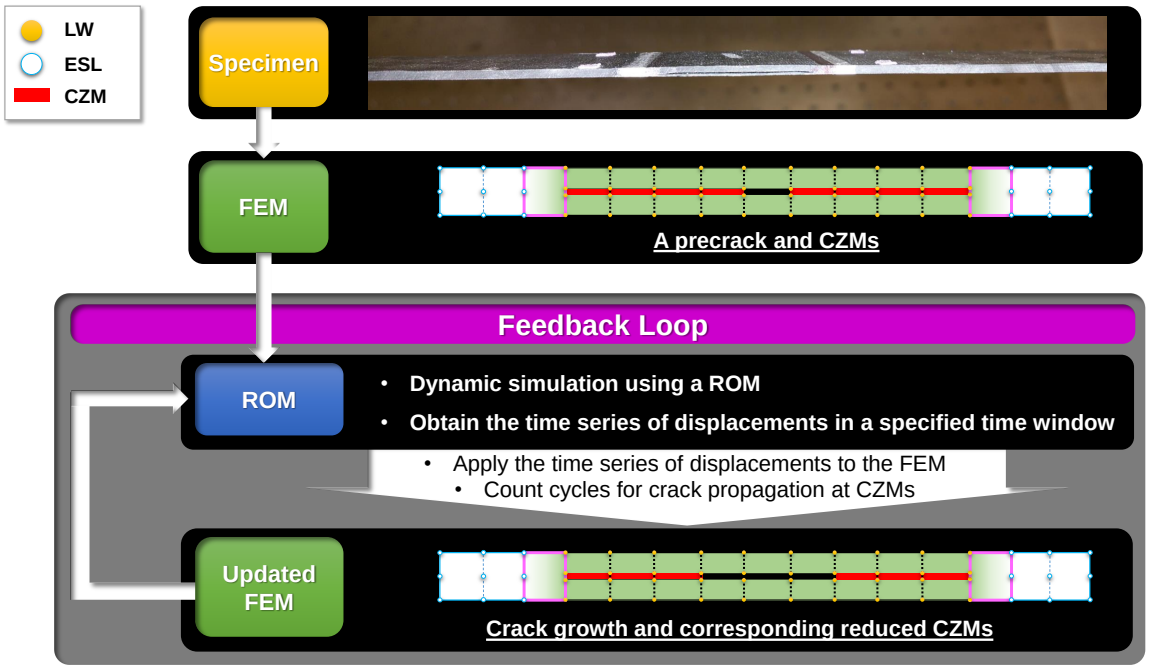

Figure 8.5: A flow chart for a hybrid simulation method using FEMs and ROMs.

parts (named less-refined zones) where crack propagation is not expected to occur will have elements comprising ESL kinematic nodes. At the interface between the two zones, transition zones will be made to ensure continuity of the two different kinematics.

8.2.3 Nonlinear reduced-order models (ROMs)

The numerical models developed in this work provided reliable simulation results; however, high computational costs of using the models can be a serious hindrance to extensive simulation of damage growth under dynamic loading. To address this issue, nonlinear ROMs will be built based on the numerical models. Nonlinear ROMs require proper orthogonal decomposition or nonlinear normal modes methods [2] and appear in the form of analytical ESL-type solutions. The applications of ROMs are extensively discussed in Refs [27, 31, 59].

In future work, fatigue induced by dynamic loading will be investigated using a hybrid

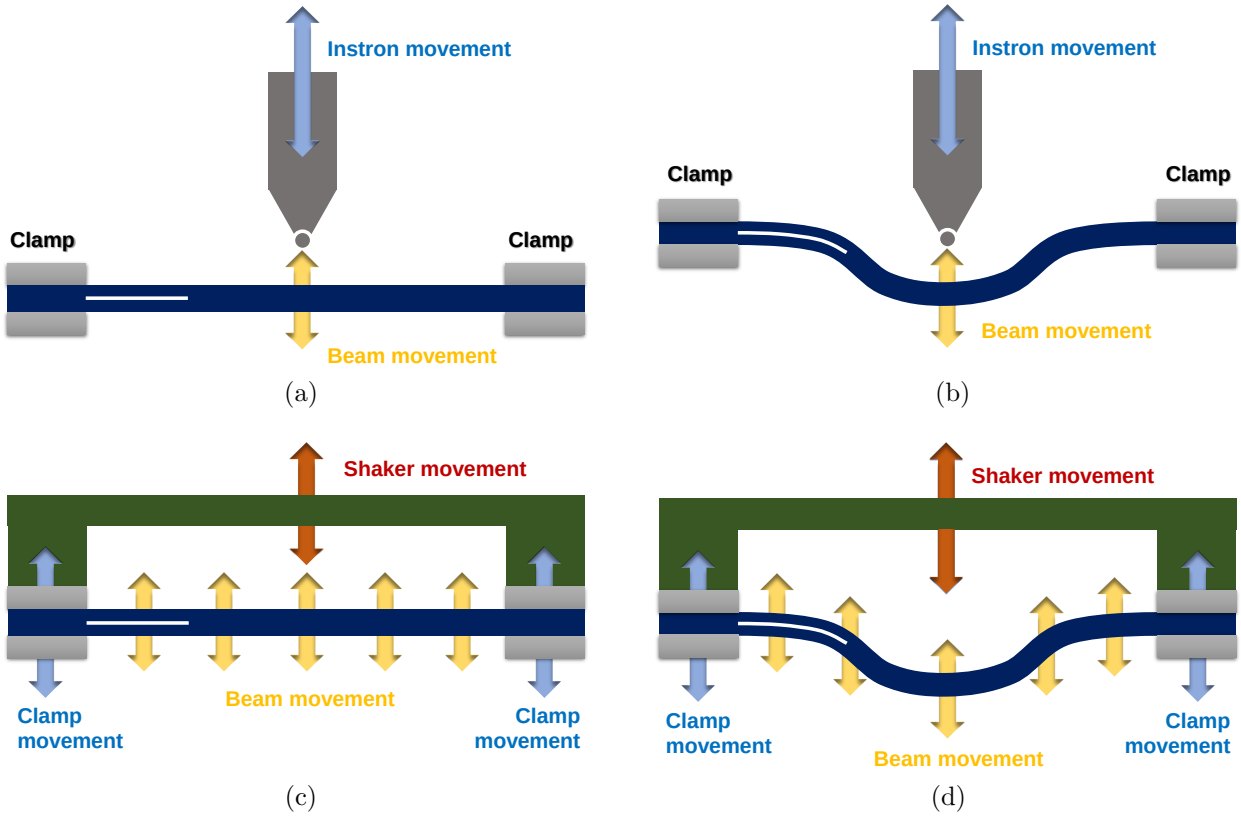

Figure 8.6: Fatigue tests under clamped boundary conditions. The white line near the left-side clamped boundary indicates a precrak. (a) Flat specimens under quasi-static cyclic loading. (b) Post-buckled or curved specimens under quasi-static cyclic loading. (c) Flat specimens under inertially-applied dynamic loading induced by a shaker movement. (d) Post-buckled or curved specimens under inertially-applied dynamic loading induced by a shaker movement.

simulation method using FEMs and ROMs. An example of the hybrid simulation method is illustrated as a flow chart in Fig 8.5. The process can be briefly described: (i) an FEM is generated using NDVK and CZMs, (ii) a ROM of the FEM is built with partially degraded stiffness for the precrack region, (iii) the dynamic response of the specimen in a specified time window is simulated using the ROM, (iv) the corresponding time series of displacements are applied to the FEM for analysis of the stress field at FPZs in front of the crack tips, (v) fatigue damage to CZMs at the FPZs and consequent degradation of the CZMs are analyzed,

(vi) the number of cycles required for crack propagation at the CZMs is obtained, (vii) the FEM is updated with increased crack length and decreased cohesive zones, and (viii) the steps (ii) to (vii) are repeated.

This hybrid simulation method will provide a new paradigm of simulation of damage growth under dynamic loading.

8.2.4 Experimental investigation of fatigue under realistic boundary and loading conditions

The ENF test illustrated in Figs 1.5 and 8.1 is an efficient and practical experimental configuration for characterization of mode-II fracture and fatigue parameters. However, its roller-roller boundary condition is not applicable to real world problems. Thus, in future work, fatigue of both flat and post-buckled/curved specimens under clamped boundary conditions will be experimentally investigated for characterization of crack growth under realistic boundary conditions as illustrated in Fig 8.6. The experimental observations from these tests will provide a better understanding in realistic problems than those from conventional ENF tests.

Fatigue induced by inertially-applied high-frequency dynamic loading will also be investigated (see Figs 8.6c and 8.6d). Given that a majority of fatigue tests are conducted in a quasi-static manner (see Figs 8.6a and 8.6b) and that most of studies on dynamic delamination growth focus on impact loading conditions, these tests can provide a new perspective on experimental characterization of fatigue. The loading amplitudes required for these tests will be estimated based on stress analysis using the EAS model developed in this work.

The experimental results obtained from these tests will provide more practical benchmark data for model validation.

Bibliography

[1] S. Akbarov. *Stability Loss and Buckling Delamination: Three-Dimensional Linearized Approach for Elastic and Viscoelastic Composites.* Springer-Verlag, Berlin, Germany, 2013.

[2] M. Amabili. *Nonlinear Vibrations and Stability of Shells and Plates.* Cambridge University Press, New York, USA, 2008.

[3] U. Andelfinger and E . Ramm. EAS-elements for 2-dimensional, 3-dimensional, plate and shell structures and their equivalence to HR-elements. *International Journal For Numerical Methods In Engineering*, 36(8):1311–1337, 1993.

[4] T. L. Anderson. *Fracture Mechanics : Fundamentals and Applications.* Taylor & Francis, Boca Raton, USA, third edition, 2005.

[5] ASTM. Standard test method for mode I interlaminar fracture toughness of unidirectional fiber-reinforced polymer matrix composites, D5528 - 94A. Technical report, 1994.

[6] ASTM. Standard test method for mode I fatigue delamination growth onset of unidirectional fiber-reinforced polymer matrix composites, D6115 - 97. Technical report, 1997.

[7] ASTM. Standard test method for determination of the mode II interlaminar fracture toughness of unidirectional fiber-reinforced polymer matrix composite, D7905/D7905M - 14. Technical report, 2014.

[8] J. A. Bannantine, J. J. Comer, and J. L. Handrock. *Fundamentals of Metal Fatigue Analysis*. Prentice Hall, Englewood Cliffs, USA, 1990.

[9] J. Barlow. Optimal stress locations in finite element models. *International Journal for Numerical Methods in Engineering*, 10:243–251, 1976.

[10] K. Bathe. *Finite Element Procedures*. Prentice Hall, Englewood Cliffs, USA, 1996.

[11] K. Bathe and E. Dvorkin. A four-node plate bending element based on Mindlin/Reissner plate theory and a mixed interpolation. *International Journal for Numerical Methods in Engineering*, 21(2):367–383, 1985.

[12] Z. P. Bazant and J. Planas. *Fracture and Size Effect in Concrete and Other Quasibrittle Materials*. CRC Press, Boca Raton, USA, 1998.

[13] A. Beheshti and S. Ramezani. Nonlinear finite element analysis of functionally graded structures by enhanced assumed strain shell elements. *Applied Mathematical Modelling*, 39(13):3690–3703, 2015.

[14] T. Belytschko, W. K. Liu, B. Moran, and K. Elkhodary. *Nonlinear Finite Elements for Continua and Structures*. Wiley, Hoboken, USA, second edition, 2013.

[15] F. K. Bogner, R. L. Fox, and L. A. Schmidt, Jr. The generation of inter-element-compatible stiffness and mass matrices by the use of interpolation formulas. In *Proceedings of the Conference on Matrix Methods in Structural Mechanics*, Dayton, USA, 1965.

[16] E. Carrera. Theories and finite elements for multilayered plates and shells: a unified compact formulation with numerical assessment and benchmarking. *Archives of Computational Methods in Engineering*, 10(3):215–296, 2003.

[17] E. Carrera and S. Brischetto. A survey with numerical assessment of classical and refined theories for the analysis of sandwich plates. *Applied Mechanics Reviews*, 62(1):010803, 2009.

[18] Y. Chandra, R. Wiebe, I. Stanciulescu, L. N. Virgin, S. M. Spottswood, and T. G. Eason. Characterizing dynamic transitions associated with snap-through of clamped shallow arches. *Journal of Sound and Vibration*, 332(22):5837–5855, 2013.

[19] H. Y. Choi and F.-K. Chang. A model for predicting damage in graphite/epoxy laminated composites resulting from low-velocity point impact. *Journal of Composite Materials*, 26:2134–2169, 1992.

[20] A. K. Chopra. *Dynamics of Structures: Theory and Applications to Earthquake Engineering*. Prentice Hall, Upper Saddle River, USA, fourth edition, 2012.

[21] L. Demasi. Hierarchy plate theories for thick and thin composite plates: the generalized unified formulation. *Journal of Composite Structures*, 84:256–270, 2008.

[22] G. Dhatt, G. Touzot, and E. Lefrancois. *Finite Element Method*. Wiley, Hoboken, USA, 2012.

[23] E. Dvorkin and K. Bathe. A continuum mechanics based four-node shell element for general non-linear analysis. *Engineering Computations*, 1(1):77–88, 1984.

[24] T. Endo and H. Anzai. Redefined rainflow algorithm: P/V difference method. *Japan Society of Materials Science*, 30(328):89–93, 1981.

[25] D. Gay. *Composite Materials: Design and Applications*. CRC Press, Boca Raton, USA, 3rd edition, 2014.

[26] R. F. Gibson. *Principles of Composite Material Mechanics*. Taylor & Francis, Boca Raton, USA, third edition, 2012.

[27] R. W. Gordon and J. J. Hollkamp. Reduced-order models for acoustic response prediction, AFRL-RB-WP-TR-2011-3040. Technical report, United States Air Force Research Laboratory, Dayton, USA, 2011.

[28] M. Grediac and F. Hild. *Full-Field Measurements and Identification in Solid Mechanics*. John Wiley & Sons, Inc., Hoboken, USA, 2012.

[29] J. Hale. Boeing 787 from the ground up. *AERO magazine*, Q406:16–23, 2006.

[30] J. J. Hollkamp, P. J. O'Hara, and T. A. Wyen. Modeling damage within a reduced-order model framework: an application. In *Proceedings of the 54th AIAA/ASME/ASCE/AHS/ASC Structures, Structural Dynamics and Materials Conference, Boston, USA*, 2013.

[31] J. J. Hollkamp, R. A. Perez, and S. M. Spottswood. Design sensitivities of components using nonlinear reduced-order models and complex variables. In *Proceedings of the 35th IMAC, Society for Experimental Mechanics, Orange County, USA*, 2017.

[32] T. J. Hughes and T. Tezduyar. Finite elements based upon mindlin plate theory with particular reference to the four-node bilinear isoparametric element. *Journal of Applied Mechanics*, 48(3):587–596, 1981.

[33] ASTM International. Standard practices for cycle counting in fatigue analysis. *E1049 - 85(2017)*, pages 1–10, 2017.

[34] M. Kawai and M. Koizumi. Nonlinear constant fatigue life diagrams for carbon/epoxy laminates at room temperature. *Composites Part A*, 38(11):2342–2353, 2007.

[35] R. Khandan, S. Noroozi, P. Sewell, and J. Vinney. The development of laminated composite plate theories: a review. *Journal of Materials Science*, 47(16):5901–5910, 2012.

[36] A. Khennane. *Introduction to Finite Element Analysis Using MATLAB and Abaqus*. CRC Press, Boca Raton, USA, 2013.

[37] H.-G. Kim. Experimental nonlinear dynamics and snap-through of post-buckled thin laminated composite plates. Master's thesis, University of Washington, 2017.

[38] H.-G. Kim and R. Wiebe. Experimental nonlinear dynamics of laminated quasi-isotropic thin composite plates. In *Proceedings of the 34th IMAC, Society for Experimental Mechanics, Orlando, USA*, 2016.

[39] H.-G. Kim and R. Wiebe. Experimental nonlinear dynamics and snap-through of post-buckled composite plates. In *Proceedings of the 35th IMAC, Society for Experimental Mechanics, Orange County, USA*, 2017.

[40] K. D. Kim, S. C. Han, and S. Suthasupradit. Geometrically non-linear analysis of laminated composite structures using a 4-node co-rotational shell element with enhanced strains. *International Journal of Non-Linear Mechanics*, 42(6):864–881, 2007.

[41] Y Ko, P Lee, and K. Bathe. The MITC4 shell element and its performance. *Computers and Structures*, 169:57–68, 2016.

[42] Y Ko, P Lee, and K. Bathe. The MITC4+ shell element in geometric nonlinear analysis. *Computers and Structures*, 185:1–14, 2017.

[43] Y Ko, P Lee, and K. Bathe. A new 4-node MITC element for analysis of two-dimensional solids and its formulation in a shell element. *Computers and Structures*, 192:33–49, 2017.

[44] Y Ko, P Lee, and K. Bathe. A new MITC4+ shell element. *Computers and Structures*, 182:404–418, 2017.

[45] S. Kobayashi, S. Ogihara, and N. Takeda. Experimental and analytical characterization of matrix cracking in quasi-isotropic CFRP laminates with interlaminar-toughened layers under fatigue loading. *Science and Engineering of Composite Materials*, 9(2):45–54, 2000.

[46] S. Kobayashi, S. Ogihara, and N. Takeda. Experimental characterization of the effects of stacking sequence on the transverse crack behavior in quasi-isotropic interleaved CFRP laminates. *Advanced Composite Materials*, 9(3):241–251, 2000.

[47] B. Landry and G. LaPlante. Modeling delamination growth in composites under fatigue loadings of varying amplitudes. *Composites: Part B*, 43:533–541, 2012.

[48] L. E. Malvern. *Introduction to the Mechanics of a Continuous Medium*. Prentice-Hall, Englewood Cliffs, USA, 1969.

[49] MathWorks. *MATLAB R2018a*. 2018.

[50] R. J. Melosh. Basis of derivation of matrices for the direct stiffness method. *AIAA Journal*, 1(7):1631–1637, 1963.

[51] R. D. Mindlin. Influence of rotatory inertia and shear in flexural motions of isotropic elastic plates. *Journal of Applied Mechanics*, 18:1031–1036, 1951.

[52] H. Murakami. Laminated composite plate theory with improved in-plane responses. *Journal of Applied Mechanics*, 53(3):661–666, 1986.

[53] N. M. Newmark. A method of computation for structural dynamics. *Journal of the Engineering Mechanics Division*, 85(3):67–94, 1959.

[54] L. Nicolais, M. Meo, and E. Milella. *Composite Materials : a Vision for the Future*. Springer, New York, USA, 2011.

[55] P. J. O'Hara and J. J. Hollkamp. A Coupled approach for modeling damage within a reduced-order model frame work. In *54th AIAA/ASME/ASCE/AHS/ASC Structures, Structural Dynamics, and Materials Conference, Boston, USA*, 2013.

[56] P. J. O'Hara and J. J. Hollkamp. Modeling crack propagation within a reduced-order model framework. In *Proceedings of the 55th AIAA/ASME/ASCE/AHS/ASC Structures, Structural Dynamics and Materials Conference, National Harbor, USA*, 2014.

[57] P. J. O'Hara and J. J. Hollkamp. Modeling crack propagation in a Ti-Alloy at elevated temperature within a reduced-order model framework. In *57th AIAA/ASCE/AHS/ASC Structures, Structural Dynamics, and Materials Conference, San Diego, USA*, 2016.

[58] P. Paultre. *Dynamics of Structures*. John Wiley & Sons, Inc., Hoboken, USA, 2010.

[59] R. A. Perez. *Multiscale reduced order models for the geometrically nonlinear response of complex structures*. PhD thesis, Arizona State University, 2012.

[60] R. A. Perez, S. M. Spottswood, and T. J. Beberniss. Nonlinear response prediction of a buckled panel in a supersonic flow. In *Proceedings of the 35th IMAC, Society for Experimental Mechanics, Orange County, USA*, 2017.

[61] R. V. Petrescu and F. I. Petrescu. *Lockheed Martin*. Books on Demand GmbH , Norderstedt, Germany, 2012.

[62] T. H. H. Pian and K. Sumihara. Rational approach for assumed stress finite elements. *International Journal for Numerical Methods in Engineering*, 20:1685–1695, 1984.

[63] Gangan Prathap and C. Ramesh Babu. Field-consistency and violent stress oscillations in the finite element method. *International Journal For Numerical Methods In Engineering*, 24(10):2017–2033, 1987.

[64] MacNeal R. H. A simple quadrilateral shell element. *Computers and Structures*, 8:175–183, 1978.

[65] M. N. Rao, R. Schmidt, and K. U. Schröder. Geometrically nonlinear static fe-simulation of multilayered magneto-electro-elastic composite structures. *Composite Structures*, 127:120–131, 2015.

[66] ADINA R&D, Inc. *ADINA 9.5*. 2019.

[67] J. N. Reddy. A generalization of two-dimensional theories of laminated composite plates. *Communications in Applied Numerical Methods*, 3:173–180, 1987.

[68] J. N. Reddy. *Mechanics of Laminated Composite Plates and Shells: Theory and Analysis*. CRC Press, Boca Raton, USA, second edition, 2004.

[69] J. N. Reddy. *An Introduction to the Finite Element Method*. McGraw-Hill Higher Education, New York, USA, third edition, 2006.

[70] J. N. Reddy. *An Introduction to Nonlinear Finite Element Analysis : with Applications to Heat Transfer, Fluid Mechanics, and Solid Mechanics*. Oxford University Press, Oxford, UK, second edition, 2014.

[71] J. Reinoso and A. Blázquez. Geometrically nonlinear analysis of functionally graded power-based and carbon nanotubes reinforced composites using a fully integrated solid shell element. *Composite Structures*, 152:277–294, 2016.

[72] E. Reissner. The effect of transverse shear deformation on the bending of elastic plates. *Journal of Applied Mechanics*, 12:69–76, 1945.

[73] D. H. Robbins. *Hierarchical modeling of laminated composite plates using variable kinematic finite elements and mesh superposition*. PhD thesis, Virginia Polytechnic Institute and State University, 1993.

[74] D. H. Robbins and J. N. Reddy. Variable kinematic modelling of laminated composite plates. *International Journal for numerical methods in engineering*, 39:2283–2317, 1996.

[75] D. H. Robbins, J. N. Reddy, and F. Rostam-Abadi. Layerwise modeling of progressive damage in fiber-reinforced composite laminates. *International Journal for mechanics and materials in design*, 2(3):165–182, 2005.

[76] M. Salviato, K. Kirane, and Z. P. Bazant. Statistical distribution and size effect of residual strength of quasibrittle materials after a period of constant load. *Journal of the Mechanics and Physics of Solids*, 64:440–454, 2014.

[77] M. Salviato, K. Kirane, S. Esna Ashari, Z. P. Bazant, and G. Cusatis. Experimental and numerical investigation of intra-laminar energy dissipation and size effect in two-dimensional textile composites. *Composites Science and Technology*, 135:67–75, 2016.

[78] K. H. Schweizerhof and P. Wriggers. Consistent linearization for path following methods in nonlinear FE analysis. *Computer Methods in Applied Mechanics and Engineering*, 59(3):261–279, 1986.

[79] J. C. Simo and F. Armero. Geometrically nonlinear enhanced strain mixed methods and the method of incompatible modes. *International Journal For Numerical Methods In Engineering*, 33(7):1413–1449, 1992.

[80] J. C. Simo and T. J. R. Hughes. On the variational foundations of assumed strain methods. *Journal of Applied Mechanics*, 53:51–54, 1986.

[81] J. C. Simo and M. S. Rifai. A class of mixed assumed strain methods and the method of incompatible modes. *International Journal For Numerical Methods In Engineering*, 29(8):1595–1638, 1990.

[82] S. Sridharan. *Delamination Behaviour of Composites*. Woodhead Publishing, Oxford, UK, 2008.

[83] W. H. Stillwell. *X-15 Research Results, with a Selected Bibliography*. National Aeronautics Space Administration, Washington, D.C., USA, 1965.

[84] H. Stolarski and T. Belytschko. Shear and membrane locking in curved c0 elements. *Computer methods in applied mechanics and engineering*, 41(3):279–296, 1983.

[85] S. H. Strogatz. *Nonlinear Dynamics and Chaos: with Applications to Physics, Biology, Chemistry, and Engineering*. Westview Press, Boulder, USA, second edition, 2015.

[86] A. B. Strong. *Fundamentals of Composites Manufacturing: Materials, Methods and Applications*. Society of Manufacturing Engineers, Dearborn, USA, second edition, 2008.

[87] Dassault Systemes. *Abaqus 2019*. 2019.

[88] R. L. Taylor, P. J. Beresford, and E. L. Wilson. A non-conforming element for stress analysis. *International Journal for numerical methods in Engineering*, 10:1211–1219, 1976.

[89] S. Timoshenko and S. Woinowsky-Krieger. *Theory of plates and shells*. McGraw-Hill, New York, USA, second edition, 1959.

[90] M. E. Tuttle. *Structural Analysis of Polymeric Composite Materials*. CRC Press, Boca Raton, USA, third edition, 2013.

[91] A. P. Vassilopoulos. *Fatigue Life Prediction of Composites and Composite Structures*. Woodhead Publishing, Oxford, UK, 2010.

[92] C. M. Wang, J. N. Reddy, and K. H. Lee. *Shear Deformable Beams and Plates: Relationships with Classical Solutions*. Elsevier, New York, USA, 2000.

[93] K. Washizu. *Variational Methods in Elasticity and Plasticity*. Pergamon Press, New York, USA, second edition, 1975.

[94] K. Washizu. *Variational Methods in Elasticity and Plasticity*. Pergamon Press, New York, USA, third edition, 1982.

[95] R. Wiebe and S. M. Spottswood. Co-existing responses and stochastic resonance in post-buckled structures: a combined numerical and experimental study. *Journal of Sound and Vibration*, 333(19):4682–4694, 2014.

[96] R. Wiebe and S. M. Spottswood. On the dimension of complex responses in nonlinear structural vibrations. *Journal of Sound and Vibration*, 373:192–204, 2016.

[97] R. Wiebe and L. N. Virgin. A harmonic balance approximation of dynamic snap-through boundaries in a single-degree-of-freedom structure. In *Proceedings of the ASME Design Engineering Technical Conference*, volume 7, Oregon, USA, 2013.

[98] R. Wiebe, L. N. Virgin, I. Stanciulescu, S. M. Spottswood, and T. G. Eason. Characterizing dynamic transitions associated with snap-through: a discrete system. *Journal of Computational and Nonlinear Dynamics*, 8(1):011010, 2013.

[99] E. L. Wilson, R. L. Taylor, W. P. Doherty, and J. Ghaboussi. Incompatible displacement models. *Numerical and computer methods in structural mechanics*, pages 43–57, 1973.

[100] D. Xie and A. M. Waas. Discrete cohesive zone model for mixed-mode fracture using finite element analysis. *Engineering fracture mechanics*, 73:1783–1796, 2006.

[101] Q. Yang and B. Cox. Cohesive models for damage evolution in laminated composites. *International Journal of Fracture*, 133(2):107–137, 2005.

[102] E. Zappino, G. L. A. Pagani, and E. Carrera. Global-local analysis of laminated plates by node-dependent kinematic finite elements with variable ESL/LW capabilities. *Journal of Composite Structures*, 172:1–14, 2017.

[103] O. C. Zienkiewicz and Y. K. Cheung. The finite element model for analysis of elastic isotropic and orthotropic slabs. In *Proceedings of the Institution of Civil Engineers*, London, UK, 1964.

[104] M. Zoghi. *The International Handbook of FRP Composites in Civil Engineering*. CRC Press, Boca Raton, USA, 2014.

[105] Y. Zou, L. Tong, and G. P. Steven. Vibration-based model-dependent damage delamination identification and health monitoring for composite structures - a review. *Journal of Sound and Vibration*, 230(2):357–378, 2000.

Appendix A

ESTIMATIONS OF THE TRANSVERSE SHEAR MODULI OF A PLAIN-WEAVE PREPREG T800H-6K/3900-2

The material properties of woven prepregs are typically not found in the literature due to difficulty in obtaining them from the complex 3-D patterns of their fibers. The plain-weave prepreg T800H-6K/3900-2 used in this work is unfortunately not an exception. To address this issue, previous work [37] estimated the in-plane properties of the plain-weave prepreg using the reported properties of a unidirectional prepreg which consists of the fibers and epoxy of the plain-weave one. In this appendix, the transverse shear moduli (G_{13} and G_{23}) of the plain-weave prepreg are estimated.

The material properties of the unidirectional prepreg are reported in the work of Kobayashi et al. [46]:

$$\begin{aligned} &E_{11}^{\mathrm{u}} = 143 \text{ GPa}, \ E_{22}^{\mathrm{u}} = E_{33}^{\mathrm{u}} = 7.99 \text{ GPa}, \ G_{12}^{\mathrm{u}} = G_{13}^{\mathrm{u}} = 3.96 \text{ GPa}, \\ &\nu_{12}^{\mathrm{u}} = \nu_{13}^{\mathrm{u}} = 0.345, \text{ and } \nu_{23}^{\mathrm{u}} = \nu_{32}^{\mathrm{u}} = 0.490, \end{aligned} \tag{A.1}$$

where the superscript u denotes the material properties of the unidirectional prepreg. It was assumed in Ref [37] that the material properties of the weave prepreg (thickness h) can be estimated by calculating the material properties of a symmetric laminate having n unidirectional layers (thickness h/n) as illustrated in Fig A.1. The laminate comprises $\frac{n}{2}$ layers of 0-degree fibers and $\frac{n}{2}$ layers of 90-degree fibers. The estimated in-plane properties (E_{11}, E_{22}, G_{12} and ν_{12}, see Eq (2.1)) were validated in the work using the experimental data of tensile-load (or pulling), static-cantilever, and free-vibration tests of specimens which were fabricated with the plain-weave prepreg.

This work adopted this assumption to estimate the transverse shear moduli (G_{13} and

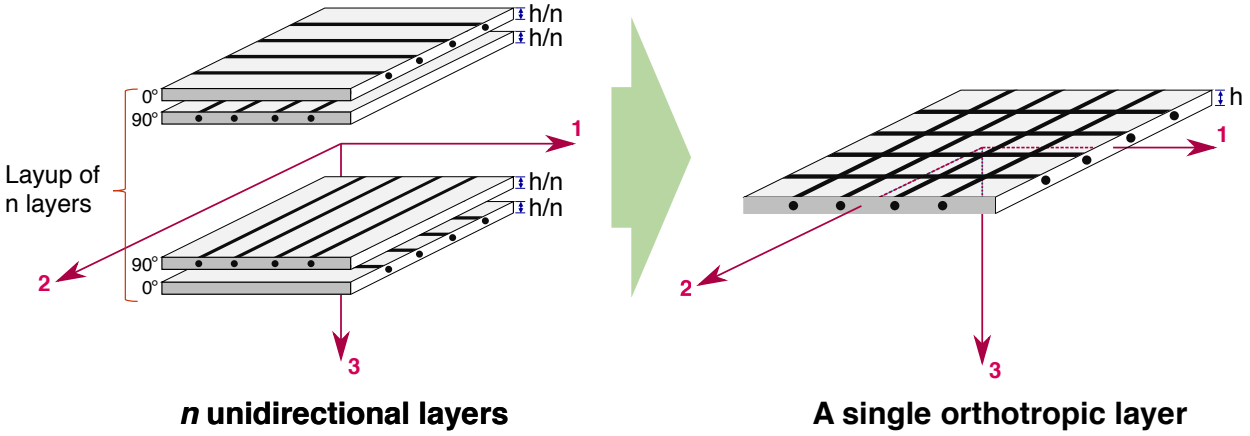

Figure A.1: A symmetric laminate consisting of n unidirectional laminae and its corresponding orthotropic lamina. The material axes are denoted by 1-, 2-, and 3-axes. The fiber angles are calculated from the 1-axis.

G_{23}) of the plain-weave prepreg. The unidirectional prepreg is transversely isotropic (i.e., isotropic in the 2-3 plane) and thus the following well-known relation of isotropic materials is valid for the unidirectional one in the 2–3 plane [26]:

$$G_{23}^{\mathrm{u}} = \frac{E_{22}^{\mathrm{u}}}{2(1+\nu_{32}^{\mathrm{u}})} = 2.68 \text{ GPa}. \tag{A.2}$$

Considering that the plain-weave prepreg was assumed to comprise an identical number of layers of 0- and 90-degree fibers, the transverse shear moduli of the prepreg can be estimated as

$$G_{13} = G_{23} = \frac{G_{13}^{\mathrm{u}} + G_{23}^{\mathrm{u}}}{2} = 3.32 \text{ GPa}. \tag{A.3}$$

Appendix B

LAMINA AND LAMINATE CONSTITUTIVE RELATIONS

The laminated composite specimen introduced in Chapter 2 has orthtropic material properties. This appendix presents lamina and laminate constitutive relations for orthotropic materials following the works of Reddy [68] and Tuttle [90].

B.1 Lamina constitutive relation for a specially orthotropic lamina

In the case where the material axes of an orthotropic lamina (1-, 2-, and 3-axes) coincide with the spatial axes (x-, y-, and z-axes), the lamina is called a specially orthotropic lamina [26]. Hooke's law for a specially orthotropic lamina is given by

$$\begin{Bmatrix} \varepsilon_{11} \\ \varepsilon_{22} \\ \varepsilon_{33} \\ \gamma_{23} \\ \gamma_{13} \\ \gamma_{12} \end{Bmatrix} = \begin{bmatrix} S_{11} & S_{12} & S_{13} & 0 & 0 & 0 \\ S_{12} & S_{22} & S_{23} & 0 & 0 & 0 \\ S_{13} & S_{23} & S_{33} & 0 & 0 & 0 \\ 0 & 0 & 0 & S_{44} & 0 & 0 \\ 0 & 0 & 0 & 0 & S_{55} & 0 \\ 0 & 0 & 0 & 0 & 0 & S_{66} \end{bmatrix} \begin{Bmatrix} \sigma_{11} \\ \sigma_{22} \\ \sigma_{33} \\ \tau_{23} \\ \tau_{13} \\ \tau_{12} \end{Bmatrix}, \tag{B.1}$$

where

$$\begin{aligned} &S_{11} = \frac{1}{E_{11}}, \quad S_{22} = \frac{1}{E_{22}}, \quad S_{33} = \frac{1}{E_{33}}, \\ &S_{44} = \frac{1}{G_{23}}, \quad S_{55} = \frac{1}{G_{13}}, \quad S_{66} = \frac{1}{G_{12}}, \\ &S_{21} = S_{12} = \frac{-\nu_{12}}{E_{11}} = \frac{-\nu_{21}}{E_{22}}, \quad S_{31} = S_{13} = \frac{-\nu_{13}}{E_{11}} = \frac{-\nu_{31}}{E_{33}}, \\ &S_{32} = S_{23} = \frac{-\nu_{23}}{E_{22}} = \frac{-\nu_{32}}{E_{33}}. \end{aligned} \tag{B.2}$$

To obtain a stress-strain relationship, that is,

$$\boldsymbol{\sigma} = \boldsymbol{C}\boldsymbol{\varepsilon}, \tag{B.3}$$

Eq (B.1) is inverted into

$$\begin{Bmatrix} \sigma_{11} \\ \sigma_{22} \\ \sigma_{33} \\ \tau_{23} \\ \tau_{13} \\ \tau_{12} \end{Bmatrix} = \begin{bmatrix} C_{11} & C_{12} & C_{13} & 0 & 0 & 0 \\ C_{12} & C_{22} & C_{23} & 0 & 0 & 0 \\ C_{13} & C_{23} & C_{33} & 0 & 0 & 0 \\ 0 & 0 & 0 & C_{44} & 0 & 0 \\ 0 & 0 & 0 & 0 & C_{55} & 0 \\ 0 & 0 & 0 & 0 & 0 & C_{66} \end{bmatrix} \begin{Bmatrix} \varepsilon_{11} \\ \varepsilon_{22} \\ \varepsilon_{33} \\ \gamma_{23} \\ \gamma_{13} \\ \gamma_{12} \end{Bmatrix}, \tag{B.4}$$

where the elastic coefficients C_{ij} of a specially orthotropic lamina are given by

$$\begin{aligned} &C_{11} = \frac{S_{22}S_{33} - S_{23}^2}{\hat{S}}, \quad C_{12} = \frac{S_{13}S_{23} - S_{12}S_{33}}{\hat{S}}, \quad C_{13} = \frac{S_{12}S_{23} - S_{13}S_{22}}{\hat{S}}, \\ &C_{22} = \frac{S_{11}S_{33} - S_{13}^2}{\hat{S}}, \quad C_{23} = \frac{S_{12}S_{13} - S_{11}S_{23}}{\hat{S}}, \quad C_{33} = \frac{S_{11}S_{22} - S_{12}^2}{\hat{S}}, \\ &C_{44} = \frac{1}{S_{44}}, \quad C_{55} = \frac{1}{S_{55}}, \quad C_{66} = \frac{1}{S_{66}}, \\ &\hat{S} = S_{11}S_{22}S_{33} - S_{11}S_{23}^2 - S_{22}S_{13}^2 - S_{33}S_{12}^2 + 2S_{12}S_{13}S_{23}. \end{aligned} \tag{B.5}$$

B.2 Lamina constitutive relation for a generally orthotropic lamina

In cases where the material and geometric axes of an orthotropic lamina differ, the lamina is called a generally orthotropic lamina [26]. The elastic coefficients matrix $\bar{\boldsymbol{C}}$ of a generally orthotropic lamina can be obtained by transforming $\boldsymbol{C}$ in Eq (B.4) as

$$\bar{\boldsymbol{C}} = \boldsymbol{T}\boldsymbol{C}\boldsymbol{T}^T, \tag{B.6}$$

where

$$\boldsymbol{T} = \begin{bmatrix} \cos^2\theta & \sin^2\theta & 0 & 0 & 0 & -\sin 2\theta \\ \sin^2\theta & \cos^2\theta & 0 & 0 & 0 & \sin 2\theta \\ 0 & 0 & 1 & 0 & 0 & 0 \\ 0 & 0 & 0 & \cos\theta & \sin\theta & 0 \\ 0 & 0 & 0 & -\sin\theta & \cos\theta & 0 \\ \sin\theta\cos\theta & -\sin\theta\cos\theta & 0 & 0 & 0 & \cos^2\theta - \sin^2\theta \end{bmatrix}, \tag{B.7}$$

where θ is an angle between the material and geometric axes.

Using this transformation, the stress-strain relationship of a generally orthotropic lamina is given by

$$\begin{Bmatrix} \sigma_{xx} \\ \sigma_{yy} \\ \sigma_{zz} \\ \sigma_{yz} \\ \sigma_{xz} \\ \sigma_{xy} \end{Bmatrix} = \begin{bmatrix} \bar{C}_{11} & \bar{C}_{12} & \bar{C}_{13} & 0 & 0 & \bar{C}_{16} \\ \bar{C}_{21} & \bar{C}_{22} & \bar{C}_{23} & 0 & 0 & \bar{C}_{26} \\ \bar{C}_{31} & \bar{C}_{32} & \bar{C}_{33} & 0 & 0 & \bar{C}_{36} \\ 0 & 0 & 0 & \bar{C}_{44} & \bar{C}_{45} & 0 \\ 0 & 0 & 0 & \bar{C}_{45} & \bar{C}_{55} & 0 \\ \bar{C}_{16} & \bar{C}_{26} & \bar{C}_{36} & 0 & 0 & \bar{C}_{66} \end{bmatrix} \begin{Bmatrix} \varepsilon_{xx} \\ \varepsilon_{yy} \\ \varepsilon_{zz} \\ \gamma_{yz} \\ \gamma_{xz} \\ \gamma_{xy} \end{Bmatrix}. \tag{B.8}$$

In the event that ε_{zz} is small and can be neglected (consequently, σ_{zz} also disappears from the strain energy formula), Eq (B.8) can be reduced to

$$\begin{Bmatrix} \sigma_{xx} \\ \sigma_{yy} \\ \sigma_{xy} \\ \sigma_{xz} \\ \sigma_{yz} \end{Bmatrix} = \begin{bmatrix} \bar{C}_{11} & \bar{C}_{12} & \bar{C}_{16} & 0 & 0 \\ \bar{C}_{12} & \bar{C}_{22} & \bar{C}_{26} & 0 & 0 \\ \bar{C}_{16} & \bar{C}_{26} & \bar{C}_{66} & 0 & 0 \\ 0 & 0 & 0 & \bar{C}_{55} & \bar{C}_{45} \\ 0 & 0 & 0 & \bar{C}_{45} & \bar{C}_{44} \end{bmatrix} \begin{Bmatrix} \varepsilon_{xx} \\ \varepsilon_{yy} \\ \gamma_{xy} \\ \gamma_{xz} \\ \gamma_{yz} \end{Bmatrix}. \tag{B.9}$$

B.3 Laminate constitutive relation

In this section, membrane, bending, and shear stress resultants ($\boldsymbol{N}$, $\boldsymbol{M}$, and $\boldsymbol{Q}$, respectively) of a laminate having N layers of orthotropic laminae and thickness h are presented in terms of a transformed elastic coefficient matrix $\bar{\boldsymbol{C}}$ and strain fields.

B.3.1 In-plane stress resultants N_{xx}, N_{yy}, N_{xy}

$$
\begin{aligned}
\begin{Bmatrix} N_{xx} \\ N_{yy} \\ N_{xy} \end{Bmatrix} &= \int_{-\frac{h}{2}}^{\frac{h}{2}} \begin{Bmatrix} \sigma_{xx} \\ \sigma_{yy} \\ \sigma_{xy} \end{Bmatrix} dz = \sum_{k=1}^{N} \int_{z_k}^{z_{k+1}} \begin{Bmatrix} \sigma_{xx} \\ \sigma_{yy} \\ \sigma_{xy} \end{Bmatrix}^{(k)} dz \\
&= \sum_{k=1}^{N} \int_{z_k}^{z_{k+1}} \begin{bmatrix} \bar{C}_{11} & \bar{C}_{12} & \bar{C}_{16} \\ \bar{C}_{12} & \bar{C}_{22} & \bar{C}_{26} \\ \bar{C}_{16} & \bar{C}_{26} & \bar{C}_{66} \end{bmatrix}^{(k)} \begin{Bmatrix} \varepsilon_{xx} \\ \varepsilon_{yy} \\ \gamma_{xy} \end{Bmatrix}^{(k)} dz \\
&= \sum_{k=1}^{N} \int_{z_k}^{z_{k+1}} \begin{bmatrix} \bar{C}_{11} & \bar{C}_{12} & \bar{C}_{16} \\ \bar{C}_{12} & \bar{C}_{22} & \bar{C}_{26} \\ \bar{C}_{16} & \bar{C}_{26} & \bar{C}_{66} \end{bmatrix}^{(k)} \begin{Bmatrix} \varepsilon_{xx}^{(0)} + z\varepsilon_{xx}^{(1)} \\ \varepsilon_{yy}^{(0)} + z\varepsilon_{yy}^{(1)} \\ \gamma_{xy}^{(0)} + z\gamma_{xy}^{(1)} \end{Bmatrix}^{(k)} dz \\
&= \begin{bmatrix} A_{11} & A_{12} & A_{16} \\ A_{12} & A_{22} & A_{26} \\ A_{16} & A_{26} & A_{66} \end{bmatrix} \begin{Bmatrix} \varepsilon_{xx}^{(0)} \\ \varepsilon_{yy}^{(0)} \\ \gamma_{xy}^{(0)} \end{Bmatrix} + \begin{bmatrix} B_{11} & B_{12} & B_{16} \\ B_{12} & B_{22} & B_{26} \\ B_{16} & B_{26} & B_{66} \end{bmatrix} \begin{Bmatrix} \varepsilon_{xx}^{(1)} \\ \varepsilon_{yy}^{(1)} \\ \gamma_{xy}^{(1)} \end{Bmatrix},
\end{aligned}
\tag{B.10}
$$

where

$$
A_{ij} = \sum_{k=1}^{N} \int_{z_k}^{z_{k+1}} \bar{C}_{ij}^{(k)} dz, \qquad B_{ij} = \sum_{k=1}^{N} \int_{z_k}^{z_{k+1}} z\bar{C}_{ij}^{(k)} dz, \tag{B.11}
$$

where the membrane strains ($\varepsilon_{xx}^{(0)}$, $\varepsilon_{yy}^{(0)}$, $\gamma_{xy}^{(0)}$) and the bending strains ($\varepsilon_{xx}^{(1)}$, $\varepsilon_{yy}^{(1)}$, $\gamma_{xy}^{(1)}$) are defined in Eqs (4.4), (4.5) and (4.7).

B.3.2 Bending stress resultants M_{xx}, M_{yy}, M_{xy}

$$\begin{aligned}
\begin{Bmatrix} M_{xx} \\ M_{yy} \\ M_{xy} \end{Bmatrix} &= \int_{-\frac{h}{2}}^{\frac{h}{2}} z \begin{Bmatrix} \sigma_{xx} \\ \sigma_{yy} \\ \sigma_{xy} \end{Bmatrix} dz = \sum_{k=1}^{N} \int_{z_k}^{z_{k+1}} z \begin{Bmatrix} \sigma_{xx} \\ \sigma_{yy} \\ \sigma_{xy} \end{Bmatrix}^{(k)} dz \\
&= \sum_{k=1}^{N} \int_{z_k}^{z_{k+1}} z \begin{bmatrix} \bar{C}_{11} & \bar{C}_{12} & \bar{C}_{16} \\ \bar{C}_{12} & \bar{C}_{22} & \bar{C}_{26} \\ \bar{C}_{16} & \bar{C}_{26} & \bar{C}_{66} \end{bmatrix}^{(k)} \begin{Bmatrix} \varepsilon_{xx} \\ \varepsilon_{yy} \\ \gamma_{xy} \end{Bmatrix}^{(k)} dz \\
&= \sum_{k=1}^{N} \int_{z_k}^{z_{k+1}} z \begin{bmatrix} \bar{C}_{11} & \bar{C}_{12} & \bar{C}_{16} \\ \bar{C}_{12} & \bar{C}_{22} & \bar{C}_{26} \\ \bar{C}_{16} & \bar{C}_{26} & \bar{C}_{66} \end{bmatrix}^{(k)} \begin{Bmatrix} \varepsilon_{xx}^{(0)} + z\varepsilon_{xx}^{(1)} \\ \varepsilon_{yy}^{(0)} + z\varepsilon_{yy}^{(1)} \\ \gamma_{xy}^{(0)} + z\gamma_{xy}^{(1)} \end{Bmatrix}^{(k)} dz \\
&= \begin{bmatrix} B_{11} & B_{12} & B_{16} \\ B_{12} & B_{22} & B_{26} \\ B_{16} & B_{26} & B_{66} \end{bmatrix} \begin{Bmatrix} \varepsilon_{xx}^{(0)} \\ \varepsilon_{yy}^{(0)} \\ \gamma_{xy}^{(0)} \end{Bmatrix} + \begin{bmatrix} D_{11} & D_{12} & D_{16} \\ D_{12} & D_{22} & D_{26} \\ D_{16} & D_{26} & D_{66} \end{bmatrix} \begin{Bmatrix} \varepsilon_{xx}^{(1)} \\ \varepsilon_{yy}^{(1)} \\ \gamma_{xy}^{(1)} \end{Bmatrix},
\end{aligned} \tag{B.12}$$

where

$$D_{ij} = \sum_{k=1}^{N} \int_{z_k}^{z_{k+1}} z^2 \bar{C}_{ij}^{(k)} dz. \tag{B.13}$$

B.3.3 Transverse shear stress resultants Q_{yz}, Q_{xz}

$$\begin{aligned}
\begin{Bmatrix} Q_{yz} \\ Q_{xz} \end{Bmatrix} &= K \int_{-\frac{h}{2}}^{\frac{h}{2}} \begin{Bmatrix} \sigma_{yz} \\ \sigma_{xz} \end{Bmatrix} dz = \sum_{k=1}^{N} K \int_{z_k}^{z_{k+1}} \begin{Bmatrix} \sigma_{yz} \\ \sigma_{xz} \end{Bmatrix}^{(k)} dz \\
&= \sum_{k=1}^{N} K \int_{z_k}^{z_{k+1}} \begin{bmatrix} \bar{C}_{44} & \bar{C}_{45} \\ \bar{C}_{45} & \bar{C}_{55} \end{bmatrix}^{(k)} \begin{Bmatrix} \gamma_{yz} \\ \gamma_{xz} \end{Bmatrix}^{(k)} dz \\
&= \sum_{k=1}^{N} K \int_{z_k}^{z_{k+1}} \begin{bmatrix} \bar{C}_{44} & \bar{C}_{45} \\ \bar{C}_{45} & \bar{C}_{55} \end{bmatrix}^{(k)} \begin{Bmatrix} \gamma_{yz}^{(0)} \\ \gamma_{xz}^{(0)} \end{Bmatrix}^{(k)} dz \\
&= K \begin{bmatrix} A_{44} & A_{45} \\ A_{45} & A_{55} \end{bmatrix} \begin{Bmatrix} \gamma_{yz}^{(0)} \\ \gamma_{xz}^{(0)} \end{Bmatrix},
\end{aligned} \tag{B.14}$$

where K is a shear correction coefficient and the transverse shear strains ($\gamma_{xz}^{(0)}$, $\gamma_{yz}^{(0)}$) are defined in Eqs (4.8) and (4.9).

Appendix C
VON KÁRMÁN STRAINS

The CLPT and FSDT models of this work adopted von Kármán strains to include geometric nonlinearity in the models. This appendix presents von Kármán strains following the works of Malvern [48] and Reddy [68].

C.1 Green-Lagrange (large) strains

Nonlinear strains based on the Green-Lagrange strain tensor are given by

$$E_{ij} = \frac{1}{2}\left(\frac{\partial u_i}{\partial X_j} + \frac{\partial u_j}{\partial X_i} + \frac{\partial u_k}{\partial X_i}\frac{\partial u_k}{\partial X_j}\right) \text{ for } i = 1, 2, 3, \tag{C.1}$$

where u_i are displacement components, and X_i are material coordinates. The material coordinates are related to spatial coordinates x_i by

$$x_i = X_i + u_i. \tag{C.2}$$

C.2 Small strains

If the partial derivatives of the displacements u_i with respect to the material coordinates X_i are all small compared to unity, that is,

$$\frac{\partial u_i}{\partial X_i} \ll 1 \text{ for } i = 1, 2, 3, \tag{C.3}$$

the squares and products of these derivatives may be neglected in comparison to the linear terms. Thus, the nonlinear strains in Eq (C.1) can be reduced to linear strains given in

Eq (C.4).

$$\varepsilon_{ij} = \frac{1}{2}\Big(\frac{\partial u_i}{\partial x_j} + \frac{\partial u_j}{\partial x_i}\Big) \text{ for } i = 1, 2, 3, \tag{C.4}$$

or in an expanded form,

$$\begin{aligned} &\varepsilon_{xx} = \frac{\partial u}{\partial x}, \quad \varepsilon_{yy} = \frac{\partial v}{\partial y}, \quad \varepsilon_{zz} = \frac{\partial w}{\partial z}, \\ &\varepsilon_{xy} = \frac{1}{2}\Big(\frac{\partial u}{\partial y} + \frac{\partial v}{\partial x}\Big), \quad \varepsilon_{xz} = \frac{1}{2}\Big(\frac{\partial u}{\partial z} + \frac{\partial w}{\partial x}\Big), \quad \varepsilon_{yz} = \frac{1}{2}\Big(\frac{\partial v}{\partial z} + \frac{\partial w}{\partial y}\Big). \end{aligned} \tag{C.5}$$

C.3 von Kármán strains

In cases where the rotations $\frac{\partial w}{\partial x}$ and $\frac{\partial w}{\partial y}$ of the transverse normal plane are moderate 10^o-15^o, while strains are small, the following terms are small but not negligible:

$$\Big(\frac{\partial w}{\partial x}\Big)^2, \quad \Big(\frac{\partial w}{\partial y}\Big)^2, \quad \frac{\partial w}{\partial x}\frac{\partial w}{\partial y}. \tag{C.6}$$

Therefore, for small strains and moderate rotations, the strain-displacement relations are given by

$$\begin{aligned} &\varepsilon_{xx} = \frac{\partial u}{\partial x} + \frac{1}{2}\Big(\frac{\partial w}{\partial x}\Big)^2, \quad \varepsilon_{yy} = \frac{\partial v}{\partial y} + \frac{1}{2}\Big(\frac{\partial w}{\partial y}\Big)^2, \quad \varepsilon_{zz} = \frac{\partial w}{\partial z}, \\ &\varepsilon_{xy} = \frac{1}{2}\Big(\frac{\partial u}{\partial y} + \frac{\partial v}{\partial x} + \frac{\partial w}{\partial x}\frac{\partial w}{\partial y}\Big), \quad \varepsilon_{xz} = \frac{1}{2}\Big(\frac{\partial u}{\partial z} + \frac{\partial w}{\partial x}\Big), \quad \varepsilon_{yz} = \frac{1}{2}\Big(\frac{\partial v}{\partial z} + \frac{\partial w}{\partial y}\Big). \end{aligned} \tag{C.7}$$

These relations are called von Kármán strains.

Appendix D

FSDT: DERIVATION OF NONLINEAR EQUATIONS OF MOTION

In this appendix, the equations of motion for FSDT are derived from the principle of virtual displacements given in Eqs (4.10) to (4.14), following the work of Reddy [68].

D.1 Virtual strain energy δU

$$
\begin{aligned}
\delta U &= \int_{\Omega_0}\int_{-\frac{h}{2}}^{\frac{h}{2}} \Big\{\sigma_{xx}\delta\varepsilon_{xx} + \sigma_{yy}\delta\varepsilon_{yy} + \sigma_{xy}\delta\gamma_{xy} + \sigma_{xz}\delta\gamma_{xz} + \sigma_{yz}\delta\gamma_{yz}\Big\} dz dx dy \\
&= \int_{\Omega_0}\int_{-\frac{h}{2}}^{\frac{h}{2}} \Big\{\sigma_{xx}\Big[\Big(\frac{\partial\delta u_0}{\partial x} + \frac{\partial\delta w_0}{\partial x}\frac{\partial w_0}{\partial x}\Big) + z\Big(\frac{\partial\delta\phi_x}{\partial x}\Big)\Big] \\
&\qquad + \sigma_{yy}\Big[\Big(\frac{\partial\delta v_0}{\partial y} + \frac{\partial\delta w_0}{\partial y}\frac{\partial w_0}{\partial y}\Big) + z\Big(\frac{\partial\delta\phi_y}{\partial y}\Big)\Big] \\
&\qquad + \sigma_{xy}\Big[\Big(\frac{\partial\delta u_0}{\partial y} + \frac{\partial\delta v_0}{\partial x} + \frac{\partial\delta w_0}{\partial x}\frac{\partial w_0}{\partial y} + \frac{\partial w_0}{\partial x}\frac{\partial\delta w_0}{\partial y}\Big) \\
&\qquad + z\Big(\frac{\partial\delta\phi_x}{\partial y} + \frac{\partial\delta\phi_y}{\partial x}\Big)\Big] \\
&\qquad + \sigma_{xz}\Big(\delta\phi_x + \frac{\partial\delta w_0}{\partial x}\Big) + \sigma_{yz}\Big(\delta\phi_y + \frac{\partial\delta w_0}{\partial y}\Big)\Big\} dz dx dy \\
&= \int_{\Omega_0} \Big\{N_{xx}\Big[\frac{\partial\delta u_0}{\partial x} + \frac{\partial\delta w_0}{\partial x}\frac{\partial w_0}{\partial x}\Big] + M_{xx}\Big[\frac{\partial\delta\phi_x}{\partial x}\Big] + N_{yy}\Big[\frac{\partial\delta v_0}{\partial y} + \frac{\partial\delta w_0}{\partial y}\frac{\partial w_0}{\partial y}\Big] \\
&\qquad + M_{yy}\Big[\frac{\partial\delta\phi_y}{\partial y}\Big] + N_{xy}\Big[\frac{\partial\delta u_0}{\partial y} + \frac{\partial\delta v_0}{\partial x} + \frac{\partial\delta w_0}{\partial x}\frac{\partial w_0}{\partial y} + \frac{\partial w_0}{\partial x}\frac{\partial\delta w_0}{\partial y}\Big] \\
&\qquad + M_{xy}\Big[\frac{\partial\delta\phi_x}{\partial y} + \frac{\partial\delta\phi_y}{\partial x}\Big] \\
&\qquad + Q_{xz}\Big[\delta\phi_x + \frac{\partial\delta w_0}{\partial x}\Big] + Q_{yz}\Big[\delta\phi_y + \frac{\partial\delta w_0}{\partial y}\Big]\Big\} dx dy.
\end{aligned}
\tag{D.1}
$$

To relieve the virtual displacements δu_0, δv_0, δw_0, $\delta\phi_x$, and $\delta\phi_y$ from the partial differ-

ential forms, integration by parts is applied to Eq (D.1) as shown in Eq (D.2).

$$
\begin{aligned}
\delta U = \int_{\Omega_0} \Big\{ & -\delta u_0 \frac{\partial N_{xx}}{\partial x} - \delta w_0 \frac{\partial}{\partial x}\Big(N_{xx}\frac{\partial w_0}{\partial x}\Big) - \delta\phi_x \frac{\partial M_{xx}}{\partial x} - \delta v_0 \frac{\partial N_{yy}}{\partial y} \\
& - \delta w_0 \frac{\partial}{\partial y}\Big(N_{yy}\frac{\partial w_0}{\partial y}\Big) - \delta\phi_y \frac{\partial M_{yy}}{\partial y} - \delta u_0 \frac{\partial N_{xy}}{\partial y} - \delta v_0 \frac{\partial N_{xy}}{\partial x} \\
& - \delta w_0 \frac{\partial}{\partial x}\Big(N_{xy}\frac{\partial w_0}{\partial y}\Big) - \delta w_0 \frac{\partial}{\partial y}\Big(N_{xy}\frac{\partial w_0}{\partial x}\Big) - \delta\phi_x \frac{\partial M_{xy}}{\partial y} - \delta\phi_y \frac{\partial M_{xy}}{\partial x} \\
& + \delta\phi_x Q_{xz} - \delta w_0 \frac{\partial Q_{xz}}{\partial x} + \delta\phi_y Q_{yz} - \delta w_0 \frac{\partial Q_{yz}}{\partial y} \Big\} dxdy \\
+ \oint_\Gamma \Big\{ & n_x \delta u_0 N_{xx} + n_x \delta w_0 N_{xx}\frac{\partial w_0}{\partial x} + n_x \delta\phi_x M_{xx} + n_y \delta v_0 N_{yy} \\
& + n_y \delta w_0 N_{yy}\frac{\partial w_0}{\partial y} + n_y \delta\phi_y M_{yy} + n_y \delta u_0 N_{xy} + n_x \delta v_0 N_{xy} \\
& + n_x \delta w_0 N_{xy}\frac{\partial w_0}{\partial y} + n_y \delta w_0 N_{xy}\frac{\partial w_0}{\partial x} + n_y \delta\phi_x M_{xy} + n_x \delta\phi_y M_{xy} \\
& + n_x \delta w_0 Q_{xz} + n_y \delta w_0 Q_{yz} \Big\} ds \\
= -\int_{\Omega_0} \Big\{ & \delta u_0 \Big[\frac{\partial N_{xx}}{\partial x} + \frac{\partial N_{xy}}{\partial y}\Big] + \delta v_0 \Big[\frac{\partial N_{yy}}{\partial y} + \frac{\partial N_{xy}}{\partial x}\Big] \\
& + \delta w_0 \Big[\frac{\partial}{\partial x}\Big(N_{xx}\frac{\partial w_0}{\partial x} + N_{xy}\frac{\partial w_0}{\partial y}\Big) + \frac{\partial}{\partial y}\Big(N_{xy}\frac{\partial w_0}{\partial x} + N_{yy}\frac{\partial w_0}{\partial y}\Big) \\
& + \frac{\partial Q_{xz}}{\partial x} + \frac{\partial Q_{yz}}{\partial y}\Big] \\
& + \delta\phi_x \Big[\frac{\partial M_{xx}}{\partial x} + \frac{\partial M_{xy}}{\partial y} - Q_{xz}\Big] + \delta\phi_y \Big[\frac{\partial M_{yy}}{\partial y} + \frac{\partial M_{xy}}{\partial x} - Q_{yz}\Big] \Big\} dxdy \\
+ \oint_\Gamma \Big\{ & \delta u_0 \Big[n_x N_{xx} + n_y N_{xy}\Big] + \delta v_0 \Big[n_y N_{yy} + n_x N_{xy}\Big] \\
& + \delta w_0 \Big[n_x N_{xx}\frac{\partial w_0}{\partial x} + n_y N_{yy}\frac{\partial w_0}{\partial y} + n_x N_{xy}\frac{\partial w_0}{\partial y} + n_y N_{xy}\frac{\partial w_0}{\partial x} \\
& + n_x Q_{xz} + n_y Q_{yz}\Big] \\
& + \delta\phi_x \Big[n_x M_{xx} + n_y M_{xy}\Big] + \delta\phi_y \Big[n_y M_{yy} + n_x M_{xy}\Big] \Big\} ds,
\end{aligned}
\tag{D.2}
$$

where $n_x = \cos\theta$ and $n_y = \sin\theta$ are the direction cosines of the unit outward normal vector $\mathbf{n}$ on Γ as illustrated in Fig 4.1.

D.2 Virtual work done δV

$$\begin{aligned}
\delta V =& -\int_{\Omega_0}\Big[q_b(x,y)\delta w\Big(x,y,-\frac{h}{2}\Big)+q_t(x,y)\delta w\Big(x,y,\frac{h}{2}\Big)\Big]dxdy \\
&-\int_{\Gamma_\sigma}\int_{-\frac{h}{2}}^{\frac{h}{2}}\Big[\hat{\sigma}_{nn}\delta u_n+\hat{\sigma}_{ns}\delta u_s+\hat{\sigma}_{nz}\delta w\Big]dzds \\
=& -\int_{\Omega_0} q(x,y)\delta w_0(x,y)dxdy \\
&-\int_{\Gamma_\sigma}\int_{-\frac{h}{2}}^{\frac{h}{2}}\Big\{\hat{\sigma}_{nn}\Big[\delta u_{0n}+z\delta\phi_n\Big]+\hat{\sigma}_{ns}\Big[\delta u_{0s}+z\delta\phi_s\Big]+\hat{\sigma}_{nz}\delta w_0\Big\}dzds \\
=& -\int_{\Omega_0} q\delta w_0 dxdy \\
&-\int_{\Gamma_\sigma}\Big[\hat{N}_{nn}\delta u_{0n}+\hat{N}_{ns}\delta u_{0s}+\hat{Q}_{nz}\delta w_0+\hat{M}_{nn}\delta\phi_n+\hat{M}_{ns}\delta\phi_s\Big]ds.
\end{aligned} \tag{D.3}$$

D.3 Virtual kinetic energy δK

$$\begin{aligned}
\delta K =& \int_{\Omega_0}\int_{-\frac{h}{2}}^{\frac{h}{2}}\rho_0\Big[\dot{u}\delta\dot{u}+\dot{v}\delta\dot{v}+\dot{w}\delta\dot{w}\Big]dzdxdy \\
=& \int_{\Omega_0}\int_{-\frac{h}{2}}^{\frac{h}{2}}\rho_0\Big\{\Big[\dot{u}_0+z\dot{\phi}_x\Big]\Big[\delta\dot{u}_0+z\delta\dot{\phi}_x\Big]+\Big[\dot{v}_0+z\dot{\phi}_y\Big]\Big[\delta\dot{v}_0+z\delta\dot{\phi}_y\Big] \\
&\qquad +\dot{w}_0\delta\dot{w}_0\Big\}dzdxdy \\
=& \int_{\Omega_0}\int_{-\frac{h}{2}}^{\frac{h}{2}}\rho_0\Big\{\dot{u}_0\delta\dot{u}_0+z\dot{\phi}_x\delta\dot{u}_0+z\dot{u}_0\delta\dot{\phi}_x+z^2\dot{\phi}_x\delta\dot{\phi}_x \\
&\qquad +\dot{v}_0\delta\dot{v}_0+z\dot{\phi}_y\delta\dot{v}_0+z\dot{v}_0\delta\dot{\phi}_y+z^2\dot{\phi}_y\delta\dot{\phi}_y \\
&\qquad +\dot{w}_0\delta\dot{w}_0\Big\}dzdxdy \\
=& \int_{\Omega_0}\Big\{\delta\dot{u}_0\Big[I_0\dot{u}_0+I_1\dot{\phi}_x\Big]+\delta\dot{v}_0\Big[I_0\dot{v}_0+I_1\dot{\phi}_y\Big]+\delta\dot{\phi}_x\Big[I_1\dot{u}_0+I_2\dot{\phi}_x\Big] \\
&\qquad +\delta\dot{\phi}_y\Big[I_1\dot{v}_0+I_2\dot{\phi}_y\Big]+\delta\dot{w}_0 I_0\dot{w}_0\Big\}dxdy,
\end{aligned} \tag{D.4}$$

where

$$I_n=\int_{-\frac{h}{2}}^{\frac{h}{2}}\rho_0 z^n dz \text{ , for } n=0,1,2. \tag{D.5}$$

$$\begin{aligned}\int_0^T \delta K dt = \int_0^T \int_{\Omega_0} \Big\{ & \delta\dot{u}_0 \Big[I_0\dot{u}_0 + I_1\dot{\phi}_x \Big] + \delta\dot{v}_0 \Big[I_0\dot{v}_0 + I_1\dot{\phi}_y \Big] + \delta\dot{\phi}_x \Big[I_1\dot{u}_0 + I_2\dot{\phi}_x \Big] \\ & + \delta\dot{\phi}_y \Big[I_1\dot{v}_0 + I_2\dot{\phi}_y \Big] + \delta\dot{w}_0 I_0 \dot{w}_0 \Big\} dxdydt \\ = \int_0^T \int_{\Omega_0} \Big\{ & - \delta u_0 \Big[I_0\ddot{u}_0 + I_1\ddot{\phi}_x \Big] - \delta v_0 \Big[I_0\ddot{v}_0 + I_1\ddot{\phi}_y \Big] - \delta\phi_x \Big[I_1\ddot{u}_0 + I_2\ddot{\phi}_x \Big] \\ & - \delta\phi_y \Big[I_1\ddot{v}_0 + I_2\ddot{\phi}_y \Big] - \delta w_0 I_0 \ddot{w}_0 \Big\} dxdydt \\ + \Big[\int_{\Omega_0} \Big\{ & \delta u_0 \Big(I_0\dot{u}_0 + I_1\dot{\phi}_x \Big) + \delta v_0 \Big(I_0\dot{v}_0 + I_1\dot{\phi}_y \Big) + \delta\phi_x \Big(I_1\dot{u}_0 + I_2\dot{\phi}_x \Big) \\ & + \delta\phi_y \Big(I_1\dot{v}_0 + I_2\dot{\phi}_y \Big) + \delta w_0 I_0 \dot{w}_0 \Big\} dxdy \Big]_0^T .\end{aligned} \tag{D.6}$$

In Eq (D.6), the terms obtained in Ω_0 and evaluated at $t = 0$ and $t = T$ can be set to zero because the virtual displacements are zero at those times. Thus, Eq (D.6) can be reduced to

$$\begin{aligned}\int_0^T \delta K dt = \int_0^T \int_{\Omega_0} \Big\{ & - \delta u_0 \Big[I_0\ddot{u}_0 + I_1\ddot{\phi}_x \Big] - \delta v_0 \Big[I_0\ddot{v}_0 + I_1\ddot{\phi}_y \Big] - \delta\phi_x \Big[I_1\ddot{u}_0 + I_2\ddot{\phi}_x \Big] \\ & - \delta\phi_y \Big[I_1\ddot{v}_0 + I_2\ddot{\phi}_y \Big] - \delta w_0 I_0 \ddot{w}_0 \Big\} dxdydt.\end{aligned} \tag{D.7}$$

D.4 Nonlinear equation of motion

Substituting δU, δV, and δK into Eq (4.10), collecting terms with respect to the virtual displacements (δu_0, δv_0, δw_0, $\delta\phi_x$, $\delta\phi_y$), and noting that the virtual displacements are zero

on Γ_u, Eq (4.10) is reorganized as

$$
\begin{aligned}
0 = \int_0^T \int_{\Omega_0} \Big\{ & - \delta u_0 \Big[\frac{\partial N_{xx}}{\partial x} + \frac{\partial N_{xy}}{\partial y} - I_0 \ddot{u}_0 - I_1 \ddot{\phi}_x \Big] \\
& - \delta v_0 \Big[\frac{\partial N_{yy}}{\partial y} + \frac{\partial N_{xy}}{\partial x} - I_0 \ddot{v}_0 - I_1 \ddot{\phi}_y \Big] \\
& - \delta w_0 \Big[\frac{\partial}{\partial x} \Big(N_{xx} \frac{\partial w_0}{\partial x} + N_{xy} \frac{\partial w_0}{\partial y} \Big) + \frac{\partial}{\partial y} \Big(N_{xy} \frac{\partial w_0}{\partial x} + N_{yy} \frac{\partial w_0}{\partial y} \Big) \\
& + q - I_0 \ddot{w}_0 \Big] \\
& - \delta \phi_x \Big[\frac{\partial M_{xx}}{\partial x} + \frac{\partial M_{xy}}{\partial y} - Q_{xz} - I_1 \ddot{u}_0 - I_2 \ddot{\phi}_x \Big] \\
& - \delta \phi_y \Big[\frac{\partial M_{yy}}{\partial y} + \frac{\partial M_{xy}}{\partial x} - Q_{yz} - I_1 \ddot{v}_0 - I_2 \ddot{\phi}_y \Big] \\
+ \int_0^T \oint_{\Gamma_\sigma} & \Big[\ \bullet \ \Big] ds dt,
\end{aligned}
\tag{D.8}
$$

where the last term $\int_0^T \oint_{\Gamma_\sigma} \Big[\ \bullet \ \Big] ds dt$ provides the boundary conditions, which are presented in the following section.

The nonlinear equations of motion are obtained by setting the coefficients of the independent variables δu_0, δv_0, δw_0, $\delta \phi_x$, and $\delta \phi_y$ over Ω_0 to zero separately as shown in Eqs (D.9) to (D.13).

$$
\delta u_0 : \ \frac{\partial N_{xx}}{\partial x} + \frac{\partial N_{xy}}{\partial y} = I_0 \ddot{u}_0 + I_1 \ddot{\phi}_x. \tag{D.9}
$$

$$
\delta v_0 : \ \frac{\partial N_{yy}}{\partial y} + \frac{\partial N_{xy}}{\partial x} = I_0 \ddot{v}_0 + I_1 \ddot{\phi}_y. \tag{D.10}
$$

$$
\begin{aligned}
\delta w_0 : \ & \frac{\partial}{\partial x} \Big(N_{xx} \frac{\partial w_0}{\partial x} + N_{xy} \frac{\partial w_0}{\partial y} \Big) + \frac{\partial}{\partial y} \Big(N_{xy} \frac{\partial w_0}{\partial x} + N_{yy} \frac{\partial w_0}{\partial y} \Big) \\
& + \frac{\partial Q_{xz}}{\partial x} + \frac{\partial Q_{yz}}{\partial y} + q = I_0 \ddot{w}_0.
\end{aligned}
\tag{D.11}
$$

$$
\delta \phi_x : \ \frac{\partial M_{xx}}{\partial x} + \frac{\partial M_{xy}}{\partial y} - Q_{xz} = I_1 \ddot{u}_0 + I_2 \ddot{\phi}_x. \tag{D.12}
$$

$$
\delta \phi_y : \ \frac{\partial M_{yy}}{\partial y} + \frac{\partial M_{xy}}{\partial x} - Q_{yz} = I_1 \ddot{v}_0 + I_2 \ddot{\phi}_y. \tag{D.13}
$$

D.5 Boundary conditions

The transformation between the coordinate systems (n, s) and (x, y) illustrated in Fig 4.1 is given by

$$\begin{aligned} \hat{\mathbf{e}}_x &= \cos\theta\hat{\mathbf{e}}_n - \sin\theta\hat{\mathbf{e}}_s = n_x\hat{\mathbf{e}}_n - n_y\hat{\mathbf{e}}_s, \\ \hat{\mathbf{e}}_y &= \sin\theta\hat{\mathbf{e}}_n + \cos\theta\hat{\mathbf{e}}_s = n_y\hat{\mathbf{e}}_n + n_x\hat{\mathbf{e}}_s. \end{aligned} \tag{D.14}$$

Using this transformation, the displacements (u_0, v_0) can be expressed in terms of (u_{0n}, u_{0s}):

$$u_0 = n_x u_{0n} - n_y u_{0s}, \quad v_0 = n_y u_{0n} + n_x u_{0s}. \tag{D.15}$$

Similarly, the normal and tangential derivatives $(\frac{\partial w_0}{\partial n}, \frac{\partial w_0}{\partial s})$ are related to the derivatives $(\frac{\partial w_0}{\partial x}, \frac{\partial w_0}{\partial y})$ by

$$\frac{\partial w_0}{\partial x} = n_x\frac{\partial w_0}{\partial n} - n_y\frac{\partial w_0}{\partial s}, \quad \frac{\partial w_0}{\partial y} = n_y\frac{\partial w_0}{\partial n} + n_x\frac{\partial w_0}{\partial s}. \tag{D.16}$$

Finally, in-plane stresses and stress resultants in both coordinate systems can be related by the stress transformation:

$$\begin{Bmatrix} \sigma_{nn} \\ \sigma_{ns} \end{Bmatrix} = \begin{bmatrix} {n_x}^2 & {n_y}^2 & 2n_x n_y \\ -n_x n_y & n_x n_y & n_x^2 - n_y^2 \end{bmatrix} \begin{Bmatrix} \sigma_{xx} \\ \sigma_{yy} \\ \sigma_{xy} \end{Bmatrix}, \tag{D.17}$$

$$\begin{Bmatrix} N_{nn} \\ N_{ns} \end{Bmatrix} = \begin{bmatrix} {n_x}^2 & {n_y}^2 & 2n_x n_y \\ -n_x n_y & n_x n_y & n_x^2 - n_y^2 \end{bmatrix} \begin{Bmatrix} N_{xx} \\ N_{yy} \\ N_{xy} \end{Bmatrix}. \tag{D.18}$$

Using the transformation relations in Eqs (D.15) to (D.18), the boundary term in Eq (D.8)

can be reorganized as

$$
\begin{aligned}
0 &= \int_0^T \oint_{\Gamma_\sigma} \Big[\ \bullet \ \Big] ds dt \\
&= \int_0^T \oint_{\Gamma_\sigma} \Big\{ \delta u_0 \Big[n_x N_{xx} + n_y N_{xy} \Big] + \delta v_0 \Big[n_y N_{yy} + n_x N_{xy} \Big] \\
&\qquad + \delta w_0 \Big[n_x N_{xx} \frac{\partial w_0}{\partial x} + n_y N_{yy} \frac{\partial w_0}{\partial y} + n_x N_{xy} \frac{\partial w_0}{\partial y} + n_y N_{xy} \frac{\partial w_0}{\partial x} \\
&\qquad + n_x Q_{xz} + n_y Q_{yz} \Big] \\
&\qquad + \delta \phi_x \Big[n_x M_{xx} + n_y M_{xy} \Big] + \delta \phi_y \Big[n_y M_{yy} + n_x M_{xy} \Big] \\
&\qquad - \hat{N}_{nn} \delta u_{0n} - \hat{N}_{ns} \delta u_{0s} - \hat{M}_{nn} \delta \phi_n - \hat{M}_{ns} \delta \phi_s - \hat{Q}_{nz} \delta w_0 \Big\} ds dt \\
&= \int_0^T \oint_{\Gamma_\sigma} \Big\{ \delta u_{0n} \Big[n_x^2 N_{xx} + n_x n_y N_{xy} + n_y^2 N_{yy} + n_x n_y N_{xy} - \hat{N}_{nn} \Big] \\
&\qquad + \delta u_{0s} \Big[- n_x n_y N_{xx} - n_y^2 N_{xy} + n_x n_y N_{yy} + n_x^2 N_{xy} - \hat{N}_{ns} \Big] \\
&\qquad + \delta w_0 \Big[n_x N_{xx} \frac{\partial w_0}{\partial x} + n_y N_{yy} \frac{\partial w_0}{\partial y} + n_x N_{xy} \frac{\partial w_0}{\partial y} + n_y N_{xy} \frac{\partial w_0}{\partial x} \\
&\qquad + n_x Q_{xz} + n_y Q_{yz} - \hat{Q}_{nz} \Big] \\
&\qquad + \delta \phi_n \Big[n_x^2 M_{xx} + n_x n_y M_{xy} + n_y^2 M_{yy} + n_x n_y M_{xy} - \hat{M}_{nn} \Big] \\
&\qquad + \delta \phi_s \Big[- n_x n_y M_{xx} - n_y^2 M_{xy} + n_x n_y M_{yy} + n_x^2 M_{xy} - \hat{M}_{ns} \Big] \Big\} ds dt \\
&= \int_0^T \oint_{\Gamma_\sigma} \Big\{ \delta u_{0n} \Big[N_{nn} - \hat{N}_{nn} \Big] + \delta u_{0s} \Big[N_{ns} - \hat{N}_{ns} \Big] \\
&\qquad + \delta w_0 \Big[n_x N_{xx} \frac{\partial w_0}{\partial x} + n_y N_{yy} \frac{\partial w_0}{\partial y} + n_x N_{xy} \frac{\partial w_0}{\partial y} + n_y N_{xy} \frac{\partial w_0}{\partial x} + n_x Q_{xz} \\
&\qquad + n_y Q_{yz} - \hat{Q}_{nz} \Big] \\
&\qquad + \delta \phi_n \Big[M_{nn} - \hat{M}_{nn} \Big] + \delta \phi_s \Big[M_{ns} - \hat{M}_{ns} \Big] \Big\} ds dt.
\end{aligned}
\tag{D.19}
$$

Collecting the terms in Eq (D.19) in terms of δu_{0n}, δu_{0s}, δw_0, $\delta \phi_n$, and $\delta \phi_s$, the natural

(or force) boundary conditions[1] on Γ_σ are obtained as

$$\delta u_{0n} : \ N_{nn} = \hat{N}_{nn}, \tag{D.20}$$

$$\delta u_{0s} : \ N_{ns} = \hat{N}_{ns}, \tag{D.21}$$

$$\delta \phi_n : \ M_{nn} = \hat{M}_{nn}, \tag{D.22}$$

$$\delta \phi_s : \ M_{ns} = \hat{M}_{ns}, \tag{D.23}$$

$$\delta w_0 : \ Q_{nz} = \hat{Q}_{nz}, \tag{D.24}$$

where

$$Q_{nz} = n_x N_{xx} \frac{\partial w_0}{\partial x} + n_y N_{yy} \frac{\partial w_0}{\partial y} + n_x N_{xy} \frac{\partial w_0}{\partial y} + n_y N_{xy} \frac{\partial w_0}{\partial x} + n_x Q_{xz} + n_y Q_{yz}. \tag{D.25}$$

Thus, the primary variables (displacements) and secondary variables (forces) are given by

$$\text{Primary variables: } u_{0n}, \quad u_{0s}, \quad w_0, \quad \phi_n, \quad \phi_s, \tag{D.26}$$

$$\text{Secondary variables: } N_{nn}, \quad N_{ns}, \quad Q_{nz}, \quad M_{nn}, \quad M_{ns}. \tag{D.27}$$

[1] Essential boundary conditions require u and its derivatives (primary variables) to vanish at the boundary while natural boundary conditions require the specification of the coefficients (secondary variables) of u and its derivatives [69].

Appendix E

FSDT: COMPONENTS OF THE STIFFNESS AND MASS MATRICES AND FORCE VECTOR

This appendix presents the components of the stiffness and mass matrices, and the force vector of FEM for FSDT shown in Eq (4.37). In this appendix, $[\ \bullet\ ]^{\mathrm{L}}$ and $[\ \bullet\ ]^{\mathrm{NL}}$ denote linear and nonlinear components, respectively.

The expanded form of Eq (4.37) is given by

$$\begin{bmatrix} \boldsymbol{M}^{11} & \boldsymbol{M}^{12} & \boldsymbol{M}^{13} & \boldsymbol{M}^{14} & \boldsymbol{M}^{15} \\ \boldsymbol{M}^{21} & \boldsymbol{M}^{22} & \boldsymbol{M}^{23} & \boldsymbol{M}^{24} & \boldsymbol{M}^{25} \\ \boldsymbol{M}^{31} & \boldsymbol{M}^{32} & \boldsymbol{M}^{33} & \boldsymbol{M}^{34} & \boldsymbol{M}^{35} \\ \boldsymbol{M}^{41} & \boldsymbol{M}^{42} & \boldsymbol{M}^{43} & \boldsymbol{M}^{44} & \boldsymbol{M}^{45} \\ \boldsymbol{M}^{51} & \boldsymbol{M}^{52} & \boldsymbol{M}^{53} & \boldsymbol{M}^{54} & \boldsymbol{M}^{55} \end{bmatrix} \begin{Bmatrix} \ddot{\boldsymbol{u}} \\ \ddot{\boldsymbol{v}} \\ \ddot{\boldsymbol{w}} \\ \ddot{\boldsymbol{X}} \\ \ddot{\boldsymbol{Y}} \end{Bmatrix} + \begin{bmatrix} \boldsymbol{K}^{11} & \boldsymbol{K}^{12} & \boldsymbol{K}^{13} & \boldsymbol{K}^{14} & \boldsymbol{K}^{15} \\ \boldsymbol{K}^{21} & \boldsymbol{K}^{22} & \boldsymbol{K}^{23} & \boldsymbol{K}^{24} & \boldsymbol{K}^{25} \\ \boldsymbol{K}^{31} & \boldsymbol{K}^{32} & \boldsymbol{K}^{33} & \boldsymbol{K}^{34} & \boldsymbol{K}^{35} \\ \boldsymbol{K}^{41} & \boldsymbol{K}^{42} & \boldsymbol{K}^{43} & \boldsymbol{K}^{44} & \boldsymbol{K}^{45} \\ \boldsymbol{K}^{51} & \boldsymbol{K}^{52} & \boldsymbol{K}^{53} & \boldsymbol{K}^{54} & \boldsymbol{K}^{55} \end{bmatrix} \begin{Bmatrix} \boldsymbol{u} \\ \boldsymbol{v} \\ \boldsymbol{w} \\ \boldsymbol{X} \\ \boldsymbol{Y} \end{Bmatrix} = \begin{Bmatrix} \boldsymbol{F^1} \\ \boldsymbol{F^2} \\ \boldsymbol{F^3} \\ \boldsymbol{F^4} \\ \boldsymbol{F^5} \end{Bmatrix}. \tag{E.1}$$

E.1 Components of stiffness matrix K

$$\left[K_{ij}^{11}\right]^{\mathrm{L}} = \int_{\Omega^e} \left[\frac{\partial \psi_i}{\partial x}\left(A_{11}\frac{\partial \psi_j}{\partial x} + A_{16}\frac{\partial \psi_j}{\partial y}\right) + \frac{\partial \psi_i}{\partial y}\left(A_{16}\frac{\partial \psi_j}{\partial x} + A_{66}\frac{\partial \psi_j}{\partial y}\right)\right] dxdy, \tag{E.2}$$

where $i, j = 1, ..., 4$ for four-node elements.

$$\begin{aligned}\Big[K_{ij}^{12}\Big]^{\mathrm{L}} &= \Big[K_{ji}^{21}\Big]^{\mathrm{L}} \\ &= \int_{\Omega^e}\Big[\frac{\partial\psi_i}{\partial x}\Big(A_{12}\frac{\partial\psi_j}{\partial y}+A_{16}\frac{\partial\psi_j}{\partial x}\Big)+\frac{\partial\psi_i}{\partial y}\Big(A_{26}\frac{\partial\psi_j}{\partial y}+A_{66}\frac{\partial\psi_j}{\partial x}\Big)\Big]dxdy.\end{aligned} \tag{E.3}$$

$$\Big[K_{ij}^{13}\Big]^{\mathrm{L}} = \Big[K_{ji}^{31}\Big]^{\mathrm{L}} = 0. \tag{E.4}$$

$$\begin{aligned}\Big[K_{ij}^{13}\Big]^{\mathrm{NL}} = \int_{\Omega^e}\frac{1}{2}\Big[&\frac{\partial\psi_i}{\partial x}\Big\{A_{11}\frac{\partial w_0}{\partial x}\frac{\partial\psi_j}{\partial x}+A_{12}\frac{\partial w_0}{\partial y}\frac{\partial\psi_j}{\partial y}+A_{16}\Big(\frac{\partial w_0}{\partial x}\frac{\partial\psi_j}{\partial y}+\frac{\partial w_0}{\partial y}\frac{\partial\psi_j}{\partial x}\Big)\Big\} \\ &+\frac{\partial\psi_i}{\partial y}\Big\{A_{16}\frac{\partial w_0}{\partial x}\frac{\partial\psi_j}{\partial x}+A_{26}\frac{\partial w_0}{\partial y}\frac{\partial\psi_j}{\partial y} \\ &+A_{66}\Big(\frac{\partial w_0}{\partial x}\frac{\partial\psi_j}{\partial y}+\frac{\partial w_0}{\partial y}\frac{\partial\psi_j}{\partial x}\Big)\Big\}\Big]dxdy.\end{aligned} \tag{E.5}$$

$$\begin{aligned}\Big[K_{ij}^{14}\Big]^{\mathrm{L}} &= \Big[K_{ji}^{41}\Big]^{\mathrm{L}} \\ &= \int_{\Omega^e}\Big[\frac{\partial\psi_i}{\partial x}\Big(B_{11}\frac{\partial\psi_j}{\partial x}+B_{16}\frac{\partial\psi_j}{\partial y}\Big)+\frac{\partial\psi_i}{\partial y}\Big(B_{16}\frac{\partial\psi_j}{\partial x}+B_{66}\frac{\partial\psi_j}{\partial y}\Big)\Big]dxdy.\end{aligned} \tag{E.6}$$

$$\begin{aligned}\Big[K_{ij}^{15}\Big]^{\mathrm{L}} &= \Big[K_{ji}^{51}\Big]^{\mathrm{L}} \\ &= \int_{\Omega^e}\Big[\frac{\partial\psi_i}{\partial x}\Big(B_{12}\frac{\partial\psi_j}{\partial y}+B_{16}\frac{\partial\psi_j}{\partial x}\Big)+\frac{\partial\psi_i}{\partial y}\Big(B_{26}\frac{\partial\psi_j}{\partial y}+B_{66}\frac{\partial\psi_j}{\partial x}\Big)\Big]dxdy.\end{aligned} \tag{E.7}$$

$$\Big[K_{ij}^{22}\Big]^{\mathrm{L}} = \int_{\Omega^e}\Big[\frac{\partial\psi_i}{\partial x}\Big(A_{26}\frac{\partial\psi_j}{\partial y}+A_{66}\frac{\partial\psi_j}{\partial x}\Big)+\frac{\partial\psi_i}{\partial y}\Big(A_{22}\frac{\partial\psi_j}{\partial y}+A_{26}\frac{\partial\psi_j}{\partial x}\Big)\Big]dxdy. \tag{E.8}$$

$$\Big[K_{ij}^{23}\Big]^{\mathrm{L}} = \Big[K_{ji}^{32}\Big]^{\mathrm{L}} = 0. \tag{E.9}$$

$$\begin{aligned}\Big[K_{ij}^{23}\Big]^{\mathrm{NL}} = \int_{\Omega^e}\frac{1}{2}\Big[&\frac{\partial\psi_i}{\partial x}\Big\{A_{16}\frac{\partial w_0}{\partial x}\frac{\partial\psi_j}{\partial x}+A_{26}\frac{\partial w_0}{\partial y}\frac{\partial\psi_j}{\partial y}+A_{66}\Big(\frac{\partial w_0}{\partial x}\frac{\partial\psi_j}{\partial y}+\frac{\partial w_0}{\partial y}\frac{\partial\psi_j}{\partial x}\Big) \\ &+\frac{\partial\psi_i}{\partial y}\Big\{A_{12}\frac{\partial w_0}{\partial x}\frac{\partial\psi_j}{\partial x}+A_{22}\frac{\partial w_0}{\partial y}\frac{\partial\psi_j}{\partial y} \\ &+A_{26}\Big(\frac{\partial w_0}{\partial x}\frac{\partial\psi_j}{\partial y}+\frac{\partial w_0}{\partial y}\frac{\partial\psi_j}{\partial x}\Big)\Big\}\Big]dxdy.\end{aligned} \tag{E.10}$$

$$\begin{aligned}\Big[K_{ij}^{24}\Big]^{\mathrm{L}} &= \Big[K_{ji}^{42}\Big]^{\mathrm{L}} \\ &= \int_{\Omega^e}\Big[\frac{\partial\psi_i}{\partial x}\Big\{B_{16}\frac{\partial\psi_j}{\partial x}+B_{66}\frac{\partial\psi_j}{\partial y}\Big\}+\frac{\partial\psi_i}{\partial y}\Big\{B_{12}\frac{\partial\psi_j}{\partial x}+B_{26}\frac{\partial\psi_j}{\partial y}\Big\}\Big]dxdy.\end{aligned} \tag{E.11}$$

$$\begin{aligned}\Big[K_{ij}^{25}\Big]^{\mathrm{L}} &= \Big[K_{ji}^{52}\Big]^{\mathrm{L}} \\ &= \int_{\Omega^e}\Big[\frac{\partial\psi_i}{\partial x}\Big\{B_{26}\frac{\partial\psi_j}{\partial y}+B_{66}\frac{\partial\psi_j}{\partial x}\Big\}+\frac{\partial\psi_i}{\partial y}\Big\{B_{22}\frac{\partial\psi_j}{\partial y}+B_{26}\frac{\partial\psi_j}{\partial x}\Big\}\Big]dxdy.\end{aligned} \tag{E.12}$$

$$\begin{aligned}\Big[K_{ij}^{31}\Big]^{\mathrm{NL}} = \int_{\Omega^e}\Big[&\frac{\partial\psi_i}{\partial x}\Big\{\frac{\partial w_0}{\partial x}\Big(A_{11}\frac{\partial\psi_j}{\partial x}+A_{16}\frac{\partial\psi_j}{\partial y}\Big)+\frac{\partial w_0}{\partial y}\Big(A_{16}\frac{\partial\psi_j}{\partial x}+A_{66}\frac{\partial\psi_j}{\partial y}\Big)\Big\}\\ &+\frac{\partial\psi_i}{\partial y}\Big\{\frac{\partial w_0}{\partial x}\Big(A_{16}\frac{\partial\psi_j}{\partial x}+A_{66}\frac{\partial\psi_j}{\partial y}\Big)\\ &+\frac{\partial w_0}{\partial y}\Big(A_{12}\frac{\partial\psi_j}{\partial x}+A_{26}\frac{\partial\psi_j}{\partial y}\Big)\Big\}\Big]dxdy.\end{aligned} \tag{E.13}$$

$$\begin{aligned}\Big[K_{ij}^{32}\Big]^{\mathrm{NL}} = \int_{\Omega^e}\Big[&\frac{\partial\psi_i}{\partial x}\Big\{\frac{\partial w_0}{\partial x}\Big(A_{12}\frac{\partial\psi_j}{\partial y}+A_{16}\frac{\partial\psi_j}{\partial x}\Big)+\frac{\partial w_0}{\partial y}\Big(A_{26}\frac{\partial\psi_j}{\partial y}+A_{66}\frac{\partial\psi_j}{\partial x}\Big)\Big\}\\ &+\frac{\partial\psi_i}{\partial y}\Big\{\frac{\partial w_0}{\partial x}\Big(A_{26}\frac{\partial\psi_j}{\partial y}+A_{66}\frac{\partial\psi_j}{\partial x}\Big)\\ &+\frac{\partial w_0}{\partial y}\Big(A_{22}\frac{\partial\psi_j}{\partial y}+A_{26}\frac{\partial\psi_j}{\partial x}\Big)\Big\}\Big]dxdy.\end{aligned} \tag{E.14}$$

$$\Big[K_{ij}^{33}\Big]^{\mathrm{L}} = \int_{\Omega^e} K\Big\{\frac{\partial\psi_i}{\partial x}\Big(A_{45}\frac{\partial\psi_j}{\partial y}+A_{55}\frac{\partial\psi_j}{\partial x}\Big)+\frac{\partial\psi_i}{\partial y}\Big(A_{44}\frac{\partial\psi_j}{\partial y}+A_{45}\frac{\partial\psi_j}{\partial x}\Big)\Big\}dxdy. \tag{E.15}$$

$$\Big[K_{ij}^{33}\Big]^{\mathrm{NL}} = \int_{\Omega^e}\Big\{\frac{\partial\psi_i}{\partial x}[\triangle]+\frac{\partial\psi_i}{\partial y}[\square]\Big\}dxdy, \tag{E.16}$$

where

$$\begin{aligned}[\triangle] = &\frac{\partial w_0}{\partial x}\Big\{\frac{1}{2}\Big[\frac{\partial w_0}{\partial x}\Big(A_{11}\frac{\partial\psi_j}{\partial x}+A_{16}\frac{\partial\psi_j}{\partial y}\Big)+\frac{\partial w_0}{\partial y}\Big(A_{12}\frac{\partial\psi_j}{\partial y}+A_{16}\frac{\partial\psi_j}{\partial x}\Big)\Big]\Big\}\\ &+\frac{\partial w_0}{\partial y}\Big\{\frac{1}{2}\Big[\frac{\partial w_0}{\partial x}\Big(A_{16}\frac{\partial\psi_j}{\partial x}+A_{66}\frac{\partial\psi_j}{\partial y}\Big)+\frac{\partial w_0}{\partial y}\Big(A_{26}\frac{\partial\psi_j}{\partial y}+A_{66}\frac{\partial\psi_j}{\partial x}\Big)\Big]\Big\},\end{aligned} \tag{E.17}$$

$$\begin{aligned}[\square] = &\frac{\partial w_0}{\partial x}\Big\{\frac{1}{2}\Big[\frac{\partial w_0}{\partial x}\Big(A_{16}\frac{\partial\psi_j}{\partial x}+A_{66}\frac{\partial\psi_j}{\partial y}\Big)+\frac{\partial w_0}{\partial y}\Big(A_{26}\frac{\partial\psi_j}{\partial y}+A_{66}\frac{\partial\psi_j}{\partial x}\Big)\Big]\Big\}\\ &+\frac{\partial w_0}{\partial y}\Big\{\frac{1}{2}\Big[\frac{\partial w_0}{\partial x}\Big(A_{12}\frac{\partial\psi_j}{\partial x}+A_{26}\frac{\partial\psi_j}{\partial y}\Big)+\frac{\partial w_0}{\partial y}\Big(A_{22}\frac{\partial\psi_j}{\partial y}+A_{26}\frac{\partial\psi_j}{\partial x}\Big)\Big]\Big\}.\end{aligned} \tag{E.18}$$

$$\Big[K_{ij}^{34}\Big]^{\mathrm{L}} = \Big[K_{ji}^{43}\Big]^{\mathrm{L}} = \int_{\Omega^e} K\Big[\Big(\frac{\partial\psi_i}{\partial x}A_{55}+\frac{\partial\psi_i}{\partial y}A_{45}\Big)\psi_j\Big]dxdy. \tag{E.19}$$

$$\Big[K_{ij}^{34}\Big]^{\mathrm{NL}} = \int_{\Omega^e} \Big[\frac{\partial\psi_i}{\partial x}\Big\{\frac{\partial w_0}{\partial x}\Big(B_{11}\frac{\partial\psi_j}{\partial x} + B_{16}\frac{\partial\psi_j}{\partial y}\Big) + \frac{\partial w_0}{\partial y}\Big(B_{16}\frac{\partial\psi_j}{\partial x} + B_{66}\frac{\partial\psi_j}{\partial y}\Big)\Big\} + \frac{\partial\psi_i}{\partial y}\Big\{\frac{\partial w_0}{\partial x}\Big(B_{16}\frac{\partial\psi_j}{\partial x} + B_{66}\frac{\partial\psi_j}{\partial y}\Big)\Big\} + \frac{\partial w_0}{\partial y}\Big(B_{12}\frac{\partial\psi_j}{\partial x} + B_{26}\frac{\partial\psi_j}{\partial y}\Big)\Big\}\Big]dxdy. \tag{E.20}$$

$$\Big[K_{ij}^{35}\Big]^{\mathrm{L}} = \Big[K_{ji}^{53}\Big]^{\mathrm{L}} = \int_{\Omega^e} K\Big[\Big(\frac{\partial\psi_i}{\partial x}A_{45} + \frac{\partial\psi_i}{\partial y}A_{44}\Big)\psi_j\Big]dxdy. \tag{E.21}$$

$$\Big[K_{ij}^{35}\Big]^{\mathrm{NL}} = \int_{\Omega^e} \Big[\frac{\partial\psi_i}{\partial x}\Big\{\frac{\partial w_0}{\partial x}\Big(B_{12}\frac{\partial\psi_j}{\partial y} + B_{16}\frac{\partial\psi_j}{\partial x}\Big) + \frac{\partial w_0}{\partial y}\Big(B_{26}\frac{\partial\psi_j}{\partial y} + B_{66}\frac{\partial\psi_j}{\partial x}\Big)\Big\} + \frac{\partial\psi_i}{\partial y}\Big\{\frac{\partial w_0}{\partial x}\Big(B_{26}\frac{\partial\psi_j}{\partial y} + B_{66}\frac{\partial\psi_j}{\partial x}\Big) + \frac{\partial w_0}{\partial y}\Big(B_{22}\frac{\partial\psi_j}{\partial y} + B_{26}\frac{\partial\psi_j}{\partial x}\Big\}\Big]dxdy. \tag{E.22}$$

$$\Big[K_{ij}^{43}\Big]^{\mathrm{NL}} = \int_{\Omega^e} \frac{1}{2}\Big[\frac{\partial\psi_i}{\partial x}\Big\{B_{11}\frac{\partial w_0}{\partial x}\frac{\partial\psi_j}{\partial x} + B_{12}\frac{\partial w_0}{\partial y}\frac{\partial\psi_j}{\partial y} + B_{16}\Big(\frac{\partial w_0}{\partial x}\frac{\partial\psi_j}{\partial y} + \frac{\partial w_0}{\partial y}\frac{\partial\psi_j}{\partial x}\Big)\Big\} + \frac{\partial\psi_i}{\partial y}\Big\{B_{16}\frac{\partial w_0}{\partial x}\frac{\partial\psi_j}{\partial x} + B_{26}\frac{\partial w_0}{\partial y}\frac{\partial\psi_j}{\partial y} + B_{66}\Big(\frac{\partial w_0}{\partial x}\frac{\partial\psi_j}{\partial y} + \frac{\partial w_0}{\partial y}\frac{\partial\psi_j}{\partial x}\Big)\Big\}\Big]dxdy. \tag{E.23}$$

$$\Big[K_{ij}^{44}\Big]^{\mathrm{L}} = \int_{\Omega^e} \Big[\frac{\partial\psi_i}{\partial x}\Big(D_{11}\frac{\partial\psi_j}{\partial x} + D_{16}\frac{\partial\psi_j}{\partial y}\Big) + \frac{\partial\psi_i}{\partial y}\Big(D_{16}\frac{\partial\psi_j}{\partial x} + D_{66}\frac{\partial\psi_j}{\partial y}\Big) + KA_{55}\psi_i\psi_j\Big]dxdy. \tag{E.24}$$

$$\Big[K_{ij}^{45}\Big]^{\mathrm{L}} = \Big[K_{ji}^{54}\Big]^{\mathrm{L}} = \int_{\Omega^e} \Big[\frac{\partial\psi_i}{\partial x}\Big(D_{12}\frac{\partial\psi_j}{\partial y} + D_{16}\frac{\partial\psi_j}{\partial x}\Big) + \frac{\partial\psi_i}{\partial y}\Big(D_{26}\frac{\partial\psi_j}{\partial y} + D_{66}\frac{\partial\psi_j}{\partial x}\Big) + KA_{45}\psi_i\psi_j\Big]dxdy. \tag{E.25}$$

$$\Big[K_{ij}^{53}\Big]^{\mathrm{NL}} = \int_{\Omega^e} \frac{1}{2}\Big[\frac{\partial\psi_i}{\partial x}\Big\{B_{16}\frac{\partial w_0}{\partial x}\frac{\partial\psi_j}{\partial x} + B_{26}\frac{\partial w_0}{\partial y}\frac{\partial\psi_j}{\partial y} + B_{66}\Big(\frac{\partial w_0}{\partial x}\frac{\partial\psi_j}{\partial y} + \frac{\partial w_0}{\partial y}\frac{\partial\psi_j}{\partial x}\Big)\Big\} + \frac{\partial\psi_i}{\partial y}\Big\{B_{12}\frac{\partial w_0}{\partial x}\frac{\partial\psi_j}{\partial x} + B_{22}\frac{\partial w_0}{\partial y}\frac{\partial\psi_j}{\partial y} + B_{26}\Big(\frac{\partial w_0}{\partial x}\frac{\partial\psi_j}{\partial y} + \frac{\partial w_0}{\partial y}\frac{\partial\psi_j}{\partial x}\Big)\Big\}\Big]dxdy. \tag{E.26}$$

$$\left[K_{ij}^{55}\right]^{\mathrm{L}} = \int_{\Omega^e} \Big[\frac{\partial\psi_i}{\partial x}\Big(D_{26}\frac{\partial\psi_j}{\partial y} + D_{66}\frac{\partial\psi_j}{\partial x}\Big) + \frac{\partial\psi_i}{\partial y}\Big(D_{22}\frac{\partial\psi_j}{\partial y} + D_{26}\frac{\partial\psi_j}{\partial x}\Big) + KA_{44}\psi_i\psi_j\Big]dxdy. \tag{E.27}$$

E.2 Components of mass matrix M

$$M_{ij}^{11} = \int_{\Omega^e} I_0\psi_i\psi_j dxdy. \tag{E.28}$$

$$M_{ij}^{14} = \int_{\Omega^e} I_1\psi_i\psi_j dxdy. \tag{E.29}$$

$$M_{ij}^{22} = \int_{\Omega^e} I_0\psi_i\psi_j dxdy. \tag{E.30}$$

$$M_{ij}^{25} = \int_{\Omega^e} I_1\psi_i\psi_j dxdy. \tag{E.31}$$

$$M_{ij}^{33} = \int_{\Omega^e} I_0\psi_i\psi_j dxdy. \tag{E.32}$$

$$M_{ij}^{41} = \int_{\Omega^e} I_1\psi_i\psi_j dxdy. \tag{E.33}$$

$$M_{ij}^{44} = \int_{\Omega^e} I_2\psi_i\psi_j dxdy. \tag{E.34}$$

$$M_{ij}^{52} = \int_{\Omega^e} I_1\psi_i\psi_j dxdy. \tag{E.35}$$

$$M_{ij}^{55} = \int_{\Omega^e} I_2\psi_i\psi_j dxdy. \tag{E.36}$$

The other mass matrix components are zero.

E.3 Components of force vector, F

$$F_i^1 = \oint_{\Gamma^e} \psi_i\Big\{n_x N_{xx} + n_y N_{xy}\Big\}ds. \tag{E.37}$$

$$F_i^2 = \oint_{\Gamma^e} \psi_i\Big\{n_x N_{xy} + n_y N_{yy}\Big\}ds. \tag{E.38}$$

$$F_i^3 = \int_{\Omega^e} \psi_i q dxdy + \oint_{\Gamma^e} \psi_i Q_{nz} ds. \tag{E.39}$$

$$F_i^4 = \oint_{\Gamma^e} \psi_i \Big\{ n_x M_{xx} + n_y M_{xy} \Big\} ds. \tag{E.40}$$

$$F_i^5 = \oint_{\Gamma^e} \psi_i \Big\{ n_x M_{xy} + n_y M_{yy} \Big\} ds. \tag{E.41}$$

Appendix F

FSDT: DERIVATION OF CLOSED FORM SOLUTIONS FOR CYLINDRICAL BENDING

In this appendix, analytical solutions to the cylindrical bending problems of FSDT illustrated in Fig 4.4 are derived by following the work of Reddy [68].

Based on the assumptions discussed in Section 4.4.1, the equations of motion presented in Eqs (4.15) to (4.19) can be reduced to Eqs (F.1) to (F.4) for static analysis.

$$A_{11}\frac{d^2u_0}{dx^2} + A_{16}\frac{d^2v_0}{dx^2} + B_{11}\frac{d^2\phi_x}{dx^2} = 0. \tag{F.1}$$

$$A_{16}\frac{d^2u_0}{dx^2} + A_{66}\frac{d^2v_0}{dx^2} + B_{16}\frac{d^2\phi_x}{dx^2} = 0. \tag{F.2}$$

$$B_{11}\frac{d^2u_0}{dx^2} + B_{16}\frac{d^2v_0}{dx^2} + D_{11}\frac{d^2\phi_x}{dx^2} - KA_{55}\Big(\frac{dw_0}{dx} + \phi_x\Big) = 0. \tag{F.3}$$

$$KA_{55}\Big(\frac{d^2w_0}{dx^2} + \frac{d\phi_x}{dx}\Big) + \frac{d}{dx}\Big(N_{xx}\frac{dw_0}{dx}\Big) + q = 0. \tag{F.4}$$

For static condensation, Eqs (F.1) and (F.2) can be reorganized to express u_0 and v_0 in terms of ϕ_x as shown in Eqs (F.5) and (F.6).

$$\frac{d^2u_0}{dx^2} = \frac{B}{A}\frac{d^2\phi_x}{dx^2}, \tag{F.5}$$

where $A = A_{11}A_{66} - (A_{16})^2$ and $B = B_{11}A_{66} - A_{16}B_{16}$.

$$\frac{d^2v_0}{dx^2} = \Big(\frac{A_{16}B - B_{16}A}{A_{66}A}\Big)\frac{d^2\phi_x}{dx^2}. \tag{F.6}$$

Substituting Eqs (F.5) and (F.6) into Eq (F.3), Eqs (F.1) to (F.3) condense into Eq (F.7).

$$D\frac{d^2\phi_x}{dx^2} - KA_{55}\Big(\frac{dw_0}{dx} + \phi_x\Big) = 0, \tag{F.7}$$

where

$$D = D_{11} - B_{11}\bar{B} - B_{16}\bar{C}, \quad \bar{B} = \frac{B}{A}, \quad \bar{C} = \frac{C}{A}, \quad C = A_{11}B_{16} - A_{16}B_{11}. \tag{F.8}$$

F.1 Linear static bending

For a plate strip clamped at both ends and subjected to uniformly distributed transverse load q_0, Eq (F.4) reduces to

$$KA_{55}\Big(\frac{d^2w_0}{dx^2} + \frac{d\phi_x}{dx}\Big) + q_0 = 0 \tag{F.9}$$

because the in-plane stress resultants N_{xx} are zero for linear static bending[1].

Differentiating Eq (F.7) with respect to x and combining it with Eq (F.9), ϕ_x can be expressed as

$$D\frac{d^3\phi_x}{dx^3} = -q_0. \tag{F.10}$$

Integrating Eq (F.10) with respect to x, a general solution for ϕ_x is obtained as

$$\phi_x(x) = \frac{1}{D}\Big[-\frac{q_0}{6}x^3 + c_1\frac{x^2}{2} + c_2x + c_3\Big], \tag{F.11}$$

where c_1, c_2, and c_3 are integration constants and can be determined using boundary conditions.

[1]For nonlinear static bending under transverse loading, the in-plane stress resultants N_{xx} would not be zero because in-plane strains and stresses are functions of transverse displacement w_0 (see Eq (C.7)).

Substituting Eq (F.11) into Eq (F.9), a general solution for w_0 is obtained as

$$\begin{aligned} w_0(x) = &-\frac{1}{D}\Big[-\frac{q_0}{24}x^4 + c_1\frac{x^3}{6} + c_2\frac{x^2}{2} + c_3x + c4\Big] \\ &+\frac{1}{KA_{55}}\Big[-\int_0^x\int_0^\xi q_0 d\zeta d\xi + c_1x\Big], \end{aligned} \tag{F.12}$$

where c_4 is an integration constant and can be determined using boundary conditions.

By applying boundary conditions, the solutions to linear static bending at the clamped boundary conditions can be obtained as

$$w_0(x) = \frac{q_0a^4}{24D}\Big\{\Big(\frac{x}{a}\Big)^2 - \Big(\frac{x}{a}\Big)\Big\}^2 + \frac{q_0a^2}{2KA_{55}}\Big\{\Big(\frac{x}{a}\Big) - \Big(\frac{x}{a}\Big)^2\Big\}, \tag{F.13}$$

$$\phi_x(x) = -\frac{q_0a^3}{12D}\Big\{2\Big(\frac{x}{a}\Big)^3 - 3\Big(\frac{x}{a}\Big)^2 + \Big(\frac{x}{a}\Big)\Big\}. \tag{F.14}$$

F.2 Buckling

For buckling analysis, q and N_{xx} are set to zero and $-N^0_{xx}$, receptively, where N^0_{xx} is a compressive in-plane stress resultant applied to the boundary. Thus, Eq (F.4) can be simplified to

$$KA_{55}\Big(\frac{d^2w_0}{dx^2} + \frac{d\phi_x}{dx}\Big) - N^0_{xx}\frac{d^2w_0}{dx^2} = 0, \tag{F.15}$$

or

$$\frac{d\phi_x}{dx} = -\Big(1 - \frac{N^0_{xx}}{KA_{55}}\Big)\frac{d^2w_0}{dx^2}. \tag{F.16}$$

Differentiating Eq (F.7) with respect to x and substituting Eq (F.16) into the equation, a new equation for w_0 is given by

$$D\Big(1 - \frac{N^0_{xx}}{KA_{55}}\Big)\frac{d^4w_0}{dx^4} + N^0_{xx}\frac{d^2w_0}{dx^2} = 0. \tag{F.17}$$

The general solution to Eq (F.17) is

$$w_0(x) = c_1 \sin\lambda x + c_2 \cos\lambda x + c_3 x + c_4, \tag{F.18}$$

where

$$\lambda^2 = \frac{N^0_{xx}}{\left(1 - \frac{N^0_{xx}}{KA_{55}}\right)D}, \tag{F.19}$$

or

$$N^0_{xx} = \frac{\lambda^2 D}{1 + \frac{\lambda^2 D}{KA_{55}}}, \tag{F.20}$$

and c_1 through c_4 are constants of integration and can be determined using boundary conditions.

For a plate strip clamped at both ends, λ is governed by

$$2(\cos\lambda a - 1)\left(1 + \frac{\lambda^2 D}{KA_{55}}\right) + \lambda a \sin\lambda a = 0. \tag{F.21}$$

The first root of Eq (F.21) is $\lambda_1 = 2\pi$ and thus the buckling load for the first mode is given by

$$N_{\text{cr}} = \left(\frac{2\pi}{a}\right)^2 D\left[1 - \frac{D(2\pi/a)^2}{KA_{55} + D(2\pi/a)^2}\right]. \tag{F.22}$$

Appendix G

MITC4: COMPONENTS OF THE STIFFNESS MATRIX K

An MITC4 model can be obtained by manipulating only the shear stiffness terms of the FSDT model in Eq (E.1). This appendix presents the components of the shear stiffness terms of MITC4: $\mathbf{K}^{33}$, $\mathbf{K}^{34}$, $\mathbf{K}^{35}$, $\mathbf{K}^{43}$, $\mathbf{K}^{44}$, $\mathbf{K}^{45}$, $\mathbf{K}^{53}$, $\mathbf{K}^{54}$, and $\mathbf{K}^{55}$.

$$
\begin{aligned}
\left[K_{ij}^{33}\right]^{\mathrm{L}} = \int_{\Omega^e} K\Big[& A_{44}\Big(-\frac{\partial\psi_i}{\partial\xi}\frac{\sqrt{J_{21}^2+J_{22}^2}}{|\det J|}\cos\beta + \frac{\partial\psi_i}{\partial\eta}\frac{\sqrt{J_{11}^2+J_{12}^2}}{|\det J|}\cos\alpha\Big) \\
& \times\Big(-\frac{\partial\psi_j}{\partial\xi}\frac{\sqrt{J_{21}^2+J_{22}^2}}{|\det J|}\cos\beta + \frac{\partial\psi_i}{\partial\eta}\frac{\sqrt{J_{11}^2+J_{12}^2}}{|\det J|}\cos\alpha\Big) \\
& + A_{45}\Big\{\Big(-\frac{\partial\psi_i}{\partial\xi}\frac{\sqrt{J_{21}^2+J_{22}^2}}{|\det J|}\cos\beta + \frac{\partial\psi_i}{\partial\eta}\frac{\sqrt{J_{11}^2+J_{12}^2}}{|\det J|}\cos\alpha\Big) \\
& \times\Big(\frac{\partial\psi_j}{\partial\xi}\frac{\sqrt{J_{21}^2+J_{22}^2}}{|\det J|}\sin\beta - \frac{\partial\psi_i}{\partial\eta}\frac{\sqrt{J_{11}^2+J_{12}^2}}{|\det J|}\sin\alpha\Big) \\
& + \Big(\frac{\partial\psi_i}{\partial\xi}\frac{\sqrt{J_{21}^2+J_{22}^2}}{|\det J|}\sin\beta - \frac{\partial\psi_i}{\partial\eta}\frac{\sqrt{J_{11}^2+J_{12}^2}}{|\det J|}\sin\alpha\Big) \\
& \times\Big(-\frac{\partial\psi_j}{\partial\xi}\frac{\sqrt{J_{21}^2+J_{22}^2}}{|\det J|}\cos\beta + \frac{\partial\psi_i}{\partial\eta}\frac{\sqrt{J_{11}^2+J_{12}^2}}{|\det J|}\cos\alpha\Big)\Big\} \\
& + A_{55}\Big(\frac{\partial\psi_i}{\partial\xi}\frac{\sqrt{J_{21}^2+J_{22}^2}}{|\det J|}\sin\beta - \frac{\partial\psi_i}{\partial\eta}\frac{\sqrt{J_{11}^2+J_{12}^2}}{|\det J|}\sin\alpha\Big) \\
& \times\Big(\frac{\partial\psi_j}{\partial\xi}\frac{\sqrt{J_{21}^2+J_{22}^2}}{|\det J|}\sin\beta - \frac{\partial\psi_i}{\partial\eta}\frac{\sqrt{J_{11}^2+J_{12}^2}}{|\det J|}\sin\alpha\Big)\Big] dxdy.
\end{aligned}
\tag{G.1}
$$

$$
\begin{aligned}
\Big[K_{ij}^{34}\Big]^{\mathrm{L}} = \int_{\Omega^e} K\Big[& A_{44}\Big(-\frac{\partial\psi_i}{\partial\xi}\frac{\sqrt{J_{21}^2+J_{22}^2}}{|\mathrm{det}J|}\cos\beta + \frac{\partial\psi_i}{\partial\eta}\frac{\sqrt{J_{11}^2+J_{12}^2}}{|\mathrm{det}J|}\cos\alpha\Big) \\
& \times \Big(-\varphi_j^{\eta x}\frac{\sqrt{J_{21}^2+J_{22}^2}}{|\mathrm{det}J|}\cos\beta + \varphi_j^{\xi x}\frac{\sqrt{J_{11}^2+J_{12}^2}}{|\mathrm{det}J|}\cos\alpha\Big) \\
& + A_{45}\Big\{\Big(-\frac{\partial\psi_i}{\partial\xi}\frac{\sqrt{J_{21}^2+J_{22}^2}}{|\mathrm{det}J|}\cos\beta + \frac{\partial\psi_i}{\partial\eta}\frac{\sqrt{J_{11}^2+J_{12}^2}}{|\mathrm{det}J|}\cos\alpha\Big) \\
& \times \Big(\varphi_j^{\eta x}\frac{\sqrt{J_{21}^2+J_{22}^2}}{|\mathrm{det}J|}\sin\beta - \varphi_j^{\xi x}\frac{\sqrt{J_{11}^2+J_{12}^2}}{|\mathrm{det}J|}\sin\alpha\Big) \\
& + \Big(\frac{\partial\psi_i}{\partial\xi}\frac{\sqrt{J_{21}^2+J_{22}^2}}{|\mathrm{det}J|}\sin\beta - \frac{\partial\psi_i}{\partial\eta}\frac{\sqrt{J_{11}^2+J_{12}^2}}{|\mathrm{det}J|}\sin\alpha\Big) \\
& \times \Big(-\varphi_j^{\eta x}\frac{\sqrt{J_{21}^2+J_{22}^2}}{|\mathrm{det}J|}\cos\beta + \varphi_j^{\xi x}\frac{\sqrt{J_{11}^2+J_{12}^2}}{|\mathrm{det}J|}\cos\alpha\Big)\Big\} \\
& + A_{55}\Big(\frac{\partial\psi_i}{\partial\xi}\frac{\sqrt{J_{21}^2+J_{22}^2}}{|\mathrm{det}J|}\sin\beta - \frac{\partial\psi_i}{\partial\eta}\frac{\sqrt{J_{11}^2+J_{12}^2}}{|\mathrm{det}J|}\sin\alpha\Big) \\
& \times \Big(\varphi_j^{\eta x}\frac{\sqrt{J_{21}^2+J_{22}^2}}{|\mathrm{det}J|}\sin\beta - \varphi_j^{\xi x}\frac{\sqrt{J_{11}^2+J_{12}^2}}{|\mathrm{det}J|}\sin\alpha\Big)\Big] dxdy,
\end{aligned}
\tag{G.2}
$$

where

$$
\begin{aligned}
\varphi_1^{\eta x} &= \varphi_2^{\eta x} = \frac{(1-\eta)(x_2-x_1)}{8}, \\
\varphi_3^{\eta x} &= \varphi_4^{\eta x} = \frac{(1+\eta)(x_3-x_4)}{8}, \\
\varphi_1^{\eta y} &= \varphi_2^{\eta y} = \frac{(1-\eta)(y_2-y_1)}{8}, \\
\varphi_3^{\eta y} &= \varphi_4^{\eta y} = \frac{(1+\eta)(y_3-y_4)}{8}, \\
\varphi_1^{\xi x} &= \varphi_4^{\xi x} = \frac{(1-\xi)(x_4-x_1)}{8}, \\
\varphi_2^{\xi x} &= \varphi_3^{\xi x} = \frac{(1+\xi)(x_3-x_2)}{8}, \\
\varphi_1^{\xi y} &= \varphi_4^{\xi y} = \frac{(1-\xi)(y_4-y_1)}{8}, \\
\varphi_2^{\xi y} &= \varphi_3^{\xi y} = \frac{(1+\xi)(y_3-y_2)}{8}.
\end{aligned}
\tag{G.3}
$$

$$\begin{aligned}\Big[K_{ij}^{35}\Big]^{\mathrm{L}} = \int_{\Omega^e} K\Big[A_{44}\Big(&- \frac{\partial\psi_i}{\partial\xi}\frac{\sqrt{J_{21}^2+J_{22}^2}}{|\mathrm{det}J|}\cos\beta + \frac{\partial\psi_i}{\partial\eta}\frac{\sqrt{J_{11}^2+J_{12}^2}}{|\mathrm{det}J|}\cos\alpha\Big)\\ &\times\Big(-\varphi_j^{\eta y}\frac{\sqrt{J_{21}^2+J_{22}^2}}{|\mathrm{det}J|}\cos\beta + \varphi_j^{\xi y}\Big(\frac{\sqrt{J_{11}^2+J_{12}^2}}{|\mathrm{det}J|}\cos\alpha\Big)\\ +A_{45}\Big\{\Big(&-\frac{\partial\psi_i}{\partial\xi}\frac{\sqrt{J_{21}^2+J_{22}^2}}{|\mathrm{det}J|}\cos\beta + \frac{\partial\psi_i}{\partial\eta}\Big(\frac{\sqrt{J_{11}^2+J_{12}^2}}{|\mathrm{det}J|}\cos\alpha\Big)\\ &\times\Big(\varphi_j^{\eta y}\frac{\sqrt{J_{21}^2+J_{22}^2}}{|\mathrm{det}J|}\sin\beta - \varphi_j^{\xi y}\frac{\sqrt{J_{11}^2+J_{12}^2}}{|\mathrm{det}J|}\sin\alpha\Big)\\ &+\Big(\frac{\partial\psi_i}{\partial\xi}\frac{\sqrt{J_{21}^2+J_{22}^2}}{|\mathrm{det}J|}\sin\beta - \frac{\partial\psi_i}{\partial\eta}\frac{\sqrt{J_{11}^2+J_{12}^2}}{|\mathrm{det}J|}\sin\alpha\Big)\\ &\times\Big(-\varphi_j^{\eta y}\frac{\sqrt{J_{21}^2+J_{22}^2}}{|\mathrm{det}J|}\cos\beta + \varphi_j^{\xi y}\frac{\sqrt{J_{11}^2+J_{12}^2}}{|\mathrm{det}J|}\cos\alpha\Big)\Big\}\\ +A_{55}\Big(&\frac{\partial\psi_i}{\partial\xi}\Big(\frac{\sqrt{J_{21}^2+J_{22}^2}}{|\mathrm{det}J|}\sin\beta + \frac{\partial\psi_i}{\partial\eta}\Big(-\frac{\sqrt{J_{11}^2+J_{12}^2}}{|\mathrm{det}J|}\sin\alpha\Big)\\ &\times\Big(\varphi_j^{\eta y}\frac{\sqrt{J_{21}^2+J_{22}^2}}{|\mathrm{det}J|}\sin\beta - \varphi_j^{\xi y}\frac{\sqrt{J_{11}^2+J_{12}^2}}{|\mathrm{det}J|}\sin\alpha\Big)\Big]dxdy.\end{aligned} \tag{G.4}$$

$$\Big[K_{ij}^{43}\Big]^{\mathrm{L}} = \Big[K_{ji}^{34}\Big]^{\mathrm{L}}. \tag{G.5}$$

$$\begin{aligned}\left[K_{ij}^{44}\right]^{\mathrm{L}} = \int_{\Omega^e} \Big[& \frac{\partial \psi_i}{\partial x}\Big(D_{11}\frac{\partial \psi_j}{\partial x} + D_{16}\frac{\partial \psi_j}{\partial y}\Big) + \frac{\partial \psi_i}{\partial y}\Big(D_{16}\frac{\partial \psi_j}{\partial x} + D_{66}\frac{\partial \psi_j}{\partial y}\Big) \\ & + KA_{44}\Big(-\varphi_i^{\eta x}\frac{\sqrt{J_{21}^2+J_{22}^2}}{|\det J|}\cos\beta + \varphi_i^{\xi x}\frac{\sqrt{J_{11}^2+J_{12}^2}}{|\det J|}\cos\alpha\Big) \\ & \quad \times \Big(-\varphi_j^{\eta x}\frac{\sqrt{J_{21}^2+J_{22}^2}}{|\det J|}\cos\beta + \varphi_j^{\xi x}\frac{\sqrt{J_{11}^2+J_{12}^2}}{|\det J|}\cos\alpha\Big) \\ & + KA_{45}\Big\{\Big(-\varphi_i^{\eta x}\frac{\sqrt{J_{21}^2+J_{22}^2}}{|\det J|}\cos\beta + \varphi_i^{\xi x}\frac{\sqrt{J_{11}^2+J_{12}^2}}{|\det J|}\cos\alpha\Big) \\ & \quad \times \Big(\varphi_j^{\eta x}\frac{\sqrt{J_{21}^2+J_{22}^2}}{|\det J|}\sin\beta - \varphi_j^{\xi x}\frac{\sqrt{J_{11}^2+J_{12}^2}}{|\det J|}\sin\alpha\Big) \\ & \quad + \Big(\varphi_i^{\eta x}\frac{\sqrt{J_{21}^2+J_{22}^2}}{|\det J|}\sin\beta - \varphi_i^{\xi x}\frac{\sqrt{J_{11}^2+J_{12}^2}}{|\det J|}\sin\alpha\Big) \\ & \quad \times \Big(-\varphi_j^{\eta x}\frac{\sqrt{J_{21}^2+J_{22}^2}}{|\det J|}\cos\beta + \varphi_j^{\xi x}\frac{\sqrt{J_{11}^2+J_{12}^2}}{|\det J|}\cos\alpha\Big)\Big\} \\ & + KA_{55}\Big(\varphi_i^{\eta x}\frac{\sqrt{J_{21}^2+J_{22}^2}}{|\det J|}\sin\beta - \varphi_i^{\xi x}\frac{\sqrt{J_{11}^2+J_{12}^2}}{|\det J|}\sin\alpha\Big) \\ & \quad \times \Big(\varphi_j^{\eta x}\frac{\sqrt{J_{21}^2+J_{22}^2}}{|\det J|}\sin\beta - \varphi_j^{\xi x}\frac{\sqrt{J_{11}^2+J_{12}^2}}{|\det J|}\sin\alpha\Big)\Big] dxdy. \end{aligned} \tag{G.6}$$

$$
\begin{aligned}
\Big[K_{ij}^{45}\Big]^{\mathrm{L}} = \int_{\Omega^e} \Big[& \frac{\partial \psi_i}{\partial x}\Big(D_{12}\frac{\partial \psi_j}{\partial y} + D_{16}\frac{\partial \psi_j}{\partial x}\Big) + \frac{\partial \psi_i}{\partial y}\Big(D_{26}\frac{\partial \psi_j}{\partial y} + D_{66}\frac{\partial \psi_j}{\partial x}\Big) \\
& + KA_{44}\Big(-\varphi_i^{\eta x}\frac{\sqrt{J_{21}^2+J_{22}^2}}{|\det J|}\cos\beta + \varphi_i^{\xi x}\frac{\sqrt{J_{11}^2+J_{12}^2}}{|\det J|}\cos\alpha\Big) \\
& \quad \times \Big(-\varphi_j^{\eta y}\frac{\sqrt{J_{21}^2+J_{22}^2}}{|\det J|}\cos\beta + \varphi_j^{\xi y}\frac{\sqrt{J_{11}^2+J_{12}^2}}{|\det J|}\cos\alpha\Big) \\
& + KA_{45}\Big\{\Big(-\varphi_i^{\eta x}\frac{\sqrt{J_{21}^2+J_{22}^2}}{|\det J|}\cos\beta + \varphi_i^{\xi x}\frac{\sqrt{J_{11}^2+J_{12}^2}}{|\det J|}\cos\alpha\Big) \\
& \quad \times \Big(\varphi_j^{\eta y}\frac{\sqrt{J_{21}^2+J_{22}^2}}{|\det J|}\sin\beta - \varphi_j^{\xi y}\frac{\sqrt{J_{11}^2+J_{12}^2}}{|\det J|}\sin\alpha\Big) \\
& \quad + \Big(\varphi_i^{\eta x}\frac{\sqrt{J_{21}^2+J_{22}^2}}{|\det J|}\sin\beta - \varphi_i^{\xi x}\frac{\sqrt{J_{11}^2+J_{12}^2}}{|\det J|}\sin\alpha\Big) \\
& \quad \times \Big(-\varphi_j^{\eta y}\frac{\sqrt{J_{21}^2+J_{22}^2}}{|\det J|}\cos\beta + \varphi_j^{\xi y}\frac{\sqrt{J_{11}^2+J_{12}^2}}{|\det J|}\cos\alpha\Big)\Big\} \\
& + KA_{55}\Big(\varphi_i^{\eta x}\frac{\sqrt{J_{21}^2+J_{22}^2}}{|\det J|}\sin\beta - \varphi_i^{\xi x}\frac{\sqrt{J_{11}^2+J_{12}^2}}{|\det J|}\sin\alpha\Big) \\
& \quad \times \Big(\varphi_j^{\eta y}\frac{\sqrt{J_{21}^2+J_{22}^2}}{|\det J|}\sin\beta - \varphi_j^{\xi y}\frac{\sqrt{J_{11}^2+J_{12}^2}}{|\det J|}\sin\alpha\Big)\Big] dxdy.
\end{aligned} \tag{G.7}
$$

$$
\Big[K_{ij}^{53}\Big]^{\mathrm{L}} = \Big[K_{ji}^{35}\Big]^{\mathrm{L}}. \tag{G.8}
$$

$$
\Big[K_{ij}^{54}\Big]^{\mathrm{L}} = \Big[K_{ji}^{45}\Big]^{\mathrm{L}}. \tag{G.9}
$$

$$
\begin{aligned}
\Big[K_{ij}^{55}\Big]^{\mathrm{L}} = \int_{\Omega^e} \Big[& \frac{\partial \psi_i}{\partial x}\Big(D_{26}\frac{\partial \psi_j}{\partial y} + D_{66}\frac{\partial \psi_j}{\partial x}\Big) + \frac{\partial \psi_i}{\partial y}\Big(D_{22}\frac{\partial \psi_j}{\partial y} + D_{26}\frac{\partial \psi_j}{\partial x}\Big) \\
& + KA_{44}\Big(- \varphi_i^{\eta y}\frac{\sqrt{J_{21}^2 + J_{22}^2}}{|\det J|}\cos\beta + \varphi_i^{\xi y}\frac{\sqrt{J_{11}^2 + J_{12}^2}}{|\det J|}\cos\alpha\Big) \\
& \quad \times \Big(- \varphi_j^{\eta y}\frac{\sqrt{J_{21}^2 + J_{22}^2}}{|\det J|}\cos\beta + \varphi_j^{\xi y}\frac{\sqrt{J_{11}^2 + J_{12}^2}}{|\det J|}\cos\alpha\Big) \\
& + KA_{45}\Big\{\Big(- \varphi_i^{\eta y}\frac{\sqrt{J_{21}^2 + J_{22}^2}}{|\det J|}\cos\beta + \varphi_i^{\xi y}\frac{\sqrt{J_{11}^2 + J_{12}^2}}{|\det J|}\cos\alpha\Big) \\
& \quad \times \Big(\varphi_j^{\eta y}\frac{\sqrt{J_{21}^2 + J_{22}^2}}{|\det J|}\sin\beta - \varphi_j^{\xi y}\frac{\sqrt{J_{11}^2 + J_{12}^2}}{|\det J|}\sin\alpha\Big) \\
& \quad + \Big(\varphi_j^{\eta y}\frac{\sqrt{J_{21}^2 + J_{22}^2}}{|\det J|}\sin\beta - \varphi_i^{\xi y}\frac{\sqrt{J_{11}^2 + J_{12}^2}}{|\det J|}\sin\alpha)\Big) \\
& \quad \times \Big(- \varphi_j^{\eta y}\frac{\sqrt{J_{21}^2 + J_{22}^2}}{|\det J|}\cos\beta + \varphi_j^{\xi y}\frac{\sqrt{J_{11}^2 + J_{12}^2}}{|\det J|}\cos\alpha\Big)\Big\} \\
& + A_{55}\Big(\varphi_j^{\eta y}\frac{\sqrt{J_{21}^2 + J_{22}^2}}{|\det J|}\sin\beta - \varphi_i^{\xi y}\frac{\sqrt{J_{11}^2 + J_{12}^2}}{|\det J|}\sin\alpha\Big) \\
& \quad \times \Big(\varphi_j^{\eta y}\frac{\sqrt{J_{21}^2 + J_{22}^2}}{|\det J|}\sin\beta - \varphi_j^{\xi y}\frac{\sqrt{J_{11}^2 + J_{12}^2}}{|\det J|}\sin\alpha\Big)\Big] dxdy.
\end{aligned}
\tag{G.10}
$$

Appendix H

EAS: HU-WASHIZU VARIATIONAL PRINCIPLE

The EAS method employs the Hu-Washizu principle as its variational basis. The principle is based on the three-field variational variables (i.e., virtual displacements, stresses, and strains), and embraces the principles of virtual work and complementary virtual work, and the Hellinger-Reissner principle as its special cases. This appendix presents the Hu-Washizu variational principle based on the work of Washizu in Refs [93, 94].

The principle of virtual work for small strains can be stated as:

$$\begin{aligned}&\int_{\Omega_0}\int_{-\frac{h}{2}}^{\frac{h}{2}}\Big[\sigma_{xx}\delta\varepsilon_{xx}+\sigma_{yy}\delta\varepsilon_{yy}+\sigma_{zz}\delta\varepsilon_{zz}+\tau_{xy}\delta\gamma_{xy}+\tau_{xz}\delta\gamma_{xz}+\tau_{yz}\delta\gamma_{yz}\Big]dzdxdy\\&-\int_{\Omega_0}\int_{-\frac{h}{2}}^{\frac{h}{2}}\Big[\bar{f}_x\delta u+\bar{f}_y\delta v+\bar{f}_z\delta w\Big]dzdxdy-\int_{\Gamma_\sigma}\Big[\bar{T}_x\delta u+\bar{T}_y\delta v+\bar{T}_z\delta w\Big]ds=0,\end{aligned}\tag{H.1}$$

where $(\bar{f}_x,\ \bar{f}_y,\ \bar{f}_z)$ are the components of body forces per unit volume, and $(\bar{T}_x,\ \bar{T}_y,\ \bar{T}_z)$ are the components of prescribed external forces per unit area of the boundary surface.

The integrand in the virtual strain energy term can be defined as

$$\delta A=\sigma_{xx}\delta\varepsilon_{xx}+\sigma_{yy}\delta\varepsilon_{yy}+\sigma_{zz}\delta\varepsilon_{zz}+\tau_{xy}\delta\gamma_{xy}+\tau_{xz}\delta\gamma_{xz}+\tau_{yz}\delta\gamma_{yz}.\tag{H.2}$$

Thus, a state function A can be obtained as

$$\begin{aligned} A(\varepsilon_{xx},\varepsilon_{yy},\varepsilon_{zz},\tau_{yz},\tau_{xz},\tau_{xy}) = \frac{1}{2}\Big[&\Big(\bar{C}_{11}\varepsilon_{xx}+\bar{C}_{12}\varepsilon_{yy}+...+\bar{C}_{16}\gamma_{xy}\Big)\varepsilon_{xx} \\ &+\Big(\bar{C}_{21}\varepsilon_{xx}+\bar{C}_{22}\varepsilon_{yy}+...+\bar{C}_{26}\gamma_{xy}\Big)\varepsilon_{yy} \\ &+\Big(\bar{C}_{31}\varepsilon_{xx}+\bar{C}_{32}\varepsilon_{yy}+...+\bar{C}_{36}\gamma_{xy}\Big)\varepsilon_{zz} \\ &+\Big(\bar{C}_{41}\varepsilon_{xx}+\bar{C}_{42}\varepsilon_{yy}+...+\bar{C}_{46}\gamma_{xy}\Big)\gamma_{yz} \\ &+\Big(\bar{C}_{51}\varepsilon_{xx}+\bar{C}_{52}\varepsilon_{yy}+...+\bar{C}_{56}\gamma_{xy}\Big)\gamma_{xz} \\ &+\Big(\bar{C}_{61}\varepsilon_{xx}+\bar{C}_{62}\varepsilon_{yy}+...+\bar{C}_{66}\gamma_{xy}\Big)\gamma_{yz}\Big], \end{aligned} \tag{H.3}$$

where $\bar{C}_{ij}$ are the components of an elastic coefficient matrix $\bar{\boldsymbol{C}}$ (see Appendix B). Thus, the total potential energy can be given by

$$\begin{aligned} \Pi = &\int_{\Omega_0}\int_{-\frac{h}{2}}^{\frac{h}{2}} A(\varepsilon_{xx},\varepsilon_{yy},\varepsilon_{zz},\tau_{yz},\tau_{xz},\tau_{xy})dzdxdy \\ &-\int_{\Omega_0}\int_{-\frac{h}{2}}^{\frac{h}{2}}\Big[\bar{f}_x u+\bar{f}_y v+\bar{f}_z w\Big]dzdxdy-\int_{\Gamma_\sigma}\Big[\bar{T}_x u+\bar{T}_y v+\bar{T}_z w\Big]ds. \end{aligned} \tag{H.4}$$

The principle of virtual work can be generalized by incorporating in it its subsidiary conditions (i.e., strain-displacement[1] and stress-strain relations[2]) using Lagrange multipliers:

[1]The strain-displacement relations of this work are described in Eq (C.7) in the form of von Kármán strains.

[2]The stress-strain relations of this work are given in Eq (B.9) in the form of lamina constitutive relation.

σ_{xx}, σ_{yy}, τ_{yz}, τ_{xz}, τ_{xy}. The functional for the generalized principle can be written as

$$\begin{aligned}\Pi_G = \int_{\Omega_0}\int_{-\frac{h}{2}}^{\frac{h}{2}} \Big[& A(\varepsilon_{xx},\varepsilon_{yy},\varepsilon_{zz},\tau_{yz},\tau_{xz},\tau_{xy}) \\ & - \Big(\varepsilon_{xx} - \frac{\partial u}{\partial x}\Big)\sigma_{xx} - \Big(\varepsilon_{yy} - \frac{\partial v}{\partial y}\Big)\sigma_{yy} - \Big(\varepsilon_{zz} - \frac{\partial w}{\partial z}\Big)\sigma_{yy} \\ & - \Big(\gamma_{yz} - \frac{\partial v}{\partial z} - \frac{\partial w}{\partial y}\Big)\tau_{xz} - \Big(\gamma_{xz} - \frac{\partial u}{\partial z} - \frac{\partial w}{\partial x}\Big)\tau_{xz} - \Big(\gamma_{xy} - \frac{\partial u}{\partial y} - \frac{\partial v}{\partial x}\Big)\tau_{xy} \\ & - \Big(\bar{f}_x u + \bar{f}_y v + \bar{f}_z w\Big)\Big] dz dx dy \\ - \int_{\Gamma_\sigma} & \Big[\bar{T}_x u + \bar{T}_y v + \bar{T}_z w\Big] ds \\ - \int_{\Gamma_u} & \Big[(u-\bar{u})T_x + (v-\bar{v})T_y + (w-\bar{w})T_z\Big] ds.\end{aligned} \tag{H.5}$$

The independent variables subject to variation in the functional are u, v, w, ε_{xx}, ε_{yy}, ε_{zz}, τ_{yz}, τ_{xz}, τ_{xy}, σ_{xx}, σ_{yy}, τ_{yz}, τ_{xz}, and τ_{xy}. Taking variations of these variables, a generalized variational principle can be obtained as

$$\begin{aligned}\delta\Pi_G = \int_{\Omega_0}\int_{-\frac{h}{2}}^{\frac{h}{2}} \Big[& \Big(\frac{\partial A}{\partial \varepsilon_{xx}} - \sigma_{xx}\Big)\delta\varepsilon_{xx} + \Big(\frac{\partial A}{\partial \varepsilon_{yy}} - \sigma_{yy}\Big)\delta\varepsilon_{yy} + \Big(\frac{\partial A}{\partial \varepsilon_{zz}} - \sigma_{zz}\Big)\delta\varepsilon_{zz} \\ & + \Big(\frac{\partial A}{\partial \gamma_{yz}} - \tau_{yz}\Big)\delta\gamma_{yz} + \Big(\frac{\partial A}{\partial \gamma_{xz}} - \tau_{xz}\Big)\delta\gamma_{xz} + \Big(\frac{\partial A}{\partial \gamma_{xy}} - \tau_{xy}\Big)\delta\gamma_{xy} \\ & - \Big(\varepsilon_{xx} - \frac{\partial u}{\partial x}\Big)\delta\sigma_{xx} - \Big(\varepsilon_{yy} - \frac{\partial v}{\partial y}\Big)\delta\sigma_{yy} - \Big(\varepsilon_{zz} - \frac{\partial w}{\partial z}\Big)\delta\sigma_{zz} \\ & - \Big(\gamma_{yz} - \frac{\partial v}{\partial z} - \frac{\partial w}{\partial y}\Big)\delta\tau_{xz} - \Big(\gamma_{xz} - \frac{\partial u}{\partial z} - \frac{\partial w}{\partial x}\Big)\delta\tau_{xz} \\ & - \Big(\gamma_{xy} - \frac{\partial u}{\partial y} - \frac{\partial v}{\partial x}\Big)\delta\tau_{xy} \\ & - \Big(\frac{\partial \sigma_{xx}}{\partial x} + \frac{\partial \tau_{xy}}{\partial y} + \frac{\partial \tau_{zx}}{\partial z} + \bar{f}_x\Big)\delta u - \Big(\frac{\partial \tau_{xy}}{\partial x} + \frac{\partial \sigma_{yy}}{\partial y} + \frac{\partial \tau_{zy}}{\partial z} + \bar{f}_y\Big)\delta v \\ & - \Big(\frac{\partial \tau_{xz}}{\partial x} + \frac{\partial \tau_{yz}}{\partial y} + \frac{\partial \sigma_{zz}}{\partial z} + \bar{f}_z\Big)\delta w\Big] dz dx dy \\ + \int_{\Gamma_\sigma} & \Big[\Big(T_x - \bar{T}_x\Big)\delta u + \Big(T_y - \bar{T}_y\Big)\delta v + \Big(T_z - \bar{T}_z\Big)\delta w\Big] ds.\end{aligned} \tag{H.6}$$

This generalized principle is called the Hu-Washizu variational principle.

Thus, the stationary conditions of the functional for the Hu-Washizu variational principle can be obtained as

$$\int_{\Omega_0}\int_{-\frac{h}{2}}^{\frac{h}{2}}\Big[\nabla^{\mathrm{s}}\delta\boldsymbol{u}\cdot\boldsymbol{\sigma}\Big]dzdxdy-\int_{\Omega_0}\int_{-\frac{h}{2}}^{\frac{h}{2}}\bar{\boldsymbol{f}}\cdot\delta\boldsymbol{u}dzdxdy=0, \tag{H.7}$$

$$\int_{\Omega_0}\int_{-\frac{h}{2}}^{\frac{h}{2}}\Big[\Big(\frac{\partial A}{\partial\boldsymbol{\varepsilon}}-\boldsymbol{\sigma}\Big)\cdot\delta\boldsymbol{\varepsilon}\Big]dzdxdy=0, \tag{H.8}$$

$$\int_{\Omega_0}\int_{-\frac{h}{2}}^{\frac{h}{2}}\Big[\Big(-\boldsymbol{\varepsilon}+\nabla^{\mathrm{s}}\boldsymbol{u}\Big)\cdot\delta\boldsymbol{\sigma}\Big]dzdxdy=0, \tag{H.9}$$

for

$$\boldsymbol{u}=\begin{Bmatrix}u\\v\\w\end{Bmatrix},\quad\boldsymbol{\sigma}=\begin{Bmatrix}\sigma_{xx}\\\sigma_{yy}\\\sigma_{zz}\\\tau_{yz}\\\tau_{xz}\\\tau_{xy}\end{Bmatrix},\quad\boldsymbol{\varepsilon}=\begin{Bmatrix}\varepsilon_{xx}\\\varepsilon_{yy}\\\varepsilon_{zz}\\\gamma_{yz}\\\gamma_{xz}\\\gamma_{xy}\end{Bmatrix},\quad\bar{\boldsymbol{f}}=\begin{Bmatrix}\bar{f}_x\\\bar{f}_y\\\bar{f}_z\end{Bmatrix}, \tag{H.10}$$

where $\nabla^{\mathrm{s}}\boldsymbol{u}$ is a symmetric gradient of a displacement field $\boldsymbol{u}$. The other stationary conditions on Γ_σ give natural (or force) boundary conditions:

$$T_x=\bar{T}_x,\quad T_y=\bar{T}_y,\quad T_z=\bar{T}_z. \tag{H.11}$$

Appendix I

EAS: COMPONENTS OF THE STIFFNESS MATRIX K

This appendix presents the components of $\boldsymbol{k}_{u\alpha}$, $\boldsymbol{k}_{\alpha u}$, and $\boldsymbol{k}_{\alpha\alpha}$ in Eq (5.103).

$$\begin{aligned}\left[k_{\mathrm{u}\alpha}^{11}\right]_{ik}^{\mathrm{L}} = \left[k_{\alpha\mathrm{u}}^{11}\right]_{ki}^{\mathrm{L}} = \int_{\Omega_e} \Big[& \frac{\partial \psi_i}{\partial x}\Big(A_{11}\mathbb{G}_m^{1k} + A_{12}\mathbb{G}_m^{2k} + A_{16}\mathbb{G}_m^{3k}\Big) \\ & + \frac{\partial \psi_i}{\partial y}\Big(A_{16}\mathbb{G}_m^{1k} + A_{26}\mathbb{G}_m^{2k} + A_{66}\mathbb{G}_m^{3k}\Big)\Big] dxdy,\end{aligned} \tag{I.1}$$

where $i = 1, ..., 4$ for four-node elements and $k = 1, ..., n$ for an $m \times n$ matrix $\mathbb{G}_m$.

$$\begin{aligned}\left[k_{\mathrm{u}\alpha}^{12}\right]_{ip}^{\mathrm{L}} = \left[k_{\alpha\mathrm{u}}^{21}\right]_{pi}^{\mathrm{L}} = \int_{\Omega_e} \Big[& \frac{\partial \psi_i}{\partial x}\Big(B_{11}\mathbb{G}_b^{1p} + B_{12}\mathbb{G}_b^{2p} + B_{16}\mathbb{G}_b^{3p}\Big) \\ & + \frac{\partial \psi_i}{\partial y}\Big(B_{16}\mathbb{G}_b^{1p} + B_{26}\mathbb{G}_b^{2p} + B_{66}\mathbb{G}_b^{3p}\Big)\Big] dxdy,\end{aligned} \tag{I.2}$$

where $p = 1, ..., n$ for an $m \times n$ matrix $\mathbb{G}_b$.

$$\left[k_{\mathrm{u}\alpha}^{13}\right]_{ip} = \left[k_{\alpha\mathrm{u}}^{31}\right]_{pi} = 0 \tag{I.3}$$

$$\begin{aligned}\left[k_{\mathrm{u}\alpha}^{21}\right]_{ik}^{\mathrm{L}} = \left[k_{\alpha\mathrm{u}}^{12}\right]_{ki}^{\mathrm{L}} = \int_{\Omega_e} \Big\{ & \frac{\partial \psi_i}{\partial y}\Big(A_{12}\mathbb{G}_m^{1k} + A_{22}\mathbb{G}_m^{2k} + A_{26}\mathbb{G}_m^{3k}\Big) \\ & + \frac{\partial \psi_i}{\partial x}\Big(A_{16}\mathbb{G}_m^{1k} + A_{26}\mathbb{G}_m^{2k} + A_{66}\mathbb{G}_m^{3k}\Big)\Big\} dxdy.\end{aligned} \tag{I.4}$$

$$\left[k_{\mathrm{u}\alpha}^{22}\right]_{ip}^{\mathrm{L}} = \left[k_{\alpha\mathrm{u}}^{22}\right]_{pi}^{\mathrm{L}} = \int_{\Omega_e} \Big[\frac{\partial\psi_i}{\partial y}\Big(B_{12}\mathbb{G}_b^{1p} + B_{22}\mathbb{G}_b^{2p} + B_{26}\mathbb{G}_b^{3p}\Big) + \frac{\partial\psi_i}{\partial x}\Big(B_{16}\mathbb{G}_b^{1p} + B_{26}\mathbb{G}_b^{2p} + B_{66}\mathbb{G}_b^{3p}\Big]\Big\}dxdy. \tag{I.5}$$

$$\left[k_{\mathrm{u}\alpha}^{23}\right]_{ip} = \left[k_{\alpha\mathrm{u}}^{32}\right]_{pi} = 0 \tag{I.6}$$

$$\begin{aligned}\left[k_{\mathrm{u}\alpha}^{31}\right]_{ik}^{\mathrm{NL}} = \int_{\Omega_0} \Big[&\frac{\partial\psi_i}{\partial x}\frac{\partial w_0}{\partial x}\Big(A_{11}\mathbb{G}_m^{1k} + A_{12}\mathbb{G}_m^{2k} + A_{16}\mathbb{G}_m^{3k}\Big) \\ &+ \frac{\partial\psi_i}{\partial x}\frac{\partial w_0}{\partial y}\Big(A_{16}\mathbb{G}_m^{1k} + A_{26}\mathbb{G}_m^{2k} + A_{66}\mathbb{G}_m^{3k}\Big) \\ &+ \frac{\partial\psi_i}{\partial y}\frac{\partial w_0}{\partial x}\Big(A_{16}\mathbb{G}_m^{1k} + A_{26}\mathbb{G}_m^{2k} + A_{66}\mathbb{G}_m^{3k}\Big) \\ &+ \frac{\partial\psi_i}{\partial y}\frac{\partial w_0}{\partial y}\Big(A_{12}\mathbb{G}_m^{1k} + A_{22}\mathbb{G}_m^{2k} + A_{26}\mathbb{G}_m^{3k}\Big)\Big]dxdy.\end{aligned} \tag{I.7}$$

$$\begin{aligned}\left[k_{\mathrm{u}\alpha}^{32}\right]_{ip}^{\mathrm{NL}} = \int_{\Omega_0} \Big[&\frac{\partial\psi_i}{\partial x}\frac{\partial w_0}{\partial x}\Big(B_{11}\mathbb{G}_b^{1p} + B_{12}\mathbb{G}_b^{2p} + B_{16}\mathbb{G}_b^{3p}\Big) \\ &+ \frac{\partial\psi_i}{\partial x}\frac{\partial w_0}{\partial y}\Big(B_{16}\mathbb{G}_b^{1p} + B_{26}\mathbb{G}_b^{2p} + B_{66}\mathbb{G}_b^{3p}\Big) \\ &+ \frac{\partial\psi_i}{\partial y}\frac{\partial w_0}{\partial x}\Big(B_{16}\mathbb{G}_b^{1p} + B_{26}\mathbb{G}_b^{2p} + B_{66}\mathbb{G}_b^{3p}\Big) \\ &+ \frac{\partial\psi_i}{\partial y}\frac{\partial w_0}{\partial y}\Big(B_{12}\mathbb{G}_b^{1p} + B_{22}\mathbb{G}_b^{2p} + B_{26}\mathbb{G}_b^{3p}\Big)\Big]dxdy.\end{aligned} \tag{I.8}$$

$$\left[k_{\mathrm{u}\alpha}^{33}\right]_{iq}^{\mathrm{L}} = \left[k_{\alpha\mathrm{u}}^{33}\right]_{qi}^{\mathrm{L}} = \int_{\Omega_0} K\Big[\frac{\partial\psi_i}{\partial x}\Big(A_{45}\mathbb{G}_s^{2q} + A_{55}\mathbb{G}_s^{1q}\Big) + \frac{\partial\psi_i}{\partial y}\Big(A_{44}\mathbb{G}_s^{2q} + A_{45}\mathbb{G}_s^{1q}\Big)\Big]dxdy, \tag{I.9}$$

where $q = 1, ..., n$ for an $m \times n$ matrix $\mathbb{G}_b$.

$$\Big[k_{\mathrm{u}\alpha}^{41}\Big]_{ik}^{\mathrm{L}} = \Big[k_{\alpha\mathrm{u}}^{14}\Big]_{ki}^{\mathrm{L}} = \int_{\Omega_0} \Big[\frac{\partial \psi_i}{\partial x}\Big(B_{11}\mathbb{G}_m^{1k} + B_{12}\mathbb{G}_m^{2k} + B_{16}\mathbb{G}_m^{3k}\Big) + \frac{\partial \psi_i}{\partial y}\Big(B_{16}\mathbb{G}_m^{1k} + B_{26}\mathbb{G}_m^{2k} + B_{66}\mathbb{G}_m^{3k}\Big)\Big] dxdy. \tag{I.10}$$

$$\Big[k_{\mathrm{u}\alpha}^{42}\Big]_{ip}^{\mathrm{L}} = \Big[k_{\alpha\mathrm{u}}^{24}\Big]_{pi}^{\mathrm{L}} = \int_{\Omega_0} \Big[\frac{\partial \psi_i}{\partial x}\Big(D_{11}\mathbb{G}_b^{1p} + D_{12}\mathbb{G}_b^{2p} + D_{16}\mathbb{G}_b^{3p}\Big) + \frac{\partial \psi_i}{\partial y}\Big(D_{16}\mathbb{G}_b^{1p} + D_{26}\mathbb{G}_b^{2p} + D_{66}\mathbb{G}_b^{3p}\Big)\Big] dxdy. \tag{I.11}$$

$$\Big[k_{\mathrm{u}\alpha}^{43}\Big]_{iq}^{\mathrm{L}} = \Big[k_{\alpha\mathrm{u}}^{34}\Big]_{qi}^{\mathrm{L}} = \int_{\Omega_0} K\psi_i\Big(A_{45}\mathbb{G}_s^{2q} + A_{55}\mathbb{G}_s^{1q}\Big) dxdy. \tag{I.12}$$

$$\Big[k_{\mathrm{u}\alpha}^{51}\Big]_{ik}^{\mathrm{L}} = \Big[k_{\alpha\mathrm{u}}^{15}\Big]_{ki}^{\mathrm{L}} = \int_{\Omega_0} \Big[\frac{\partial \psi_i}{\partial x}\Big(B_{16}\mathbb{G}_m^{1k} + B_{26}\mathbb{G}_m^{2k} + B_{66}\mathbb{G}_m^{3k}\Big) + \frac{\partial \psi_i}{\partial y}\Big(B_{12}\mathbb{G}_m^{1k} + B_{22}\mathbb{G}_m^{2k} + B_{26}\mathbb{G}_m^{3k}\Big)\Big] dxdy. \tag{I.13}$$

$$\Big[k_{\mathrm{u}\alpha}^{52}\Big]_{ip}^{\mathrm{L}} = \Big[k_{\alpha\mathrm{u}}^{25}\Big]_{pi}^{\mathrm{L}} = \int_{\Omega_0} \Big[\frac{\partial \psi_i}{\partial x}\Big(D_{16}\mathbb{G}_b^{1p} + D_{26}\mathbb{G}_b^{2p} + D_{66}\mathbb{G}_b^{3p}\Big) + \frac{\partial \psi_i}{\partial y}\Big(D_{12}\mathbb{G}_b^{1p} + D_{22}\mathbb{G}_b^{2p} + D_{26}\mathbb{G}_b^{3p}\Big)\Big] dxdy. \tag{I.14}$$

$$\Big[k_{\mathrm{u}\alpha}^{53}\Big]_{iq}^{\mathrm{L}} = \Big[k_{\alpha\mathrm{u}}^{35}\Big]_{qi}^{\mathrm{L}} = \int_{\Omega_0} K\psi_i\Big(A_{44}\mathbb{G}_s^{2q} + A_{45}\mathbb{G}_s^{1q}\Big) dxdy. \tag{I.15}$$

$$\begin{aligned}\left[k_{\alpha u}^{13}\right]_{gj}^{\mathrm{NL}} = \int_{\Omega_0} \frac{1}{2}\Big\{ & \mathbb{G}_m^{1g}\Big[A_{11}\frac{\partial w_0}{\partial x}\frac{\partial \psi_j}{\partial x} + A_{12}\frac{\partial w_0}{\partial y}\frac{\partial \psi_j}{\partial y} \\ & + A_{16}\Big(\frac{\partial w_0}{\partial y}\frac{\partial \psi_j}{\partial x} + \frac{\partial w_0}{\partial x}\frac{\partial \psi_j}{\partial y}\Big)\Big] \\ & + \mathbb{G}_m^{2g}\Big[A_{12}\frac{\partial w_0}{\partial x}\frac{\partial \psi_j}{\partial x} + A_{22}\frac{\partial w_0}{\partial y}\frac{\partial \psi_j}{\partial y} \\ & + A_{26}\Big(\frac{\partial w_0}{\partial y}\frac{\partial \psi_j}{\partial x} + \frac{\partial w_0}{\partial x}\frac{\partial \psi_j}{\partial y}\Big)\Big] \\ & + \mathbb{G}_m^{3g}\Big[A_{16}\frac{\partial w_0}{\partial x}\frac{\partial \psi_j}{\partial x} + A_{26}\frac{\partial w_0}{\partial y}\frac{\partial \psi_j}{\partial y} \\ & + A_{66}\Big(\frac{\partial w_0}{\partial y}\frac{\partial \psi_j}{\partial x} + \frac{\partial w_0}{\partial x}\frac{\partial \psi_j}{\partial y}\Big)\Big]\Big\} dxdy,\end{aligned} \tag{I.16}$$

where $j = 1, ..., 4$ for four-node elements and $g = 1, ..., n$ for an $m \times n$ matrix $\mathbb{G}_m$.

$$\begin{aligned}\left[k_{\alpha u}^{23}\right]_{fj}^{\mathrm{NL}} = \int_{\Omega_0} \frac{1}{2}\Big\{ & \mathbb{G}_b^{1f}\Big[B_{11}\frac{\partial w_0}{\partial x}\frac{\partial \psi_j}{\partial x} + B_{12}\frac{\partial w_0}{\partial y}\frac{\partial \psi_j}{\partial y} \\ & + B_{16}\Big(\frac{\partial w_0}{\partial y}\frac{\partial \psi_j}{\partial x} + \frac{\partial w_0}{\partial x}\frac{\partial \psi_j}{\partial y}\Big)\Big] \\ & + \mathbb{G}_b^{2f}\Big[B_{12}\frac{\partial w_0}{\partial x}\frac{\partial \psi_j}{\partial x} + B_{22}\frac{\partial w_0}{\partial y}\frac{\partial \psi_j}{\partial y} \\ & + B_{26}\Big(\frac{\partial w_0}{\partial y}\frac{\partial \psi_j}{\partial x} + \frac{\partial w_0}{\partial x}\frac{\partial \psi_j}{\partial y}\Big)\Big] \\ & + \mathbb{G}_b^{3f}\Big[B_{16}\frac{\partial w_0}{\partial x}\frac{\partial \psi_j}{\partial x} + B_{26}\frac{\partial w_0}{\partial y}\frac{\partial \psi_j}{\partial y} \\ & + B_{66}\Big(\frac{\partial w_0}{\partial y}\frac{\partial \psi_j}{\partial x} + \frac{\partial w_0}{\partial x}\frac{\partial \psi_j}{\partial y}\Big)\Big]\Big\} dxdy,\end{aligned} \tag{I.17}$$

where $f = 1, ..., n$ for an $m \times n$ matrix $\mathbb{G}_b$.

$$\left[k_{\alpha\alpha}^{11}\right]_{gk}^{\mathrm{L}} = \int_{\Omega_0} \Big[\mathbb{G}_m^{1g}\Big(A_{11}\mathbb{G}_m^{1k} + A_{12}\mathbb{G}_m^{2k} + A_{16}\mathbb{G}_m^{3k}\Big) + \mathbb{G}_m^{2g}\Big(A_{12}\mathbb{G}_m^{1k} + A_{22}\mathbb{G}_m^{2k} + A_{26}\mathbb{G}_m^{3k}\Big) + \mathbb{G}_m^{3g}\Big(A_{16}\mathbb{G}_m^{1k} + A_{26}\mathbb{G}_m^{2k} + A_{66}\mathbb{G}_m^{3k}\Big)\Big] dxdy. \tag{I.18}$$

$$\left[K_{\alpha\alpha}^{12}\right]_{gp}^{\mathrm{L}} = \left[K_{\alpha\alpha}^{21}\right]_{pg}^{\mathrm{L}} = \int_{\Omega_0} \Big[\mathbb{G}_m^{1g}\Big(B_{11}\mathbb{G}_b^{1p} + B_{12}\mathbb{G}_b^{2p} + B_{16}\mathbb{G}_b^{3p}\Big) + \mathbb{G}_m^{2g}\Big(B_{12}\mathbb{G}_b^{1p} + B_{22}\mathbb{G}_b^{2p} + B_{26}\mathbb{G}_b^{3p}\Big) + \mathbb{G}_m^{3g}\Big(B_{16}\mathbb{G}_b^{1p} + B_{26}\mathbb{G}_b^{2p} + B_{66}\mathbb{G}_b^{3p}\Big)\Big] dxdy. \tag{I.19}$$

$$\left[k_{\alpha\alpha}^{13}\right]_{ip} = \left[k_{\alpha\alpha}^{31}\right]_{pi} = 0 \tag{I.20}$$

$$\left[k_{\alpha\alpha}^{22}\right]_{fp}^{\mathrm{L}} = \int_{\Omega_0} \Big[\mathbb{G}_b^{1f}\Big(D_{11}\mathbb{G}_b^{1p} + D_{12}\mathbb{G}_b^{2p} + D_{16}\mathbb{G}_b^{3p}\Big) + \mathbb{G}_b^{2f}\Big(D_{12}\mathbb{G}_b^{1p} + D_{22}\mathbb{G}_b^{2p} + D_{26}\mathbb{G}_b^{3p}\Big) + \mathbb{G}_b^{3f}\Big(D_{16}\mathbb{G}_b^{1p} + D_{26}\mathbb{G}_b^{2p} + D_{66}\mathbb{G}_b^{3p}\Big)\Big] dxdy. \tag{I.21}$$

$$\left[k_{\alpha\alpha}^{23}\right]_{ip} = \left[k_{\alpha\alpha}^{32}\right]_{pi} = 0 \tag{I.22}$$

$$\left[k_{\alpha\alpha}^{33}\right]_{eq}^{\mathrm{L}} = \int_{\Omega_0} \Big[\mathbb{G}_s^{4e}\Big(A_{45}\mathbb{G}_s^{2q} + A_{55}\mathbb{G}_s^{1q}\Big) + \mathbb{G}_s^{5e}\Big(A_{44}^s\mathbb{G}_s^{2q} + A_{45}^s\mathbb{G}_s^{1q}\Big)\Big] dxdy, \tag{I.23}$$

where $e = 1, ..., n$ for an $m \times n$ matrix $\mathbb{G}_s$.